STRESS-STATE AND STRAIN-RATE DEPENDENT MULTISCALE CHARACTERIZATION OF ARMOX 500T

Diego Mateos

A Thesis submitted to the Faculty of Graduate Studies in Partial Fulfillment of the Requirements for the Degree of Master of Applied Science

Mechanical Engineering

York University, Toronto, Ontario

August 2023

ABSTRACT

A strain-rate and stress-state dependent experimental characterization is conducted for the parameterization of a triaxiality and lode angle parameter (LAP) dependent Generalized Incremental Stress-State Dependent Damage Model (GISSMO) for ARMOX 500T (AX500) armour steel. 100+ mechanical tests have been conducted which differentiate the effects of triaxiality, LAP, and strain-rate on instability and fracture strains. Quasistatic characterization tests have been conducted at 18 different stress-states abiding by previous GISSMO literature and ASTM standards. LaVision's Digital Image Correlation (DIC) system is employed in 2D & stereo 3D configurations to acquire high resolution full-field strain measurements. The stain-paths are quantified in the fracture regions of all specimens, from which in-situ equivalent plastic strains are derived.

A novel and low-cost Tensile Hopkinson bar has been designed and constructed for dynamic characterization of ductile metals at intermediate to high strain rates (500-1500 /s). High strain rate mechanical tests coupled with high-speed 2D-DIC have been conducted to provide a strain-rate dependent GISSMO extension to the model. Two Hopkinson bars (direct compression, split-tension) have been used to provide lode angle dependent strain-rate hardening data on stress-states of axisymmetric compression and tension covering the lode angle parameter values of -1 and 1, respectively. In addition, two cylindrical inclined compression-shear specimens with varied angles have been impacted at high strain rate to quantify the effect of stress-state on the formation and evolution of Adiabatic Shear Bands (ASBs) and their consequential effect on ductility. This innovative dynamic characterization procedure is conducted to stipulate diligent test matrices and enable improved multiscale terminal ballistics simulations on novel combat vehicle development, with the purpose to increase the predictability of shear plugging.

High strain rate axisymmetric compression, compression-shear and tension specimens have been investigated using a combination of optical (OM) and electron microscopy (SEM/TEM) to elucidate their microstructural evolution. Ductile fracture is observed under all stress-states, with changes from mode I to mode II crack formation from positive to negative lode angles. Under axisymmetric dynamic tension, enhanced damage tolerance in comparison to quasistatic loading is found attributed to increased dislocation pileups (work hardening) and subsequent ductile void growth responsible for enhanced plastic flow during necking. Axisymmetric dynamic compression reveals a severe loss of global ductility and strengthening not observed under quasistatic loading, with continuous work hardening until premature fracture and localized hardening in the ASB regions. Compression-shear specimens reveal higher susceptibility to ASB initiation with increasing angle of inclination (shear stress) and corresponding ductility loss due to increased strain localization along the plane of maximum shear. Lastly, ASB multisite microcrack initiation and coalescence, multi-directional cracking, secondary ASBs and bifurcation, nanosized grain refinement, nanoscale twinning, and dislocation cell networks are found within triaxial ASB regions revealing that AX500 has various energy absorbing mechanisms to delay crack propagation and fracture after the onset of ASB initiation.

DECLARATION

This work is supported by Defense Research and Development Canada (DRDC), General Dynamics Land Systems – Canada, and NP Aerospace through the NSERC Alliance project ALLRP 560447-2020. The observations, views, and conclusions in this document are those of the authors and should not be interpreted as representing the official policies, either expressed or implied, of General Dynamics, NP Aerospace, DRDC or the Government of Canada.

ACKNOWLEDGEMENTS

First and foremost, I would like to thank my supervisor, Dr. Solomon Boakye-Yiadom for his guidance, patience, mentorship, and for his dedication, trust, and commitment to enable me to drive and manage my own innovative research. Thank you for pushing me to think critically and skeptically, to rely on evidence, and for diligently reminding me to follow scientific principles.

I would also like to thank Dr. Garrett Melenka, for his support during my thesis and for his guidance and expertise in digital image correlation and optical measurement techniques. Thank you for providing me with the knowledge and tools to produce reliable high quality full-field data. In addition, I would like to thank my friend and colleague Alexander Dondish, for his expertise in digital image correlation, technical discussions on the matter, and non-technical discussions in the lab.

A special thanks as well to Norman Nichols, who helped me with the installation, setup, and maintenance of the electrical and pneumatic components of my tensile Hopkinson bar. Thank for your time and dedication to the project. By extension I would like to thank the mechanical technicians, Armando Azevedo and Florin Alexandru, for their time and dedication in training me on all mechanical equipment and helping with troubleshooting issues whenever requested.

I would also like to thank my colleagues Solomon Hanson-Duntu and Joseph Agyapong for their time in supporting me with my work and training me on metallography, materials science, metallurgy, and material characterization. In addition, I am grateful to my good friend and colleague Nikeet Pandit with whom I could share technical thoughts and discussions on data analysis and scientific principles.

I am extremely grateful to my parents for their unconditional love, guidance, belief in me, and endless support. Thank you to my sister, Celina Sieber-Espidio, for being the best and most beautiful sister ever inside and out. It warms my heart to see you thrive at the things you love.

Finally, I would like to express my heartfelt gratitude to my beautiful wife, Tamila Mateos. Thank you for tolerating my inexplicable excitement over fracture mechanics and materials science, for dealing with my unpredictable work habits and further for supporting me in my work, and most of all, for your endless and kind-hearted love.

DEDICATION

To my beautiful wife, *Tamila Mateos,* for your selfless love, encouragement, endless support, and lovingkindness, you inspire me everyday by your empathy, grace, faith, and embodiment of the holy spirit.

To my wonderful sister, *Celina Sieber-Espidio,* your strength, skill, passion, energy, and willful spirit inspires me and makes me very happy.

To my parents, *Flor Corina Morales Espidio* and *Rafael Mateos Zenteno*, for encouraging my curiosity, inception of hope, and for your sacrificial & unconditional love.

"God is omnipresent not virtually only, but also

substantially, for virtue cannot subsist

without substance" – Isaac Newton

Table of Contents

List of Figures

List of Tables

List of Abbreviations

AHSS	Advanced High Strength Steel
APFSDS	Armour Piercing Fin Stabilized Discarding Sabot
ASB	Adiabatic Shear Band
ASTM	American Society for Testing and Materials
AX500	ARMOX 500T
B_4C	Boron Carbide
BCC	Body Centered Cubic
BCT	Body Centered Tetragonal
BF	Bright Field
CNC	Computer Numerical Control
DF	Dark Field
DHA	Dual Hardness Armour
DHF	Ductile Hole Formation
DIC	Digital Image Correlation
DIHB	Direct Impact Hopkinson Pressure Bar
DRX	Dynamic Recrystallization
EBSD	Electron Backscatter Diffraction
EELS	Electron Energy Loss Spectroscopy
EDM	Electric Discharge Machining
EHF	Electrohydraulic Forming
FCC	Face Centered Cubic
FMLB	Flange Mounted Linear Bearing
GISSMO	Generalized Incremental Stress-State Dependent Damage Model
HCP	Hexagonally Closed Packed
HRC	Rockwell Hardness
HV	Vickers micro-hardness
IRT	Infrared Thermography
ISS	International Space Station
JC	Johnson-Cook model

KEP	Kinetic Energy Penetrator
LAP	Lode Angle Parameter
LEO	Low Earth Orbit
MMOD	Micro-Meteorite and Orbital Debris
MRHA	Modified Rolled Homogenous Armour
NTSDI	Normalized Third Deviatoric Stress Invariant
OM	Optical Microscope
RDRX	Rotational Dynamic Recrystallization
RHA	Rolled Homogenous Armour
SADP	Selected Area Diffraction Pattern
SEM	Scanning Electron Microscope
TEM	Transmission Electron Microscope
TSHB	Tensile Split Hopkinson Pressure Bar
TQ	Taylor Quinney Coefficient
UHSS	Ultra High Strength Steel

1.0 Background & Introduction

1.1 Lightweight Armoured Vehicles

With rising population densities, oil and gas prices, migration rates and ever-growing natural disasters due to the inescapable rise of global warming and geopolitical conflict, there is a continuously growing burden on resources leading to major conflict zones across the globe [1], [2]. Canadian military allies and their citizens require various forms of military aid for the foreseeable future. In modern warfare environments such as Ukraine, major combat vehicle battles have occurred, commanding the defence against armour piercing fin-stabilized discarding sabot (APFSDS) kinetic energy impactors [3]. Canada is uniquely positioned to provide military aid in these present and potential conflict zones, with an emphasis on provision of modern vehicles able to defeat modern threats, aiding mass migrations, monitoring the arctic northwest passage, facilitating search and rescue operations, and providing infrastructure and transportation services for Canadian armed forces, first aid response teams, and civilians [1]. Canadian soldiers and medics must have the capability to move swiftly and safely throughout these conflict zones which drives the need for vehicles equipped with lightweight armour with high ballistic performance. This thesis will focus on the metallic material characterization of a ceramic based multi-material armour solution which provides protection against a Tungsten (W) 30mm APFSDS surrogate threat.

The armour baseline design shall consist of an ARMOX 500T (AX500) steel backing plate bonded to ceramic tiles bonded to a carbon fiber reinforced cover. The mechanical performance and contact/interaction mechanics between the layers of the armour solution will have a profound effect on its ballistic performance. It is therefore critical to develop and understand the plastic deformation mechanics, failure mechanisms, and fracture modes of the metallic backing plate. The primary purpose of this thesis is to provide a mechanical and material characterization of the metallic backing plate; with an emphasis on high strain rate effects, stress state and strain-path dependency, and underlying microstructural deformation and failure mechanisms, to enable multiscale finite element analysis (FEA) simulations in LS-DYNA using the GISSMO.

Stress state dependent damage modeling enables simulation driven design practices, facilitating an engineering capability to increase the predictability of ductile metal plasticity and fracture during processing and service conditions. Traditionally, metallic alloy engineering structures in the aerospace, automotive, defence and energy industries are conservatively designed to mitigate failure. Accurate prediction of their deformation and failure behavior enables performance optimization, structural light weighting, and a reduction of greenhouse gas emissions and manufacturing costs. While the effects of stress-state have been well characterized for many ductile metals at quasistatic strain rates, the effects of stress-state on the mechanical behavior of materials at dynamic strain rates has not been suitably investigated. At these high strain rates, a narrow region of strain localization known as adiabatic shear localization or adiabatic shear band (ASB) formation is the dominant mechanism of failure in compressive and shear stress-states. Stress-state and strain-rate dependent effects on plasticity are critically important in dynamic deformation applications such as automotive and aircraft structures, advanced manufacturing, turbomachinery, spacecraft Whipple shields, and military vehicle armour.

Currently, there is a lack of a sophisticated predictive multi-scale numerical modeling capability based on empirical data for modern challenges such as impact resistant armour for medium caliber threats. There is also a lack of an experimental calibration procedure for higher strain rates in fracture models such as GISSMO; usually, insubstantial results at one stress state are extrapolated to obtain fracture loci. In terminal ballistics, prediction of the shear plugging failure mode, which occurs due to ASB formation, remains elusive due to the lack of methodical high strain rate test matrices.

Systematic studies of the effects of stress-state and strain-rate on ASBs also remain largely uninvestigated. With respect to AX500, no stress-state effects on ASB formation and its consequential effects on ductility have been quantified for fracture models. Additionally, no microstructural investigation of its behavior under high strain rate tension has been conducted. This can often be overlooked and is critical supplementary data for the development of empirical fracture initiation and instability criteria, which can improve the accuracy of the model and its prediction of the ensuing failure mode. This is particularly critical in high strain rate ballistic applications using high hardness ductile steels which are prone to stress state dependent instabilities. This information offers insight into the macroscale plasticity behavior and understanding the limitations of ARMOX 500T enables the future development of steels with improved ballistic performance. Multiscale material characterization is therefore an important procedure for researchers and designers interested in simulations which use a combination of phenomenological / micromechanical modeling approaches to increase accuracy and sophistication of plasticity models. Rigorous experimental data and numerical modeling is required for this endeavour, and the conducted research will focus on the experimental data development for AX500.

1.2 Engineering Applications

1.2.1.1 Terminal Ballistics

Ballistic impact is primarily dictated by impact and wave mechanics where plastic stress waves propagate at the speed of the sound of the material [4]. For this thesis, the proposed ceramic based composite armour solution can be visualized in Figure 1.1 where the backing layer is the metallic armour plate. It is designed for an impact angle of 60 degrees which is a common impact angle for medium caliber threats and is expected to have a minimum areal density of 170 kg/m^3.

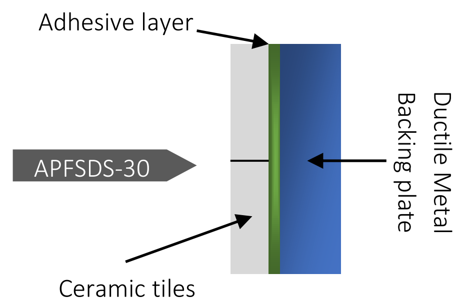

Figure 1.1: Ceramic based multi-material armour with ductile metal backing plate

The high impact velocities associated with the impact of APFSDS rounds on armour have ultra-high kinetic energy resulting in the propagation of stress waves within the material. This leads to exceptionally high loading rates in the order of 10^2-10^5 s^{-1} throughout the event [4]. At these strain rates, dislocations do not have the time to bow out or slip as they do in quasistatic regimes. Consequentially, there is a strengthening effect due to decreased dislocation mobility, thereby changing the dominant microstructural deformation mechanisms as a function of strain rate [5]. There are also viscous and thermal inertia effects taking place which lead to phonon drag and adiabatic heating effects in the microstructure, respectively. These mechanisms depend on the applied stress, the stress-state, and the microstructure of the material. Furthermore, the strain rates may increase drastically throughout the impact process in localized regions of the armour thereby affecting the local material properties of the material. All these factors can ultimately change the ensuing fracture propagation and failure mode of the metallic armour [4], [6], [7]. It is therefore especially critical to account for strain-rate and stress-state in damage models for ballistic simulations involving APFSDS kinetic energy impactors.

1.2.1.2 Advanced Manufacturing

Intermediate to high strain rates ($1\text{-}10^3\ s^{-1}$) have been known to occur during various manufacturing processes including high speed machining, cold spray additive manufacturing, explosive welding, and various forming processes such as forging and electrohydraulic forming [8]–[11]. The metal production industry must therefore have the means to produce a well-standardized and metallurgically characterized product with maximum production efficiency. Therefore, it is important to understand all process parameters that affect the microstructure and develop computational models to predict resulting material properties. Simultaneously, clients must account for any pre-damage from the production process in their service life simulations. This drove the development of the GISSMO in the sheet metal forming and automotive industry [12]

It is highlighted by Guo et al. [9] that the propagation of stress waves in bimetallic joints such as those created by explosive welding is rarely characterized and can have a significant effect on the dynamic material strength due to the materials impedance mismatch. Rajani et al. [11] also highlight that that there is a material and process dependent critical impact energy at which initiation of unwanted adiabatic strain localization will occur during the explosive cladding process. Another bimetallic joining process is cold spray such as those used in multi-layer vehicle armour bonding layers where stress waves are known to have dominant effects on failure modes [2]. In addition, the velocity of particle impact during cold spray has been demonstrated to influence the quality of the resulting coating [8]. The critical adhesion velocity for bonding to occur is dependent on the strain-rate dependent dynamic strength of the material. An emerging application of both cold spray and explosive welding is in rocket engine combustors [13]–[15].

Lastly, high strain characterization is critical in electrohydraulic forming (EHF) processes [10]. The high strain rate characterization of oxygen-free electronic copper for use in EHF simulations is vital to the development of superconducting radiofrequency cavities. The cavities will be employed in the future circular particle collider currently under development by CERN [16][17], which will have a 100 TeV collision energy, a tenfold increase over the large Hadron collider.

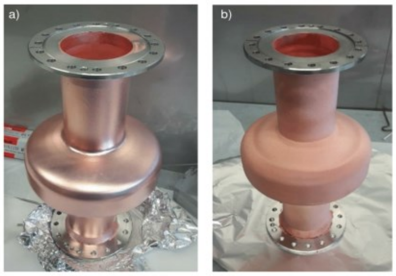

Figure 1.2: SRC's manufactured by electrohydraulic forming at CERN [17]

Figure 1.3: Additively manufactured bimetallic copper-nickel alloy rocket combustors developed by NASA [14]

1.2.1.3 Crashworthiness

The GISSMO was primarily developed for crashworthiness simulations in the automotive industry in 2008 by Neukamm et al. [12][18]. In the industry, companies continued to spend heavy budgets on destructive crash testing and while damage modeling was available, it was often not robust enough to qualify the new advanced high strength steel (AHSS) structures to the required regulated standards. There were a few problems, the first of which was that automotive material standards are based on ASTM, and this dictates quasistatic regimes. There are currently no standards for dynamic or high strain rate mechanical characterization of metallic materials, which; during crash, steel structures can reach strain rates of 1-10^3 s^{-1}.

Figure 1.4: Typical metal alloys used in automotive chassis

Another problem was the lack of predictive capacity of non-proportional loading, which is the change of the stress state of the structure throughout loading. The renowned Johnson and Cook (JC) model and many of its extensions often could not predict ductility losses during non-proportional loading from uniaxial tension to plane strain, or the loss of ductility under shear-dominated stress-states. Another limitation was that during forming of the sheet metal parts making up the chassis structure, the components build up microstructural damage in localized regions due to intense plastic deformations resulting in cracks or pre-sustained damage which could not be accounted for. Some innovative work is being done in the development of Advanced and Ultra High Strength Steels (AHSS/UHSS) with tailored properties in specific regions where high plastic strains are expected during forming or crash. Novel steels such as tailored hot formed boron steels can be mechanically characterized for GISSMO parameterization, and this is a currently a frontier of research [19], [20].

1.2.1.4 Gas Turbines and Air-breathing Propulsion

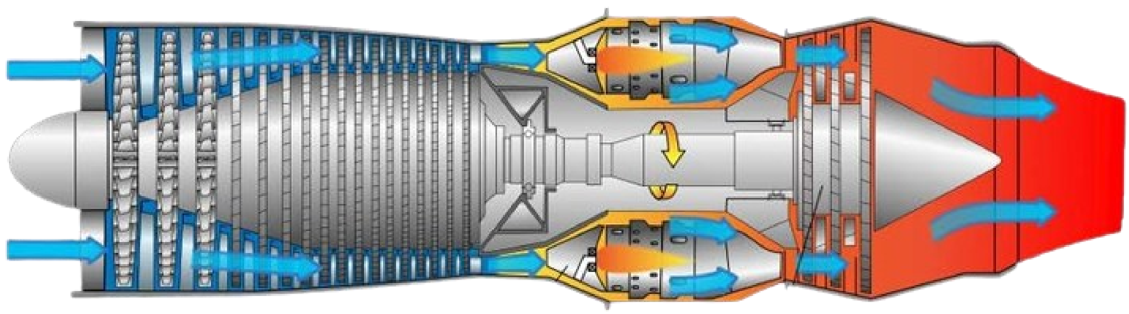

Figure 1.5: Turbojet Engine [21]

The aerospace and energy industries are drastically shifting towards sustainable supply chains with a focus on reducing emissions while optimizing power to weight ratios [21]. This is pushing the boundaries of materials science and engineering with respect to high temperature phase stability of the utilized materials, and simulation driven design optimization enabled by additive manufacturing to maximize work output through minimization of thermodynamic losses. An example is the design of geometrically complex injector assemblies, and intake/exhaust ducts and manifolds to minimize fluid pressure losses [22].

In air breathing subsonic and hypersonic propulsion, the high strain rate characterization of jet turbine engine materials is critical to the system. Specifically, blade loss, burst disk, and foreign object damage scenarios such as bird strikes must be accounted for, and containment of the damage must be demonstrated prior to flight qualification [23], [24]. Materials must have stress-state, strain-rate, and temperature dependent models for accurate prediction of their behavior in these conditions. This enables investigations into novel materials such as phase transformation strengthened superalloys, or hyperdimensional design of additively manufactured high entropy alloys for critical components such as turbine blades, combustor domes, exhaust casings, afterburners, and adjustable nozzle vanes [25]–[33].

1.2.1.5 Hypervelocity Impact

Amongst anti-satellite missile tests, spacecraft collisions, and micrometeorites, there is an unsustainable increase of orbital debris in low earth orbit (LEO). There is therefore a requirement for micrometeorite and orbital debris mitigation (MMOD). Small objects less than 1 cm that cannot be tracked/avoided impose the greatest risk which can travel at relativistic speeds of 1-16 km/s in LEO [34]. At velocities greater than 4-5 km/s, the speed of sound of materials is less than the impact velocity. This induces the formation of shockwaves in the material, resulting in the superimposition of progressing and reflecting shock waves throughout the structure, having significant effects on dislocation mechanics through phonon drag effects [35], [36]. This type of hypervelocity impact is mitigated with strategically located Whipple shields, such as those on the international space station (ISS) shown in Figure 1.6. At these impact momentum's, the strain rates are on the order of 10^4-10^7 s^{-1} [4]. Both front and back plates in Whipple shields require accurate modeling to predict if penetration will occur, especially when human spaceflight is involved. There are also hypersonic weapons and threats which are reaching this velocity regime requiring the need for military vehicles with suitable armour to mitigate these threats [37].

Figure 1.6: Whipple shields on the Columbus science laboratory on the ISS [10].

With the new era of space exploration, human presence in space will increase and so will the demand for low design margin solutions for MMOD. Impact risk analysis guides systems engineering decisions for shielding locations, an example for the ISS can be seen in Figure 1.7 [38]. Notably, the risk of impact varies as a function of orbital debris flux, and Figure 1.7 is at one instance of true anomaly. Conclusively, there is a requirement for the development of phenomenological hypervelocity impact models for Defence and space applications with adequate incorporation of inertial effects as a function of impact energy.

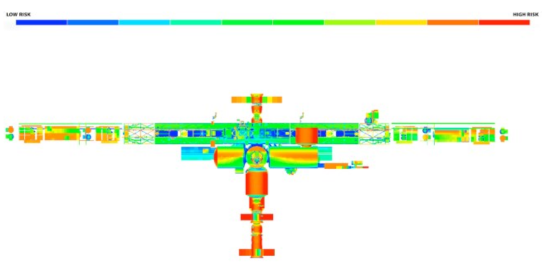

Figure 1.7: Impact risk of the ISS by NASA, at specific true anomaly [38]

1.3 Objectives and Outline of Thesis

1.3.1.1 Objectives

The primary objective of this research is to quantitatively capture the stress state and strain rate dependent plasticity behavior and strain-path history during quasistatic and dynamic loading of AX500 using the full field measurement technique known as digital image correlation (2D/3D-DIC). This will enable the mechanical characterization of AX500 to find plasticity parameters such as the empirical strain hardening, strain-rate hardening, and softening parameters and identify the stress state dependent fracture and instability strains required for GISSMO parameterization. Acquiring statistically robust and accurate in-situ equivalent plastic instability and fracture strains under strain-rate and stress-state effects using DIC is the primary objective of the research. Part of this objective is to provide a unique continuum mechanics based dynamic characterization test matrix with lode angle dependence, which is usually ignored at dynamic strain rates. This test matrix aims to capture the effect of stress-state on adiabatic shear bands (ASBs) and provide parametrization data from stress-strain and DIC sources using tensile and compressive Hopkinson bars.

The secondary objective of this research constitutes investigating the underlying deformation and failure mechanisms with dependence on stress-state and strain rate. Specifically, systematic microstructural investigations of AX500 under high strain rate compression and tension have not been conducted. The mechanisms of deformation will differ depending on the stress-state and strain-rate and understanding these failure mechanisms will offer insight into the performance and limitations of AX500 with respect to terminal ballistics. Therefore, it is an objective of this research to conduct high strain rate tests which differentiate the effects of stress-state, strain-rate, and strain on the microstructural evolution of the material. Based on macroscopic observations of the force-time curves, it is an objective to conduct deeper microstructural investigations with as received and post-mortem electron microscopy.

Ultimately, the dynamic GISSMO characterization procedure, coupled with ultra-high-speed imaging and multiscale microscopy techniques will offer insights into understanding the structure-property relationships between the microstructure and macroscale response of the material. The objective is to enable multiscale finite element simulations in LS-DYNA for the armour solution.

1.3.1.2 Outline of Thesis

The Thesis is divided into 6 sections which are summarized as follows:

1. Introduces the reader to the motivation behind the research. Provides insight into the cross-disciplinary nature of the materials science and characterization research, and the multi-faceted approach of high strain rate characterization with a range of engineering applications.
2. A literature review of metallic armour in terminal ballistics, stress-state dependent damage modeling, dynamic characterization, and the full-field measurement techniques employed.
3. An overview of the experimental methods used, including the author's design and construction of a tensile Hopkinson bar testing machine, a description of all the Hopkinson bar systems used for dynamic characterization, and the methodologies employed for quasistatic, dynamic, and microstructural material characterization for the multiscale GISSMO model data development.
4. Experimental analysis of the mechanical and microstructural as received condition of the AX500 steel from SSAB, Sweden. Results, analysis, and discussion of the quasistatic characterization for traditional phenomenological GISSMO model parameterization.
5. Results, analysis, and discussion of the dynamic characterization of AX500 for a strain-rate dependent GISSMO extension. Results, analysis, and discussion of microstructural characteristics of AX500 to reveal the underlying deformation and failure mechanisms under high strain rate tension, compression, and compression-shear stress states.
6. Conclusions and outcomes of the research are summarized, and suggestions for future work are offered to improve upon Hopkinson bar design and dynamic calibration procedures for stress-state dependent damage models, while highlighting the shortcomings of the current work.

2.0 Literature Review

2.1 Overview of Terminal Ballistics

This section provides an overview of the physics of kinetic energy penetrator (KEP) impacts on metallic armour and on the mechanical metallurgy of metallic armour. Typically, KEP impact velocities range from 1000-2000 m/s [4], [39]. In this regime, plastic stress waves propagate through the material at the speed of sound of the material which is generally above 4000 m/s in metal alloys, resulting in greater stress-wave propagation velocity than impact velocity. This consequentially results in plastic deformation in the metallic armour ahead of the impactor, resulting in microstructural changes in the material ahead of the impactor. These stress waves are also transmitted and reflected at interfaces in multi-armor systems and free ends in both multi-armor and monolithic systems. Furthermore, as mentioned previously in section 1.2.1.1, the plastic flow of the armour is a dynamic process meaning there are viscous and thermal inertia effects taking place which result in severe strain localization, localized pressures, and localized high strain rates and temperatures. Simultaneously, the nose shape, impact energy, angle of impact, and in-situ deformation of the impactor will affect the deformation and failure mechanisms of the armour.

2.1.1 Metallic Armour Failure Mechanisms

2.1.1.1 Ductile Hole Formation (DHF)

This is an efficient energy absorbing mechanism known to occur in ductile metallic armour, usually resulting from pointed KEP's. In this deformation mechanism, plastic deformation occurs with no mass loss of the armour and volume is constant. Energy of the impact is absorbed as plastic deformation of the material. The plastic flow direction is outward (rearward) ahead of the round due to the plastic waves, resulting in a rear bulge of the armour plate. This has the potential to evolve into a failure mechanism known as petalling in the entry (frontward) point of the KEP which occurs primarily due to tensile and tensile-shear stresses.

The resistance of the armor is primarily attributed to the in-plane compression yield and ultimate strengths, which is strain-rate and temperature dependent. However, due to the nature of impact mechanics, this is a dynamic process where adiabatic heating and viscous inertia will occur in highly localized zones. Furthermore, the hydrostatic pressure and deviatoric stress components will have a strong effect on the compressive strength of the material and its consequential plastic behavior. Ultimately, this is a desirable deformation mechanism with proven penetration resistance and minimization of rearward fragmentation effects that could damage personnel in combat vehicles [4]. Figure 2.1 illustrates the failure mode for a pointed projectile revealing the rear bulging and front petalling mechanisms.

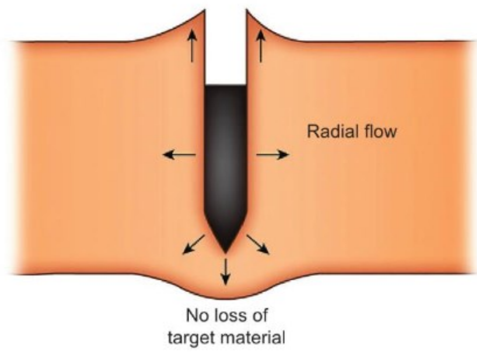

Figure 2.1: Ductile hole formation with constant volume. Rear bulging and front petalling mechanisms shown.

2.1.1.2 Shear Plugging

This is a failure mechanism occurring due to adiabatic shear banding of the armour plate. It absorbs a reduced amount of energy compared to DHF and usually occurs when impacted by blunted projectiles as shown in Figure 2.2. Due to the propagation of plastic stress waves ahead of the material, ASBs may form depending on the impact energy and the ability of the material to resist ASB formation. Naturally, the blunted projectile creates a region of intense localized shear stress and strain, resulting in a state of transverse shearing which are favourable conditions for shear plugging to occur. Furthermore, ASB formation has been demonstrated to be stress-state [40], [41] and strain-rate dependent [42]. This means that the angle of impact and ensuing deformation of the plate will have a strong effect on the resistance of the armour plate to this failure mode. The target thickness and caliber of the projectile have a strong effect on this failure mechanism; as a reference, usually a 1:1 ratio between the two results in shear plugging [4].

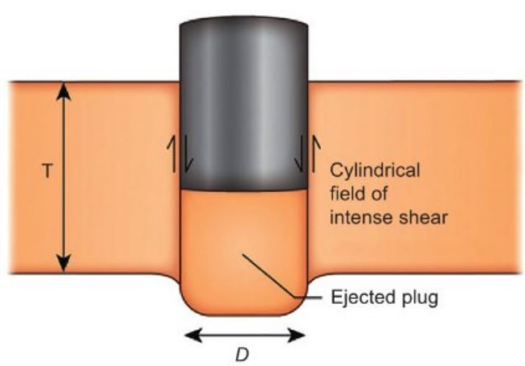

Figure 2.2: Shear plugging and formation of dangerous rearward ejected plug, with intense evolution of shear localization zones shown

2.1.1.3 Spallation

Spalling is a typical failure mode which usually occurs during blast loading or explosive rounds. The shock loading results in very high magnitudes of propagating plastic stress waves which result in scabbing of the material in the free (rearward) end of the plate. The primary measure of armor resistance to spalling is the strain-rate dependent tensile fracture strength of the material. If the tensile fracture strength is less than the magnitude of the superposition of the reflected tensile wave from the rear end combined with the incoming of compression waves, spalling will occur. For this reason, the thickness of the plate is very important and recreating these conditions of superposition is important. Damage could also occur in the material under these conditions without failure which could affect the material properties of the armour affecting its performance against other threats. There are specialized methods of recreating shock impact conditions such as laser spall setup [43].

2.1.1.4 Brittle Failure Modes

There are various brittle failure modes in armour such as conoidal fracture, comminution, fragmentation, and radial and circumferential cracking [4]. They tend to occur in ceramic armour, and sometimes in ultra-high strength steels with relatively low toughness, which exhibit a ductile to brittle transition at higher strain rates. ARMOX 500T is not known to exhibit these brittle modes. The reader is referred the book 'Science of Armour Materials' [4], which provides a very good discussion on the metallurgy and materials science of armour materials, their ballistic performance and overall science of terminal ballistics.

2.1.2 Metallurgy of Armour Steels

By far, with respect to metallic alloys, steels demonstrate their superior areal density to other metals [6]. With the interest of providing a practical comparison parameter for considering different steel alloys, the traditional method is the calculation of the V_{50} ballistic limit. This value is a measure of ballistic resistance for KEP's which represents the velocity at which point a steel plate will have a greater than 50% chance of penetration. In the literature, this is the most widespread method to compare the performance of different steel armours. This value is dependent on the thickness of the plate, the geometry of the projectile, and the material properties.

There are processing and compositional effects on the structure and properties of armour steels. From a metallurgical standpoint however, certain microstructural aspects have been demonstrated to be required for an optimal performance of ballistic resistance [4], [44]. For example, mitigation of the micro-segregation of alloying elements is required to not have an inhomogeneous microstructure such that localized regions in the armour change the properties of the material and compromise its performance. This tends to occur during manufacturing methods such as over-tempering martensite in certain steels such as ARMOX 500T, where relatively low tempering temperature can lead to the diffusion of alloying elements resulting in reduced strength and hardness with no toughness advantage [45].

In addition to the above examples for adequate microstructures, it is also claimed that fine equiaxed grains are preferred to take advantage of the Hall-Petch relationship to increase material strength [4]. Furthermore, it is claimed that it is preferable to have fine carbide dispersion strengthened steels as opposed to coarse carbides / precipitates and carbides settling on grain boundaries [4]. However, Boakye-Yiadom demonstrates that coarse carbide structures with reduced distribution density increases resistance to adiabatic shear banding in 4340 steels as opposed to fine carbides with increased distribution density [46]. It is also well-known that with increase in strength due to the hall-petch relationship, there is also a decrease in toughness. It is emphasized that while micro segregation and MnS stringers are detrimental to material properties and is to be avoided, fine equiaxed grains and fine carbide dispersion strengthening are microstructural tailoring techniques that have trade-offs with other properties and caution should be taken with respect to desiring these microstructures for specific steel armour applications.

2.1.2.1 Tempered Martensitic Steel

There have been significant developments in the steel industry since the standard rolled homogenous armours (RHA) used in the early 20th century, resulting in a variety of steels to consider for armour applications. However, it has been demonstrated by various authors that for practical purposes, the best performing steel armour plates with respect to ballistic resistance are those with a tempered martensite microstructure [4], [7].

Martensite is a metastable (non-equilibrium) phase with a body centered tetragonal (BCT) lattice structure. It is formed when quenched from an annealed solid solution of face centered cubic (FCC) austenite. During cooling of austenite from its solution temperature, as the FCC cools, it begins to form body centered cubic (BCC) ferrite, and sometimes intermetallic cementite or a mix of both depending on the carbon content. However, when a rapid cooling rate is imposed on this transformation, the carbon diffusion process from FCC to BCC is suppressed, they get trapped in the octahedral sites of the BCC structure, thereby stretching it into a supersaturated BCT structure via diffusion-less transformation [42]. The supersaturation occurs since the FCC is able retain more carbon than the BCT structure, resulting in the formation of carbides. The size and distribution of these carbides are critical to the properties of the steel. Furthermore, defect analysis using electron microscopy has established that the distortions of the BCT crystal results in a high dislocation density and consequential internal stresses [42]. This property of martensite makes it hard, shear-stress resistant, and brittle. For this reason, martensite is often tempered to relieve the internal stresses (dislocations) and add some toughness to the material at the expense of hardness and strength. Tempering allows trapped carbon atoms in the BCT structure to diffuse out as energy in the form of heat is added to the system, thereby changing the carbide characteristics of the microstructure. Simultaneously, the tetragonality of the BCT structure is reduced [42]. If retained austenite is present in the martensite, it may also transform to pearlite or cementite depending on alloying and carbon content during tempering. This microstructural tailoring of steels critically affects their macroscale material properties and thereby their ballistic performance.

In tempered martensitic structures, there are some primary metallurgical factors affecting ballistic performance [4]. The first and foremost is the alloying content and its effect on the hardenability of the steel. Greater hardenability is required for thicker grades of steel plates for certain structural applications, and therefore the same steel grades may have slight compositional changes to account for this hardenability requirement. It is not desired to have a steel plate with reduced hardness in the center of the plate, since this will affect its through thickness strength properties and compromise the stiffness of the plate, thereby reducing its performance. Other important considerations include the martensite start and finish temperatures and the levels of retained austenite. Jo et al. [47] demonstrated that improved ballistic performance can be obtained for a tempered martensitic steel when a small level of retained austenite is added to the microstructure, since transformation induced plasticity (TRIP) can serve as an effective energy absorbing mechanism.

2.1.2.2 Hardness & Toughness

It is generally observed and accepted that higher hardness results in greater ballistic performance. However, it is also demonstrated that beyond a certain level of hardness, ballistic performance is compromised due to brittle failure modes. Hu and Lee [7] performed ballistic tests on various martensitic steels with a focus on a modified RHA (MRHA) steel. AerMet 100, and AISI 1045 and 4130 steel plates were also impacted for comparison with the MRHA. They highlight that the American army research laboratory learned over many years of research that when a certain hardness threshold is surpassed (> 52 HRC), the ballistic performance against KEP's is compromised. Cimpoeru [44] highlights that beyond a certain hardness threshold, there is an increased susceptibility to ASBs.

Hardness is important due to its ability to deform and erode the projectile, decreasing its penetration capacity and generally increasing ballistic performance. However, this must be carefully balanced with toughness, which is usually inversely proportional to hardness, and is also critically important due to its ability to absorb the impact energy via plastic flow of the material. Hu and lee highlight its importance in absorbing energy adjacent to the point of impact of the material, as the stress-waves propagate ahead and to the side of the impactor. When high-hardness armour steels become too hard, they begin to exhibit brittle cracking and failure modes such as those observed in ceramics, especially at higher strain rates where many steels are revealed to have a ductile to brittle transition mode [4], [7], [44]. Furthermore, due to their increased resistance to deformation, harder steels have more increased stress and strain localization, resulting in increased stress concentration factors and reducing the material's ability to resist crack propagation. Tougher more ductile steels have larger plastic zones in the vicinity of a notch or a crack and thereby exhibit increased crack propagation resistance due to their higher fracture toughness.

Cimpoeru [44] accentuates that there are strain-rate / impact velocity dependent failure modes occurring in steels, affecting their ballistic performance. Illustrated in Figure 2.3 it is revealed that there is a hardness range where for a given plate thickness, the dominant failure mode is by ASBs and when the hardness is decreased or increased beyond this range, the ballistic performance is increased due to plastic flow (DHF) or projectile shattering, respectively.

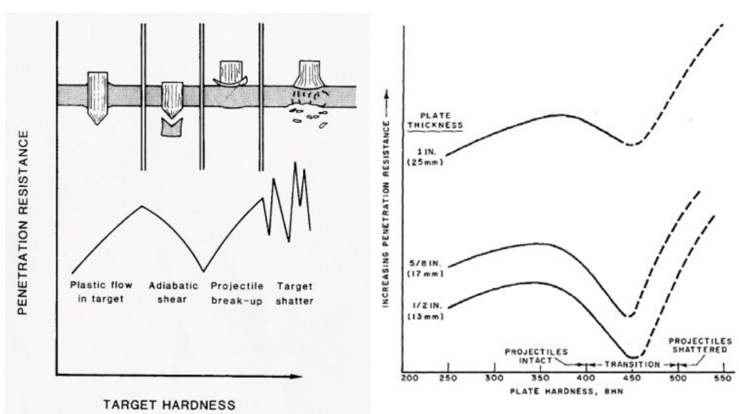

Figure 2.3: Armour plate failure modes and corresponding ballistic performance as a function of armour hardness [44].

It is important to emphasize that a hardness measurement for material characterization is a measure of its quasistatic yield stress. It is not a measure of the dynamic yield stress, which may differ under compression, tension, or shear stress-states. It is not an adequate measure of work hardening, strain-rate hardening, and plastic flow behaviour of the material [44]. While hardness is an important parameter to quantify, it is an inadequate parameter yielding insufficient information to quantify the ballistic performance of an armour material.

2.1.2.3 Dual Hardness Armour & Other Steel Grades

In modern steel metallurgy, materials science has enabled the fabrication of other grades of steel such as roll or explosively bonded dual hardness armor (DHA). This steel consists of a monolithic plate with a hard frontward facing steel metallurgically bonded to a tough rearward facing steel. The high hardness erodes and deforms the projectile while the back deforms plastically to resist crack propagation and absorb energy. Explosive welded DHA's are particularly attractive since this technique requires to clean metal oxides on the bonded surfaces prior to bonding, thereby producing a clean and wavy interface with fine grain size and maximized shear strength. This technique therefore mitigates delamination failure modes from bending deformation of the plate [4]. Another type of steel manufacturing method is electroslag refining which produces cleaner steel with reduced sulfur content, which increases ASB resistance [4], however it is expensive and rare due to the success of continuous casting techniques. There are also super and flash processed bainitic steels which currently have impractical limitations but show plenty of potential for the next generation of steel armour with increased ballistic performance [47]–[52].

2.1.3 Characterization of ARMOX 500T

Various authors have performed stress-state and strain-rate dependent calibration tests on AX500 for parameterization of different fracture models [53]–[57]. Iqbal et al. [55] created a Johnson Cook (JC) fracture model with strain-rate and temperature dependence. In addition to quasistatic tests, high strain rate tensile tests were conducted on axisymmetric specimens at 850 and 950 /s, Significant high strain-rate hardening of about 40% increase was observed in comparison to quasistatic tension. Simultaneously, a significant 50% ductility loss was observed at high strain rates. This strain-rate dependent strengthening and ductility loss has not been investigated in the literature and a satisfying reason for its occurrence has not been provided. In contradiction to this work, Nilsson created various fracture models and compared them for ARMOX 500T and ARMOX 600T and concluded that there was a low strain rate hardening or ductility effect at strain rates up to 1000 /s on both steels [53]. Figure 2.4 illustrates the ductility loss of AX500 in comparison to other armour steel materials for quasistatic to high strain rate tension [6].

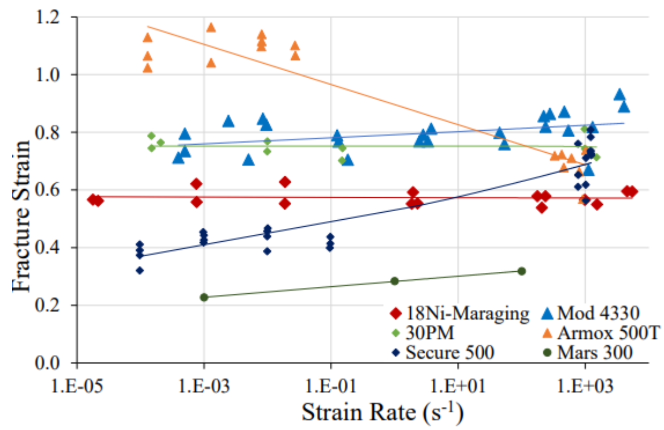

Figure 2.4: Strain-rate dependent fracture strains in various armour steels [6]

Saleh et al. [6] parametrized the JC model using high strain-rate compression tests up to 3000 /s, they quantified the effect of rolling texture with neutron diffraction, and a moderate strain-rate hardening effect was observed. Saxena et al. [7] conducted temperature dependent quasistatic and high strain rate compression tests up to 3000 /s to determine the constitutive model parameters of various phenomenological and physics-based fracture models. They observed a high strain-rate hardening effect and temperature softening effect in the material. Lastly, Poplawski et al. [54] incorporate the first fracture model for AX500 with lode angle dependence, using a carefully selected series of quasistatic tests. They obtain a 3D fracture locus of AX500 with improved accuracy over previous author's which can predict various penetration failure modes with flat, pointed, and hemispherical projectiles.

Jo et al. [58] conduct high strain rate compression tests on AX500 with increasing strain levels at 3900 /s. They identified the formation of ASBs, which show severe strain localization before grain refinement with increasing strain level at constant strain-rate. They also did SEM-EBSD and TEM analysis on ASBs tested by dynamic compression tests and ballistic tests, to identify the same microstructure ASB regions of specimens and armour plates. They claimed to identify grain growth, severe grain rotation, and distorted selected area diffraction patterns in the ASB which they deemed as evidence for the occurrence of rotational dynamic recrystallization as the deformation mechanism of the ASB. In another study, Jo et al [47], [52] demonstrate that a different steel based on AX500 with retained austenite or bainite structure improves ballistic performance.

2.2 Full-Field Measurement Techniques

2.2.1 Digital Image Correlation

Digital Image Correlation (DIC) is a non-contact optical measurement method which uses image correlation and continuum mechanics to quantify full-field displacement, velocity, and strain fields. It is a well-known and quantitatively robust full-field technique commonly used in quasistatic solid mechanics [59], [60]. The image correlation is based on the pixel greyscale intensity values and is conducted on subsets of pixels within the image. To achieve good image correlation, a physical randomized speckle pattern is placed on the surface of interest with adequate contrast.

Based on the location of the correlation peak obtained from the correlation from image to image, displacement vectors can be obtained within the subset and then algorithms can be applied to obtain strain fields defined by continuum mechanics formulations. The step size is the size within the subset on which strain formulations are preformed to obtain the strain fields. For practical DIC measurements, some common best practices should be followed/considered [60].

Table 2.1: Digital Image Correlation best practices

Test Conditions	Common practice	Description
All applications	Speckles should have minimum 3-5 pixels within it	Anything less could have inaccurate strains from image to image due to low spatial resolution
	Subsets should have ~5 speckles within it	Must have random subsets which can be differentiated from other subsets
	Step sizes should be 1/3 the subset size	Good balance between noise reduction and spatial resolution. Can modify slightly for highly localized strain measurements or noisy data.
	Smooth spatial gradients in pixel grayscale intensity transitions	In other words, blurred > sharp speckles. This improves subset interpolation. Avoid sharpening filters.
Curved surface profiles or expected 3D deformation	Selection between 2D or 3D strain measurements	Stereo measurements recommended even for flat samples. However, in plane accuracy is decreased.
	Stereo angle must be between 15-35 degrees	Higher stereo angle improves out of plane accuracy at the cost of in-plane accuracy.
Ductile materials or high strain rate testing	Large strains relative to subset size expected	Incremental or partitioned correlation as opposed to relative to first correlation must be done (surface will move out of subset completely, resulting in no correlation to the reference image at time = 0)

Full-field strain data enables characterization experiments to be compared to stress and strain fields in finite element analysis (FEA) simulations. In addition to a secondary measurement of axial engineering strain and strain-rate, time dependent transverse strains, principal strains, and shear strains are observable, enhancing the strain measurement using DIC by obtaining the constitutive full-field in-situ strain tensor. For example, in tensile testing, this enables the observation of the strain localization in the necking region which differs from the strain in the rest of the gauge section after the onset of necking. One can also derive the time dependent equivalent plastic strain including instability and fracture strains, and the strain-path evolution under different stress-state dependent tests such as shear, shear-tension, and biaxial tension tests ideal for GISSMO model parametrization [19], [61]-[63].

It is less common in applications of high strain rate due to the high frame rates required, resulting in the requirement for expensive high speed camera setups. Considering the importance of providing strain-rate dependent material property data for computational model development, it is desirable to obtain full-field strain information during Hopkinson bar tests. By directly observing the specimen, it also avoids the problem of wave dispersion possibly affecting strain/strain rate information, where the conditions in the incident bar strain gauge location may differ from those at the specimen.

Dunand and Mohr [64] use 2D-DIC on flat tensile specimens to measure the axial fracture strains in a TRIP steel for the parameterization of a physics-based mechanical threshold model. Owolabi et al. [65]-[67] use 2D-DIC on axisymmetric compression and torsion specimens to measure the strain field evolution throughout loading. Strain localization can be observed and quantified in regions of fracture initiation, and validation of the method with the Hopkinson bar strain gauge data is also provided. They also observe a linear evolution of strain with time, implying a constant strain-rate during Hopkinson bar tests. Pierron and Zhu [68] offer a method to evaluate the stress fields in compressive Hopkinson bar tests though full-field observation exclusively, and no strain gauge data required as in traditional Hopkinson bar tests. They derive the acceleration and strain fields from DIC data to obtain the required information to conduct their virtual fields method. For 2D-DIC measurements of 3D axisymmetric specimens, it is highlighted by Vilamosa et al [69] that a valid measurement can be obtained assuming isotropic plastic flow and axisymmetric deformation is maintained throughout loading (cross-section remains circular after the onset of necking).

2.2.2 Infrared Thermography

A typical assumption for infrared imaging is the grey body assumption, which assumes that the emissivity is lower than that of a blackbody, yet constant with wavelength and thereby temperature, resulting in an equivalent spectral density distribution with lower peak radiance. The analysis by Schlosser demonstrates that for a material coated in matte black paint, this is a reliable assumption that does not influence results for temperatures up to 353 K [72]. In addition, assuming a constant surface roughness and solid phase, authors have shown that objects with high emissivity will have a negligible decrease of emissivity up to temperatures of 2000 K [70], [71].

A non-contact infrared detector such as a thermal camera will measure the spectral radiance emitted by an object. A thermal camera uses specific detectors of specific material, which are sensitive to a voltage change for a certain wavelength range. For ranges near room temperature to high temperatures up to 1000 K, indium antimonide (InSb2) detectors are often employed. The detectors consist of focal plane arrays, such that an array of InSb2 detectors are placed on the cameras focal plane to capture the emitted radiation. For high-speed imaging purposes, sub-windows can be used such that resolution is lost to increase the frame rate alike to optical cameras.

In addition to accounting for emissivity through the grey body assumption, Schlosser demonstrates that to obtain adequate measurements, the camera focal plane must be at least 45 degrees or less to the surface it is measuring. Otherwise, decreased radiance is captured which would severely affect temperature measurements making them inaccurate. Mollmann and Volmer [70] also show directional dependency and support Schlosser's study.

Due to the conversion of plastic work to heat, it has been demonstrated that during high strain rate deformation temperatures in localized regions can increase significantly due to thermal inertia [70]-[77]. This information can offer insights into the levels of localized adiabatic heating, for example in strain-rate dependent tensile tests, which can affect the plasticity behavior of the material [79]. Furthermore, the temperatures reached can give indication as to whether transformation, homologous, or recrystallization temperatures are reached, resulting in the ongoing discussion of the cause and effect of ASBs under compression and shear stress-states and possible mechanisms of formation, deformation, propagation and ultimately failure [75]-[78]. While some thermal camera data was acquired during the characterization of AX500, it was tangential to the primary objectives and the data was not of sufficient quality to be presented.

2.3 Stress State Dependant Fracture Characterization

2.3.1 Damage Evolution & Fracture Modeling in Ductile Metals

There is unequivocal evidence that the mechanical properties in ductile metals such as work hardening rate, tensile strength and fracture strain is stress state dependent [80]-[93]. In continuum mechanics, the Cauchy stress tensor is the method of defining the normal and shear stress components in a material to define a multiaxial (triaxial) stress state. Triaxiality is defined as the ratio between the hydrostatic stress; obtained from the first invariant of the Cauchy stress tensor representing a volume change, to the equivalent stress; obtained from the second invariant of the deviatoric tensor representing a shape change. The three equations below define the triaxiality as per the continuum mechanics definition.

$$\sigma_H = \frac{I_1}{3}, \qquad I_1 = \sigma_{11} + \sigma_{22} + \sigma_{33} \tag{2.5}$$

$$\sigma_{eq} = \sqrt{3J_2} = \sqrt{\frac{(\sigma_1 - \sigma_2)^2 + (\sigma_2 - \sigma_3)^2 + (\sigma_3 - \sigma_1)^2}{2}} \tag{2.6}$$

$$\eta = \frac{\sigma_H}{\sigma_{eq}} \tag{2.7}$$

Where I_1 is the first invariant and σ_H is the hydrostatic stress and is a function of the normal stress components of the Cauchy stress tensor. σ_{eq} is the equivalent or von mises stress and is a function of the principal stresses and is proportional to the second deviatoric stress invariant J_2. The triaxiality η is simply the ratio of hydrostatic stress to equivalent stress. Bridgman derives the state of triaxiality in a tensile specimen as a function of its geometry in axisymmetric specimens [80]:

$$\eta_{max} = \frac{1}{3} + \ln\left(\frac{r}{2R} + 1\right) \tag{2.8}$$

$$\varepsilon_f = 2\ln\left(\frac{r_0}{r}\right) \tag{2.9}$$

Where r is the radius of the minimum cross section, R is the radius of the notch, r_0 is the initial value of r and ε_f is the equivalent fracture strain. This formulation showed that a triaxiality of 1/3 is achieved with an unnotched specimen for which $R = \infty$; correlating to a uniaxial stress state, and that the triaxiality increased with decreasing notch radius, resulting in a decrease of fracture strain.

An important precursor to the modeling work for quasistatic stress state dependent fracture characterization is the damage evolution methodology developed by Johnson in 1980 [86]. It is a simple accumulation of damage methodology where damage accumulates linearly with the increment of plastic strain, and reaches one; indicating failure, when the equivalent plastic strain is equal to the fracture strain. It is shown in equation 2.10. This is the methodology used by Johnson and Cook for their renowned fracture model, for which the formulation for the flow stress and fracture strain is shown in equations 2.11 and 2.12, respectively. This formulation and modified versions of it have been used extensively in stress state dependent fracture modeling of ductile metals since 1985.

$$dD = \frac{d\varepsilon_p}{\varepsilon_f} \tag{2.10}$$

$$\sigma_f = [A + B\varepsilon^n][1 + C\,ln(\varepsilon^*)][1 - T^{*m}] \tag{2.11}$$

$$\varepsilon_f = [D_1 + D_2 e^{D_3\eta}][1 + D_4\,ln(\varepsilon^*)][1 + D_5 T^*] \tag{2.12}$$

Where D is the damage accumulated defined as $d\varepsilon_p$; the increment in plastic strain at every timestep, over the fracture strain. A, B, C, n and m are material constants representing the yield stress, the strain hardening coefficient, strain rate coefficient, strain hardening exponent and softening exponent, respectively. ε^* is a dimensionless plastic strain rate parameter, defined as the ratio of the equivalent strain rate to the reference strain rate, T^* is the homologous temperature, and D_1−D_5 are coefficients calibrated from experimental triaxiality vs plastic strain plots. The model attempts to account for path dependency by accumulating damage throughout loading for a specific set of temperature and strain rate conditions. Upon the damage ratio reaching one, fracture occurs.

Bao & Wierzbicki [87] observed that the fracture modes and ductility of metals were different at varied triaxiality. They decided to build a fracture locus for the entire range from negative triaxiality under uniaxial compression to positive triaxiality in tension, to quantify ductility loss in tension dominated loading. They performed quasistatic compressive, shear, shear tension, round tension, and notched round tension tests. They observed that shear failure modes dominate in compressive and low triaxiality tests, and ductile failure due to void growth and coalescence dominated the tension tests and high triaxiality range, resulting in a slope discontinuity of the fracture locus at the transition point between failure modes at a triaxiality of 1/3 which represents uniaxial tension. Their work serves as a robust baseline for future mechanical testing for stress state dependent calibration.

There was a discrepancy for tests which were under the same triaxiality and yet there was a variation in fracture strain, this indicated that another stress state parameter would be required to fully capture this behavior. Wierzbicki et al. [88] performed flat grooved plate tests and round bar tests and incorporated the normalized third deviatoric stress invariant (NTSDI) of the deviatoric stress tensor (J3) as a stress state variable to predict the fracture strain. Wierzbicki and Xue developed a lode angle dependence parameter based on the NTDSI defined as a function of the triaxiality [89], [90]. The formulation is shown in equations 2.13 and 2.14.

$$\zeta = 1 - \frac{2}{\pi}\cos^{-1}\xi \qquad (2.2.13)$$

$$\xi = -\frac{27}{2}\eta\left(\eta^2 - \frac{1}{3}\right) = \cos(3\theta) \qquad (2.14)$$

Where ζ is the lode angle parameter (LAP), θ is the lode angle and ξ is the NTDSI. Ultimately, this resulted in a formulation that effectively predicted fracture strains with the effect of lode angle dependence, explaining the ductility loss under plane strain conditions. Xue used the weighted average values of triaxiality and LAP; taking the initial values and values just before fracture due to their non proportional loading, to calibrate a fracture strain-based 3D fracture locus quantifying the differentiated effects of both triaxiality and lode angle parameter.

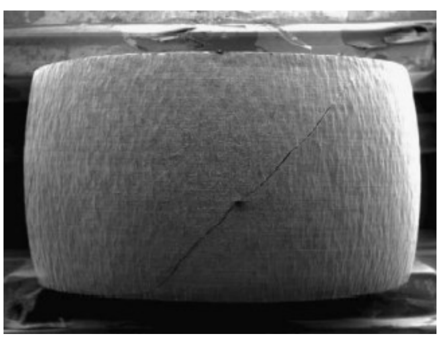

Figure 2.5: Failure of axisymmetric compression specimen along the shear plane predicted by MSS

Wierzbicki et al. [88] performed the experimental calibration and evaluation of seven fracture models including the Xue-Wierzbicki (XW) and the JC models. It is important to note that most of these fracture models do not predict accurate fracture strains in ductile metals in the entire triaxiality range. This is due to the complexity of fracture mechanics, and there is no universal theory of fracture mechanics for all materials due to the high number of variables which affect metal plasticity. As such, some models might have very practical applications in narrow regions of triaxiality, such as the fracture forming limit diagram (FFLD) which is heavily used in sheet metal forming where there is a predominant biaxial stress state or the maximum shear stress criterion (MSS) which predicts shear failure very well. This criterion states that ductile fracture will occur on the planes of maximum shear stress. A good example is the failure of axisymmetric compression tests, which fail along the 45-degree plane of maximum shear stress, illustrated in Figure 2.5.

Wierzbicki & Xue [89] have highlighted that the MSS considers the second and third stress invariants, but not the hydrostatic state. For this reason, a major drawback is that it cannot predict fracture under axisymmetric loading conditions. Alternatively, the JC model considers the first and second stress invariants, but not the third invariant. For this reason, the JC fails to predict or explain the loss of ductility under plane strain and fails to predict the change in failure mode from shear to tensile stress state. The XW model is the only model that considers all three stress invariants, and the fracture locus is therefore defined in three dimensions, where the triaxiality considers the hydrostatic and second stress invariants, and the lode angle parameter considers the third stress invariant. The conclusion is that although some models such as the MSS or the FFLD are very good for narrow ranges of triaxiality tailored to very specific applications, no fracture model is truly constitutive such that it can predict the ductility under any stress state except the XW which incorporates all three invariants. This results in unmatched sophistication of the model which can approximately predict fracture under any stress state.

Building on the work of Xue, Bai and Wierzbicki [91] proceeded to develop a new fracture model. They differed from Xue's work by developing an asymmetric fracture locus, where the axisymmetric compression and tension states defined by the lode parameter extremes where both experimentally calibrated, as opposed to Xue where it was assumed symmetric and extrapolated from tensile tests to provide a symmetric fracture locus. Figure 2.6 shows both fracture loci.

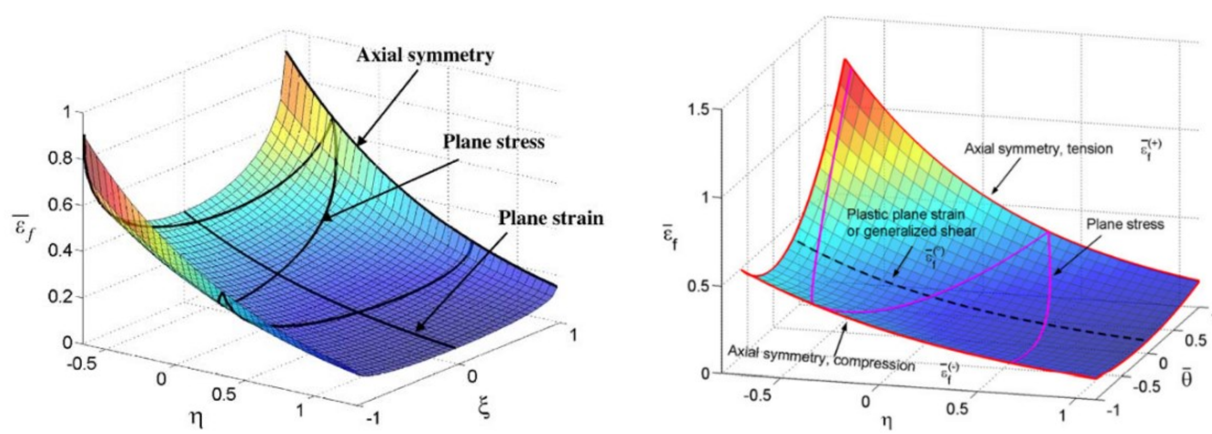

Figure 2.6: Xue-Wierzbicki & Bai-Wierzbicki Fracture Loci

An important outcome of this research was outlining the experimental procedures for calibration in which the effects of triaxiality and lode angle parameter were differentiated. Bai [92] showed the effect of lode parameter dependence by conducting tests on axisymmetric round tensile specimens, grooved flat plate specimens (tensile plane strain), and axisymmetric compression specimens to cover the constant LAP values of 1, 0 and -1, respectively. The effect of triaxiality was then quantified by doing notched tests in axisymmetric round tensile and grooved plate tests and varying the length to diameter ration in compression tests. Figure 2.7 illustrates the LAP-triaxiality plot with indication of the initial triaxiality and LAP in each experimental calibration test. Building on Xue's work, this model had a non-linear damage evolution methodology as opposed to the linear methodology of the JC model. This methodology attempts to empirically quantify the non-linear micromechanical evolutions throughout loading in practical continuum damage models.

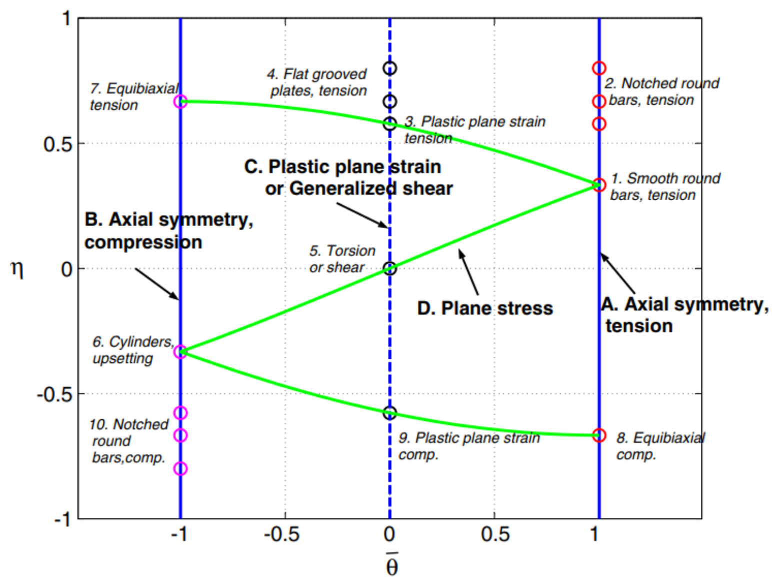

Figure 2.7: Triaxiality-LAP stress state map for Bai's calibration tests

2.3.2 Stress State Evolution During Loading

To the author's knowledge, Bao [87] was the first to quantify the evolving stress state in compressive and tensile specimens using a hybrid experimental numerical approach. Using experimental mechanical testing data, simulations are performed which use the geometrical state of the specimen during loading to predict the triaxiality inside the specimen as a function of the plastic strain or displacement. Bao showed that there was non-proportional loading taking place in standardized mechanical tests, including round smooth and notched tensile specimens. Figure 2.8 shows the evolution of stress triaxiality in smooth and notched round tensile tests.

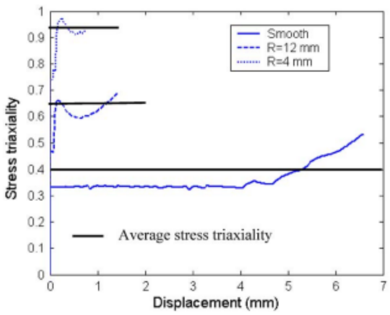

Figure 2.8: Evolution of triaxiality in flat tensile smooth and notched

Bai & Wierzbicki [93] determine the evolution of stress state in a plane strain specimen. They highlight that Bridgman showed that the range of stress triaxiality at the center of a plane strain specimen is equal to or greater than 1/3. They also derived their own formulation to show that the lode angle parameter is always zero in a plane strain specimen. Basaran [94] observed the same results and extended the analysis for the lode angle parameter for four notched plane strain and notched round tension specimens and created FEA plots of the stress state and plastic strain contours at fracture. The plots reinforce the work of Bai and Wierzbicki. Basaran also showed that the lode angle parameter is constant throughout tensile plane strain and axisymmetric tensile loading at 0 and 1, respectively. This proportional loading of the lode angle makes it preferable for stress-state dependent calibration testing. In addition, Basaran analyzed the triaxiality and LAP evolution of Nakazima specimens in hemispherical punch tests for biaxial tension. Basaran revealed that in equi-biaxial tension specimens there is proportional loading with triaxiality of 2/3 & lode angle parameter of -1.

A closer look has been taken at the non-proportional loading of smooth and notched flat tensile specimens by various authors [87], [94]-[96]. Dunand observed that the stress state and strain rate at the specimen surface of a flat tensile specimen is different that that of the midplane, especially after the post critical deformation (necking) phase. Dunand [95] states that triaxialities ranging from uniaxial tension (1/3) to tensile plane strain (0.58) can be obtained with flat tension specimens. Dunand observed that there is a strong gradient along the thickness direction of the notched flat specimens with a central zone of strain localization where fracture occurs, unobservable to DIC surface measurements. This localized necking leads to out of plane stresses in the center of the specimen, as opposed to the surface which deforms under plane stress conditions. Throughout loading, Dunand observes that this increases the triaxiality in the localized necking region up to tensile plane strain resulting in low fracture strains due to the evolution of the stress state into plane strain.

A topic which has been explored little in the literature is multi-stage deformation tests with changes in the strain path. Bai emphasizes that fracture loci are currently calibrated using non-proportional tests, and this is far from ideal [92]. Bai reviews the work of Johnson and Cook [86] who performed two step experiments of torsion followed by tension. They observed a peculiar decrease of total damage in the specimens as the initial torsion damage increased. Basaran [94] emphasizes that such tests can be beneficial, since future work can build on this to create multi-stage calibration experiments to maintain the stress state parameters constant at crack initiation, which would aid in finding an adequate non-linear damage exponent, as currently the damage exponent is approximated.

McDonald [6] conducted some noteworthy work on the stress state evolution in blast loading of armor steel plates and incorporated a new formulation into the GISSMO damage model. McDonald developed a new definition of damage, based on Basaran's nonlinear definition as a function of the triaxiality and NTDSI. However, McDonald did not use weighted average stress state parameters, instead a time-dependent formulation which updates on every step of the simulation was employed to quantify the strain path dependence. Furthermore, McDonald quantified the average stress states across the width of the plates under blast loading, and their evolution during impact to reveal localized non-proportional loading preceding failure locations.

2.3.3 Generalized Incremental Stress State Dependent Damage Model

2.3.3.1 Overview

GISSMO is an empirical stress-state dependent strain-based continuum damage model which uses tailorable parameters (damage, fading exponents) to match simulations to experiments. Instability and fracture strains are obtained experimentally as a function of stress-state to create stress-state variable dependent failure and instability curves. It requires a hybrid experimental-numerical approach to parameterize the model with a material model for a given ductile metal, and the process is optimized for practical engineering purposes.

Neukamm et al. [18] reviewed the Johnson and Cook (JC) model and the FFLD and highlighted their shortcomings with regards to accurate numerical prediction during crash simulations in the automotive industry. A large problem in the industry that was identified is the lack of quantification of damage accumulated during sheet metal forming, that was important to the initial state of the structural automotive frame during the crash simulation. Therefore, to close the gap between forming and crash simulation, GISSMO was developed [12], [97]. They employed the JC fracture model which is easy to calibrate and can predict the 2D fracture locus in the space of triaxiality independent of the flow behavior. Furthermore, they enabled the prediction of deformation during forming simulation as well as crash simulation with consideration of the load path history during forming. Basaran developed a fracture locus defined by three bounding curves for the lode angle parameter values of -1, 0 and 1 representing axisymmetric compression and equi-biaxial tension, generalized shear and plane strain, and axisymmetric tension, respectively. These bound curves define fracture strain as a function of triaxiality, and the lode angle influence is defined using a quadratic function with 9 coefficients indicated as D in Figure 2.9 (3 for each bound term). Notably, upon meeting certain conditions, the fracture locus definition of previous literature is obtained. Such as symmetry condition to obtain the Xue-Wierzbicki locus and eliminating lode angle influence to obtain the 2D JC definition of failure. The constitutive 3D Basaran fracture locus is integrated with the GISSMO damage model, demonstrating the flexibility of the GISSMO with different types of constitutive material models.

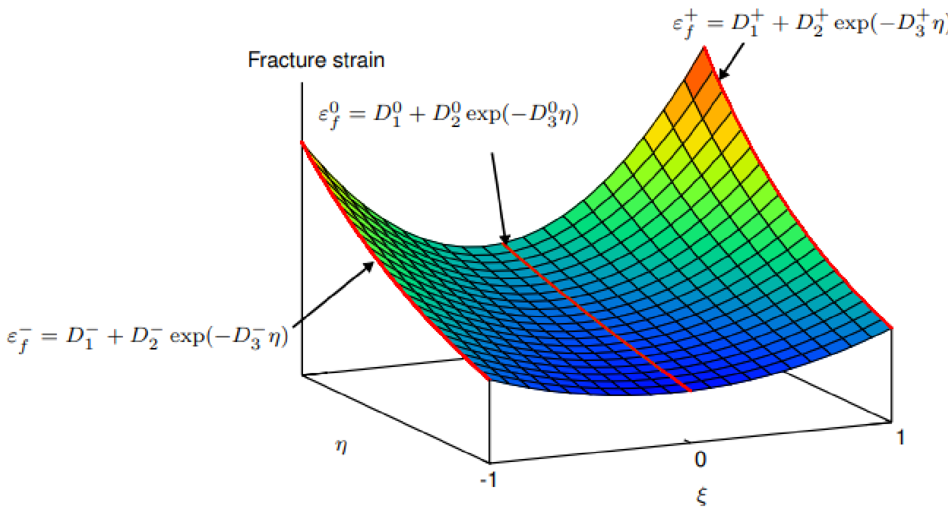

Figure 2.9: Basaran fracture locus with three bound curves for triaxiality and a quadratic function quantifying the lode angle

2.3.3.2 Non-linear damage accumulation

Using tensile loading as an example, ductile metals deform plastically by dislocation motion followed by non-linear void growth as plastic strain increases, which influences the evolution of microstructural damage in the material, affecting the flow stress behavior. For the development of GISSMO, an empirical nonlinear damage accumulation methodology is important for predicting non-proportional loading paths and accounting for non-linear microstructural evolution and this was incorporated by Neukamm into the model. The incremental damage formulation can be expressed as follows in equation 2.15, where if the damage exponent n = 1, the JC linear damage accumulation formulation is obtained. This function is evaluated at every time-step during simulation and uses the current plastic strain increment value, triaxiality, lode parameter, and damage from the previous step.

$$\Delta D = \frac{n}{\varepsilon_f(\eta, \zeta)} D^{1-\frac{1}{n}} \Delta\varepsilon_p \qquad (2.15)$$

Where $\varepsilon_f(\eta, \zeta)$ is the plastic fracture strain definition as a function of both triaxiality and lode angle parameter, D is the damage accumulated, and n is the damage exponent. Failure occurs when D reaches unity. For crash simulations, and important note is that the initial D value is based on damage that occurs during forming.

2.3.3.3 Instability criterion

The same nonlinear damage evolution formulation is used for an instability criterion known as the forming intensity parameter, which is a measure of instability at which stress relaxation takes over work hardening, equation 2.16 shows this definition. For the formulation, the strain at which localization begins to occur is used instead of the fracture strain. This is a difficult strain to obtain experimentally. For practical applications, the strain at the ultimate strength is used known as the effective stress concept.

$$\Delta F = \frac{n}{\varepsilon_{loc}(\eta, \xi)} F^{1-\frac{1}{n}} \Delta\varepsilon_p \qquad (2.16)$$

2.3.3.4 Post critical deformation

When F reaches 1, this is interpreted as the instability criterion and damage will be coupled with plasticity via the piecewise function shown in equation 2.17. Stress is defined as a function of damage and a critical damage parameter, where DCRIT is the damage (D) value at which F=1. When damage is greater than this value, damage is coupled with the flow stress and the stress relaxation takes over defined by the fading exponent m which is found iteratively through simulation or using LS-OPT. Mesh regularization is incorporated into the model by defining the fading exponent (m) as a function of the mesh size to govern the rate of stress relaxation and therefore is related to the energy dissipated by the material during the propagation of a crack.

$$\sigma^* = \begin{cases} \sigma & , \quad D \le D_{crit} \\ \sigma\left(1 - \left(\frac{D - D_{crit}}{1 - D_{crit}}\right)^m\right), & D > D_{crit} \end{cases} \qquad (2.17)$$

This methodology enables the prediction of post-critical deformation behavior (e.g., post-necking deformation). It allows an adjustable prediction of the rate of stress relaxation to match experiments under different stress states for full parametrization and enables the semi-empirical prediction of the energy absorption and dissipation of the material during the plastic deformation process. The GISSMO material damage model has since been successfully implemented into LS-DYNA for various metals and successfully used in engineering applications [6], [19], [61]-[63].

2.4 High Strain-Rate Characterization

2.4.1 The Hopkinson Bar

The Kolsky/Hopkinson bar; first developed by Herbert Kolsky in 1949, was developed to quantify the compression stress-strain response of materials under high strain-rates in the region of 10^2–10^4 /s [98]. It was inspired by the Hopkinson bar setup to measure the force-time curves of stress waves during ballistic impact developed by Bertram Hopkinson. The Hopkinson bar is prominent in high strain rate characterization due to its ability to reproduce the conditions of stress-wave propagation which occurs in high strain-rate applications such as terminal ballistics. In terminal ballistics, plastic stress waves propagate in the armour plate which plastically deform the material ahead of the projectile, having effects on material response. These stress-waves reflect from free-ends and partially transmit/reflect from interfaces due to wave mechanics, resulting in superimposing plastic stress-waves in armour plates [4]. Due to inhibition of dislocation mobility, the material strengthens with increasing strain-rate.

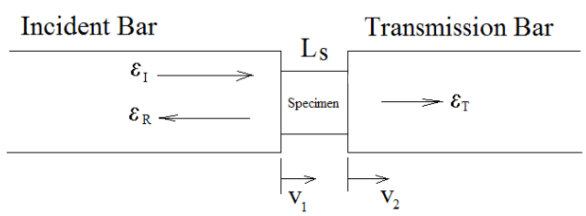

Figure 2.10: Schematic of a typical compression Hopkinson bar machine

To illustrate the Hopkinson bar setup, a schematic of the central section of a split-Hopkinson pressure bar is shown in Figure 2.10 [98]. Long incident and transmitted bars are used to abide by 1D longitudinal wave propagation. The Hopkinson bar recreates the conditions of plastic stress-wave propagation in the specimen of interest, while using 1D wave mechanics principles to capture the input and output conditions through elastic stress-waves propagating through the two bars. The input strain/strain rates can be obtained using strain gauges on the incident bar which captures the reflected pulse, and the stress history of the specimen can be obtained using strain gauges on the transmitted bar to capture the transmitted pulse. Therefore, the Hopkinson bar is a preferable machine for dynamic characterization of materials.

2.4.1.1 The Tensile Hopkinson Bar

Different designs of the Tensile Hopkinson Bar (THB) have been used for high strain rate material characterization since the first design of Harding et al. in the year 1960. The first THB designs from the 20th century had certain limitations [98]. Primarily, the gas gun was coaxial with the incident bar to enable the hollow impactor to be linearly actuated by the gas pressure and slide over the incident bar in the direction opposite from the specimen location. The impactor could then create the tensile wave pulse by hitting the flange on the end of the incident bar, which was within the gas gun. Different designs have been developed such as direct tensile bars, or modified compression bars with a load transfer component to bypass the specimen and create the tensile pulse on the bar on the other end of the specimen. However, all three designs have limitations and are far from ideal. The traditional design of Harding is difficult due to the necessity to provide a good seal. In addition, there is no access to the impact flange, limiting access to pulse shaping experiments. The direct bar designs do not have incident bars, and therefore do not have well-known input strain/strain-rate conditions. They also usually involve pre-stressing of the bar, which is usually done with a bolting mechanism which involves the fracturing of the bolt to release the stress wave. The fractured bolt becomes a flying projectile imposing a safety concern that must be addressed in designs. Lastly, the load transfer design pre-loads the specimen in compression which may affect material response, and the presence of the load transfer part introduces an axially offset impedance mismatch which is undesirable for 1D wave propagation and introduces unwanted wave reflections to the system. Gerlach et al. [99] developed a novel THB design which overcomes all these issues. It is a split-Tensile Hopkinson bar with an axially offset gas gun and uses a pulling rod to move the hollow impactor along brass railings. This design avoids the limitations previously discussed, enables access to the impact flange for pulse shaping techniques, and features a long input pulse of 1 ms due to the long U-shaped projectile used.

2.4.1.2 The Torsional Hopkinson Bar

Baker and Yew [98]; in 1966, were the first to adapt the Hopkinson bar for torsion. It used a hydraulic clamp on the incident bar with a torquing mechanism using a lathe chuck at the end of the bar, and on the other side of the clamp on the other end of the bar was the torsion specimen. The clamp must then be quickly released, allowing the elastic torsional stress wave to propagate through the bar and onto the specimen. Unlike the tensile bars, designs don't vary much from this arrangement. Torsional bar designs primarily differ in their clamping, torquing, and quick release mechanisms [98].

2.4.2 Stress-State and Strain-Rate Dependence

Generally, there has been very little study of the effect of stress state on the strength, ductility, and overall flow stress behavior during high strain rate loading. As previously mentioned, typically, fracture models are extended to account for strain rate dependence by doing multiple tests at different strain rates, at one stress state such as uniaxial tension or compression. From this, the rest of the fracture locus is extrapolated from this one data point [6], [55], [64], [100], [101]. Even less attention is paid to the effect on microstructural evolution, which is the ultimate factor that affects the flow stress behavior. Meyers provides an in-depth overview of the microstructural mechanisms of deformation and failure under dynamic compression, shear, and tension independently [102]. It is clear from the overview that the macroscale mechanical behavior is different under the different stress states due to fundamental differences in microstructural evolution and variance in the underlying deformation mechanisms under different stress states.

2.4.2.1 Compression and Compression-Shear Specimens

Axisymmetric compression cylinders are the most common specimens used for high strain rate characterization using a split Hopkinson pressure bar. ASBs are the failure mechanism in these specimens, which occur in concentric rings on both impacted faces slightly offset from the specimen edges. These two concentric rings are connected in a 3D hourglass shape along which the ASB forms and the subsequent fracture path propagates [46], [103]. However, various authors have used different length to diameter (L/D) ratios on these specimens, which can have effects on the malleability of the specimen and therefore affect the perceived material properties. In quasistatic compression, an L/D ratio of 2 is common [87]. In addition to minimizing friction to maintain uniaxial compression conditions, it is highlighted by various authors [5], [98] that it is critical to eliminate radial and tangential inertia effects in uniaxial compression tests. Authors who have diligently investigated ASB morphology and microstructure evolution using transmission electron microscopy have settled on specimens of size Ø9.5x10.5mm with L/D ratio of 1.1 [104]-[107].

L.W Meyer et al. [40] have demonstrated that by introducing an angle into traditional axisymmetric uniaxial compression specimens, a shear/compression load ratio ($\lambda = \frac{\tau}{\sigma}$) is realized which changes the stress-state of the specimen into a biaxial stress state. They demonstrate that with a higher angle/λ, there is a significant loss of ductility due to a greater susceptibility to form ASBs. It is emphasized that these specimens are desired due to their ability to maintain a consistent stress state in the area where the ASB forms and failure occurs, making them very practical for damage model parameterization. It is further noted that the biaxial compression specimens favor characterization by ASB formation of the material, since it suppresses the influence of microstructural inhomogeneities which are more prominent for failure initiation in uniaxial compression specimens. Inclined cylindrical compression shear specimens are therefore favourable for characterization of ASBs by the material properties of the material. Figure 2.11 illustrates these specimens and their effects on ductility as a function of λ.

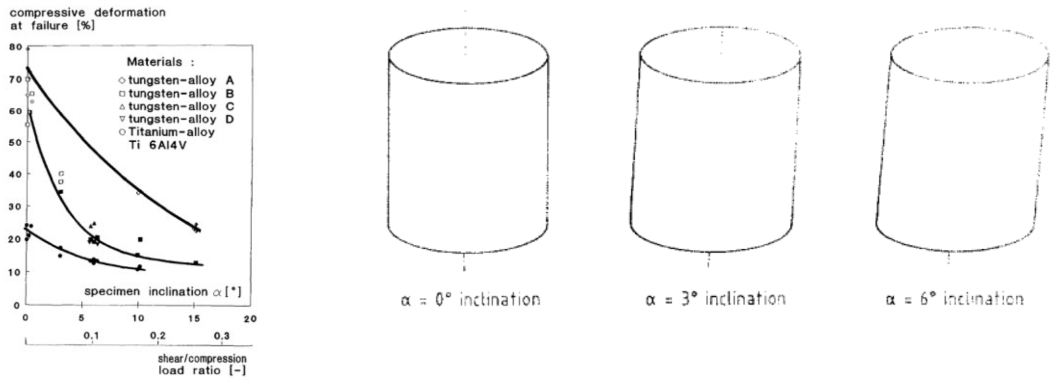

Figure 2.11: LW Meyer's inclined compression-shear specimens and ductility loss with increasing shear stress component

2.4.2.2 Top-Hat Specimens

Meyer and Manwaring [108] developed an axisymmetric hat-shaped specimen to study adiabatic shear localization under a different stress-state than that of traditional cylindrical compression specimens. This a stress-state where forced localized pure shear failure was imposed on the specimen due to its geometrical design. Couque [109] developed a modified version of the axisymmetric hat specimen which maintained a consistent hydrostatic pressure in the localized region creating a consistent compressive-shear stress-state, which was deemed hydrodynamic hat specimen. Pursche and LW Meyer [110] reveal that there is a linear correlation between the axial strains of the cylindrical inclined compression-shear specimens and the shear strains of the axisymmetric top-hat specimens. In addition, they highlight that both compression shear and top hat specimens are important for characterization of ASBs.

2.4.2.3 Localized Shear Compression Specimens (SCS)

Rittel et al. [111] developed a shear compression specimen which favored failure by ASB, which could be observed in-situ. This specimen uses a geometrical design to force failure in ASB region, it is important to note that this specimen exhibits a feedback effect, such that once failure by ASB begins in the forced strain region, all strain is now localized in this region and promotes further strain evolution in this region [75]. The ASB evolution is then dependent on the geometry of the specimen as opposed to the material properties. This makes this specimen adequate for in-situ ASB studies, however it is limited for characterization of ASBs in damage models.

2.4.2.4 Torsion Specimens

Chen and Song [99] and Marchand and Duffy [75] provide a discussion on torsional specimens. Unlike compression and compression shear specimens used in the compressive Hopkinson bar systems, torsion specimens are more straightforward and only one type of design is really used. The torsion specimen must have a short thin-walled tubular section to maintain a consistent stress-state and strain evolution during loading, with Hex cap ends to secure it to the incident and transmitted bars. They are the most favorable specimens for the study of ASBs, since they maintain a pure shear stress state with no compressive stress component in the ASB region until fracture, ensuring a mode II adiabatic strain localization and subsequent crack propagation through the ASB.

2.4.2.5 Stress-State Dependent Characterization at High Strain-Rate

Whittington et al. clearly portray the stress state dependence of the dynamic flow stress under tension, compression and torsion using split compressive, and direct tension and torsion Hopkinson bars [112]. In this work they calibrated a physics-based micromechanical fracture model for rolled homogenous armor (RHA) steel. Figure 2.12 illustrates the stress-state dependent plasticity of the RHA. Zhu et al. [41] evaluated the stress state dependence of Ti6Al4V at high strain rate using split compression, tension, and torsion Hopkinson bar systems on localized modified shear compression / tension specimens and the traditional thin-walled tubular torsion specimens. They quantify the effect of both lode angle and triaxiality on ASB localization and created an empirical computational model. They obtained full field strain measurements using high speed cameras and observed the evolution of adiabatic shear bands with dependence on the angle and hence stress state. They found a strong dependence of stress state on the materials plasticity parameters for model parameterization and initiation and evolution of adiabatic shear bands.

Walters did strain rate dependent biaxial punch tests using a drop tower on an AHSS [113]. Walter concludes that there is an increase in ductility for negative lode angle parameters, and that both punching and pure shear stress states are important to quantify for the purpose of developing strain-based fracture criteria. It is noted by the author that this evolving stress state is commonly found in sheet metal punching and ballistic impact conditions. Wang et al. [114] performed high strain rate triaxiality dependent plane strain shear tests using flat-top-hat specimens. They maintained a lode angle parameter of 0 for all tests, maintained a consistent triaxiality evolution up until failure, and observed a consistent strain distribution throughout most of the loading process. They created a stress state dependent fracture model for Ti6Al4V, in which they identified a stress state dependent transition in failure mode. In negative triaxiality they observed ductile trans-granular fracture which transitioned into brittle inter-granular cleavage fracture as the stress state changed from compressive shear to tensile shear in positive triaxiality.

Herzig et al. [115] performed a dynamic characterization of GISSMO using uniaxial tension, uniaxial compression and in plane shear, including compression shear states and tension-shear states. However, this was only done for intermediate strain rates up to about 1000 /s. This is a great baseline for future work. Polyzois and Toussaint [116] performed dynamic fracture characterization of armor steel AlgoTuf 400F for GISSMO parameterization using dynamic compression and torsion. They also used a series of notched round tension specimens for quasistatic characterization. They obtained very accurate predictions of blast loading failure in armor plates. Edwards [117] used cylindrical top-hat specimens on a split Hopkinson pressure bar for dynamic characterization of Al-2024-T351. Edwards' work was motivated by a desire to better predict shear plugging in armour failure modes, as it remains a gap in the literature. In this work, Edwards identified the critical shear strain rates and shear strains for initiation of ASB's within the specimen relevant for GISSMO parameterization at higher strain rate. Specifically, this was used for an empirical based strain rate dependent instability criterion in the GISSMO. Edwards varied the stress state of the top hat specimens under shear compression to shear stress states and observed effects on the flow stress and fracture strains. Edward accentuates that lode angle dependent high strain rate calibration tests are not conducted and would be beneficial for characterization of metallic armour for numerical models.

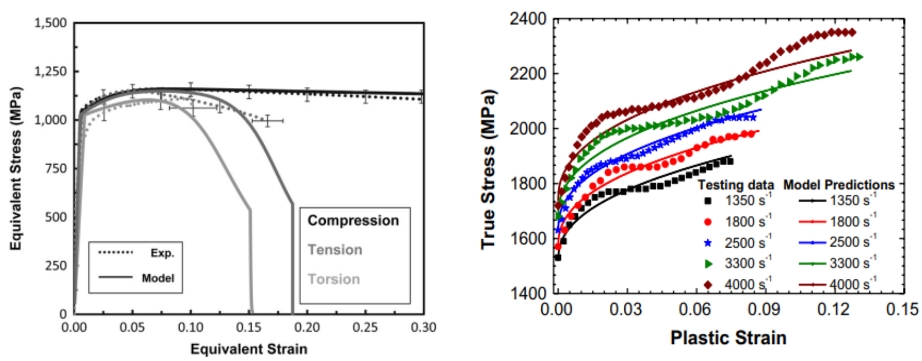

Figure 2.12: Stress-state and strain-rate effect on plasticity and fracture

2.4.2.6 Strain Rate Effects on Plasticity

Various authors report strain-rate dependent hardening in ductile metals, with greater load bearing capacity at higher strain-rates [5], [42], [107]. It is generally accepted and demonstrated that thermal and viscous inertia effects play a large role during high strain rate deformation. Couque highlights that as strain rate increases, the viscous drag effect on dislocation motion increases, and there is a threshold strain rate beyond which the strength of the material greatly increases. This is attributed to the time dependent mechanics of dislocations; as an example, for reduced loading times there is not enough time for dislocation bowing to occur around precipitates.

Kumar et al. [118] reveal that there is a strong strain-rate dependence of the onset of twinning resulting in strain-rate dependent yield strength and work hardening in a high entropy alloy. Moon et al. [119] reveal that short range order microstructural obstacles play a larger role in high strain-rate or low temperature deformation, influencing dislocation mechanics and thereby observed macroscale hardening. Cao et al. [120] observed a strain rate dependent change in failure mode from ductile void growth to quasi-cleavage brittle fracture in high strain rate tension tests of a high entropy alloy. McDonald [6] used a two-stage strain hardening term which enabled the prediction of viscous effects which occur at higher strain rates such as dislocation drag. Dunand and Mohr found a peculiar decrease of the fracture strain in a TRIP steel at intermediate strain rates, followed by an increase at higher strain rates [64]. Figure 2.4 from section 2.1.3 also illustrates the fracture strain dependence of various armour steels. Ting Wang et al. [121] observe an increasing fracture strain with increasing strain rate in uniaxial compression, with typical strain-rate hardening occurring in the material as expected due to the viscous inertia effects, illustrated in Figure 2.12.

2.4.3 Adiabatic Shear Bands

Adiabatic Shear Bands (ASBs) have been observed during high strain rate deformation environments such as those mentioned in section 1.2. They are known to be narrow regions of intense shear strain localization, which are precursors to cracking and fracture of the material. To this day, it is still unknown what the mechanism of formation of ASBs is, and it is a heavily debated topic. Many authors define the ASB as a narrow region of localized softening which forms as an inhomogeneous temperature distribution due to thermal inertia, and attribute ASB formation as a thermomechanical instability defined as the overcoming of thermal softening over strain hardening [102]. However, this is disputed by many authors, which indicate that a microstructural mechanism is responsible for the ASB deformation mechanism as opposed to a thermal softening mechanism. In addition, authors propose different microstructural mechanisms for a variety of different metallic materials.

Different metallographic techniques are used to study the formation and evolution of ASBs. The transmission electron microscope (TEM) is dutifully employed to see the nanoscale mechanisms which are important to quantify for a constitutive understanding of the phenomenon.

2.4.3.1 Macroscale Thermomechanical Characterization

Zener and Hollomon [122] highlight that there is a material dependent critical strain rate at which point adiabatic shear bands will form due to the transition of isothermal to adiabatic deformation. They define this as an instability; analogous to tensile necking or compressive barreling, at high strain rates where intense shear strains occur in a narrow region of the deformed material.

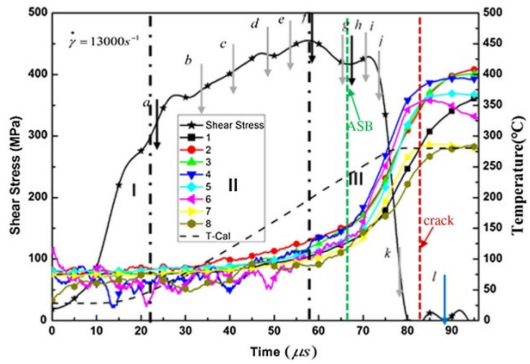

Figure 2.13: Stress-time curve and temperature rise timing of an Adiabatic Shear Band [76]

Marchand and Duffy [75] performed high strain rate torsion experiments on HY-100 steel to observe adiabatic shear band formation with indium antimonide (InSb) elements for discrete temperature measurements and three cameras for discrete strain measurements. They used a gold plated Cassegrain mirror arrangement for the infrared detectors with a 15:1 magnification ratio. They characterize three distinct stages of deformation. Stage 1 is Homogenous strain distribution, stage 2 is inhomogeneous strain localization, and stage 3 is adiabatic shear band formation. They observed a drop in the flow stress during stage 3 and an associated temperature rise of 863 K. Rittel and Wang [77] used Ti6Al4V and Magnesium AM-50 alloy shear-compression specimens with a high-speed camera setup temporally coupled with InSb infrared detectors. They used a dual Cassegrain mirror as well and identified a maximum temperature rises of 336 K and 445 K for AM-50 and TiAl64V, respectively. They demonstrate that the temperature rise in AM-50 was approximately around the homologous temperature, while the temperature rise in Ti6Al4V was about 23 % of the melting point, far from the homologous temperature. Using an identical setup, Guo et al. [76] identify that the temperature rise associated with an ASB in commercially pure grade 2 hexagonally closed packed (HCP) Titanium occurs after the formation of the ASB, and that the ASB occurs after stress relaxation of the flow stress. They measured a temperature rise of less than 400 K with their method. Zhu, Guo et al. [123] measured a temperature rise of about 368 K for Ti6Al4V, also using a shear compression specimen, in addition, they measured a shear strain of up to 60% in the ASB. Using flat top-hat specimens, Nie et al. [124] used a similar setup with a Telops M3K infrared camera and X-ray phase contrast imaging (PCI) system, to find that the temperature rise occurred before stress relaxation in the face centered cubic (FCC) Aluminum alloys. For AA6061-T6 and AA7075-T6, they observed a prolonged temperature rise of 770 K and 720 K, respectively. This is higher than the homologous temperatures for both alloys.

Lastly, Goviazin et al. [78] compared the use of infrared detectors with infrared thermography techniques to estimate the Taylor Quinney coefficient. It is concluded that for accurate measurements of the differential TQ coefficient, detectors are more adequate due to their high sampling rates. However, for temperature distribution in the specimen and highly localized temperature rises such as ASBs, thermographic imaging is necessary.

Digital image correlation and other in-situ strain localization detection methods have been used to measure the shear strains in ASBs [41], [65]-[67], [75], [114], [123], [124] on different specimens. Primarily, Marchand and Duffy's method of using grid lines to detect the shear strain is commonly used using optical or X-ray imaging techniques. Shear strains greater than 60% have been observed in highly localized regions with accompanying temperature rises, which usually occur after the onset of the ASB. This in-situ strain measurement method is advantageous due to the ability to identify the critical shear strain for the onset of the ASB.

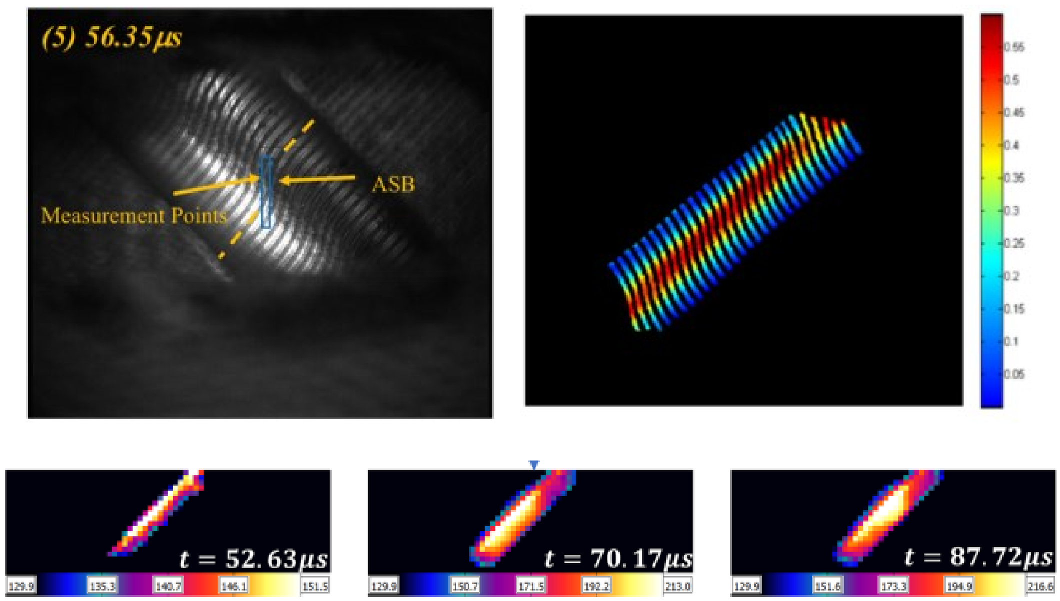

Figure 2.14: Full-field optical and infrared observations of adiabatic shear bands [41], [78]

2.4.3.2 Microscale Microstructural Characterization (OM/SEM)

An indisputable observation of ASBs is their high hardness, various authors have demonstrated that ASBs are harder than the pre-impact condition and the regions outside of the ASB regardless of their crystal structure, stress-state, or temper condition [42], [58]. [117], [125], [126]. Furthermore, systematic microstructural evolution studies of ASBs have revealed that after the onset of white-etching bands and severe plastic deformation, cracks initiate along the central path within the ASB on the impact plane, and void coalescence occurs leading to fracture and fragmentation. Boakye-Yiadom performs systematic testing with increasing strain rates/strains to show that the ASBs increase in hardness with increasing strain-rate for 4340 steel specimens, regardless of their initial microstructure [42].

Figure 2.15 shows the typical morphology of an ASB in a uniaxial compression specimen, as well as an illustration of its complex hourglass shape under uniaxial compression accompanied by macroscale fractography [42], [107]. Woei-Shyan Lee illustrates very well and characterizes the complex hourglass shape and stress-state present in a traditional axisymmetric compression specimen which leads to combination of shear, compressive and tensile stresses on the plane of maximum shear where the ASB forms [103]. Boakye-Yiadom [46] illustrates and demonstrates that upon the occurrence of plastic deformation, dislocations sources are activated, and they multiply, resulting in dislocation cell formation within grains along lattice planes. It is illustrated that an intersection of an activated dislocation source with the direction of maximum shear is the necessary condition for the initiation of the ASB. This is illustrated in Figure 2.15.

Fractography has revealed that ASBs fracture surfaces may have random regions consisting of highly smeared material, severely ductile elongated dimples, knobby morphology, and microvoid patches [107], [127]. Generally, increasingly fine dimples indicate fracture areas which retain more load and coarse dimples indicate areas with decreased load bearing capacity [107]. The different regions have been attributed to highly localized temperature rises and severely localized shear strain with respect to observed severely elongated and coarse dimples [127].

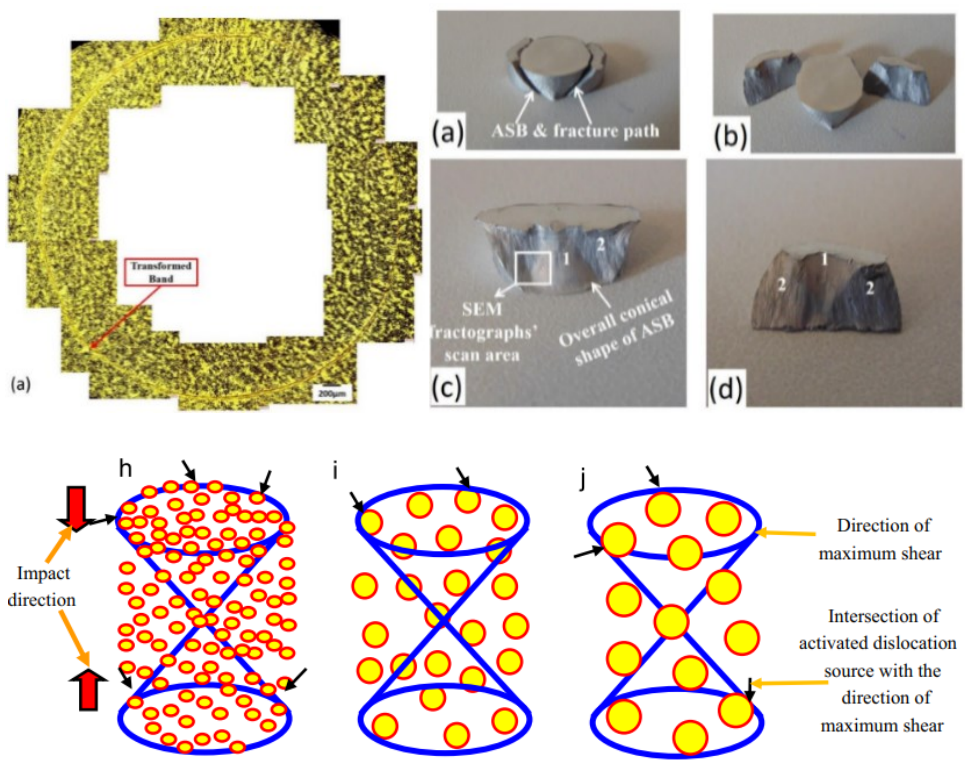

Figure 2.15: Typical ASB cross section and fracture path [107]. Illustration to visualize maximum shear plane and fracture conditions [46].

2.4.3.3 Nanoscale Microstructural Characterization (TEM)

Systematic and diligent constitutive studies of ASBs using pre-impact and post-mortem TEM analysis are rare. Systematic TEM analysis is necessary to discern the ASB evolution mechanisms, since SEM does not offer the required resolution to observe nanoscale effects where dislocation mechanics, lattice interfaces, and carbide evolutions are revealed.

On steel alloys, it has been demonstrated that the temper condition has significant effects on a materials propensity to ASB formation. Boakye-Yiadom [46] reveals that ASB initiation in 4340 steel specimens is dependent on the temper condition, which affects the size and distribution of carbides. It is found that with increasing tempering temperature, the consequential increase of carbide size and decrease of their distribution density results in greater ASB resistance [46]. Based on observations of refined equiaxed grains and void coalescence leading to cracking along the ASB, it has been suggested by various authors that dynamic recrystallization, dynamic recovery, or phase transformation is responsible for the ASB mechanism [58], [128]. in steels. However, no irreputable evidence for these mechanisms in steel structures has been shown [127]. For example, amidst a high density of dislocations, Landau et al. propose DRX in the ASB of a titanium alloy [128]. However, some authors have disputed this theory, demonstrating that the ASB's consist of a high-density dislocation network and trans granular dislocation cell formation [42], [104], [105], [129] prior to the evolution of refined grains observed universally.

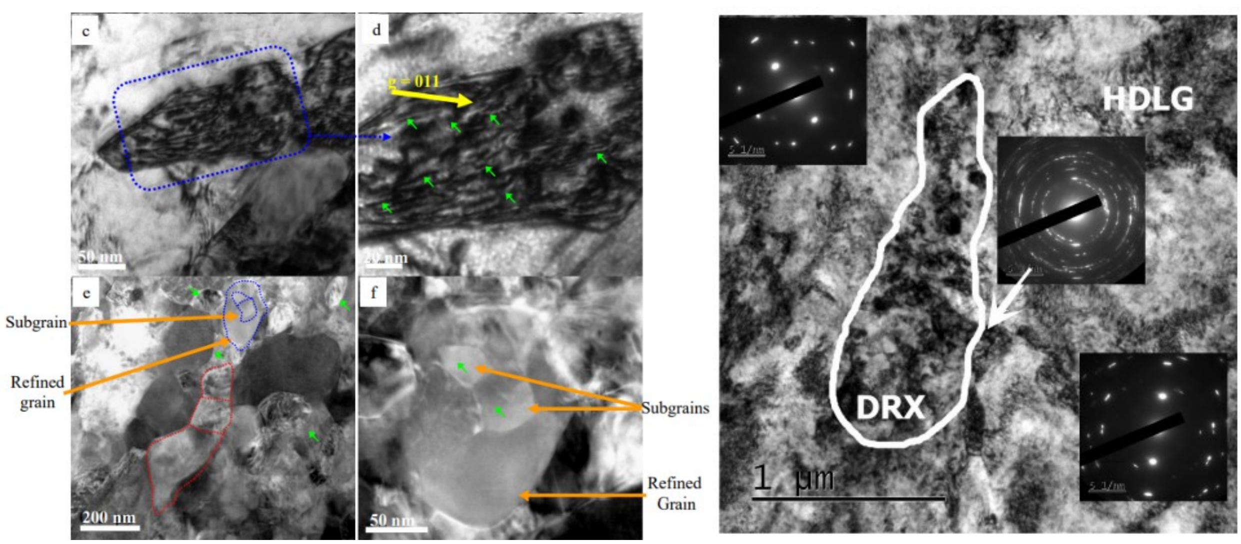

Figure 2.16: Different mechanisms perceived by different authors for 4340 steel [42] and Ti alloys [128] from left to right. Dislocation networks observed in both alloys indicated by dark regions.

Figure 2.16 shows typical refined grains and sub-grains with dislocation networks in a 4340 steel specimen [42] and also shows dislocation networks in a titanium alloy [128]. Between dislocation multiplication and pile-up and refined grains, this explains high hardness regions, and it is highlighted that a high density of dislocations cannot coexist with a rise in temperature. This has been demonstrated by Boakye-Yiadom in his work where 4340 steel was impacted and transformed ASBs formed where no cracks initiated, and post impact annealing heat treatment was done. It was observed that as the heat treatment temperature increased, the microstructure of the shear bands would start to have significant changes and start to disappear. After post impact annealing at 850 C, the ASBs disappeared completely [130]. Edwards, Tiamiyu, Boakye-Yiadom [42], [107], [117] all provide a detailed literature review on the microstructural aspects of ASB's.

The absence of carbides has been observed in ASBs in steels. M.A Meyers [129] highlights that no phase transformation is possible in 4340 steel specimens, primarily due to the length of time required for this to occur. Further, no austenite is observed in the ASBs, rather carbide dissolution is identified in the ASB regions with refined grains. Boakye-Yiadom [105] supports this evidence with TEM analysis, revealing with irreputable evidence that very refined residual carbide particles are present in the ASB, and normally sized carbide particles outside of the ASB. Upon post-impact annealing, the carbides reappear in their larger configuration within the ASB [42]. Perez-Prado et al. [131] perform systematic stopping ring tests on top-hat specimens to reveal that only dynamic recovery and no dynamic recrystallization occurs in Ta and TaW alloys. They highlight that the temperature rise is insufficient to reach the recrystallization temperature. They propose a mechanical driving force for the development of rotated refined grains, which they named the progressive subgrain misorientation (PriSM) model.

Authors have demonstrated that FCC alloys such as pure copper can develop dynamic recovery and dynamic recrystallization failure mechanisms [132], [104]. Boakye-Yiadom produces evidence for this by performing increasing strain/strain-rate tests. With increasing strain levels, increasing plastic strain formed an increasing density of dislocation cells and structures, which disappeared upon the appearance of recrystallized grains and deformation twinning. Notably, the deformation twins were dislocation free as opposed to pre-impact twins observed which had residual dislocation structures [104]. Hines and Vecchio [132] demonstrate that there is no effect of the temperature change on the microstructure of the ASB for pure copper. It must be noted that copper is an FCC metal and does not have a ductile to brittle transition temperature. Pure copper is highly conductive, and yet, when initiating the test at a temperature of 77 K, the microstructure of the ASB post-impact was the same as when impacted at room temperature. It is accentuated that this kind of evidence has not been observed in steel alloys [104].

2.4.4 Dynamic Tensile Fracture

Krauss, Wilsdorf discuss the ductile and brittle mechanisms observable on the fracture surfaces of tempered martensite tensile specimens [133], [134]. Krauss quantifies the effects of carbon content, carbide morphology, and tempering temperature on the ductility of axisymmetric tensile specimens. Both authors separately discuss the void initiation sites and growth mechanisms present and observable by SEM or TEM analysis. It is primarily discussed that second phase particles or carbides are critical in the study of void initiation and growth. Anderson et al. [101] analyzed the stress state evolution of strain rate dependent notched and unnotched dual phase steel flat tensile specimens. They correlated non-proportional triaxiality effects with the fractographic features of the specimens, identifying that as the initial triaxiality increased, the void growth rate and sizes increased as well resulting in lower fracture strains. They identified that the voids nucleated at martensitic islands and their nucleation was more prominent as deformation progressed and in specimens with higher triaxialities, since the geometry of the specimen would restrict deformation in the width direction. They concluded that the strain rate had no effect on the failure mechanism.

Alternatively, Whittington reveals a ductile to brittle transition for RHA steel from quasistatic to dynamic tension [112]. It is attributed to a greater void nucleation rate with reduced growth at high strain-rate, indicated by the smaller voids with greater distribution density in high strain rate specimens. Cao et al. also observe a ductile to brittle transition in a high entropy alloy, indicated by the image below where transgranular quasi-cleavage fracture is observed [120].

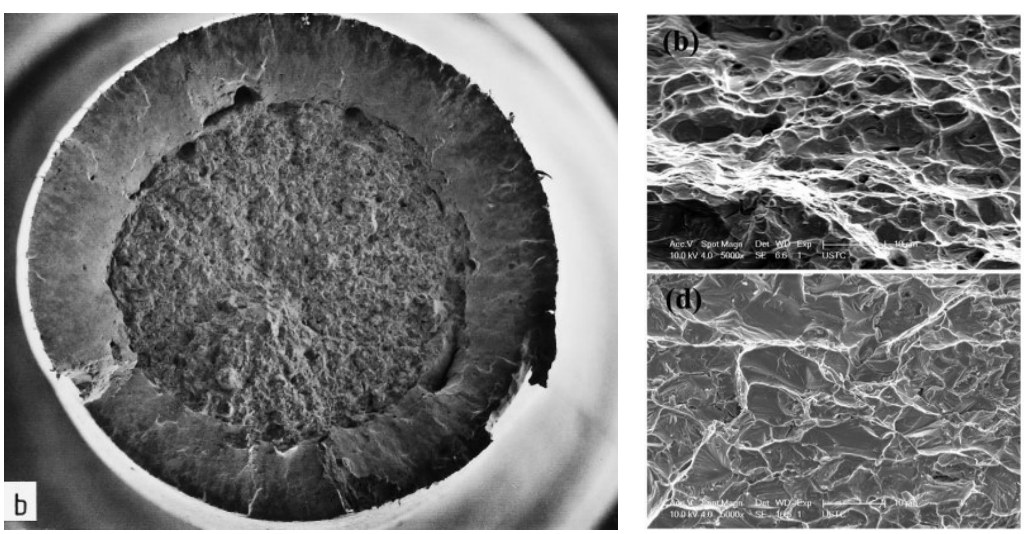

Figure 2.17: Round tension specimen fracture surface with central voids and dimples and shear lips along the radius [133], and a rate-dependent ductile to brittle transition of a HEA [120]

3.0 Experimental Methods

3.1 Design and Construction of Tensile Hopkinson Bar

3.1.1.1 Mechanical Design

A unique and practical Tensile Split Hopkinson Bar (TSHB) testing facility was exclusively designed and constructed by the author to enable high strain rate tension experiments for damage model parameterization. Two 6' ft (1.83 m) long 1" in (25.4 mm) diameter bars made of aluminum 7075-T651 (7075-T6) alloy were employed as the incident and transmitted bars. Figure 3.1 illustrates the details and mechanical components of the facility. Images of the machine under construction are also provided in Figure 3.3. An offset gas gun arrangement was utilized to create the tensile force, primarily to avoid any hermetic issues. In addition, this arrangement is beneficial since there is access to the impact flange, enabling ease of use for pre-positioning a major strain limit and pulse shaping techniques. The offset piston consists of the pneumatic tie-rod cylinder gas gun, powered by a compressed nitrogen system, which converts compressed nitrogen into linear motion. The stroke length is 16" in (0.4 m) and the piston bore diameter is 3" in (76.2 mm). The threaded rod from the cylinder piston is threaded to a pushing cap, which transfers the load to a hollow impactor.

The impactor (1.75" OD x 0.25" thickness and 3' ft long) is also manufactured from 7075-T6 tube stock and is centerless grinded about its circumference and flat grinded on the flat ends. The centerless grinding enables precision circularity on the cylindrical face OD to the required shaft fit class for a high-speed sleeve bearing. Shaft fit class selection for the OD on the impactor is critical for adequate clearance to minimize friction and wear while maximizing velocity. The impactor freely slides along bronze Oilite sleeve bearings mounted on D2 steel mounts, with 0.25" clearance over the incident bar. Bronze Oilite bearings are selected due to their capacity to minimize friction and noise while maintaining high wear resistance. The clearance over the incident bar allows the strain gauges wires to fit between the incident bar and impactor. The incident bar is supported solely by the impact flange and a mounted linear sleeve bearing on the other end near the specimen. Careful selection of the interference fit on the mount-bearing interface is also crucial to grip the bearing without elastically deforming it into an oval cross section, impeding the movement of the impactor. A long impactor was crucial to the design to enable an input stress pulse of 360 μs to reach fracture for lower strain rates and ductile materials.

The impactor strikes the 7075-T6 impact flange with 2" in (50.8 mm) OD, which is mounted on a flange mounted linear bearing (FMLB) mounted on D2 mounts. This FMLB also houses a 2" in x 6" long rod acting as a momentum trap, which is supported at the end by energy dampening material and a momentum trap end block fixed to the aluminum extrusion. The flange is threaded by a 3A/B fit class to the incident bar and as the flange slides along the FMLB, the elastic stress wave is created in the incident bar. The higher thread fit class increases thread contact surface area, reducing stresses and increasing wave propagation through the interface. The incident bar pulls on the specimen, creating plastic stress waves in the specimen and the wave is transmitted to the transmitted bar which captures the stress history of the specimen. The incident and transmitted bars use mounted linear sleeve bearings lined with FRELON bearings, which minimize friction and noise for high-speed applications. These sleeve bearings are mounted on A36 steel mounts from rectangular bar stock, which are manufactured to high tolerance to ensure alignment of the system.

This bar was designed for round tension; however, the two 7075-T6 bars can easily be interchanged with two bars for flat tension if desired in the future. The bars have flat bottomed threaded holes at the specimen interfaces. Round tension was selected primarily due to its axisymmetric nature which maintains the lode angle parameter consistent throughout loading at 1 making it preferable for stress state dependent calibration [94]. Appendix B presents the safety operations procedure for the machine, and the safety factor for the most vulnerable component (gas gun mounts) using the highest theoretical load that could be applied to the system, which would never be reached in practice.

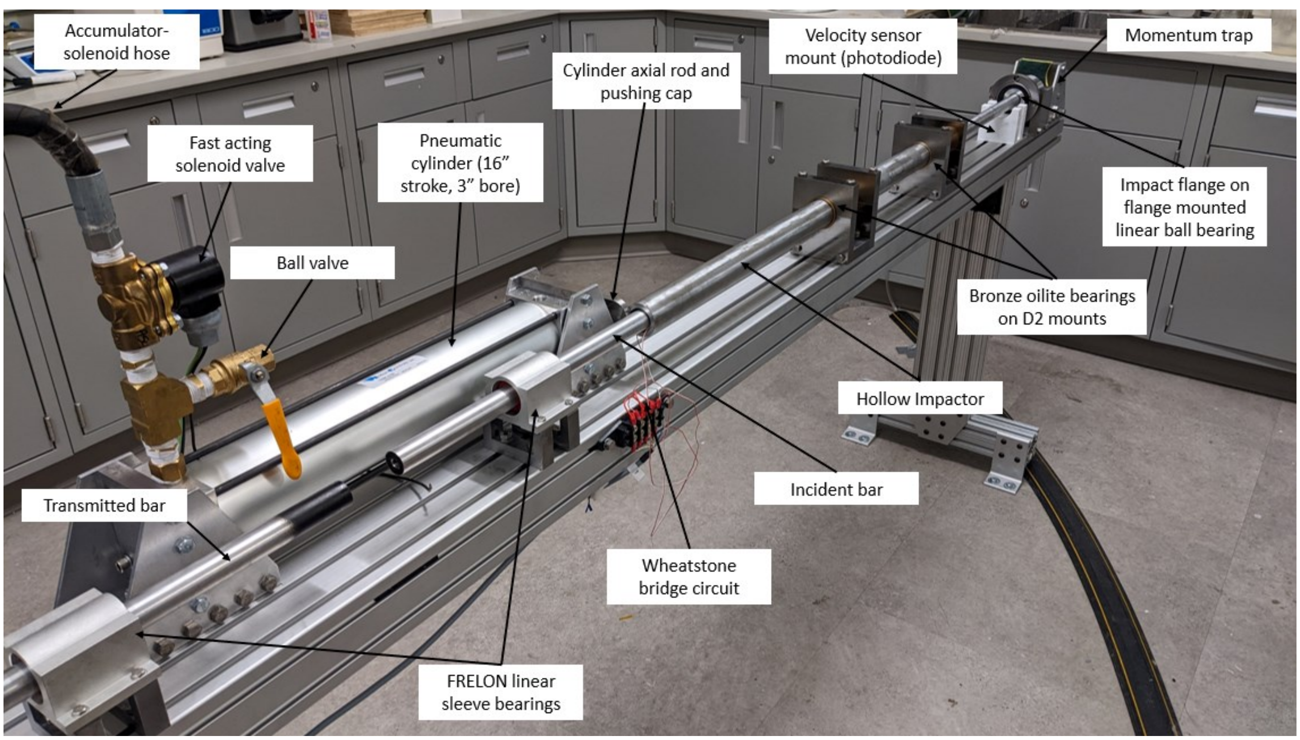

Figure 3.1: Tensile Hopkinson bar schematic

3.1.1.2 Electrical Design

Two constantan alloy strain gauges have been mounted at the halfway point of both bars in an orientation 180 degrees to each other. They were installed using a 3d printed PLA fixture and adequate adhesive. Each set of two strain gauges on each individual bar is arranged in a half-bridge Wheatstone configuration. This electrical configuration is used to eliminate any measurement of strain due to bending and provide solely 1D axial strains. The strain of the incident and transmitted bars is acquired from voltage measurements using the factory calibrated gauge factor of 2.09. The Wheatstone bridge signals are amplified by a factor of 100 and zeroed before entering the DAQ system, which is set at a sampling rate of 125 MHz for 25 MHz data acquisition frequency. Two photodiode probes are mounted on a PLA fixture just before the impact flange, to serve as a velocity measurement of the impactor once it has stopped accelerating from the pneumatic piston impulse stroke. Given the known distance between the two probes and the time stamp of the measurement when the impactor passes through it, the velocity is attained.

3.1.1.3 Summary

The numerical details of the bar can be summarized in table 1, including the strain gage locations, length of incident pulse, material properties of the bar, and geometry of the system. Figure 3.2 displays the geometry of the tensile specimens selected for this machine after a study on geometric effects with 3mm gauge diameter (D), and 9mm gauge length. This is a length to diameter ratio of 3. The length of the grip section ensures bottoming in the threaded portions of the 7075-T6 bars. The end specifications of the specimen ensure that stress wave reflections are minimized by maximizing bearing contact area and reducing its surface roughness, while also ensuring alignment through the parallelism callout. The specimen also has grips for tightly threading the specimen.

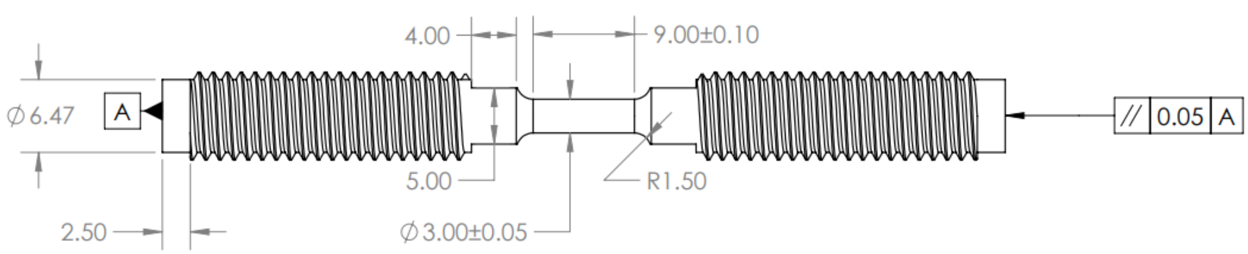

Figure 3.2: High Strain-Rate Round Tensile Specimen

Table 3.1: Hopkinson bar parameters

Bar/Impactor/Flange Material	Al 7075-T651
E - Elastic Modulus (GPa)	71.70
p - Density (kg/m^3)	2810
v - Poisson ratio	0.33
K - Bulk Modulus (MPa)	70.30
Yield Strength (MPa)	500
Max impact velocity (m/s)	71.15
C - Elastic wave speed (m/s)	5002
Pulse length (us)	360
L - Length of Bars (mm)	1829
r – Radius of bars (mm)	12.70
Bars aspect ratio	72
Location of strain gauges	L/2
Length of Impactor (mm)	900
Impactor cross section (mm)	44.45 OD x 6.35 WT
Impact Flange OD (mm)	50.8
Gas gun bore (mm)	76.2
Gas gun stroke length (mm)	406

Figure 3.3: Construction of the tensile Hopkinson bar

3.2 Stress-State Dependent Quasistatic GISSMO Parameterization

3.2.1 Mechanical Testing Matrix

A total of 72 mechanical tests covering 18 different stress-states were conducted at a strain-rate of 0.6/min (0.01 /s) for parameterization of the GISSMO. This includes 18 ASTM E8 flat tension tests in 6 different orientations to acquire the plastic strain ratios (PSR) of ARMOX 500T on different planes relative to the rolling direction. The details of the PSR testing are provided in section 4.1.1.2. The other 17 specimens were designed and drafted according to ASTM or the GISSMO literature, based on the work of Wierzbicki et al. and Basaran to differentiate the effects of LAP and triaxiality.

Three samples of each specimen are created for statistical robustness. Note that the statistical significance (T test) of all material property data of this thesis is reported in Appendix A. With regards to the design of notch radii in specific specimens, equations can be used to determine the initial triaxiality of the specimen based on its minimum cross-sectional radius or width and notch radius. All flat notched tensile specimens maintain a minimum width to thickness ratio of 4 [135]. Equation 2.8 was presented earlier as the formulation for the triaxiality in axisymmetric round tension specimens. Equation 3.1 is the equation for triaxiality for flat tension plane stress specimens [136], and equation 3.2 is the triaxiality in tensile plane strain specimens [93]. The LAP is then found using equations 2.13 and 2.14. Tensile plane strain specimens were drafted according to Basaran's iterations to identify specimen geometries to maintain consistent stress states under plane strain with an adequate thickness to ligament ratio of 12.5 [94]. Shear and shear-tension specimens were carefully selected as well to maintain consistent stress-states until fracture with observable crack growth regions in the expected locations that maintain the desired shear stress [62], [137]. Axisymmetric compression and compression-shear specimens were selected based on the design of LW Meyer, the same specimens are used for dynamic characterization, and they provide a quasistatic reference. For compression-shear specimens, the determination of initial stress-state is described in section 3.3.2.

$$\eta = \frac{1+2A}{3\sqrt{A^2+A+1}} \qquad A = \ln\left(1+\frac{a}{2R}\right) \tag{3.1}$$

$$\eta = \frac{\sqrt{3}}{3}\left[1+2\ln\left(1+\frac{t}{4R}\right)\right] \tag{3.2}$$

All quasistatic tests are conducted under displacement control at a constant strain-rate. All specimens are acquired from a 30mm thick 500x500mm ARMOX 500T plate from SSAB, Sweden. All specimens except round tensile specimens are machined by electric discharge machining (EDM). Round tension specimens are traditionally machined by CNC lathe due to lack of access to rotary EDM. Aside from compression specimens, all specimens are acquired such that the tensile loading direction is perpendicular to the rolling direction (in same direction as 90-degree flat tensile specimen). Flat tension specimens are acquired under all orientations specified under section 4.1.1.2. Compression and compression-shear specimens are loaded in the out of plane direction relative to the plate. All crosshead speeds were determined based on the specimen gauge lengths, information which is again acquired through the damage model literature [19], [62], [137]. The crosshead speed is simply the gauge length multiplied by the desired strain-rate of 0.01 /s. All drafted specimens are shown in Figure 3.4, except compression specimens which are defined later in section 3.3.2. Additionally, a table summarizing their stress-state and test matrix with an illustration of the stress-state map for the GISSMO parameterization is provided in Table 3.2 and Figure 3.5. Lastly, Appendix C provides all specimen engineering drawings.

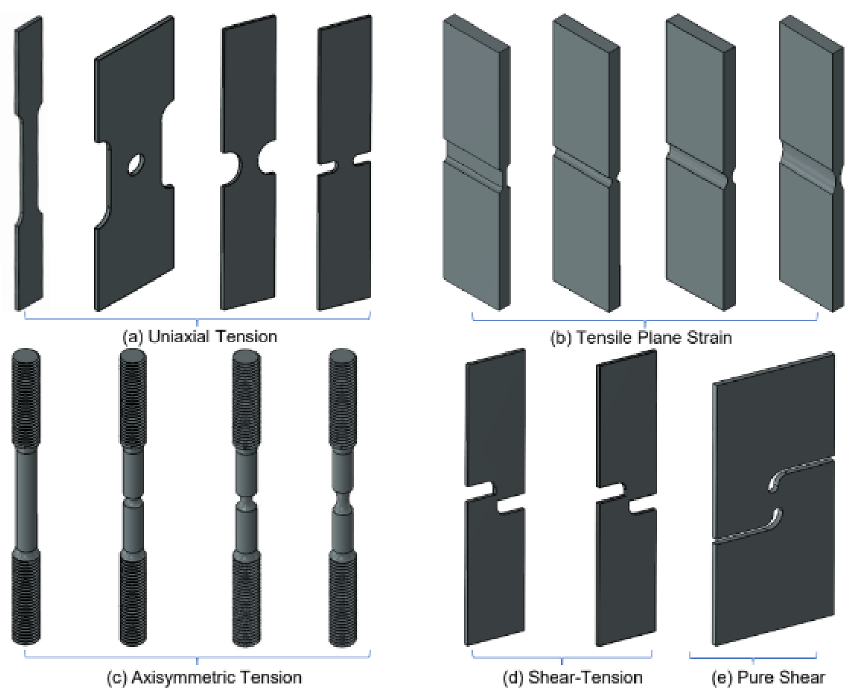

Figure 3.4: Dimensions of quasi-static specimens

Table 3.2: Quasistatic test matrix

Stress State	Specimen	Initial Triaxiality (η)	Initial Lode Angle Parameter (ζ)	Crosshead Speed (mm/s)
Uniaxial Flat Tension	Flat Tensile	1/3	1	0.500
	Hole Tensile	1/3	1	0.180
	Flat Tensile (R6)	0.43	0.67	0.120
	Flat Tensile (R2)	0.52	0.31	0.040
Tensile Plane Strain	Grooved flat plate	0.58	0	0.060
	Grooved flat plate (R8)	0.65	0	0.160
	Grooved flat plate (R4)	0.71	0	0.080
	Grooved flat plate (R2)	0.84	0	0.040
Axisymmetric Round Tension	Round Tensile	1/3	1	0.300
	Round Tensile (R12)	0.45	1	0.240
	Round Tensile (R6)	0.56	1	0.120
	Round Tensile (R3)	0.74	1	0.060
Axisymmetric Compression	Compression L/D = 1.1	- 1/3	-1	0.070
	Compression Shear 6	- 2/7	-0.84	0.064
	Compression Shear 10	- 1/4	-0.73	0.064
Pure Shear	Shear (Angle=0)	0	0	0.030
Shear-Tension	Shear (Angle=10)	[0, 1/3]	[0, 1]	0.020
	Shear (Angle=30)	[0, 1/3]	[0, 1]	0.020

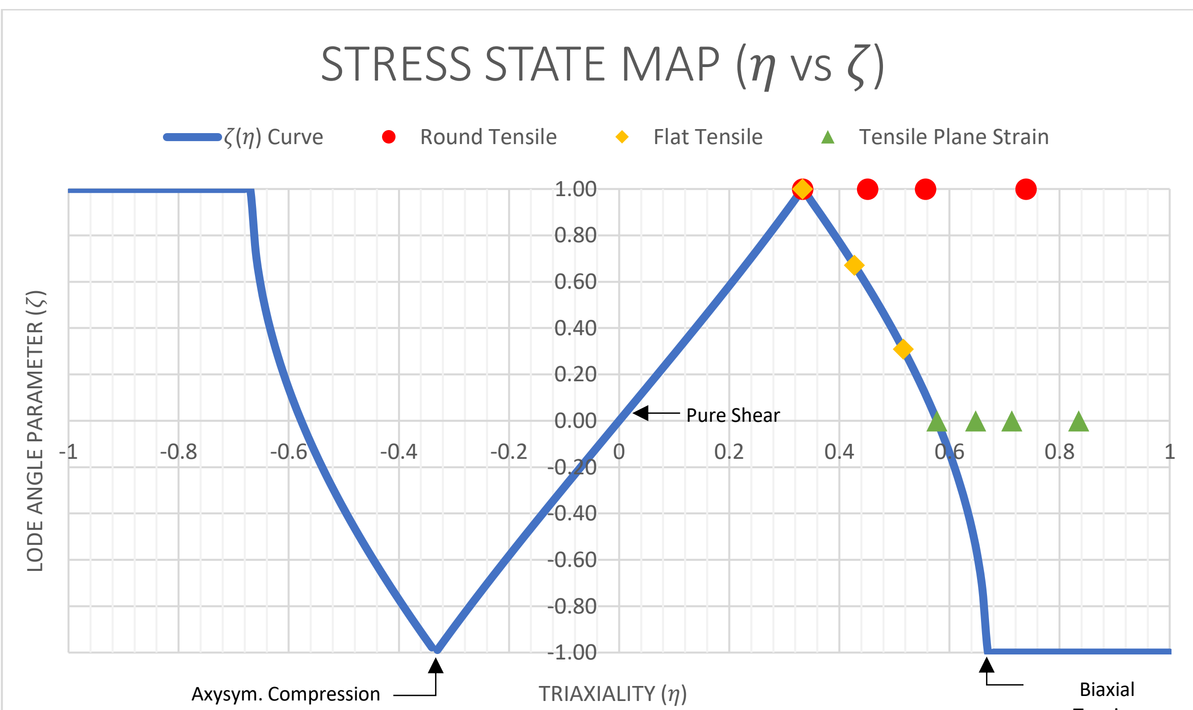

Figure 3.5: Triaxiality vs Lode Angle Parameter Stress-State map

3.2.2 Digital Image Correlation

To enable DIC, a speckle pattern is applied to all specimens. Rust-oleum painters touch matte black spray paint is applied as the dark background, and acrylic polyurethane white primer with airbrush thinner is applied with an airbrush as the white speckle pattern. The quality of all speckle patterns is checked with a normalized 8-bit histogram and image correlation peak checks during times of severe deformation near fracture for all specimens. Figure 3.6 illustrates a typical check from a hole tension test presenting the subset size and histogram with a bimodal distribution revealing good image contrast. All experiments use a sum of differences incremental correlation algorithm. This allows high strains relative to the subset size to be recorded, however the displacement errors are also accumulated with each image.

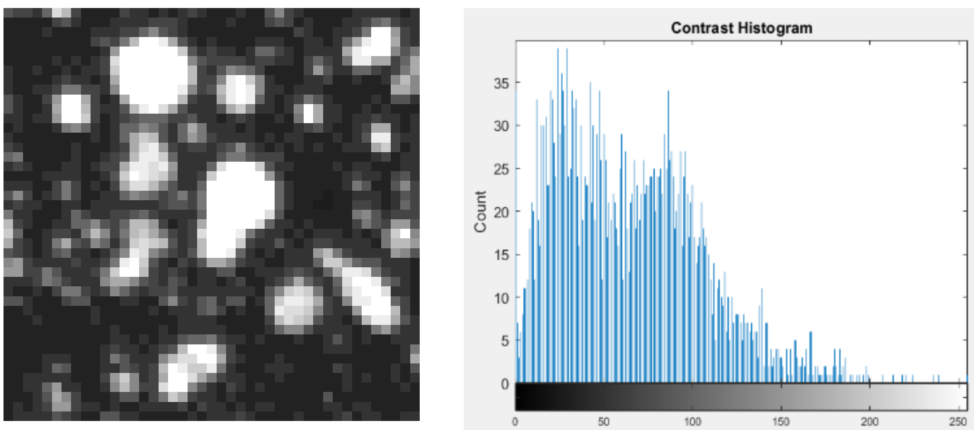

Figure 3.6: Typical subset in a hole tensile specimen and normalized histogram

For quasistatic testing, 2D-DIC was conducted for all specimens except those with cylindrical profiles (axisymmetric compression and tension tests). It was ensured to align the camera 90 degrees to the surface of interest to acquire adequate in-plane accuracy. To obtain displacement data, all tests are calibrated by scaling images given a known geometric measurement.

A 100 kN rated MTS machine was used for all quasistatic tests. All tests were temporally synchronized with LaVision's DIC system using an M-Lite 5m camera of 2448x2048 pixel resolution. For specimens with small gauge sections, a Basler 150mm macro lens was used on the camera to obtain a high spatial resolution. For stereo DIC, 2x Basler 50mm lenses were used. Figure 3.7 shows the setup on the MTS in preparation for a pure shear test. Axisymmetric compression and tension tests were conducted with stereo 3D-DIC. The stereo calibration is conducted with LaVision's standardized 106-10 SSDP calibration plate, which scales all images and computes the stereo angle. Table 3.3 summarizes the algorithm parameters used for all sets of experiments.

Table 3.3: Digital Image Correlation algorithm parameters

Specimen	Pixel size (μm)	Subset size (pixel)	Step Size (pixel)	Stereo Angle (deg)
Flat Tension	8.5	54	17	N/A
Flat Notched and Hole Tension	8.5	63	21	N/A
Shear and Shear-Tension	3.5	105	25	N/A
Tensile Smooth and notched Plane Strain	8.1	117	39	N/A
Axisymmetric Tension and Compression	3.45	63	21	17.4

Figure 3.7: MTS machine and LaVision's DIC setup with Basler lens

From DaVis software, virtual extensometer and strain gauge measurements can be extracted. The details of the location of these measurements on a specimen basis are provided with the results in chapter 4.0. They are selected based on the gauge length as per the literature, and strain gauge sizes are kept consistent and within the severe localization and instability region where fracture initiates. Using MATLAB, in-situ time dependent strain tensor from the measurements are imported from which the principal strains and the equivalent plastic strain can be derived. The following continuum mechanics relations are employed to all data [138].

$$\varepsilon_{xx} = \frac{\partial u}{\partial x}, \quad \varepsilon_{yy} = \frac{\partial v}{\partial y}, \quad \varepsilon_{xy} = \frac{1}{2}\left(\frac{\partial u}{\partial y} + \frac{\partial v}{\partial x}\right) \tag{3.3}$$

$$\varepsilon_{11} = \frac{\varepsilon_{xx} + \varepsilon_{yy}}{2} + \sqrt{\left(\frac{\varepsilon_{xx} - \varepsilon_{yy}}{2}\right)^2 + \varepsilon_{xy}^2} \tag{3.4}$$

$$\varepsilon_{22} = \frac{\varepsilon_{xx} + \varepsilon_{yy}}{2} - \sqrt{\left(\frac{\varepsilon_{xx} - \varepsilon_{yy}}{2}\right)^2 + \varepsilon_{xy}^2} \tag{3.5}$$

Where $\frac{\partial u}{\partial x}, \frac{\partial v}{\partial y}, \frac{\partial u}{\partial y}, \frac{\partial v}{\partial x}$ are the components of the 2D Cauchy strain tensor obtained from the full field specimen surface measurement, and $\varepsilon_{11}, \varepsilon_{22}$ are the surface principal strains. Furthermore, to acquire the load-path dependent equivalent plastic strains, the following formulation is employed [139]. Where the z strain is acquired with 2D-DIC using the constant volume assumption for isotropic materials. For an isotropic material, it can also be assumed that $\varepsilon_{xy} = \varepsilon_{xz} = \varepsilon_{yz}$.

$$\varepsilon_{eq} = \frac{\sqrt{2}}{3}\sqrt{\left(\varepsilon_{xx} - \varepsilon_{yy}\right)^2 + \left(\varepsilon_{yy} - \varepsilon_{zz}\right)^2 + (\varepsilon_{zz} - \varepsilon_{xx})^2 + 6\left(\varepsilon_{xy}^2 + \varepsilon_{xz}^2 + \varepsilon_{yz}^2\right)} \tag{3.6}$$

This enables the full-field parametrization of the material for the GISSMO and enables a simplified procedure for the computational calibration of the model. In addition, FEA fields can be compared to the DIC fields and extrapolations from the surface can be employed to acquire the equivalent plastic failure strain at the non-visible central fracture regions of the specimen mid-planes. Figure 3.8 shows all plane stress and plane strain specimens as received from EDM machining before and after speckling, with a couple of examples as viewed through the LaVision camera, and below are all flat tensile specimens before and after speckling, with 2 backup specimens for each orientation.

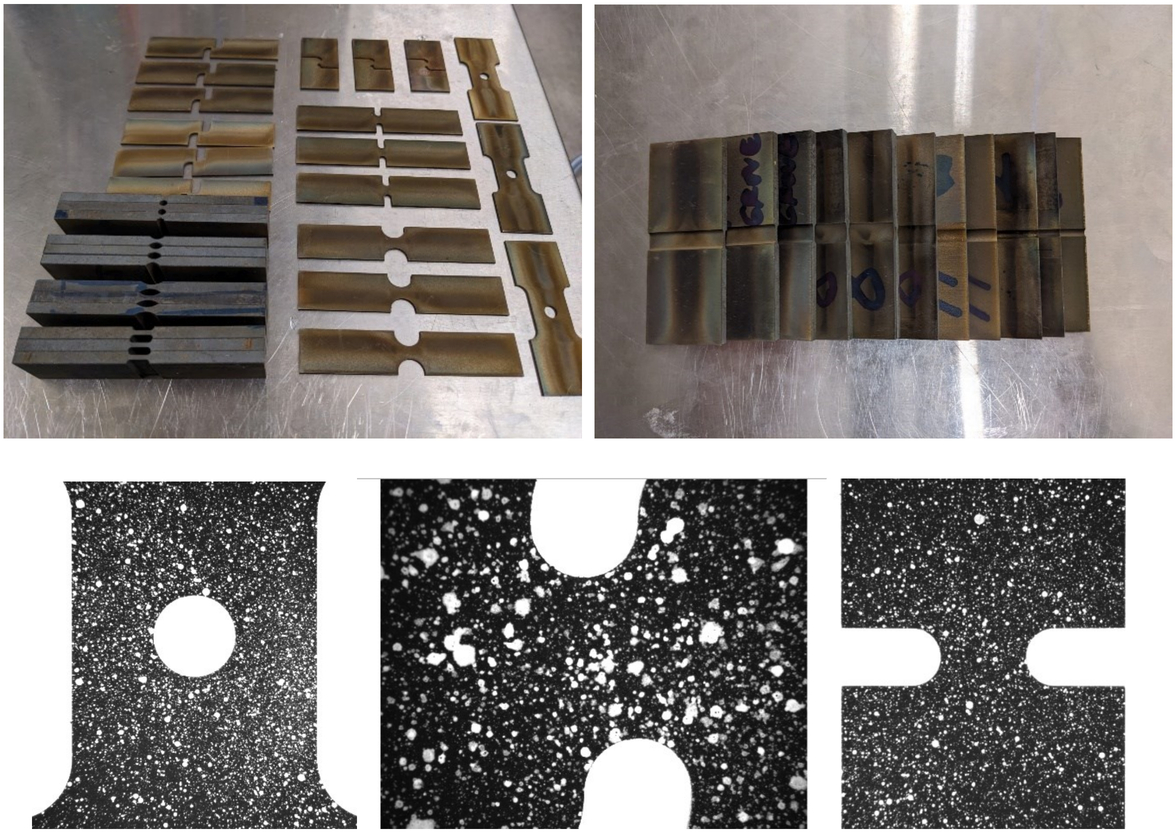

Figure 3.8: As-received plane strain and plane stress specimens from EDM and speckled specimens viewed through cameras

Figure 3.9: Quasistatic flat tensile specimens before and after speckling

3.3 Strain-Rate Dependent Extension with Lode Angle Dependence

3.3.1 Hopkinson Bar Systems

Four specimens are used in a novel lode angle dependent methodology for high-strain rate characterization to provide an empirical strain-rate dependent extension to material damage models. It is designed to quantify the effect of stress-state in terms of shear stress on the propensity of the material to form ASBs. Ideally, three specimens should be used to provide strain-rate strengthening data (compression, torsion, tension) at LAP's of -1, 0 and 1, respectively. All three maintain consistent lode angles up to fracture. However, the torsional Hopkinson bar was under construction during the writing of the thesis and therefore the data could not be added. The data will be added to the final GISSMO model of ARMOX 500T.

In addition, two compression-shear specimens quantify the effect of shear stress on ASB formation. It is developed by LW Meyer as described in section 2.4.2.1. The initial stress state in the angled cylindrical specimens is quantified by a shear/compression load ratio; deemed λ, determined by stress transformation equations. This research further defines a unique empirical instability criterion based on the correspondence of axial elongation to equivalent strain at ASB initiation.

3.3.1.1 Direct Impact Hopkinson Pressure Bar

The Direct Impact Hopkinson Pressure Bar (DIHB) consists of a nitrogen gas gun system which provides the impulse energy. A 0.15m long 1.5" OD heat treated (55 HRC) 1.37 kg AISI 4140 steel projectile is fired inside a barrel directly at the specimen which is mounted on the 4140 transmitted bar. The projectile was annealed at 850 C for 2 hours followed by oil quenching. It is chamfered at the edges to avoid mushrooming and flat grinded and polished to attain a flat and smooth surface. Molybdenum disulfide (MoS2) extreme pressure grease is used to reduce friction at the specimen-bar and specimen-projectile interfaces. A DIHB schematic is shown in Figure 3.10. The force-time history of the specimen is obtained via load cell calibration method [42] and the following true stress-strain curves can be derived.

$$\sigma_t(t) = \frac{F(t)\left(L_i - \left(L_i - L_f\right)\left(\frac{t_s}{t_f}\right)\right)}{A_s L_i} \tag{3.9}$$

$$\varepsilon_t(t) = \ln\left(\frac{L_i}{L_i - \left(L_i - L_f\right)\left(\frac{t_s}{t_f}\right)}\right) \tag{3.10}$$

Where $F(t)$ is the force history of the specimen and is acquired via calibration of the entire signal chain as per the aforementioned compressive calibration setup. L_i, L_f are the initial and final specimen lengths, A_s is the cross-sectional area of the specimen, and $\frac{t_s}{t_f}$ is a linear time array ranging from 0 to 1 where t_s is the iterative time step starting at t0 and t_f is the final instant of time. This normalizes the stress and strain to the linear deformation assumption.

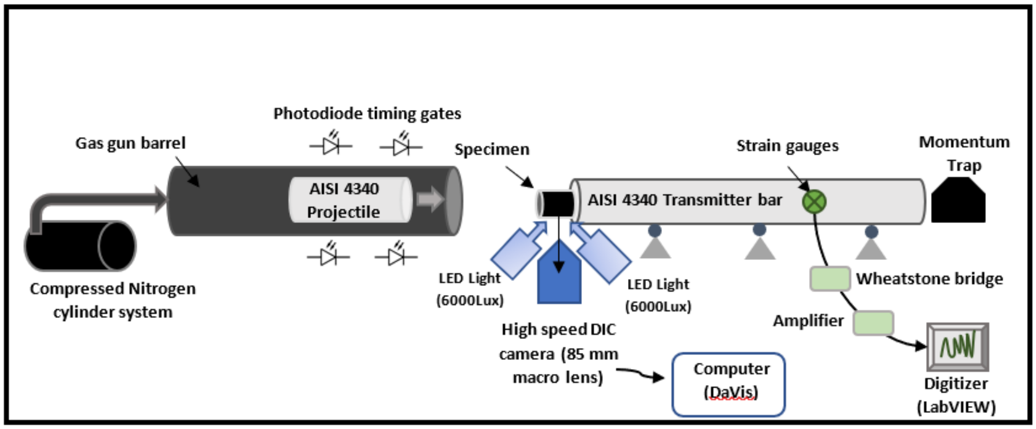

Figure 3.10: Direct Impact Hopkinson Pressure Bar

3.3.1.2 Tensile Split Hopkinson Bar

Once built, traditional elastic wave equations can be applied to the incident and transmitted bar strains obtained from the strain gauges. Assuming perfect 1D wave propagation (no wave dispersion due to poisson ratio effects), and stress equilibrium, the bar strains can be translated into the specimen's stress-strain response. The stress equilibrium assumption is required for a valid Hopkinson bar test in uniaxial tension, since if not met, the homogenous deformation condition is not met, and stress in not distributed evenly in the specimen. Depending on the specimen gauge length and shape of the incident pulse, it takes some time to reach stress equilibrium. Equations 3.11-3.13 dictate the stress equilibrium condition:

$$\sigma_1 = \frac{A_b}{A_s} E(\varepsilon_i + \varepsilon_r) \tag{3.11}$$

$$\sigma_s = \sigma_2 = \frac{A_b}{A_s} E(\varepsilon_t) \tag{3.12}$$

$$\sigma_1 = \sigma_2 \qquad \varepsilon_i + \varepsilon_r = \varepsilon_t \tag{3.13}$$

Where σ_1, σ_2 are the stresses at both ends of the specimen at the incident and transmitted bars, respectively. A_b, A_s are the cross-sectional bar and specimen areas, E is the elastic modulus of the bar material, and ε_i, ε_r, ε_t are the incident, reflected, and transmitted bar strains respectively.

Using a MATLAB script, strain gauge datasets are imported into the script and a digital Butterworth filter is added to the pulse-shaped data to eliminate the noise floor of the electrical signal. The normalized cut-off frequency is determined by $w_n = \frac{2f_c}{f_s}$ where $f_c = \frac{C\sqrt{2}}{6\pi r v}$ is the cut-off frequency at a given signal sampling rate f_s, for bar radius r and Poisson ratio v. This filter is applied to all incident and transmitted signal data prior to any data reduction or formulations. Stress-equilibrium is then checked for every test. Once stress equilibrium is ensured, equation 3.12 can be used to obtain the specimen stress response (1-wave analysis). Alternatively, equation 3.11 can be used (2-wave analysis) or an average of both can be taken (3-wave analysis). 1-wave analysis is used in this system and σ_s is denoted the specimen engineering stress. Lastly, the following equations can be employed to obtain the strain and strain-rate from the reflected pulse:

$$\dot{\varepsilon} = -\frac{2C}{L_s}\varepsilon_r \qquad (3.14)$$

$$\varepsilon = -\frac{2C}{L_s}\int_0^t \varepsilon_r \, dt \qquad (3.15)$$

Where C is the elastic wave speed in the bar material, and L_s is the specimen gauge length. Given the previously stated assumptions and assuming insignificant energy loss at all interfaces, the above equations can be used to estimate the strain rate dependent stress-strain response of the specimen. Some wave dispersion will always be present in Hopkinson bar tests. In 1D wave propagation theory, the wavelength of the elastic wave dictates its speed. A higher frequency elastic stress wave will travel slower than a lower frequency wave [98]. When the impact flange is impacted, a spectrum of frequencies is present in the step function incident stress pulse. Furthermore, as the elastic wave propagates through the bar, the bar cross section changes slightly due to the poisson ratio effect, altering the local wave speed in that section due to its dependence on the cross-sectional area of the bar. When the higher frequency components propagate slower behind the low frequency components, in combination with poisson ratio effects occur, wave dispersion occurs. These are known as Pochhammer-Chree oscillations, and they are observed in all Hopkinson bar tests.

Pulse shaping is a technique used to mitigate Pochhammer-Chree oscillations by placing a plastically deformable material on the impact flange (or impacted face on the incident bar under compression) [98]. The material filters out the high frequency components of the stress-wave and changes the incident pulse of the stress-wave. Often, it can serve the dual purpose of mitigating wave dispersion and reducing the time to reach stress-equilibrium as it changes the rise profile of the traditional step function incident pulse [98]. The reader is referred Vecchio and Jiang who discuss pulse shaping techniques in detail [140].

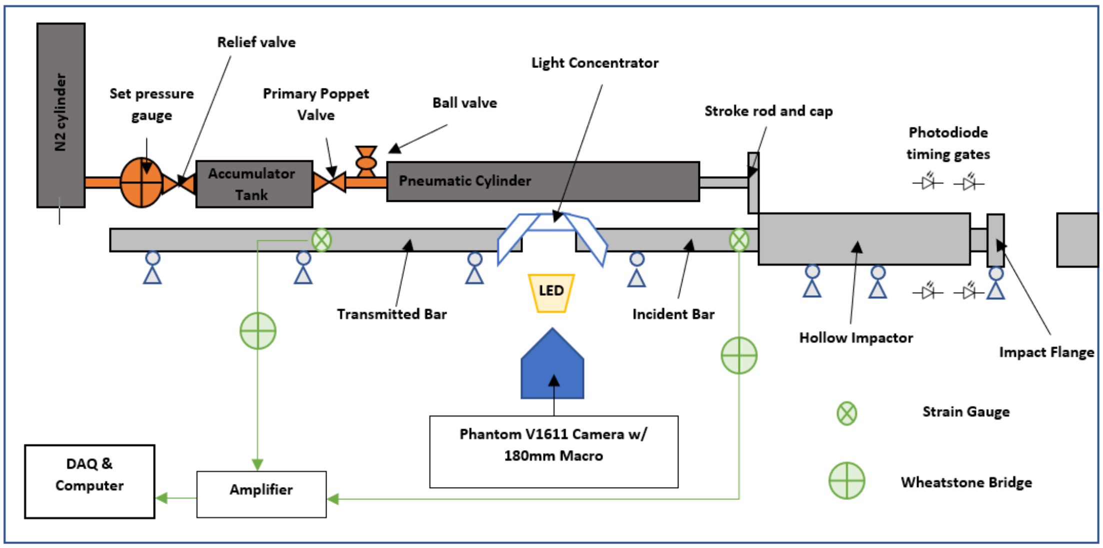

Figure 3.11: Tensile-Split Hopkinson Bar

3.3.2 Dynamic Testing Matrix

In addition to the tensile specimen used (Figure 3.2), the other three specimens used are presented as well in Figure 3.12, with a graphical illustration of the stress-states in Figure 3.13. All specimens indicate stress-states quantitatively and respective λ's. Axisymmetric compression specimens have dimensions Ø6.35x7mm, such as to maintain a 1.1 L/D ratio alike to the Ø9.5x10.5mm specimens discussed in section 2.4.2.1, which are preferable for microstructural characterization of ASBs. Multiaxial specimens have L/D ratio of 1 and are identical to LW Meyer's specimens. Employing stress transformation equations and assuming a biaxial stress-state [138], the principal stresses and corresponding λ can be obtained based on the angle of inclination. Then, the initial triaxiality and lode angle parameter can be quantified in both the uniaxial and multiaxial specimens as per equations 2.5-2.7 and 2.13-2.14 in section 2.3.1. As per the work of LW Meyer, these specimens maintain consistent stress-states in the maximum shear planes making them preferable for material characterization of ASBs.

For high strain-rate, four repeats are conducted for all tests. 32 axisymmetric compression (C) tests are conducted to acquire 4 non-fracture strain-rates and 4 fractured strain rates such as to acquire strengthening stress data (no fracture) and fracture strain data. This is done because during the creation of the fracture surface, work is done, and energy is lost which is not captured by the transmitted strain gauge and this is observable in the data with a significant loss of flow stress. For high strain-rate tension (T), 16 tests are conducted. This is to provide 4 fracture strain rates for both strengthening and DIC strain data. It was found that the work lost to the fracture surface was negligible in the data and no difference was found between fractured and non-fractured tensile tests. Lastly, 6 tests are conducted on compression-shear (CS) specimens (3 at each angle) for comparison to axisymmetric compression. Note, the number on CS specimens indicates the angle.

Furthermore, 6 additional tests are performed on compression-shear specimens (three at each angle) with increasing strain levels at a constant impact momentum. This is achieved using a stopper ring of a specific high tolerance length to achieve a desired pre-determined strain. These specimens are then used for post-mortem microstructural characterization and metallography.

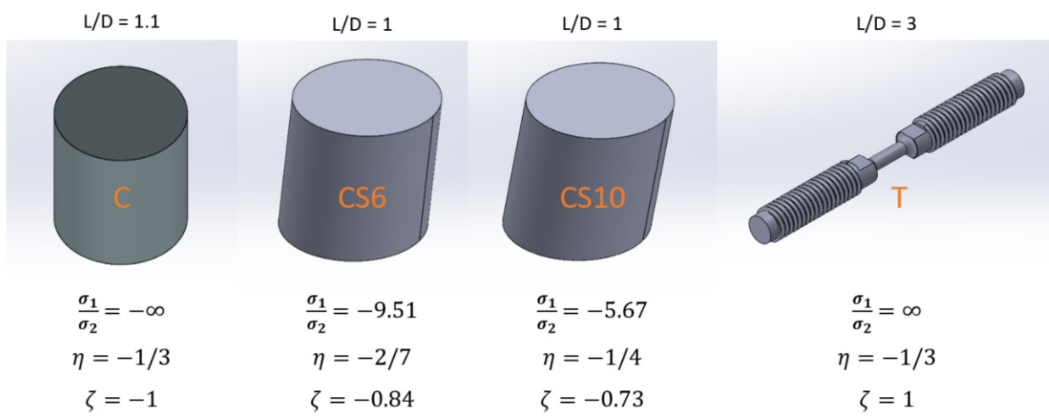

Figure 3.12: Depiction of the high strain-rate specimens with constitutive stress-state definitions.

Table 3.4: Dynamic test matrix (torsion outside scope of thesis)

Specimen	Angle of inclination (deg)	Principal Stress Ratio ($\frac{\sigma_1}{\sigma_2}$)	Initial Triaxiality (η)	Initial Lode Angle Parameter (ζ)	Shear / Compression Load Ratio (λ)
Axisymmetric Compression	0	$-\infty$	- 1/3	-1	0
Compression Shear 6	6	-9.51	- 2/7	-0.84	0.10
Compression Shear 10	10	-5.67	- 1/4	-0.73	0.17
Axisymmetric Tension	0	∞	1/3	1	0

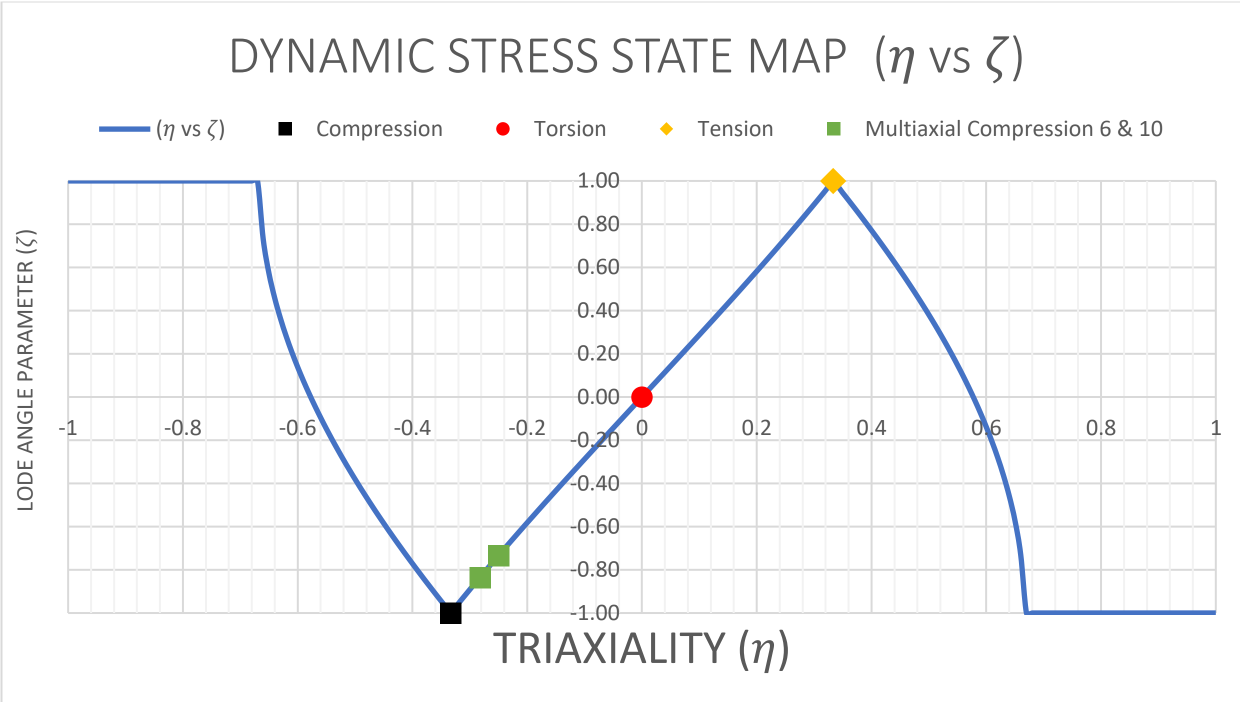

Figure 3.13: Dynamic stress-state map (torsion outside scope of thesis)

3.3.3 High-Speed Optical Imaging

3.3.3.1 Optical Camera Setup

Figure 3.14 illustrates the LED light and camera setup arrangement. To optimize image quality, the LED light produces 13,000 lux and has a hemispherical dome coated with reflective material to promote diffuse lighting conditions. The setup features a novel 3D-printed PLA light concentrator to reflect and focus the LED light onto the specimen, illustrated as well in Figure 3.14.

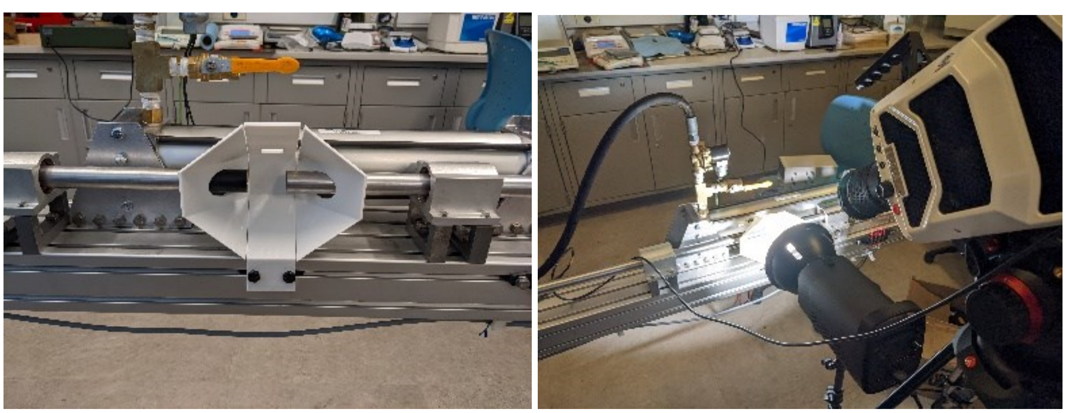

Figure 3.14: High-speed optical camera experimental setup on TSHB 3.14a: light concentrator. 3.14b: Camera & LED.

The camera is a Phantom V1611 high speed camera and is attached to a C-mount 180mm macro lens with a large, fixed aperture number f/2.4. This narrows the depth of focus while maximizing the amount of light passed through the lens. This setup enables the LED light to be very close the specimen and maximize the usage of its light by directly focusing its beam to the light concentrator.

3.3.3.2 Digital Image Correlation

The camera frame rate is set at 100 kHz, constraining the spatial resolution to 384x256 pixels. For all high strain-rate experimental setups, with the macro lens the FOV at this resolution is approximately ~24x16 mm. This frame rate enabled a temporal resolution of 10 μs. Speckle sizes were on average in the range of 0.05 - 0.2 mm diameter. Given the FOV and spatial resolution, the pixel size is about 0.06 mm (60 μm).

Figure 3.15 shows speckled tensile and compression-shear specimens before testing viewed through the Phantom camera, with their subsets and typical correlation peak just before fracture. Given good image contrast and image correlation, no image pre-processing is required and therefore not conducted. Images were post processed using LaVision's DaVis software using the sum of differences incremental correlation method. If a relative to first correlation is conducted, only noise peaks are observed. For the given FOV, a subset size of 21 was used with a step size of 3. Smaller subset sizes increase noise with no increase of accuracy, and larger sizes lose resolution. A finer step size is implemented to increase resolution of strain localization in the fracture regions, larger step sizes provide identical homogenous strain results, but reduced localization strains.

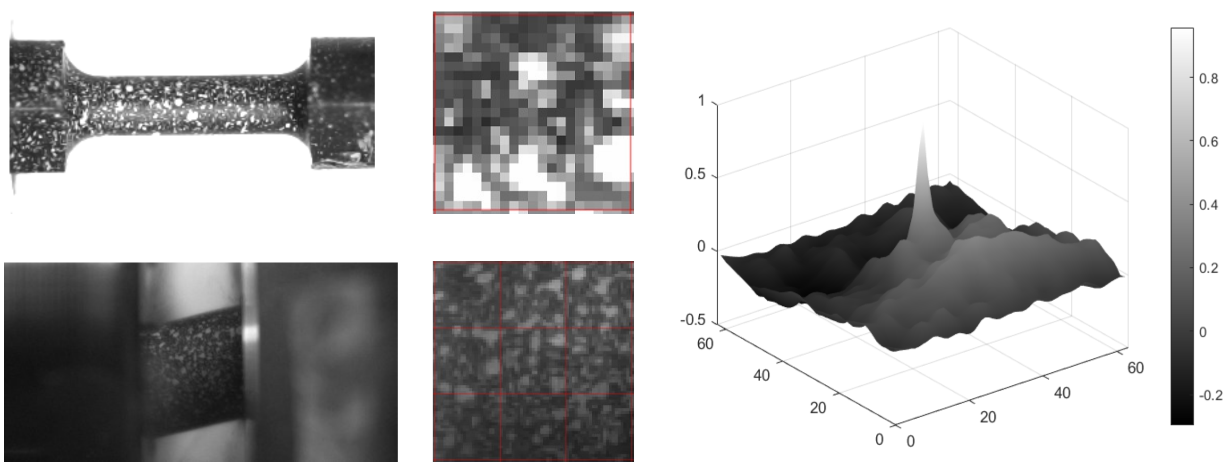

Figure 3.15: Speckled tensile and compression-shear specimens viewed through the high-speed camera with respective subsets and correlation peak of the necking region of the tensile specimen

3.4 Microstructural Characterization

3.4.1 Light Optical Microscopy (OM)

As received and post-impact non-fractured specimens were observed under an optical microscope to observe and characterize the initiation, mechanical properties, and evolution of adiabatic shear bands in axisymmetric compression and compression-shear specimens. As-received specimens are sectioned using water-jet cutting from the as-received ARMOX plate, away from the flame-cut edges. 3 different as-received specimens are observed to quantify any rolling texture and possible microhardness differences on the three different planes.

To avoid inadvertent tempering, all specimens were cold mounted using an epoxy-hardener mix and prepared using standard metallographic procedures. Silicon carbide grinding papers of 400/600/800/1200 grit were used before fine polishing with 0.05 um alumina powder to obtain a flat and mirror-like surface. All ARMOX 500T specimens were etched with 2% Nital full immersion for 15 s, followed by ethanol and water cleaning, respectively. They were then dried with a low-pressure air nozzle. The Zeiss Axio-Imager 2.0 optical microscope was used to observe ASBs using 5x, 10x, 20x, and 50x objectives with differential interference contrast. The Vickers microhardness tester was used with a 40x objective to perform standard microhardness testing. 10 microhardness tests were conducted in all measured regions using 100 gf (0.98 N) and 15 s dwell time. Figure 3.16 shows the sectioning strategy for observing the different planes, and the as-received polished specimen with a mirror surface.

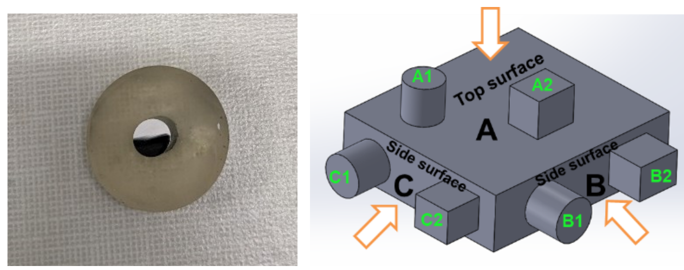

Figure 3.16: Cold-mounted post-impact ground and polished specimen and as-received sectioned specimen illustration

3.4.2 Scanning Electron Microscopy (SEM)

As-received specimens were observed with a field-emission scanning electron microscope (FE-SEM) with a vacuum pump. The same 2% Nital etched cold-mounted sectioned specimens are used and coated with pure platinum in an argon atmosphere to produce a clean, contaminant free micrometer thin conductive surface coating. In addition, carbon tape is added to ground the specimen and ensure electrons have a conductive path and mitigate charging the specimen. The sectioned specimens enable the observation of the microstructure before impact. Primarily, secondary electron images are acquired to observe the morphology of the microstructure at high spatial resolution.

For fractographic imaging, fracture surfaces were mounted directly into the SEM and grounded with carbon tape. Post-mortem failure analysis under quasistatic and high strain rate tension was conducted. Post-mortem high strain-rate compression and compression shear specimens were also observed to elucidate the fracture surfaces of ASBs.

3.4.3 Transmission Electron Microscopy (TEM)

To access the nanostructure and atomic scale resolution of materials, the transmission electron microscope (TEM) is required. Like the SEM, the TEM depends on the wave-particle duality of electrons. However, rather than depending on the backscatter or secondary electron emittance of materials the SEM depends on, the TEM produces a beam of electrons which is transmitted through the specimen. Therefore, in preparation for TEM, the specimen must be a thin lamella which is transparent to electrons. This is accomplished by focused ion beam milling (FIB). For this thesis, three impacted specimens using stop rings (described in section 3.3.2 and discussed in chapter 5.6) have been selected for FIB and TEM to discern the underlying mechanism of ASB formation.

3.4.3.1 Focused Ion Beam Milling

Figure 3.18 shows the process of the FIB for one of the specimens. The FIB process uses a beam of ions from a liquid metal source (gallium ions). The gallium metal heated onto a tungsten needle, and through carefully controlled electric fields forms into a cusp at the tip of the needle. This cusp is known as a Taylor cone and has a very small nanoscale tip, which in combination to the high electric field density at this point can ionize and create field emission of gallium ions. The ions are then accelerated through magnetic fields and focused into a highly concentrated ion beam through electrostatic lenses onto the specimen. Due to this nanoscale accuracy of beam control and area, the FIB process can select the exact region of interest for TEM specimen preparation. This is critically important in ASBs where they can be as thin as 3 μm.

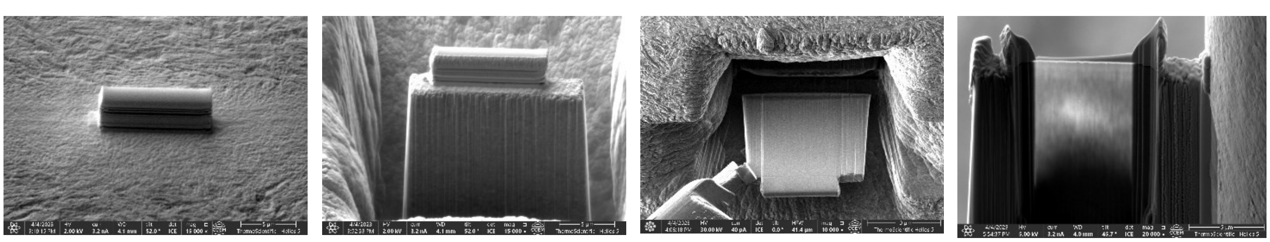

Figure 3.18: FIB milling preparation of an ASB in an AX500 specimen for TEM

3.4.3.2 Physics of TEM

The TEM consists of a voltage driven electron gun, such that upon a carefully controlled voltage applied to it, electrons are emitted by thermionic field emission into a vacuum as an electromagnetically controllable electron beam. The condenser lens and aperture manipulate and configurate the power, size, and shape of the beam (magnification level). The condenser aperture focuses this beam onto the desired size and shape according to the specimen. When passing through the specimen, the wave-particle duality nature of the electron captures information when interacting with the atoms in the specimen. After passing through the specimen, a series of electrostatic plates and electromagnetic fields enables manipulation of the beam configuration to acquire a variety of different information from the material.

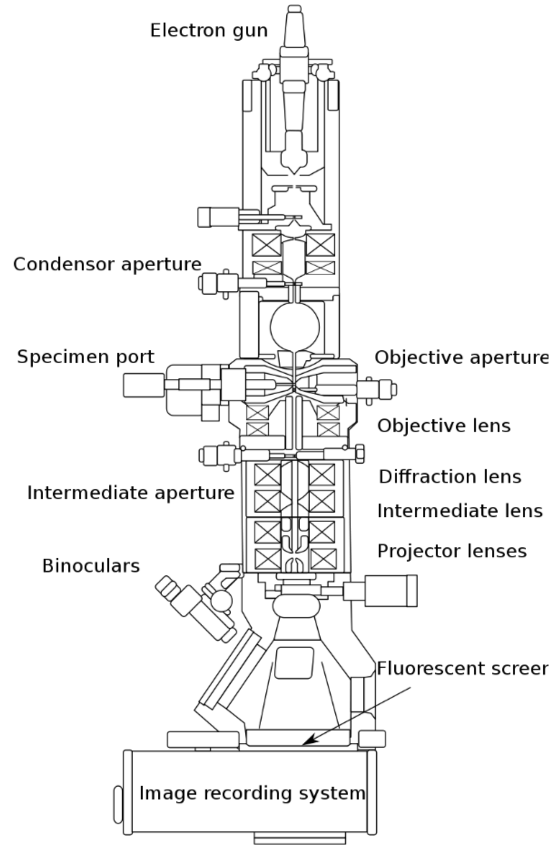

Figure 3.19: Transmission Electron Microscope (TEM)

3.4.3.3 Imaging Contrast Mechanisms

Upon interaction with the sample, electrons may change their trajectories via diffraction (scattered) or will remain unaffected and maintain their initial path (un-scattered). When the objective aperture is placed in the back focal plane of the objective lens, only the un-scattered bright central beam electrons are passed through the aperture resulting in a bright field (BF) image. Alternatively, if the objective aperture is disengaged and the selected area aperture engaged behind the back focal plane of the objective lens, only the diffracted un-scattered electrons are passed through the aperture and a dark field (DF) image is obtained. As observed in section 4.1.2.3 and section 5.6.3, bright and dark field images reveal different phenomena.

3.4.3.4 Selected Area Diffraction Mode

The concentration and directionality of atomic planes in individual crystals are revealed using selected area diffraction (SADP). Attainable lattice planes for BCT are acquired as expected in as-received lamella. Different orientations of different lath grains reveal different zone axes. Each dot is a plane of atoms as various planes are present in a crystal lattice system. This is acquired by the physical process of diffraction as atomic wavelengths interfere with one another as the electrons are passed and interact trough the atomic configuration in the ARMOX 500T specimen.

4.0 Quasistatic Characterization

4.1 As-received ARMOX 500T

4.1.1 Mechanical Characterization

All ARMOX 500T (AX500) specimens for microstructural and mechanical characterization were attained from 30mm thick 508x508mm plates of AX500 received from SSAB, Sweden. SSAB produces very clean steel free of MnS stringers and highly reduced levels of Phosphorus and sulfur, thereby eliminating possible failure modes experienced by unclean steels. SSAB is also in the process of becoming the first 100% green steel production plant, thus giving AX500 the potential to be a green steel with no carbon footprint in the future.

4.1.1.1 Metallurgy of ARMOX 500T

ARMOX 500T is exclusively produced by SSAB, Sweden and available in plates ranging from 3mm to 80mm thickness. It is a medium-carbon (0.32 %) low-alloy hot rolled quenched and tempered martensitic steel with very high strength and balanced toughness tailored primarily for armour applications. The carbon amount is selected to avoid conditional embrittlement such as in high carbon steels. The quench & tempering procedure is unknown; however, it is carefully controlled such as to avoid retained austenite and create a pure tempered martensite microstructure with a selected balance of strength and toughness. It is alloyed in small percentages primarily by nickel, manganese, molybdenum, silicon, and a small boron percentage. Figure 4.1 illustrates the fabrication process for AX500, as received 30mm plates, and chemical composition of the alloy.

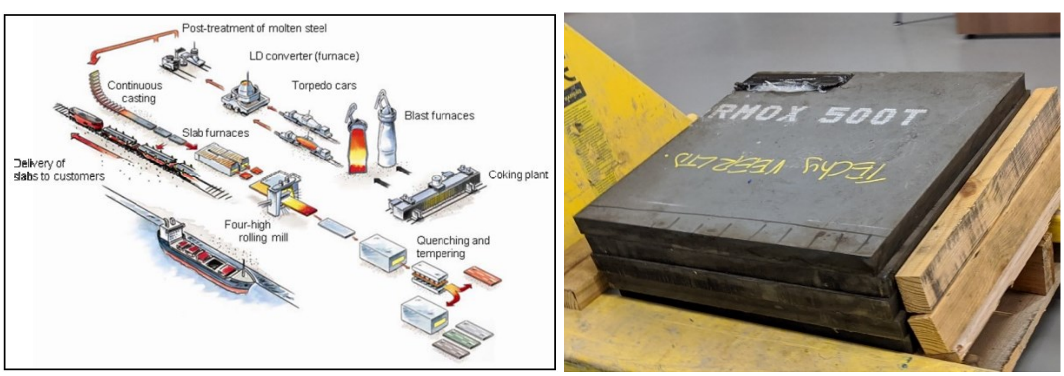

Chemical Composition (ladle analysis)

C *) (max %)	Si *) (max %)	Mn *) (max %)	P (max %)	S (max %)	Cr 1) (max %)	Ni 1) (max %)	Mo *) (max %)	B *) (max %)
0.32	0.4	1.2	0.010	0.003	1.0	1.8	0.7	0.005

Figure 4.1: Process metallurgy [142], as-received plates, and chemical composition of ARMOX 500T [141]

4.1.1.2 *Flat Tension Plastic Strain Ratio*

Flat tension tests were conducted on a 100 kN MTS machine in accordance with the ASTM E517-19 standard. To determine the plastic strain ratio, 2D-DIC was used to acquire direct high resolution surface axial (y) and width (x) measurements. To acquire the thickness strain measurement, the constant volume assumption can be used for any material undergoing plastic deformation. The plastic strain ratio, or commonly known as the R-value, is then the width strain over the thickness strain. Thus, the following formulation is used.

$$\varepsilon_{xx} + \varepsilon_{yy} + \varepsilon_{zz} = 0$$

$$R = \frac{\varepsilon_{xx}}{-(\varepsilon_{yy} + \varepsilon_{\mathrm{xx}})} = \frac{\varepsilon_{xx}}{\varepsilon_{zz}}$$

18 tests are conducted to quantify any rolling texture effects on material properties. Three repeated tests are conducted on each of 6 different orientations. 3 orientations or 9 tests are conducted on top surfaces of the 30mm plate (surface A, or rolling-transverse RD-TD plane). The other 3 orientations or 9 tests are conducted on side surfaces, of waterjet cut out rectangular prisms taken from the RD-TD plane. The side specimens are on surface B or normal-rolling plane (0), surface C or the normal-transverse plane (90) or on a diagonal 45-degree cut-out. Figure 4.2 illustrates the different orientations, the specimens acquired via EDM from the waterjet cut prisms, and the maximum principal strain field just before fracture initiation. To acquire good in-plane accuracy, the camera optical axis must be perpendicular to the surface of interest. This is achieved by aligning the digital straight red line indicators on LaVision's software with the geometric axial side of the specimen, such that there is a maximum 1-pixel deviation along the full gauge length of the specimen. Calibration is done by scaling to the known width of the specimen.

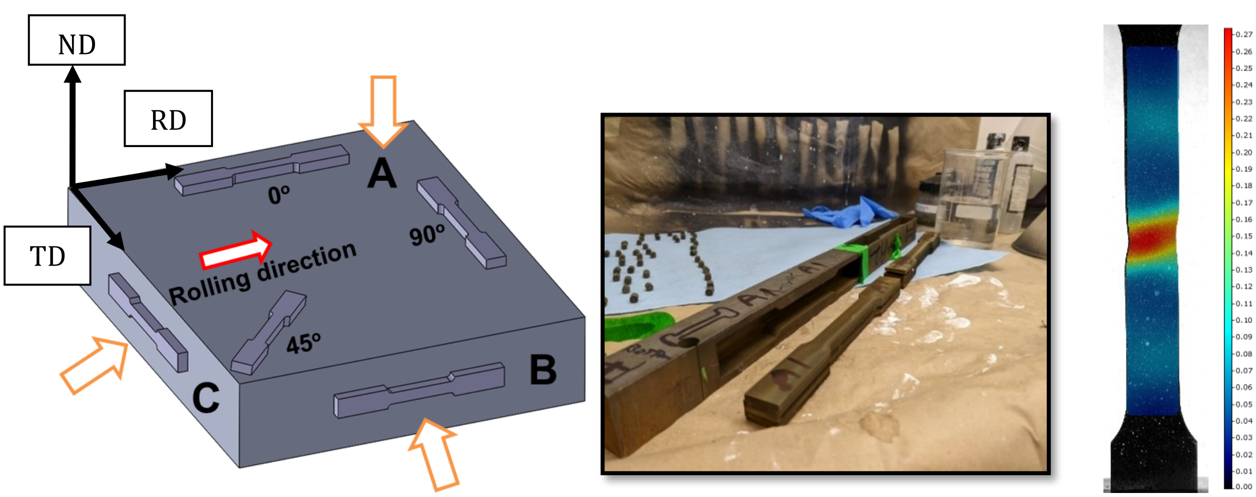

Figure 4.2: Different orientations for flat tensile specimens, cut-out specimens, and principal strain field

To determine the R-value, measurements are taken beyond the yield point and before the ultimate tensile strength is reached. Simultaneously, the hardening curves of the material are obtained including the yield, ultimate tensile strength, and elongation. It was found that the side surfaces provided very inconsistent stress-strain results for repeated test, and often the fracture locations were not centrally located on the specimen. The results are therefore not presented. For the top surfaces, the stress-strain curves and the measured R-values are shown in Figure 4.3. Table 6 then shows the precision of the tests for the hardening, elongation, R-value data. Note that the statistical significance of these tests, as well as all other data of this thesis is reported in Appendix A.

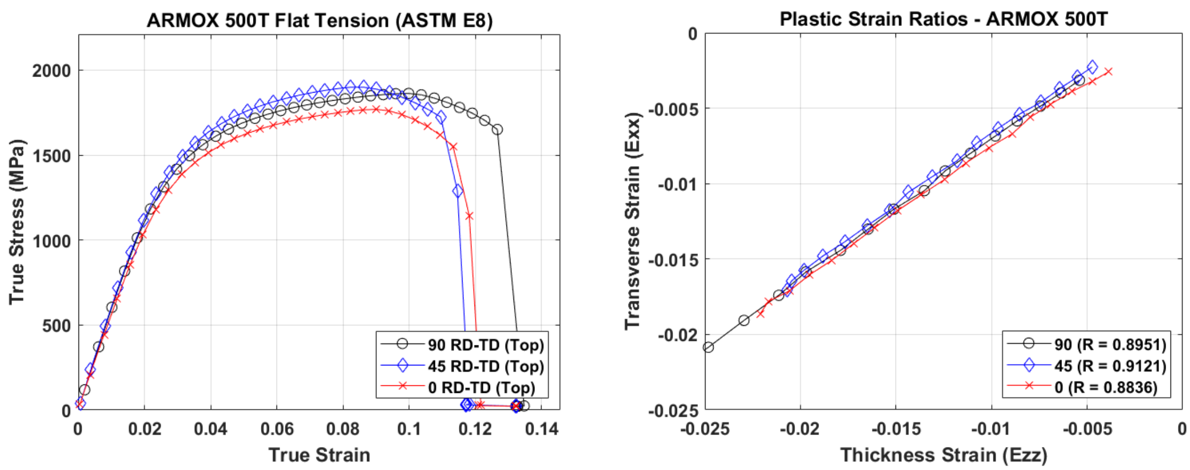

Figure 4.3: Flat tension stress-strain & plastic strain ratio results

Table 4.1: Precision and averages of all flat tension tests in three top directions

Direction (Top)	Dataset	Yield Strength (MPa)	Ultimate Strength (MPa)	Elongation (%)	R-value
90	Test 1	1360	1866	12.37	0.873
	Test 2	1210	1862	12.66	0.895
	Test 3	1283	1867	12.08	0.845
	Average ± STD	*1284 ± 61*	*1865 ± 2*	*12.37 ± 0.24*	*0.871 ± 0.02*
45	Test 1	1266	1898	10.99	0.910
	Test 2	1228	1899	10.95	0.912
	Test 3	1295	1899	10.77	0.774
	Average ± STD	*1263 ± 27*	*1899 ± 1*	*10.90 ± 0.10*	*0.865 ± 0.06*
0	Test 1	1177	1773	11.55	0.846
	Test 2	1151	1768	11.33	0.884
	Test 3	1244	1841	11.29	0.875
	Average ± STD	*1191 ± 39*	*1794 ± 33*	*11.39 ± 0.11*	*0.868 ± 0.02*

4.1.2 Microstructural Characterization

4.1.2.1 Microscale Structure

Specimens were cut-out by water jetting and prepared for optical microscopy and microhardness testing as per section 3.4.1. ARMOX 500T consists of a tempered martensite microstructure, as described in detail in section 2.1.2.1. During the growth of martensite from austenite, multiple laths nucleate unidirectionally from a nucleation point, known as a packet. The lath grains have high aspect ratio due to the BCT lattice elongation. Due to multiple nucleation sites, the packets meet to form packet boundaries. Therefore, there are both lath boundaries and packet boundaries present in the microstructure. Figure 4.4 displays micrographs under the optical and scanning electron microscopes to reveal the microstructure. No differences in texture were observed for the three different planes. This reference microstructure is critical to understand prior to any post-mortem metallurgical failure analysis.

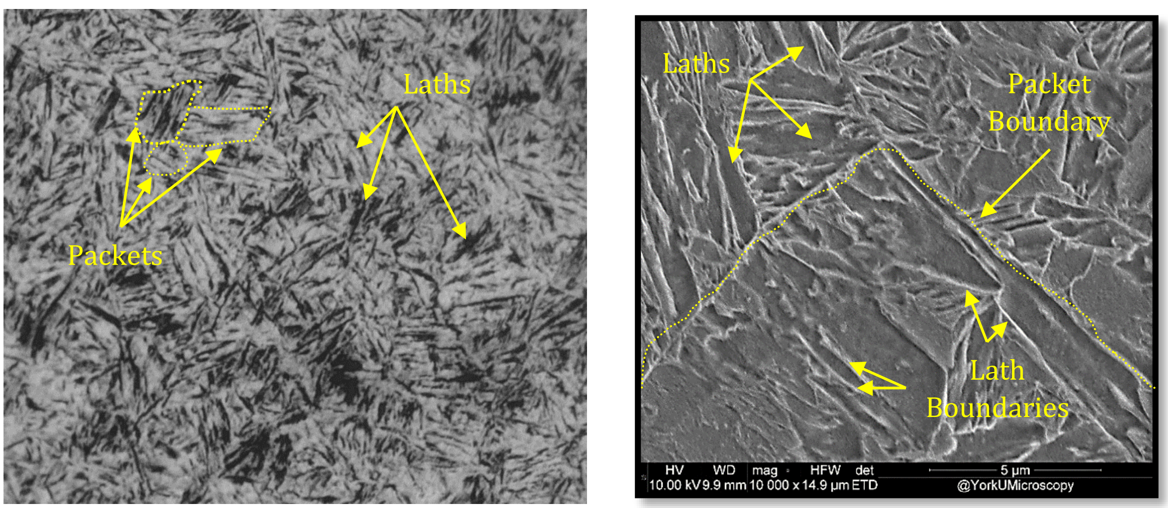

Figure 4.4: Optical and scanning electron micrographs of as-received ARMOX 500T

4.1.2.2 Vickers Microhardness

No significant differences in microhardness were observed for the three different planes obtained from the 30mm plates. Non-discriminatory repeated tests (10x) were conducted on each surface and the average was taken. The hardness values for the rolling-transverse (RT), normal-rolling (NR), and normal-transverse (NT) planes were $596 \pm x$, $588 \pm x$, and $585 \pm x$ HV, respectively.

4.1.2.3 Nanoscale Structure

Information on the nanoscale structure is acquired using the transmission electron microscope (TEM) to acquire a reference pre-impact microstructure prior to any adiabatic shear localization.

The TEM provides evidence of the nanoscale structure of the material including lattice structure and carbide composition, morphology, directionality, and distribution in the material. Individual laths can be resolved, and their structure can be revealed down to atomic scale resolution. Notably, due to the small size of the TEM specimen, naturally a large portion of the specimen is one packet.

Figure 4.5 reveals Electron Energy Loss Spectroscopy (EELS) analysis conducted on intralath carbides within the material. It is revealed that the carbides are composed of carbon and boron with minimal iron. Carbides grow in the structure with tempering, a higher tempering temperature will result in larger carbides which toughen the steel at the expense of strength and hardness. These carbides provide an explanation for the unique strength and toughness of AX500. There are two different types of carbides which evolve in the microstructure: interlath and intralath carbides. Both interlath and intralath carbides have consistent directionality within a respective packet. Interlath carbides are in between two different laths on lath grain boundaries. Intralath carbides are within laths and have a different orientations within a distinctive martensite packet.

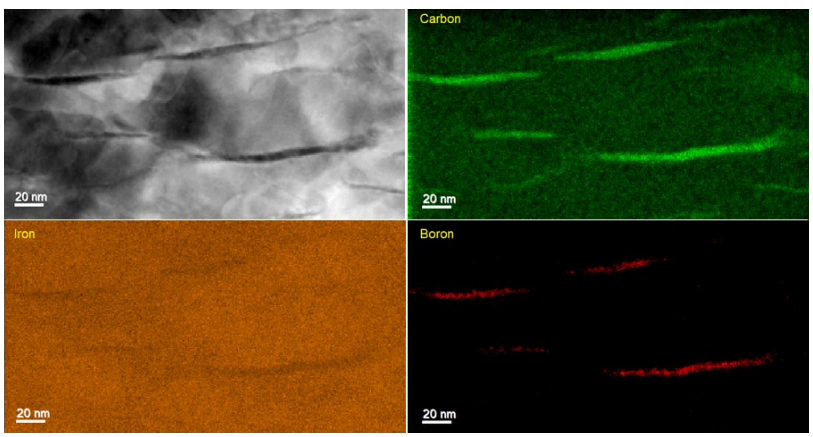

Figure 4.5: EELS elemental analysis revealing carbide composition

In Figure 4.6, lath grains can be observed which are shaded differently. Each lath grain is unique with its own internal structure, dependent on the crystal growth during quenching and subsequent tempering process. In the tempering process, carbide diffusion and growth occurs along with dislocation annihilation which toughens the material and alleviates internal residual stress, respectively. Some lath grains contain intralath carbides and others don't. Simultaneously, some lath grains are dislocation rich and some are dislocation poor. In addition, different stages of carbide growth can be observed. The intralath carbides start to diffuse out from the saturated BCT structure and begin as small acicular carbides, which then grow into thicker platelet carbides. From EELS, the intralath carbides are most likely boron carbides and are deemed B_4C.

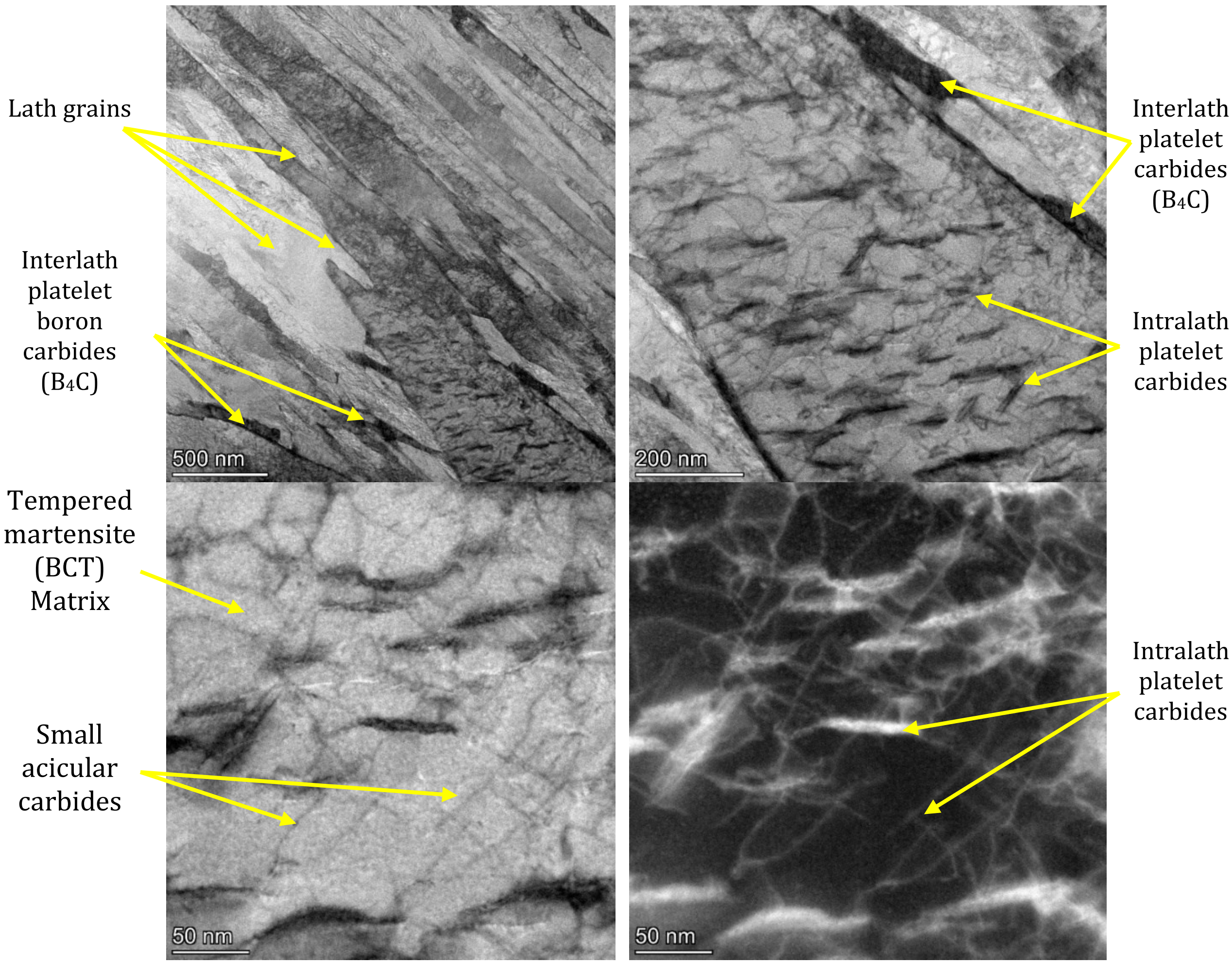

Figure 4.6a: Inhomogeneity of lath grains. 4.6b: Nanoscale intralath and interlath carbide distribution and morphology. 4.6c: Close up view of a carbide rich lath. 4.6d: dark field image of carbide rich lath.

These B_4C carbides along the lath grain boundaries can have significant effects on the damage resistance and toughening mechanisms of the material under loading. It is a hard material along a grain boundary which can have both positive and negative effects. For example, it could inhibit dislocation motion through a grain acting as a strengthening mechanism, however, it could also be a source of embrittlement and crack initiation. In Figure 4.7a, dislocation rich and dislocation poor regions are highlighted. Figure 4.7b presents a relatively larger scale overview of all regions. Dark regions in bright field images indicate dislocation rich regions, due to the increased interatomic spacing and voids present in those regions. Contrarily, white regions are dislocation poor regions with more densely packed BCT lattice structure. Figure 4.7c presents a closer look at these regions, where various dislocations can be clearly spatially resolved. Figure 4.7d reveals an interlath carbide along a lath grain boundary, it is clearly visible that dislocations have accumulated on the upper side of the carbide-matrix interface. Additionally, two colored dots indicate locations for selected area diffraction patterns (SADP) which correlate to SADP images Figure 4.7e and Figure 4.7f.

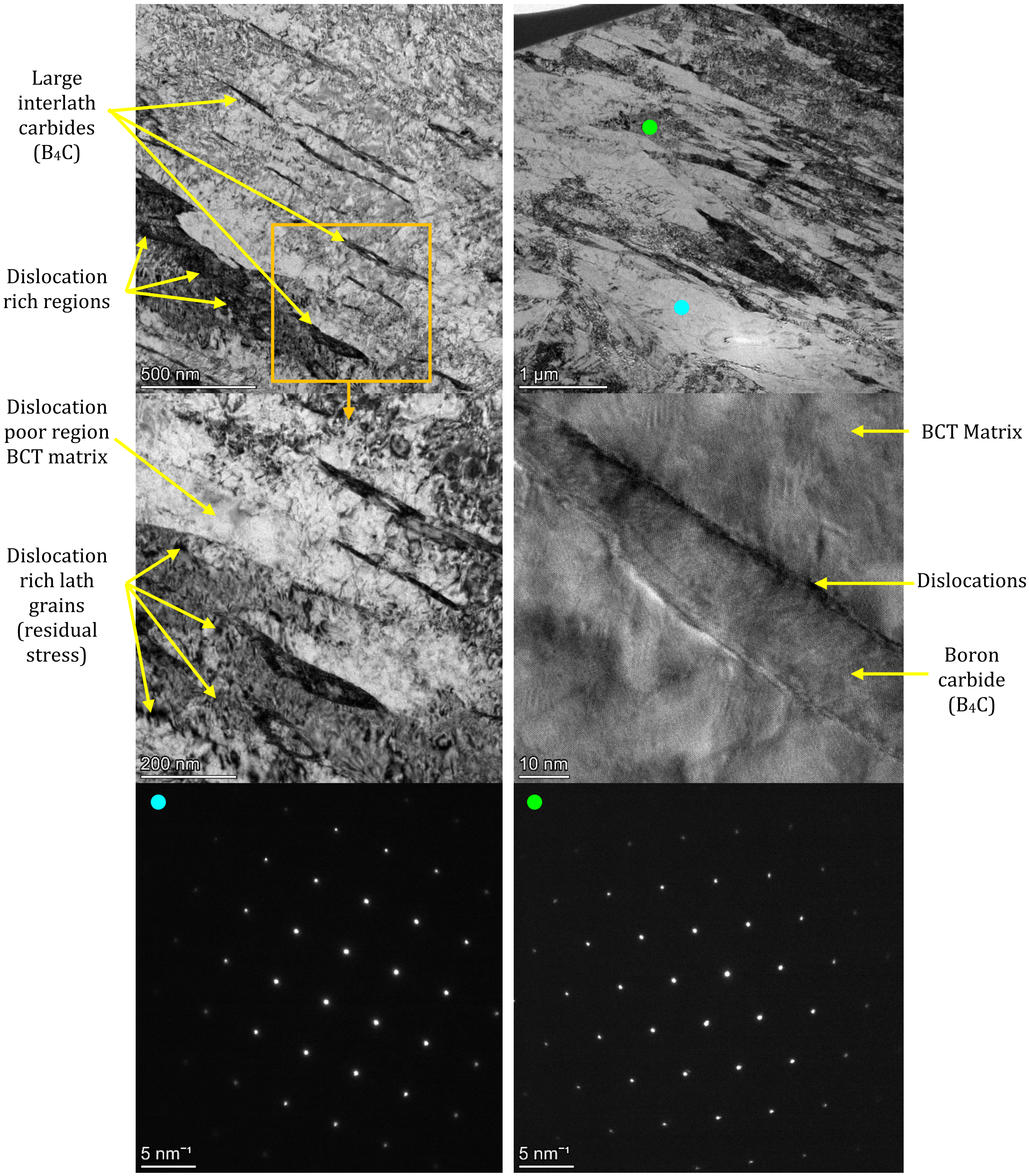

Figure 4.7a: Interlath carbide orientation within packet along lath grain boundaries. 4.7b: Locations for SADP. 4.7c: BF image revealing dislocation poor and rich laths 4.7d: Interlath B4C carbide with dislocation rich boundary interface with BCT matrix. 4.7e: SADP of BCT attainable lattice structure on a zone axis. 4.7f: SADP from a different zone axis of BCT structure.

4.2 Axisymmetric Compression

It must be noted that for all DIC data results presented in this chapter, the presented strains are representative of the surface strains, and not the strains at the midplane or center of the material which is unobservable to the camera. In the center, the strains are expected to be higher as discussed in the literature review. For further computational modeling (outside scope of this thesis), the strains within the specimen are calculated/extrapolated from the surface and verified with the simulated surface strain comparison to the DIC measurements.

Quasistatic axisymmetric compression and compression shear tests were conducted with oil quenched AISI 4140 steel platens and MoS2 extreme pressure grease. No fracture in any of the three different specimens (9 tests) was possible due to limitations of the 100 kN MTS machine as the maximum force was reached. This is due to the increase in area during compression loading, requiring greater force to continue straining the specimen. Using specimens of diameter of 6.35mm, requiring a force of 55 kN assuming an 1800 MPa ultimate strength, the specimens cross sectional diameter increased to > 8 during loading resulting in maximizing the force of the machine. 3D-Stereo DIC was utilized for all axisymmetric compression and tension tests (sections 4.2 and 4.3) as per the procedure presented in section 3.2.2. Figure 4.8 shows the deformed DIC images within their respective platens, and Figure 4.9 presents the incomplete stress-strain curves which did not fracture, however effectively show the loss of strength with increasing shear stress.

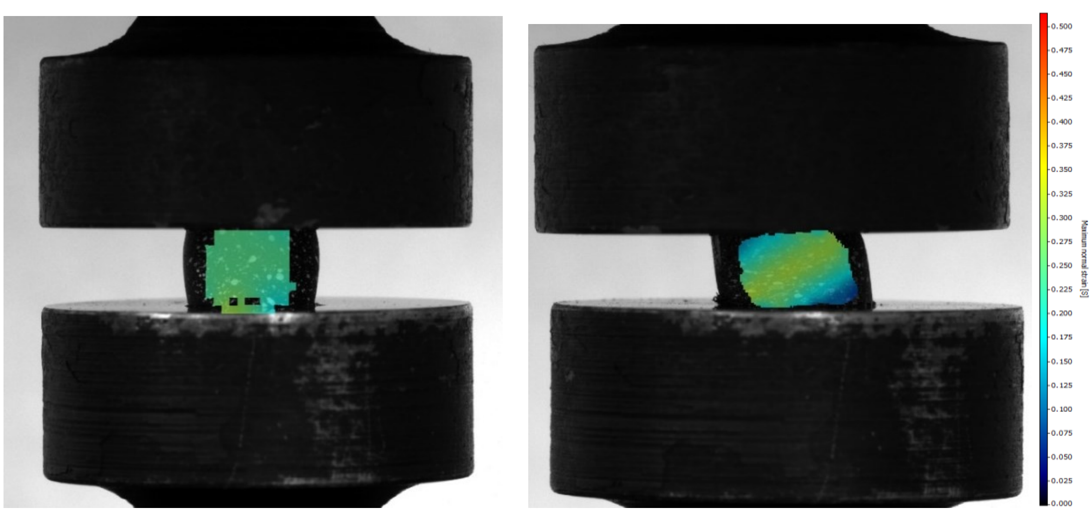

Figure 4.8: Quasistatic uniaxial compression (left) and compression-shear (right) testing of AX500 with principal strain fields

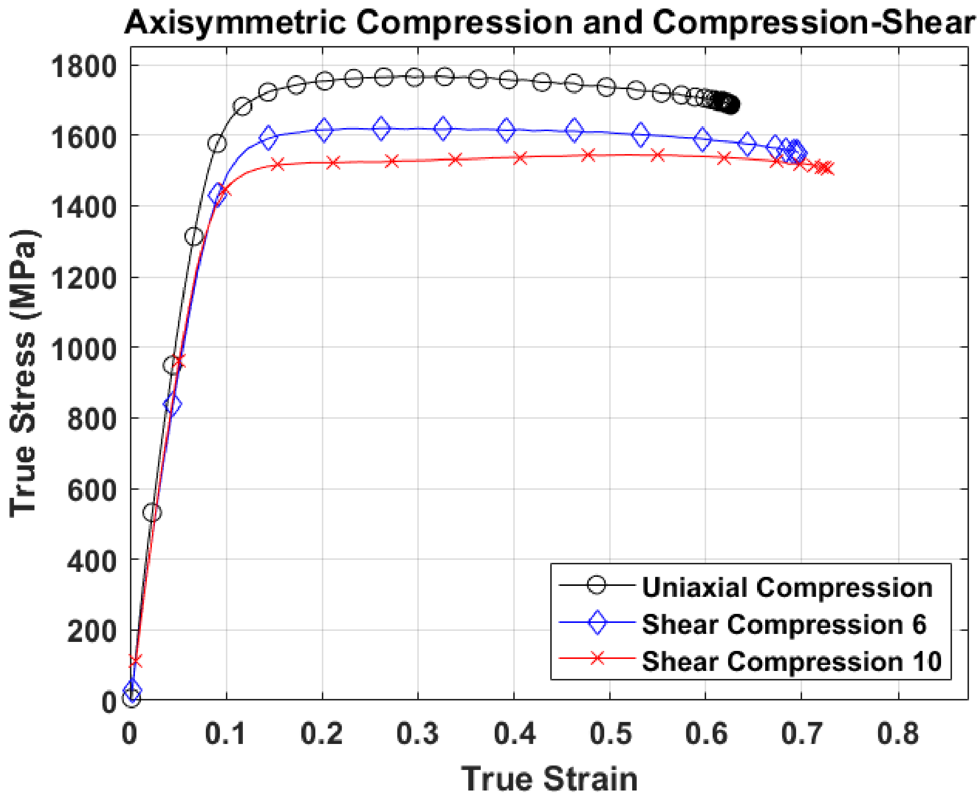

Figure 4.9: Effect of increasing shear stress on the flow stress during quasistatic compression

Even without fracture, these tests provide a qualitative baseline for the same dynamic tests in terms of the plasticity behaviour of the flow stress, degree of work hardening, and providing measurements of elongation and equivalent plastic strain under quasistatic loading. Primarily, under negative lode angles, AX500 is very tough and ductile. Furthermore, there is a clear decrease of the flow stress with increasing triaxiality/LAP as the stress-state is changed from uniaxial compression at LAP of -1 towards pure shear at LAP of 0. In other words, as the shear to compression load ratio increases thereby increasing shear stress, the material weakens. As a quantitative reference for high strain-rate testing, the average of three maximum equivalent strains attained for each specimen were 0.386, 0.381 and 0.396 for uniaxial compression, CS6, and CS10 specimens respectively. In addition, the elongation was greater than 60% for all tests. If they were further loaded, it would be expected that they would all have the capacity to withstand significantly more elongation and equivalent plastic strain.

4.3 Axisymmetric Round Tension

Round Tensile specimens are deigned according to equation 2.8 such as to acquire triaxiality dependent tests at a constant LAP of 1. This produces datapoints along the upper bound of the triaxiality-LAP fracture surface to be developed in future computational modeling. The minimum cross-sectional radius (a) of all smooth and notched specimens is 3 mm, providing comparable force-displacement curves for each specimen. Notch radii are designed to 1a, 2a, and 4a dimensions, selected such that the datapoints on the triaxiality-LAP stress-state map (Figure 3.5) are adequately spaced out to enable accurate fitting methods. These specimens are the only specimens prepared by CNC lathe as opposed to EDM, with high tolerance along gauge sections. The work of Mohr [100] is used as a baseline to measure the elongation in these specimens using a virtual extensometer three times the minimum cross-sectional width which is 18mm. Strain gauges are located on central regions of the fracture initiation points of size 2 mm^2. Figure 4.10 illustrates the method of virtual strain measurements, smooth and notched fractured specimens viewed through the optical cameras, and the principal strain fields.

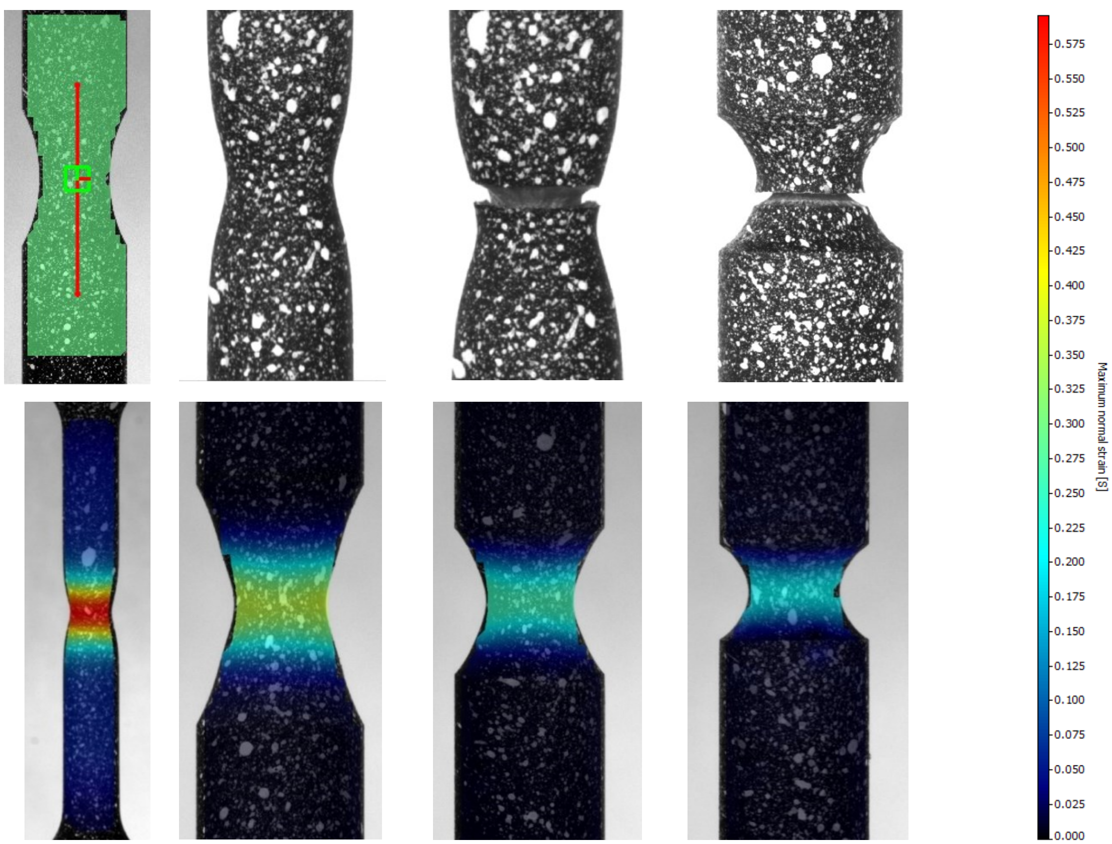

Figure 4.10: Round tensile specimens, virtual measurement method, necked and fractured specimens and strain fields

The major principal strain fields just before fracture initiation are depicted in Figure 4.10 clearly revealing the loss of ductility with increasing triaxiality. In addition, Figure 4.11a presents the stress-strain curves of the four specimens, demonstrating the simultaneous increase in strength and ductility loss. Figure 4.11b illustrates the triaxiality dependent strain-path for the four different specimens, revealing the ductility loss in terms of equivalent plastic strain ($\boldsymbol{\varepsilon_{eq}}$). Figure 4.11c presents three repeated round tensile tests demonstrating the precision and repeatability of the stress-strain curves and DIC equivalent plastic strain measurement. It is the thought of the author that round axisymmetric tension is a more accurate representation of uniaxial tension than a flat specimen, due to its consistent LAP at 1. Lastly, Table 4.2 present all DIC measurements of equivalent plastic strain evolution to illustrate the ductility loss with increasing triaxiality by decreasing notch radii. Figure 4.12 presents all prepared specimens ready for testing.

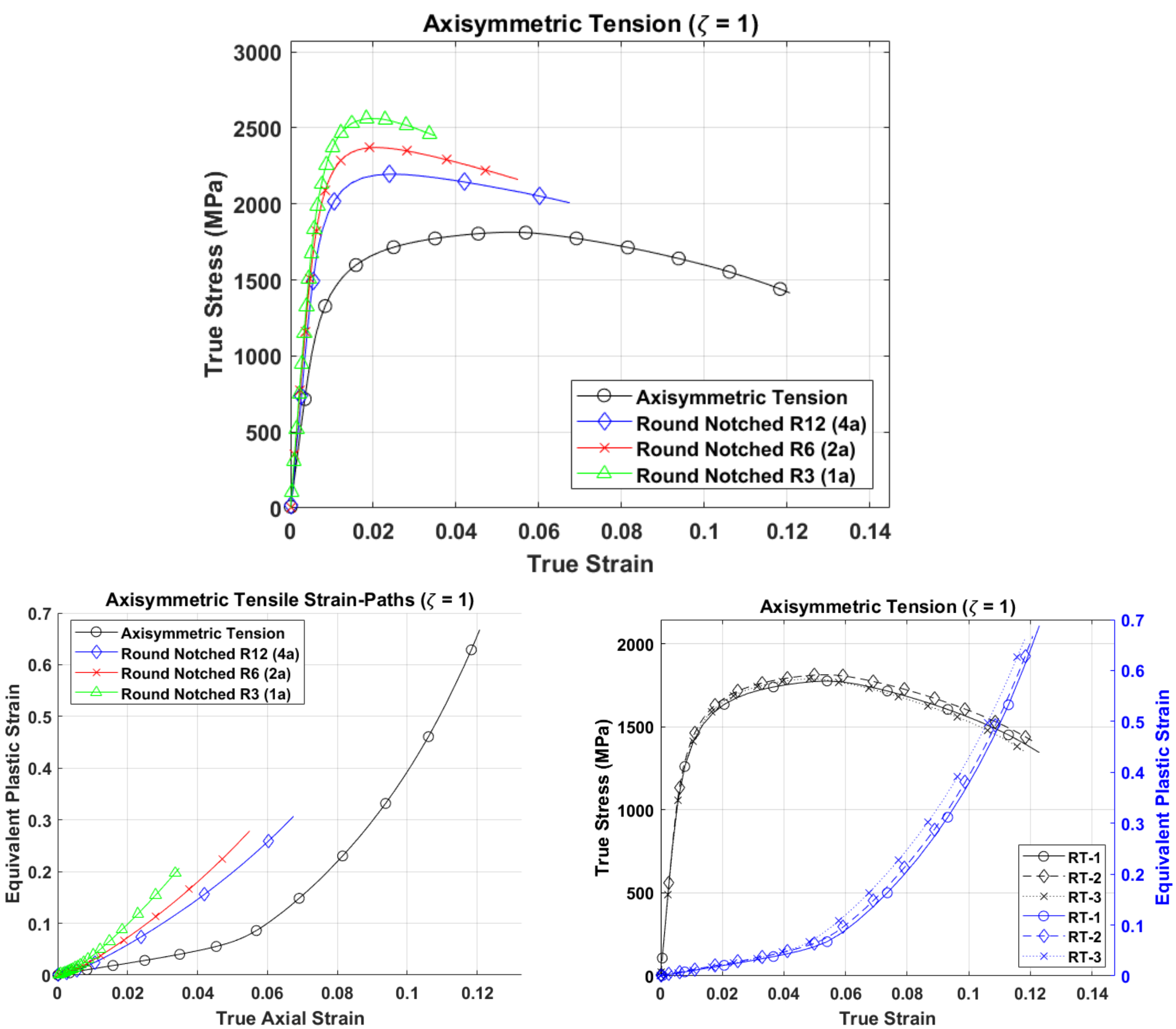

Figure 4.11: Effect of increasing triaxiality on stress-strain and equivalent plastic strain. Repeated test on round tensile tests

Table 4.2: All round tensile data for GISSMO

Specimen	Dataset	Ultimate Strength (MPa)	Axial Elongation (%)	Equivalent Plastic Instability Strain (ε_{eq}^{i})	Equivalent Plastic Fracture Strain (ε_{eq}^{f})
Axisymmetric Tension	Test 1	1777	12.29	0.067	0.688
	Test 2	1814	12.07	0.070	0.668
	Test 3	1789	11.82	0.067	0.662
	Average ± STD	*1793 ± 16*	*12.06 ± 0.19*	*0.068 ± 0.001*	*0.672 ± 0.011*
R12	Test 1	2192	7.44	0.072	0.343
	Test 2	2196	6.75	0.074	0.307
	Test 3	1952	7.51	0.064	0.358
	Average ± STD	*2113 ± 114*	*7.23 ± 0.34*	*0.070 ± 0.005*	*0.336 ± 0.022*
R6	Test 1	2106	4.87	0.068	0.241
	Test 2	2372	5.50	0.075	0.279
	Test 3	2362	5.12	0.074	0.245
	Average ± STD	*2280 ± 123*	*5.16 ± 0.26*	*0.072 ± 0.003*	*0.255 ± 0.017*
R3	Test 1	2531	3.91	0.093	0.225
	Test 2	2562	3.48	0.094	0.207
	Test 3	2532	3.70	0.092	0.214
	Average ± STD	*2541 ± 13*	*3.69 ± 0.17*	*0.093 ± 0.001*	*0.215 ± 0.007*

Figure 4.12: All CNC machined and speckled notched round tensile specimens

4.4 Flat Notched and Hole Tension

Flat notched specimens are known to have a significant stress-state evolution during loading. Nevertheless, they are very common data points in the GISSMO. The work of Mohr [100] is again used as a baseline for a gauge length definition of 3x(w) at 18mm. In addition, a virtual strain gauge is used in the center of the specimen of size 1 mm^2 to acquire the principal and equivalent plastic strains up until fracture. The hole tensile specimen has been designed to have the same size gauge length of 18mm. The same strategy is used in the hole tensile specimen to acquire the uniaxial strain-path up until fracture using a virtual strain gauge. As previously mentioned, the hole tensile specimen is used over the flat tensile to acquire the strain-path since it maintains a more consistent uniaxial stress-state due to its ability to supress necking under uniaxial tension. Figure 4.13 illustrates the DIC measurements on flat notched and hole specimens. Note that the strain gauge location on the hole tensile specimen has been carefully selected such that it is in uniaxial tension up until fracture (shear strains cancel to 0) and away from the stress concentration at the edge.

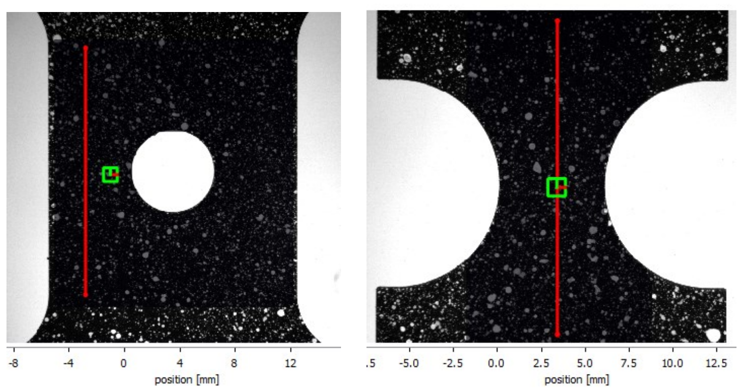

Figure 4.13: Virtual DIC measurement extraction on FT-R6 and hole tensile specimens

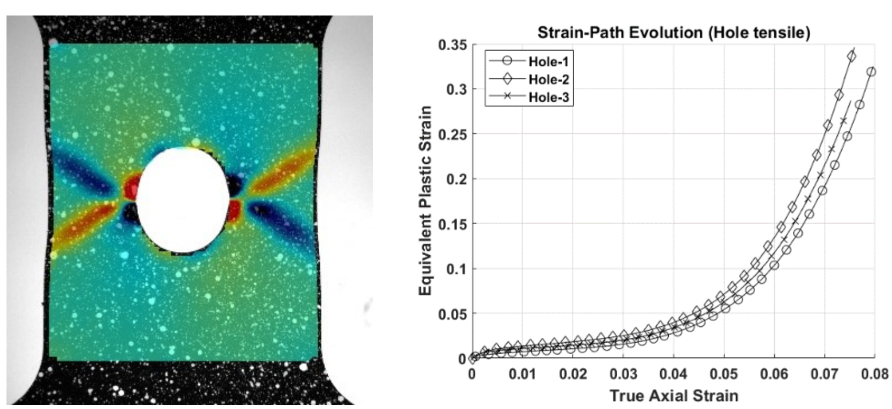

Figure 4.14: Shear strain (exy) field and equivalent plastic strain evolution (e1) in hole tension

Figure 4.14 above shows the shear strain field, which adequately showed the optimal strain gauge location where the shear strains cancel out. In tests outside the scope of this thesis, it is found that there is an effect of strain gauge location and size on the strain results. In the same figure, the in-situ equivalent plastic strain evolution is shown for the three tests, demonstrating the repeatability and precision of the experimental measurement.

The results for the uniaxial smooth, hole, and R6 and R2 flat notched tensile specimens are illustrated in Figure 4.15. These tests quantify the effect of triaxiality (and consequentially, lode angle) on the equivalent plastic instability and fracture strains from uniaxial tension towards plane strain along the $\zeta(\eta)$ curve. With increasing triaxiality as the stress-state moves towards tensile plane strain, there is a loss of ductility and simultaneous strengthening effect. To capture the hardening effect, notched flat tensile specimens are compared to the flat dogbone tests used in section 4.1.1.2, perpendicular to the rolling direction such as to have a consistent tensile loading direction for comparison. To capture the loss of ductility in terms of ε_{eq}, hole tension is used as the uniaxial reference to the notched specimens.

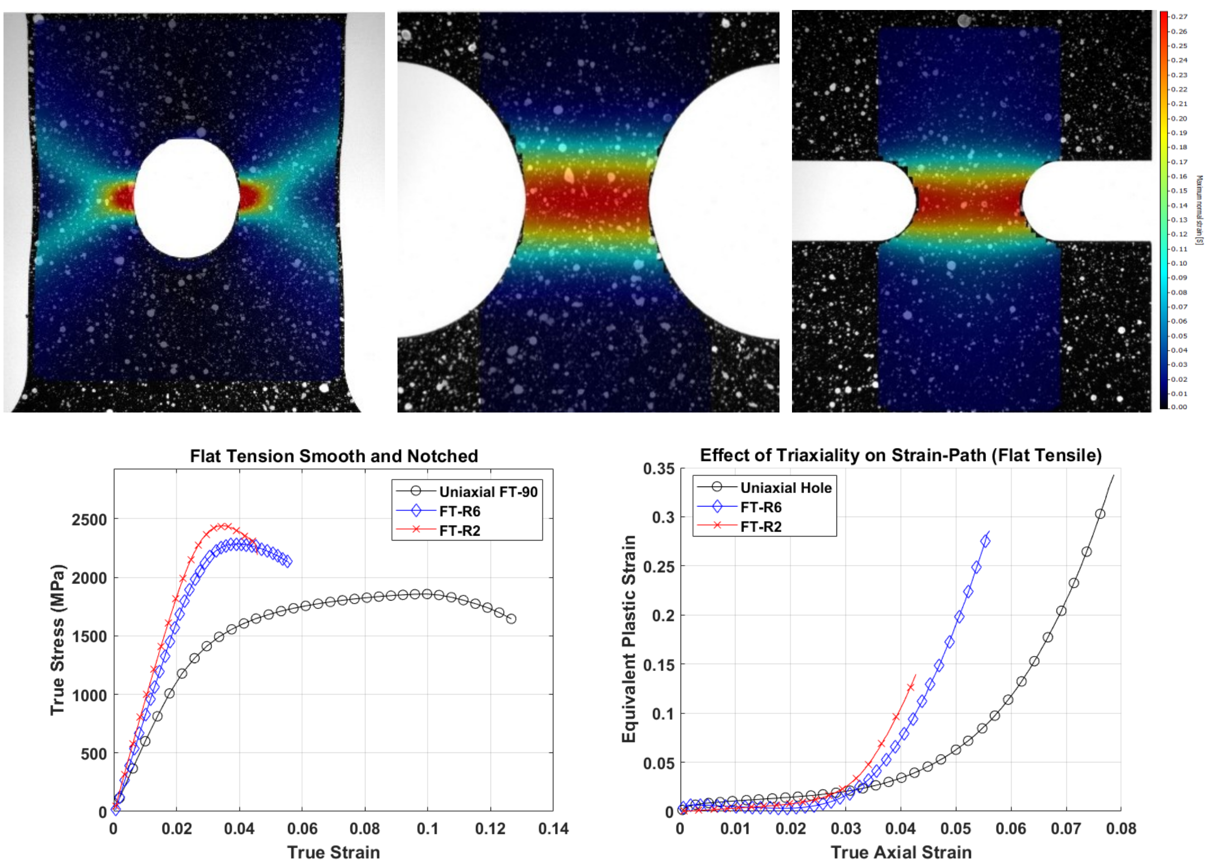

Figure 4.15a-c: Maximum principal strain fields in uniaxial hole and notched specimens. 4.15d: Effect of plane stress triaxiality increase on strength and ductility. 4.15e: Effect of plane stress triaxiality increase on equivalent plastic strain

From the results above, just as in round tension, there is a clear effect of stress-state on the yield strength, work hardening, and softening after instability in AX500, the degree of which has been quantified for these stress-states. Table 4.3 displays all the parameterization data for the repeated tests in this section.

Table 4.3: Uniaxial and notched tension strength and GISSMO strain data

Specimen	Dataset	Ultimate Strength (MPa)	Axial Elongation (%)	Equivalent Plastic Instability Strain (ε_{eq}^{i})	Equivalent Plastic Fracture Strain (ε_{eq}^{f})
Uniaxial (Dogbone / Hole)	Test 1	1866	12.37	0.121	0.325
	Test 2	1862	12.66	0.161	0.366
	Test 3	1867	12.08	0.128	0.343
	Average $\pm$ STD	*1865 $\pm$ 2*	*12.37 $\pm$ 0.24*	*0.136 $\pm$ 0.017*	*0.345 $\pm$ 0.017*
R6	Test 1	1981	5.53	0.081	0.283
	Test 2	2289	5.57	0.057	0.286
	Test 3	2107	5.16	0.067	0.342
	Average $\pm$ STD	*2126 $\pm$ 126*	*5.42 $\pm$ 0.18*	*0.068 $\pm$ 0.010*	*0.304 $\pm$ 0.027*
R2	Test 1	2441	5.43	0.051	0.182
	Test 2	2920	4.57	0.054	0.226
	Test 3	2459	4.39	0.052	0.157
	Average $\pm$ STD	*2607 $\pm$ 222*	*4.80 $\pm$ 0.45*	*0.052 $\pm$ 0.001*	*0.188 $\pm$ 0.029*

4.5 Tensile Plane Strain

According to equation 3.2 derived by the work of Bai and Wierzbicki [93], notched plane strain specimens are designed to quantify the effect of increasing triaxiality at a constant LAP of 0. In addition, the work of Clausing [81] is used to design a pure tensile plane strain specimen with no notch. Four specimens are tested with no notch, and notch radii of 8, 4 and 2mm. The length to ligament width ratio is 12.5, abiding by the work of Basaran [94]. Naturally, the most brittle stress-state and lower bound of the fracture surface is in tensile plane strain specimens with increasing brittleness expected with increasing triaxiality. The gauge length is designed to be 6mm in all specimens (3x the ligament width).

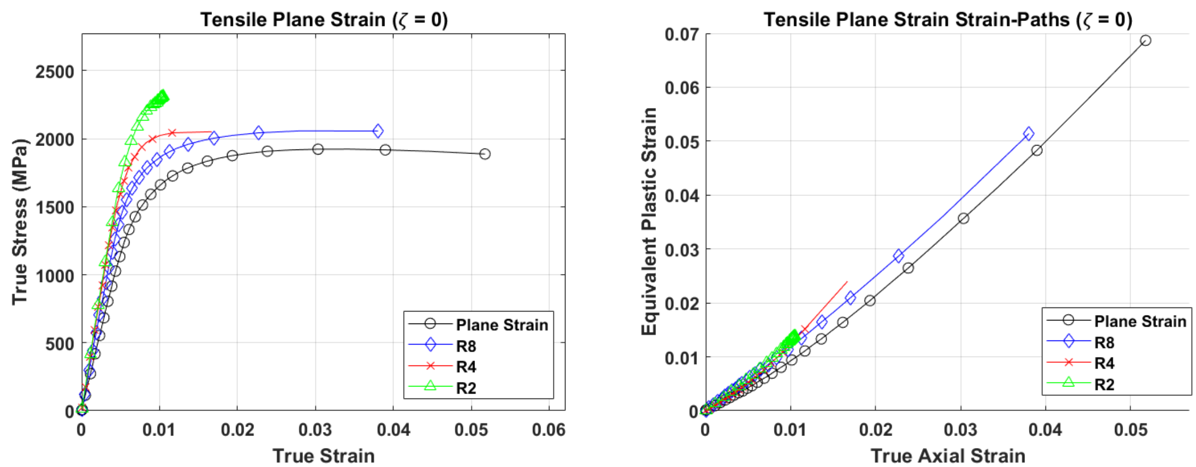

Figure 4.16: Tensile plane strain tests stress-strain and equivalent plastic strain evolution

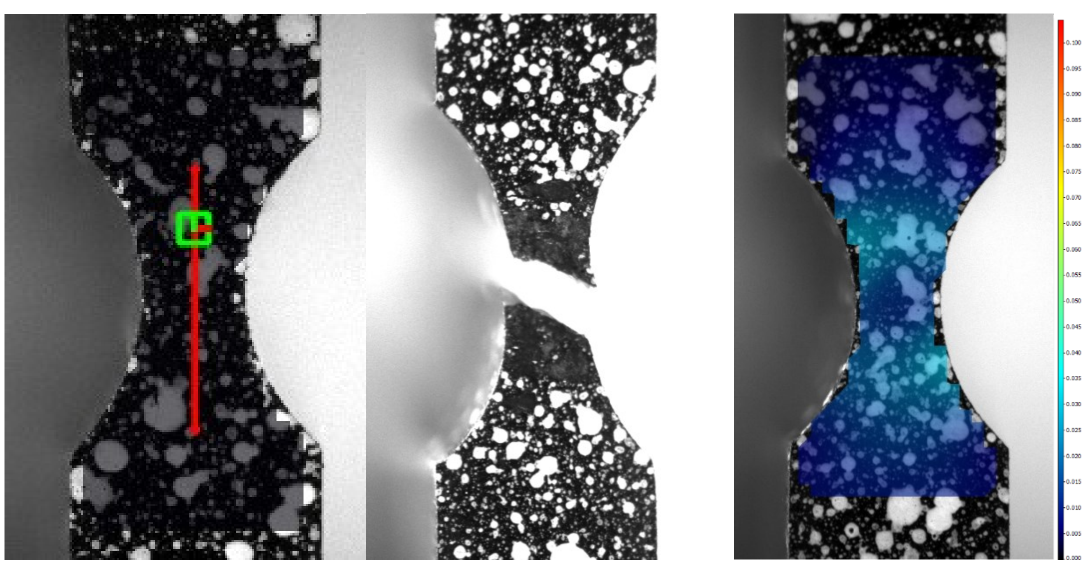

Figure 4.17: Virtual measurements, fractured image and maximum principal strain field before fracture on R4 notched tensile plane strain specimen

As expected, there is an increase in stress and corresponding ductility loss with increasing triaxiality due to decreasing notch radius. Figure 4.16 presents the results of the effect of decreasing notch radii on stress-strain and equivalent strains from 2D-DIC. Figure 4.17 reveals the virtual extensometer and strain gauge for data acquisition using 2D-DIC, a fractured image and corresponding strain field before fracture in the R4 specimen. Lastly, Table 4.4 presents all the data. Note that the second test for R2 is in italics and indicated by *. This indicates that the specimen did not fracture, since the maximum load capacity of the MTS machine was reached. However, given the very low strain and brittleness of the material at this very high triaxiality (0.84) along the constant LAP=0 lower bound of the fracture surface, this has a minimal effect on the curve fitting.

Table 4.4: Tensile plane strain data (indicates did not fracture)*

Specimen	Dataset	Ultimate Strength (MPa)	Axial Elongation (%)	Equivalent Plastic Instability Strain (ε_{eq}^{i})	Equivalent Plastic Fracture Strain (ε_{eq}^{f})
Flat Grooved	Test 1	1952	3.50	0.030	0.060
	Test 2	1924	5.18	0.041	0.069
	Test 3	1980	6.72	0.051	0.072
	Average $\pm$ STD	1952 $\pm$ 23	5.13 $\pm$ 1.31	0.041 $\pm$ 0.008	0.067 $\pm$ 0.005
R8	Test 1	2295	3.18	0.028	0.043
	Test 2	2044	3.80	0.036	0.051
	Test 3	2127	2.93	0.037	0.037
	Average $\pm$ STD	2155 $\pm$ 104	3.30 $\pm$ 0.37	0.034 $\pm$ 0.004	0.044 $\pm$ 0.006
R4	Test 1	2233	2.72	0.031	0.031
	Test 2	2152	1.67	0.024	0.024
	Test 3	2205	1.18	0.014	0.014
	Average $\pm$ STD	2197 $\pm$ 34	1.86 $\pm$ 0.64	0.023 $\pm$ 0.007	0.023 $\pm$ 0.007
R2	Test 1	2297	0.40	0.003	0.005
	Test 2*	2313	1.05	0.014	0.014
	-				
	Average $\pm$ STD	2305 $\pm$ 8	0.73 $\pm$ 0.32	0.009 $\pm$ 0.005	0.010 $\pm$ 0.004

4.6 Shear and Shear-Tension

To quantify the state of pure in-plane shear, the pure-shear specimen designed by Abedini is employed [137]. The eccentricity of the cut-outs promotes a consistent pure shear stress-state up until fracture. To quantify the effect of stress-state on the plastic strains from shear towards tension, shear-tension specimens are used from Xiao's GISSMO work [62]. They are carefully designed such as to ensure fracture occurs along intended location of localized deformation, from the two corner edges of the cut-outs. Figure 4.18 presents the fractured specimens viewed through the Basler lens and optical camera, and the maximum principal strain fields in the pure shear and 10- and 30-degree shear-tension specimens.

With a greater tensile/shear loading ratio, AX500 reduces in ductility and increases in strength. The equivalent strains and elongation are simultaneously reduced as the triaxiality increases for tension shear specimens. This is due to the combined effect of mode I and mode II cracking. The equivalent plastic failure strain in pure shear is greater than 1.0, indicating that AX500 is highly resistant to shear loads in quasistatic loading. Figure 4.19 is obtained from the DIC data and quantifies the ductility loss and change of stress-state / strain-path. Lastly, Table 4.5 presents the DIC data from maximum and principal strains and relevant GISSMO equivalent strains in repeated tests.

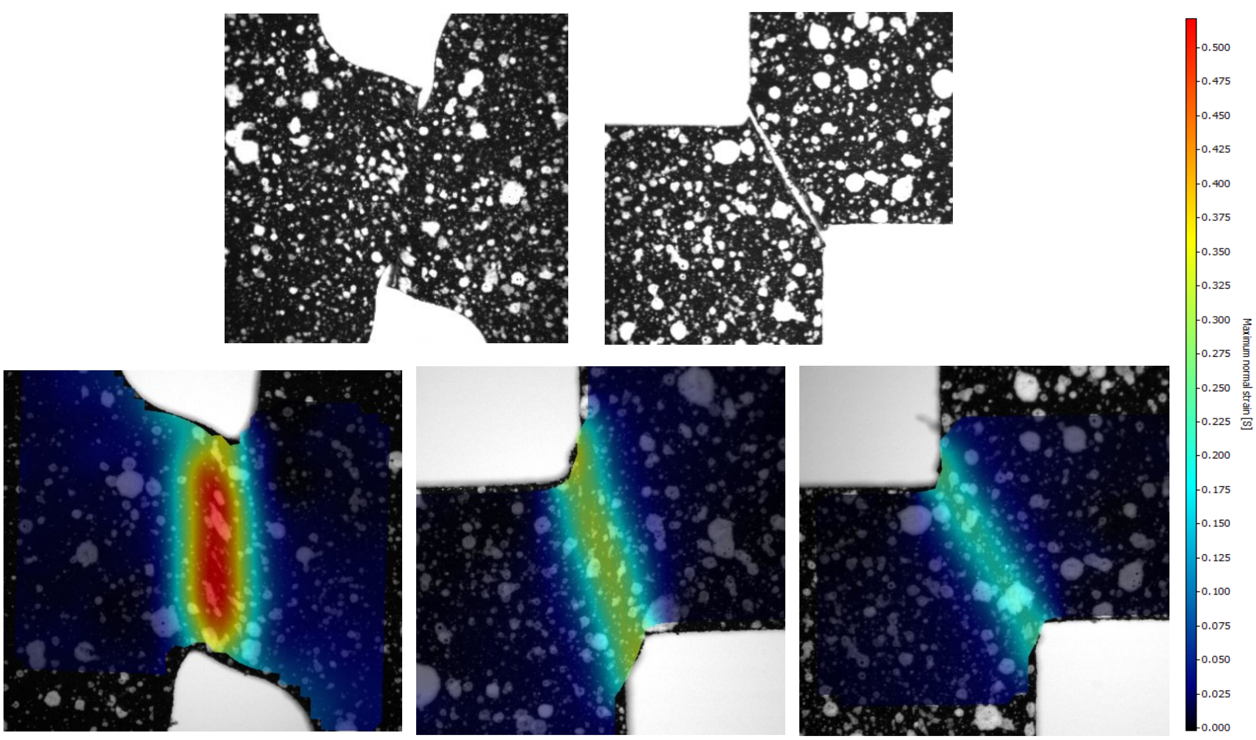

Figure 4.18a-b: Fractured shear specimens along intended locations. 4.18c-e: Maximum principal strain fields in pure shear, shear-tension 10, and shear-tension 30-degree specimens, respectively.

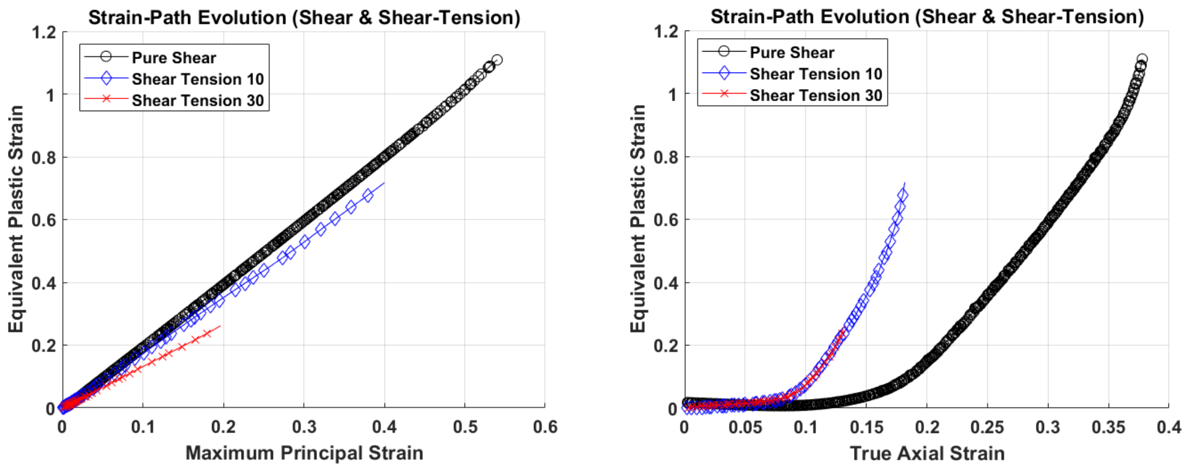

Figure 4.19: Effect of combined triaxiality/LAP increase from pure shear towards uniaxial tension on the strain-path evolution

*Table 4.5: DIC data for all shear and shear tension tests (*did not fracture)*

Specimen	Dataset	Maximum Principal Strain	Minimum Principal Strain	Equivalent Plastic Instability Strain (ε_{eq}^{i})	Equivalent Plastic Fracture Strain (ε_{eq}^{f})
Pure Shear	Test 1	0.488	-0.538	0.928	1.025
	**Test 2*	*0.398*	*-0.411*	*0.800*	*0.804*
	Test 3	0.540	-0.568	0.929	1.109
	Average $\pm$ STD	0.476 $\pm$ 0.059	-0.506 $\pm$ 0.068	0.885 $\pm$ 0.060	0.979 $\pm$ 0.129
Shear Tension 10	Test 1	0.336	-0.362	0.492	0.720
	Test 2	0.393	-0.426	0.521	0.714
	Test 3	0.400	-0.413	0.394	0.717
	Average $\pm$ STD	0.376 $\pm$ 0.029	-0.400 $\pm$ 0.027	0.469 $\pm$ 0.054	0.717 $\pm$ 0.003
Shear Tension 30	Test 1	0.235	-0.242	0.186	0.352
	Test 2	0.238	-0.202	0.180	0.303
	Test 3	0.197	-0.178	0.177	0.262
	Average $\pm$ STD	0.223 $\pm$ 0.019	-0.207 $\pm$ 0.027	0.181 $\pm$ 0.004	0.305 $\pm$ 0.037

4.7 Summary

Unfortunately, due to lack of access of to equi-biaxial Nakazima dome testing at York University, the tests could not be completed at the time of writing of this thesis. The tests are currently underway at the University of Waterloo and are to be added to the data for the GISSMO. This datapoint would have completed the stress-state dependent characterization under quasistatic loading.

To summarize the other tests, Figure 4.20 presents four stress-strain plots. The first shows three different uniaxial tension specimens under quasistatic (0.01 /s) loading using the MTS machine under displacement control. The three specimens are the ASTM-E8 flat and round tension, and the high strain rate (HSR) specimen used on the Hopkinson bar. While the yield and ultimate flow stresses are comparable for all three tests, there are some notable and important differences. The first and most notable difference is that the HSR specimen clearly has a larger elongation (20%) compared to the ASTM specimens (~12%). A strain gauge with 3D-DIC on the surface to identify the equivalent plastic strain yields a low value on flat tension (~30%) and comparable values (~67%) on the two-round tension (ASTM and HSR) specimens. Comparing the two ASTM specimens (both of which have been used in different damage models in the literature), there are clear differences in work hardening, instability strain (strain at ultimate stress), and softening (post-critical deformation after necking) behaviour. This will significantly affect the derived material plasticity parameters to define the flow stress with damage accumulation as per the JC equation 2.11 used in GISSMO. When it comes to the two round specimens (ASTM and HSR), their instability strain, ultimate flow stress, and fracture stress are very comparable however will also have slightly different; albeit comparable, material plasticity parameters for hardening and softening behaviour. It is important to remember that the round tensile specimens maintain a consistent LAP of 1 throughout loading until fracture and thus are preferable for damage model parameterization.

The second plot on the top right shows the asymmetricity between uniaxial tension and compression at consistent LAP of 1 and -1, respectively. The uniaxial compression test was an inadequate representation of the Young's Modulus and stress-strain for the elastic portion of the curve. It is unknown why this is the case. It could be due to machine compliance, platen compliance, both, an inadequate ramp definition and rise time of the control sequence of the MTS t loading onset, or a mixture of all three. Regardless, the plastic flow behaviour of the material is captured, and it is deformed via ductile slip beyond 60% elongation in comparison to round tension which fractures at 12% due to void growth and coalescence. Lastly, the two plots on the bottom simply highlight the upper and lower bound curves of the envisaged fracture surface, with consistent LAP of 1 and 0 with at axisymmetric tension and plane strain stress-states with changing notch size / triaxiality, respectively. The equivalent plastic strain under plane strain is about an order of magnitude lower than that under axisymmetric tension, for comparable values of stress and hardening with increasing triaxiality and different plasticity behaviour overall.

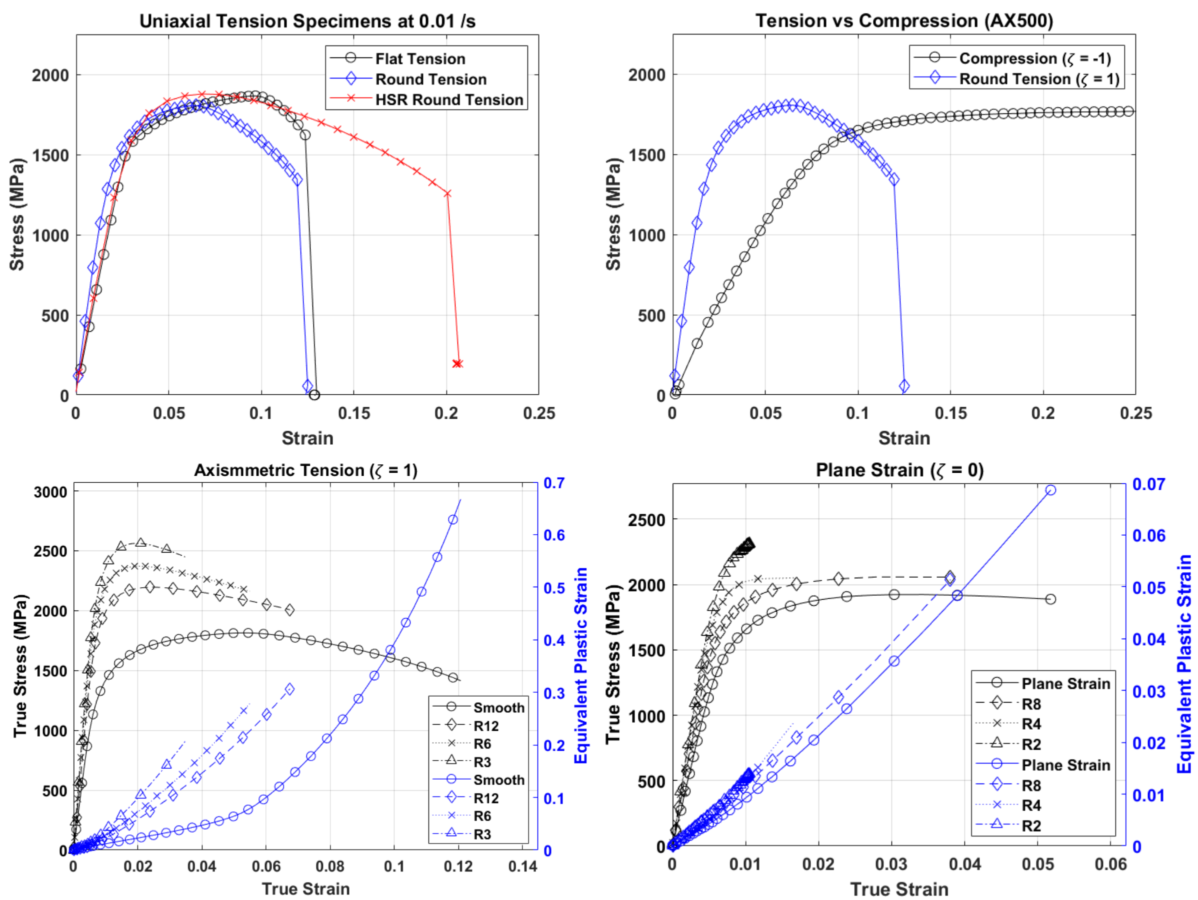

Figure 4.20a: Three different uniaxial tension specimens used under quasistatic loading (0.01 /s). 4.20b: Asymmetric Tensile and Compressive plasticity. 4.20c: Effect of triaxiality on stress-strain and strain-path at constant LAP of 1. 4.20d: Effect of triaxiality on stress-strain and strain-path and constant LAP of 0.

5.0 Dynamic Characterization

It is critically important to quantify the dynamic plasticity behavior of AX500 primarily to enable strain rate dependent strengthening and adiabatic shear susceptibility into the model. Primarily, ASBs are an instability that occurs at high strain-rate and is responsible for the significant loss of ductility in AX500 from quasistatic to dynamic strain-rates. It is demonstrated in this chapter; through full field macroscale data and microscale electron microscopy data, that high strain-rates create favourable conditions for ASBs which embrittle the material. In addition, it is demonstrated that there is an intrinsic effect of stress-state on ASB susceptibility quantified by the shear to compression load ratio, λ. This load ratio can also be mapped to a stress-state definition in terms of triaxiality and LAP as defined earlier in section 3.3.2. As previously mentioned, this stress-state effect is critical to quantify for many engineering applications where failure seldom occurs under a uniaxial state of stress and rather occurs under a state of multiaxial stress.

It is also demonstrated in this chapter; through full field macroscale data and SEM fractography, that ARMOX 500T has higher damage tolerance under dynamic tension as compared to quasistatic strain-rates. The high strain-rate data reveals that with increasing strain-rate, AX500 has increased work-hardening, ultimate flow stress, and enhanced plastic flow without any ductility loss.

5.1 Axisymmetric Compression

In Figure 5.1, five datasets are shown at 5 different strain-rates including 1 quasistatic strain rate using the MTS machine and 4 dynamic strain rates using the DIHB. None of the specimens fractured. The specimens loaded at an impact momentum just above the test at 2061 /s at roughly ~2100 /s began to fracture. These tests (not shown) provide a baseline fracture strain for the dynamic tests which ranges from 0.22 to 0.37 compressive elongation. The quasistatic test did not fracture, as explained in chapter 4.2 as the maximum load was reached with the area expansion of the specimen. The dynamic tests did not fracture since not enough energy was provided by the impactor to reach the fracture strain, and the end of the curve is simply the unloading curve.

Figure 5.1 reveals that at high strain-rate there is a clear strengthening and work hardening effect that does not occur in quasistatic conditions. This would have a significant effect on material plasticity parameters with strain-rate dependence. In quasistatic loading, there is minimized work hardening as slip occurs in the microstructure. Under dynamic loading, the work hardening curve indicates a different mechanism of strengthening is occurring in the microstructure. In addition, there is clear embrittlement of the material in comparison to quasistatic loading conditions. The quasistatic test reached up to 62% axial strain without any signs nearing fracture. This is confirmed by visual observation of pure uniaxial compression loading (expansion of faces, no barreling) and further confirmed by DIC data displaying a homogenous field and linear evolution of strain on the surface throughout the test up to 62% strain, showing no signs of strain localization as per Figure 4.8. For dynamic compression tests, tests ranging from 2200-3000 /s fracture at an average of ~30.5% compressive axial strain.

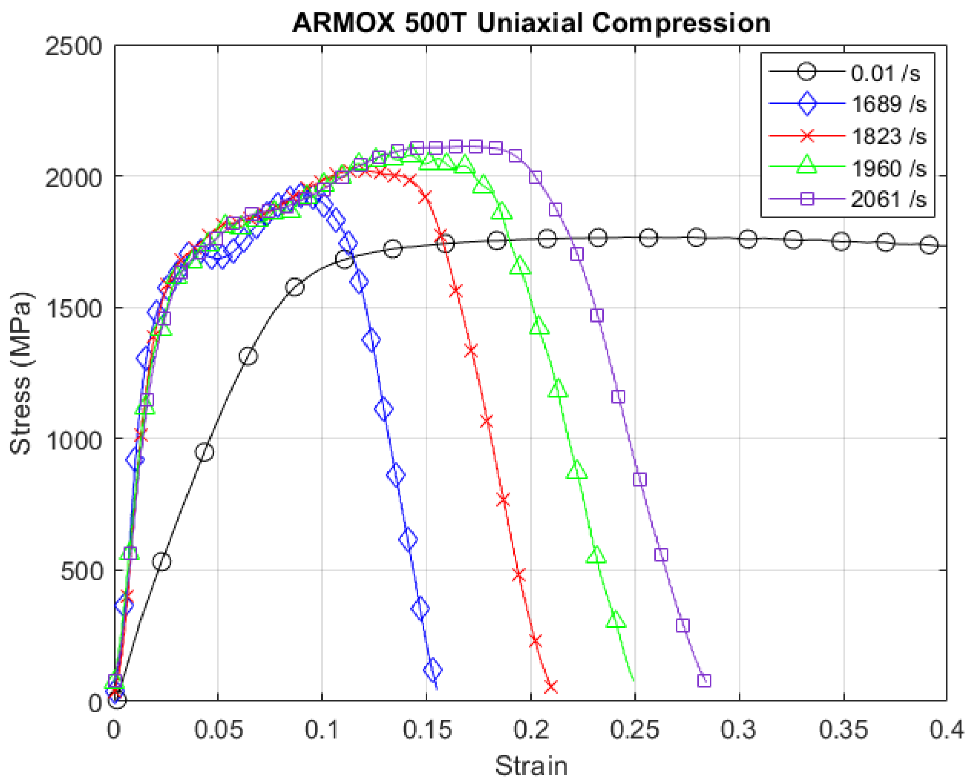

Figure 5.1: Dynamic compression strain-rate dependent stress-strain curves

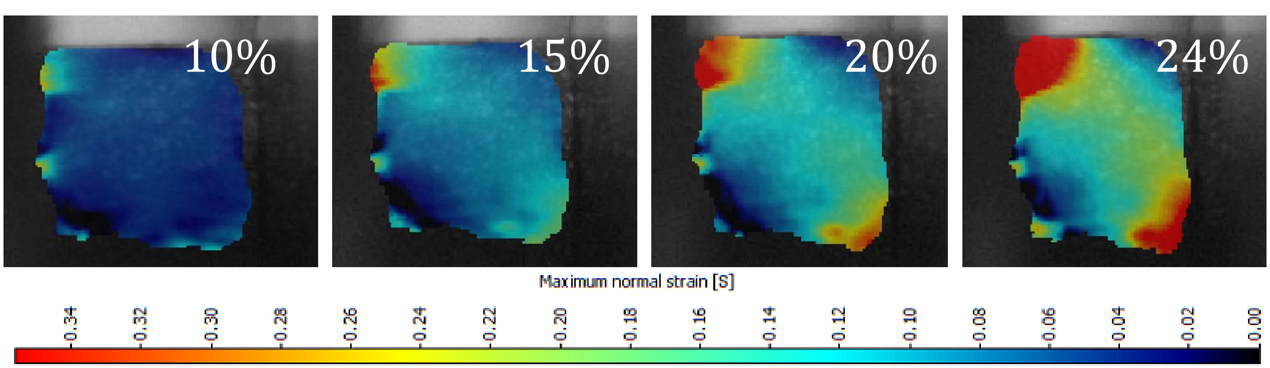

Figure 5.2: Principal strain during dynamic compression and onset of localized shear plane after homogenous deformation

To further support evidence of embrittlement due to an intrinsic instability, Figure 5.2 reveals the full-field strain evolution of a uniaxial compression test at ~2500 /s, the percentages refer to the percent axial elongation. In comparison to quasistatic loading; where homogenous deformation occurs until 62% axial elongation, at 2500 /s, strain localization occurs along the plane of maximum shear (45 degrees to the loading principal stress direction) at roughly 20% axial elongation which leads to premature fracture of the material. Note that since only 2D-DIC is conducted at high strain-rate and the cylindrical profile of the specimen, the data near the edges of the specimen are erroneous and thereby ignored. In the DIC strain-field, the red contoured areas are erroneous and not legitimate representations of the strain in this area. The center of the specimen, however, is perpendicular to the camera optical axis and therefore all measurements are taken from the central section. The principal strain in this region just before fracture in the image above is about 24%.

Figure 5.3 and Table 5.3 demonstrate the repeatability and reliability of the tests. Table 5.3 is presented in the axisymmetric tension chapter (5.3) as all strain-rate dependent strengthening compression and tension data is presented together. Only three repeated tests are presented in the table even though four were conducted, since on average at least 1 test was too noisy or an outlier. Note that the naming convention for dynamic compression is C#-L. C indicates compression, # is a number indicating a difference in testing condition (strain-rate), and L is a letter indicating a repeated test for the same testing condition (e.g., C1-A). It is the same for tension with T instead of C (e.g., T1-A). Note also that the specimen in Figure 5.3 is C5-B, which is referenced afterwards.

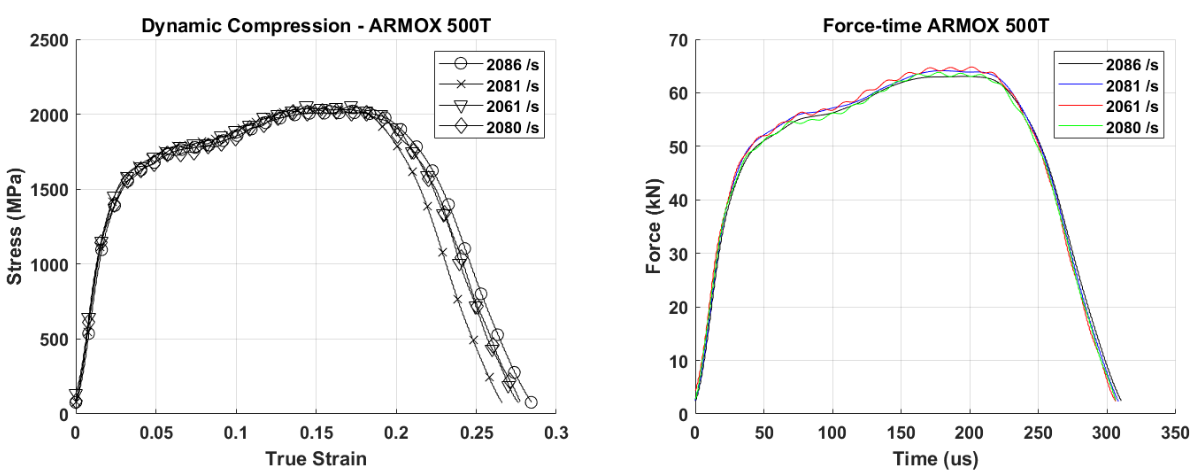

Figure 5.3: Four repeated dynamic compression tests at ~2000 /s

5.2 Axisymmetric Compression-Shear

No strengthening data is provided for compression-shear stress-states. This is primarily because for Hopkinson bar, the 1D wave propagation assumption is not met with the inclined specimens. While an approximation can be obtained, it is not necessary for the purposes of this thesis or model. GISSMO is a strain-based damage model and thus, all full-field axisymmetric compression and axisymmetric compression-shear data is presented in this section.

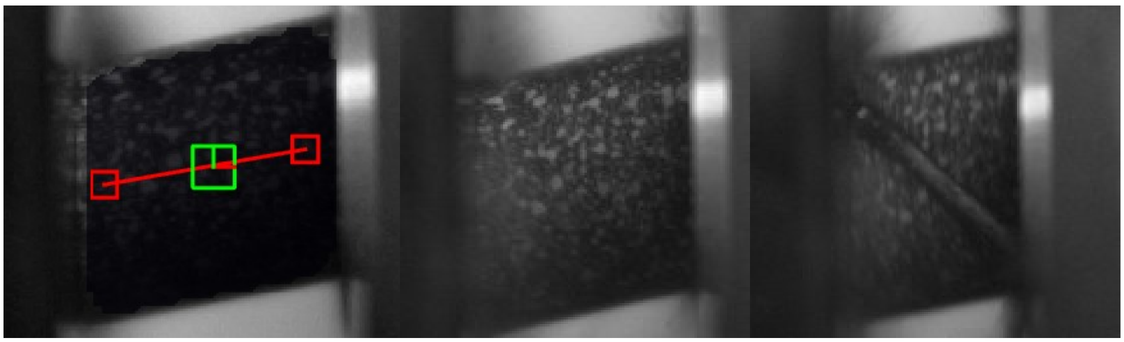

Figure 5.4: Virtual DIC measurements and optical images of inclined compression-shear specimen

Table 5.1: DIC extensometer data for dynamic compression and compression-shear

Stress-State	Specimen	Initial Length (mm)	Impact Momentum (Kgm/s)	Strain Rate (/s)	Axial Fracture Elongation
Axisymmetric Compression - C ($\lambda = 0$)	C4-F	6.96	20.43	2158	-0.269
	C4-G	6.96	20.92	2210	-0.287
	C4-H	6.97	20.30	2142	-0.332
	C5-A	6.91	**23.16**	2465	-0.270
	C5-B	6.99	**23.31**	2452	-0.300
	C5-C	6.98	**23.47**	2473	-0.345
	C6-A	6.97	25.74	2716	-0.227
	C6-B	6.99	25.68	2701	-0.382
	C6-C	7.01	25.85	2716	-0.331
	Average $\pm$ STD	*6.97*	*23.21*	*2448*	*-0.305 $\pm$ 0.045*
Compression-Shear - CS6 ($\lambda = 0.10$)	CS6-A	6.35	**23.15**	2666	-0.148
	CS6-B	6.36	**22.63**	2602	-0.156
	CS6-C	6.34	**23.08**	2662	-0.142
	Average $\pm$ STD	*6.35*	*22.95*	*2643*	*-0.149 $\pm$ 0.006*
Compression-Shear - CS10 ($\lambda = 0.17$)	CS10-A	6.37	**23.07**	2622	-0.107
	CS10-B	6.35	**23.34**	2661	-0.104
	CS10-C	6.35	**23.23**	2649	-0.117
	Average $\pm$ STD	*6.36*	*23.21*	*2644*	*-0.109 $\pm$ 0.005*

Figure 5.4 illustrates the method of measuring extensometer-based elongation and strain-gauge based strain-path data for all dynamic compression and compression-shear tests. Additionally, two optical images from the high-speed camera are presented for an inclined compression-shear specimen, CS10. CS indicates Compression-shear and 10 indicates the angle of inclination. The images shown are the image just before the fracture event and the image just after the fracture event. It is observable that the fracture event is sudden under compression-shear, and the resulting fracture surface is very straight, revealing the crack path along the ASB on the shear plane and indicating rapid crack propagation along a well-defined path of shear stress concentration.

Table 5.1 presents the DIC extensometer data for all uniaxial compression and multiaxial compression-shear tests that fractured. Note the naming convention is continued from the uniaxial specimens. The shear compression specimens are named as per their angles of inclination of 6 and 10. Only three tests of each inclined specimen are presented at a constant impact momentum / test condition. More tests were conducted at varying strain rates (2000-3500 /s) to find that there was no strain-rate effect on the extensometer data for fracture elongation and is therefore not reported.

From the table, three things should be noted.

1. C5 uniaxial specimens are conducted at the same impact momentum than CS6 and CS10 specimens to provide an adequate comparison between the three stress-states.
2. There is a decrease of the fracture elongation with increasing angle of inclination (shear stress) defined by the Compression-shear load ratio, λ.
3. The fracture elongation under uniaxial stress-state is variable over a wide range. While under compression-shear stress state (CS6, CS10), it is consistent. Note that the standard deviation is an order of magnitude higher under uniaxial compression.

No correlation between strain-rate and fracture elongation on axisymmetric compression specimens could be found. The variability of the fracture elongation must be attributed to a different mechanism. Figure 5.5 illustrates this phenomenon, plotting the extensometer data from Table 5.1 against time. In Figure 5.6a, the strain-time curves of the CS10 tests are illustrated. The fracture elongation on the y-axis is consistent under a well-defined multiaxial stress-state of compression-shear. Therefore, on a microstructural scale, a consistent evolution of the microstructure occurs under compression-shear but not under uniaxial compression. This is supporting evidence to the claim of Boakye-Yiadom [42], [46] that for traditional cylindrical uniaxial compression steel specimens, the mode of failure is by ASB, and further that the ASB must initiate at a microstructural homogeneity at which point an activated dislocation source intersects

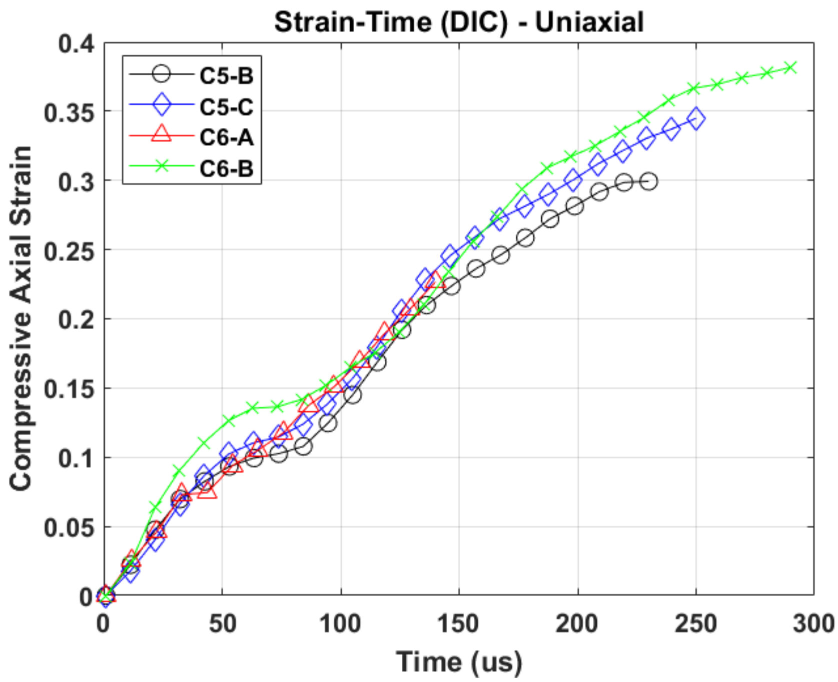

Figure 5.5: Strain-time curves of various axisymmetric compression tests with variability in fracture elongation

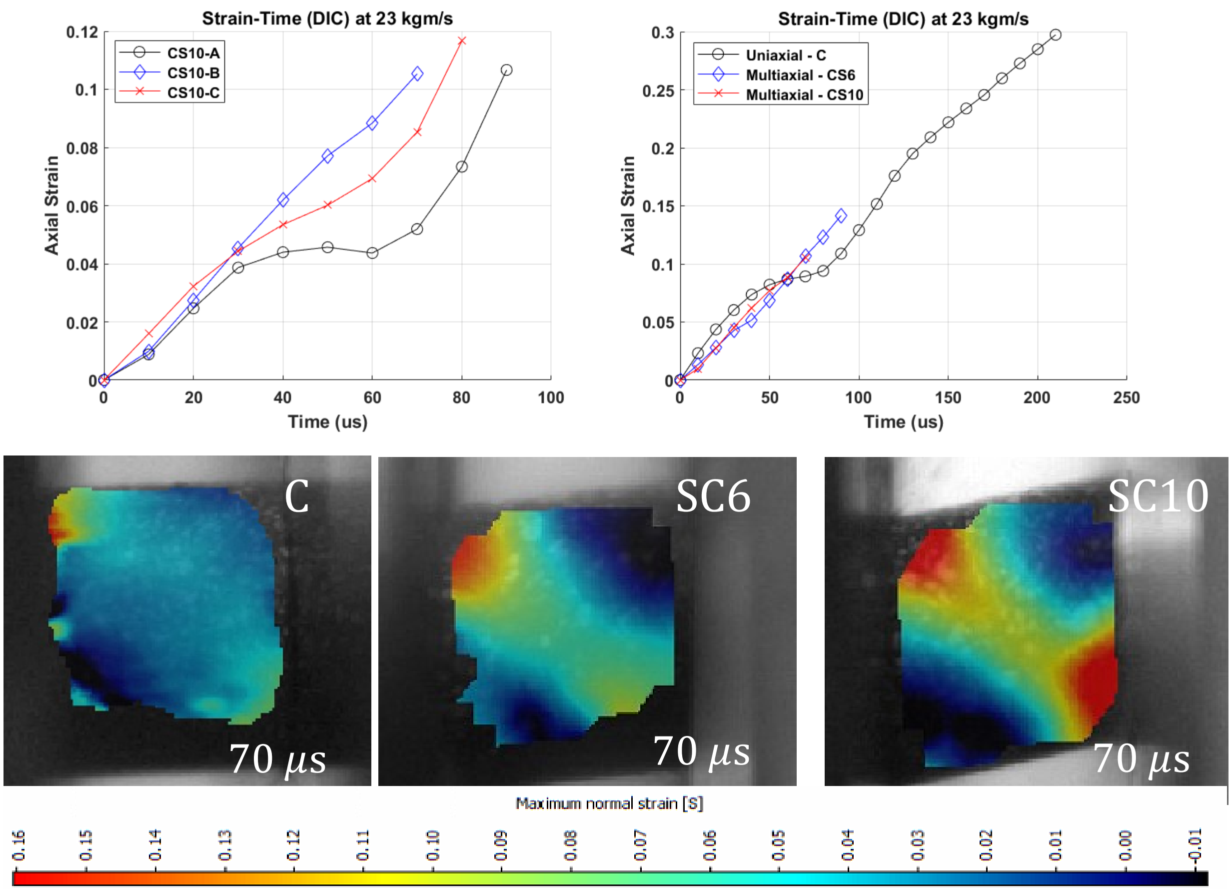

Figure 5.6a: Consistent strain-time in compression-shear (CS10) specimen. 5.6b: Effect of load ratio (λ) on fracture elongation. 5.6c-e: Effect of load ratio (λ) on strain localization along maximum shear plane.

with the plane of maximum shear. It also supports the claim by LW Meyer [40], [110] that the compression-shear specimens have a well defined and consistent stress-state along the shear plane throughout loading, which favours characterization of the ASB instability by material property as opposed to by microstructural inhomogeneity or geometrical forced localization effects.

In Figure 5.6b and c, the effect of load ratio (λ), or increasing shear stress by increased angle of inclination, on the ductility of the material is quantitatively demonstrated. Using fracture elongation and maximum principal strain as criteria, it is evident that with an increasing in λ, there is a corresponding increase in strain localization along the plane of maximum shear resulting in reduced ductility. Note that Figure 5.6b and c correlate to specimens C5-B, CS6-B, and CS10-B. Note also that the strain-time curves should be linear, like CS10-B or all the curves in Figure 5.6b. In Figure 5.6a, clearly, not all the repeats for CS10 are linear. This is primarily due to the usage of an overdamped momentum trap on the DIHB for some of the tests, such that the transmitted bar translated a small amount during deformation captured by the high-speed camera during loading of the specimen. None of these tests are used for microstructural characterization as they are deemed ineligible. However, it has had no effect on the relevant macroscale data.

Taking this further with data processing, the strain gauge measurement can provide supporting evidence for the effect of stress-state on strain localization. The in-situ equivalent plastic strain on the surface of the specimen can be derived. On the compression-shear specimens, the equivalent plastic strain differs from the principal strain in the uniaxial specimen due to the added shear stress component, where the surface axial (Ex), transverse (Ey), and shear (Exy) strains will deviate from a uniaxial state. The equivalent plastic strain also differs from the axial and principal strains in the compression-shear specimens, due to their inclination and thereby initial variation of the stress-state at the onset of loading. For GISSMO, it is important to match computational simulations to the experiment, and so, the equivalent plastic surface strains are reported. For future computational modeling, the reported equivalent strains can be used as a reference datapoint from which the rest of the stress-field can be predicted in the simulation. Table 5.2 presents this strain-gauge data for nine specimens (3 repeats for each stress-state) tested and Figure 5.7 depicts the effect of the inclination angle or added shear stress (λ) on the ductility of AX500. A higher shear/compression load ratio (λ) increases the degree of strain localization along the shear plane and embrittles the material. Ultimately, this DIC data empirically quantifies the effect of a multiaxial shear stress component on adiabatic shear band initiation and subsequent premature fracture of AX500.

Table 5.2: Effect of stress-state (λ) on DIC surface strain data for GISSMO

Specimen	Strain-Rate (/s)	Axial Fracture Elongation	Axial Fracture Strain (Ex)	Transverse Fracture Strain (Ey)	Equivalent Plastic Instability Strain (ε_{eq}^{i})	Equivalent Plastic Fracture Strain (ε_{eq}^{f})
C5-B	2452	-0.300	0.248	-0.297	0.206	0.319
C6-A	2716	-0.227	0.179	-0.292	0.241	0.300
C7-A	2891	-0.331	0.266	-0.246	0.248	0.297
Average $\pm$ STD	*2686 $\pm$ 180*	*0.286 $\pm$ 0.044*	*0.231 $\pm$ 0.038*	*0.278 $\pm$ 0.023*	*0.232 $\pm$ 0.019*	*0.305 $\pm$ 0.010*
CS6-A	2666	-0.148	0.165	-0.225	0.135	0.235
CS6-B	2602	-0.156	0.092	-0.192	0.169	0.201
CS6-C	2662	-0.142	0.143	-0.182	0.130	0.202
Average $\pm$ STD	*2643 $\pm$ 29*	*0.149 $\pm$ 0.006*	*0.133 $\pm$ 0.031*	*0.200 $\pm$ 0.019*	*0.144 $\pm$ 0.018*	*0.213 $\pm$ 0.016*
CS10-A	2622	-0.107	0.111	-0.147	0.106	0.157
CS10-B	2661	-0.104	0.110	-0.157	0.116	0.166
CS10-C	2649	-0.117	0.100	-0.134	0.117	0.142
Average $\pm$ STD	*2644 $\pm$ 16*	*0.109 $\pm$ 0.005*	*0.107 $\pm$ 0.005*	*0.146 $\pm$ 0.009*	*0.113 $\pm$ 0.005*	*0.155 $\pm$ 0.010*

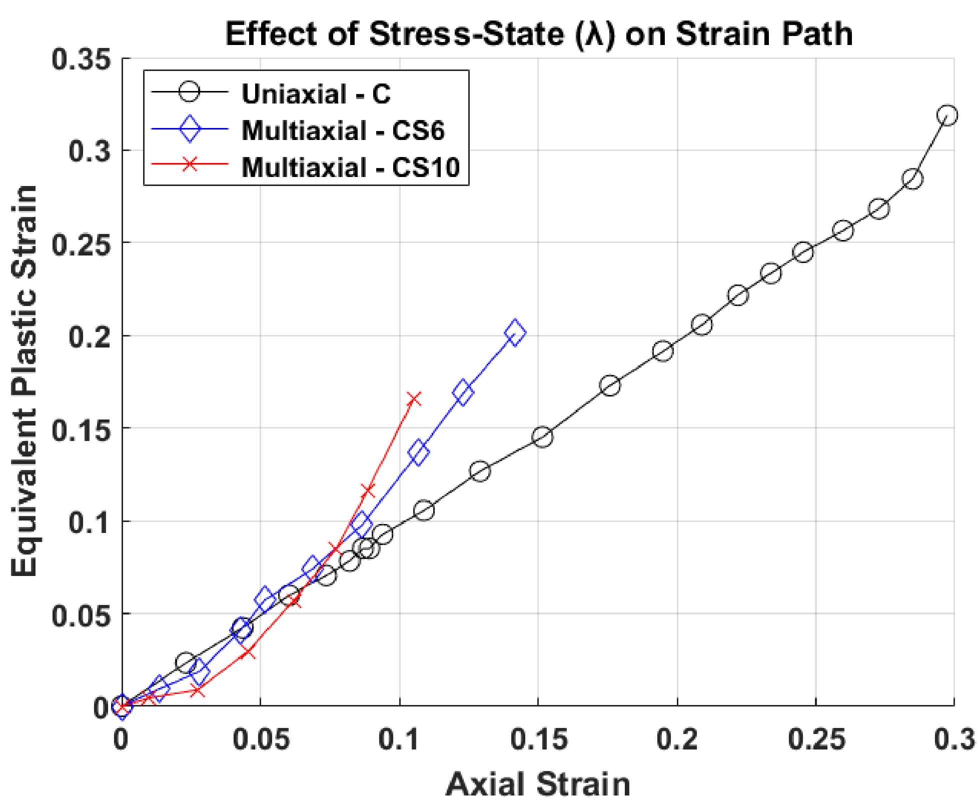

Figure 5.7: Effect of stress-state (λ) on equivalent plastic strain evolution in dynamic compression and compression-shear

5.3 Axisymmetric Tension

All experiments conducted under dynamic axisymmetric tension fractured. All experiments followed the DIC practices mentioned in section 3.3.3.2. In Figure 5.8a, the method of virtual DIC measurements to acquire elongation and surface equivalent plastic strains (strain gauge) is presented. In addition, to demonstrate the confidence in results, Figure 5.8b presents three centrally fractured specimens. When specimens fracture closer to the fillet region it is inadmissible. Note that some specimens fracture slightly to the left of the dead center, and some slightly to the right. Indicating that it is it is likely due to crack initiation at some microstructural region as opposed to a consistent faulty region which may indicate an experimental setup condition.

Figure 5.8c-f reveal the principal strain field evolution during dynamic tensile loading of specimen T1-B at about 678 /s. Notably, the localization at the central region occurs relatively early in the deformation stage, and then sustains necking for a prolonged period as observed in the TSHB strain gauge data. This corresponds well to the stress-strain curves shown in this section.

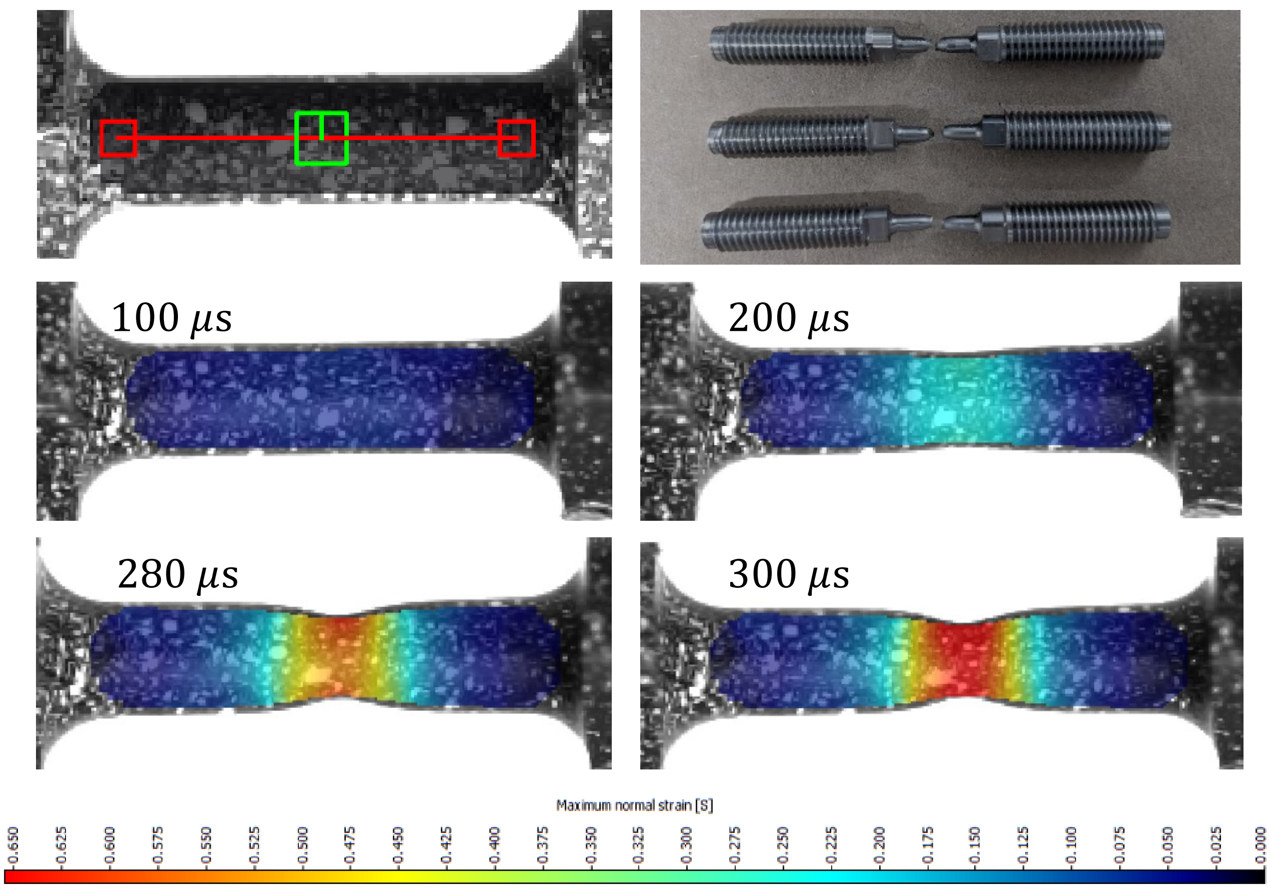

Figure 5.8a: DIC measurements in dynamic tension. 5.8b: Specimens with central fracture location. 5.8c-f: Maximum principal strain fields for T1-B at 678 /s revealing early and prolonged strain localization and necking.

As mentioned in section 3.3.1.2, a MATLAB code was created which accepts text files input from the DAQ for the TSHB strain gauges (time and voltage), filters the data, and then converts voltage to strain using the strain gauge factor and electrical setup constants for bridge voltage (5 V) and amplifier gain (100). Once incident/transmitted bar strains are acquired, using 1D wave mechanics equations 3.11-3.15, the specimen stress and strain is acquired. For all code runs, the incident and transmitted waves are presented to the user as well as a comparison between 1-wave and 2-wave analysis to check stress equilibrium. The code also presents the strain-time and strain-rate-time curves to ensure a linear strain evolution at constant strain-rate. Meeting these two conditions of stress equilibrium and linear axial strain evolution, the test is a valid Hopkinson bar test for material characterization. Lastly, the stress-strain curves are presented.

Figure 5.9 presents a comparison between a pulse shaped experiment using corrugated fiberboard (blue lines), and a non pulse shaped experiment (black lines). Clearly, wave dispersion is prominent in the non-pulse shaped experiment. In the Figure, it is clearly shown that the fiberboard pulse shaper successfully filters out the high frequency components of the stress-wave, thus mitigating wave dispersion effects. This results in an improved experiment such that stress equilibrium is reached and maintained almost instantly as opposed to the non pulse shaped experiment. For this reason, all characterization experiments used corrugated fiberboard pulse shaping.

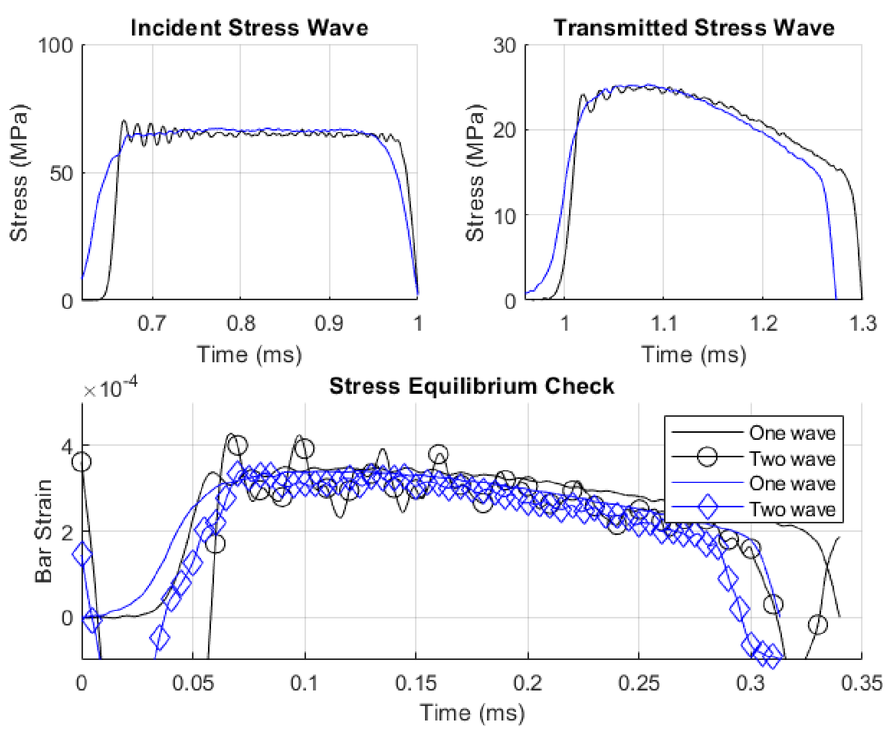

Figure 5.9: Pulse shaped TSHB experiment with corrugated fiberboard (blue) and a non pulse shaped experiment (black)

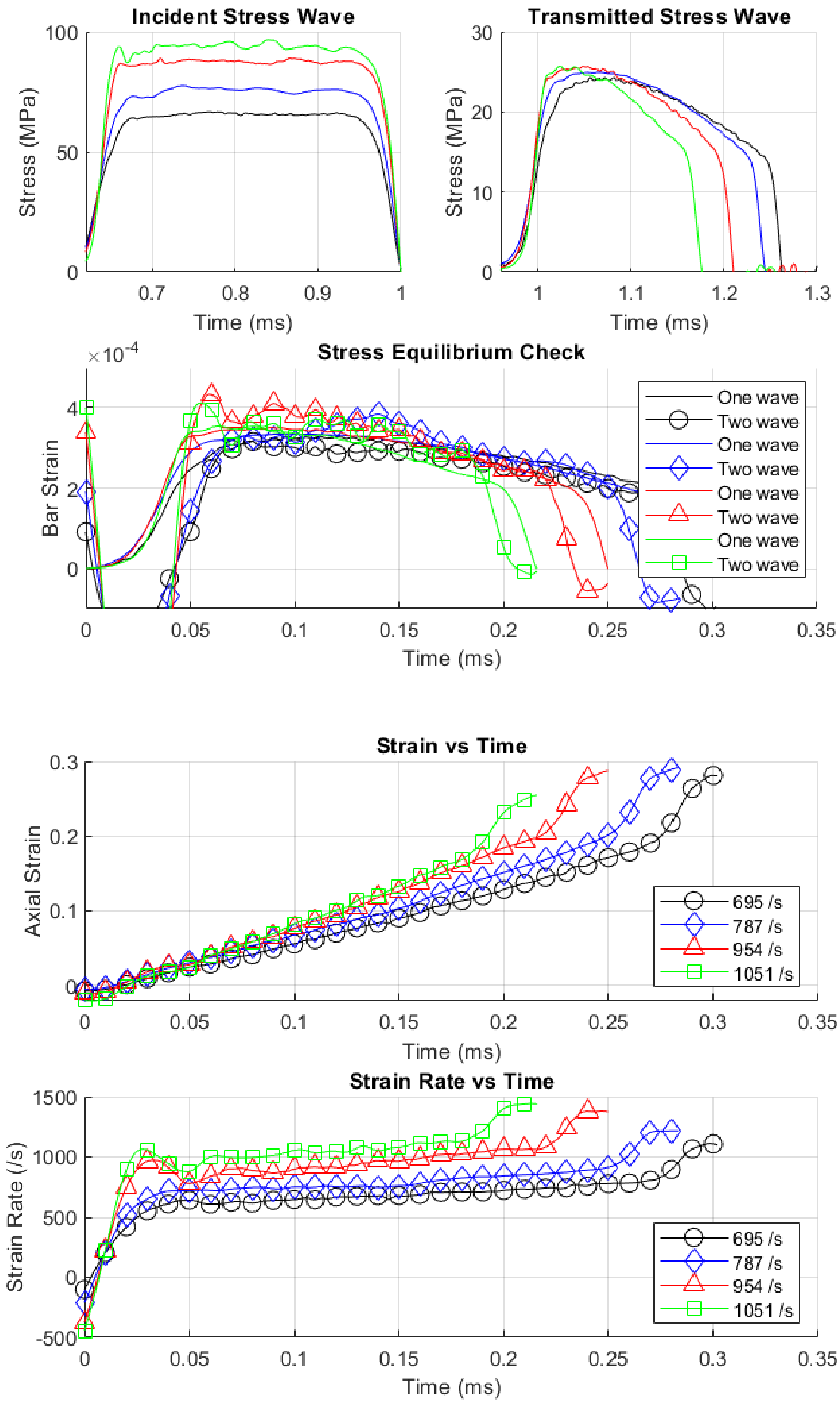

Figure 5.10: Four TSHB tests at varying impact momentum. Stress equilibrium check and linear strain evolution check.

In Figure 5.10, the MATLAB code outputs are presented displaying the incident (Figure 5.10a) and transmitted (Figure 5.10b) pulses which confirm stress equilibrium (Figure 5.10c) and linear strain evolution (Figure 5.10d, e) for four tests at four varying impact momentums. As expected, the incident wave stress increases with increasing impact momentum, imposing a higher strain-rate onto the specimen. The effect of this higher strain-rate can be visualized in Figure 5.10b, where the transmitted wave is clearly shorter for each increasing impact momentum. Simultaneously, the strain-rate hardening effect can be visualized in the transmitted wave. As expected, with increasing impact momentum / strain-rate, the transmitted wave stress increases indicating a strengthening effect with increasing strain-rate. Figure 5.10d and e illustrate the increasing strain-rate effect.

Figure 5.11a presents the stress-strain curves at four varying strain-rates, effectively demonstrating the strain-rate hardening effect. Figure 5.11b presents the same data (note the color change / dataset) compared with the quasistatic test using the same HSR specimen. Looking in further detail at the stress-strain curves, the increased strengthening seems to take effect at the initial work hardening phase just after the yield point at the onset of dislocation generation and motion. The strain-rate has a substantial effect in this region of the curve such that increasing strain-rate results in increased work hardening rate and sustainment leading to greater load-bearing capacity. After reaching the ultimate stress, the necking is comparably prolonged demonstrating high plastic flow at all strain rates including quasistatic and the fracture stress is also comparable at all strain-rates.

Systematic high strain-rate testing showing the effect of increasing strain-rate with multiple data points on stress-strain is unprecedented in AX500. This experimental data explicitly demonstrates that AX500 has increased damage tolerance up to 1100 /s as it strengthens without losing ductility.

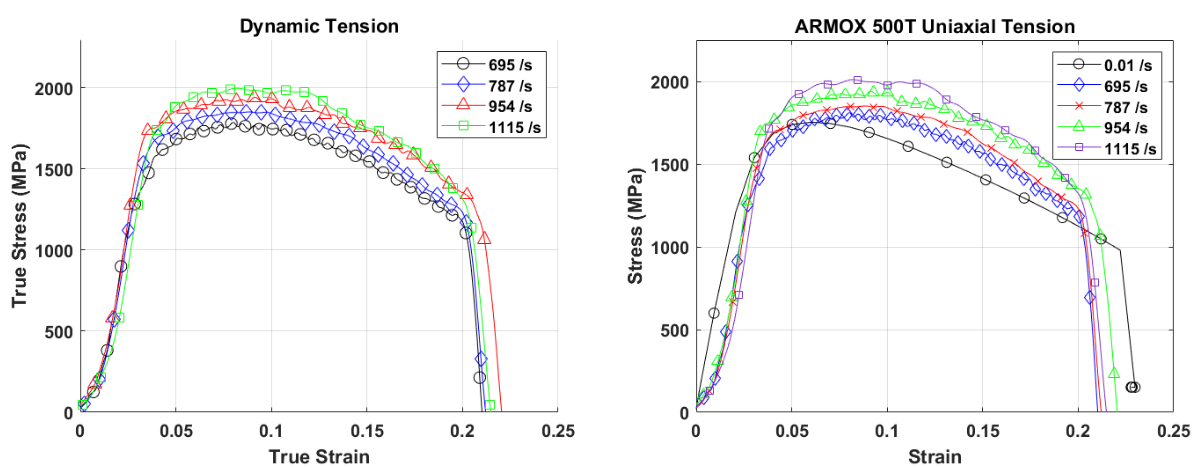

Figure 5.11a: Dynamic tension results at four strain-rates. 73b: HSR tension specimen compared with quasistatic tension.

Table 5.3 presents all strain-rate dependent strengthening data for axisymmetric round compression and tension specimens. Note that all tension specimens fractured, and none of the compression specimens fractured due to the nature of DIHB testing.

*Table 5.3: All dynamic compression and tension stress and strain data (*fractured)*

Specimen	Impact Momentum (Kgm/s)	Strain Rate (/s)	Ultimate Flow Stress (MPa)	Axial Elongation at Instability	Maximum Axial Elongation
C1-A	15.97	1689	1949	-0.089	-0.147
C1-B	16.02	1690	1928	-0.091	-0.155
C1-C	15.78	1657	1986	-0.090	-0.156
Average $\pm$ STD	*15.92 $\pm$ 0.10*	*1679 $\pm$ 15*	*1954 $\pm$ 24*	*-0.090 $\pm$ 0.001*	*-0.153 $\pm$ 0.004*
C2-B	17.38	1805	1904	-0.095	-0.178
C2-C	17.29	1834	2023	-0.116	-0.210
C2-D	17.49	1806	2075	-0.122	-0.210
Average $\pm$ STD	*17.39 $\pm$ 0.08*	*1815 $\pm$ 13*	*2001 $\pm$ 72*	*-0.111 $\pm$ 0.011*	*-0.199 $\pm$ 0.015*
C3-A	18.66	1940	2084	-0.130	-0.249
C3-C	18.65	1944	2097	-0.131	-0.242
C3-D	18.59	1955	2109	-0.148	-0.226
Average $\pm$ STD	*18.63 $\pm$ 0.03*	*1946 $\pm$ 6*	*2097 $\pm$ 10*	*-0.137 $\pm$ 0.008*	*-0.239 $\pm$ 0.010*
C4-A	19.72	2086	2111	-0.170	-0.284
C4-B	19.76	2081	2140	-0.147	-0.266
C4-C	19.52	2061	2163	-0.173	-0.276
Average $\pm$ STD	*19.67 $\pm$ 0.11*	*2076 $\pm$ 11*	*2138 $\pm$ 21*	*-0.163 $\pm$ 0.012*	*-0.276 $\pm$ 0.008*
*T1-B**	30.57	678	1869	0.087	0.217
*T1-C**	30.39	695	1811	0.080	0.198
*T1-D**	29.59	663	1882	0.105	0.226
Average $\pm$ STD	*30.18 $\pm$ 0.43*	*679 $\pm$ 13*	*1854 $\pm$ 31*	*0.091 $\pm$ 0.011*	*0.213 $\pm$ 0.012*
*T1-A**	35.31	787	1863	0.088	0.200
*T2-B**	35.29	810	1908	0.088	0.200
*T2-C**	36.15	819	1854	0.086	0.192
Average $\pm$ STD	*35.58 $\pm$ 0.40*	*805 $\pm$ 13*	*1875 $\pm$ 23*	*0.087 $\pm$ 0.001*	*0.197 $\pm$ 0.004*
*T3-A**	40.53	954	1941	0.091	0.208
*T3-B**	40.38	975	1841	0.064	0.162
*T3-C**	41.61	889	1958	0.048	0.179
Average $\pm$ STD	*40.84 $\pm$ 0.55*	*939 $\pm$ 37*	*1913 $\pm$ 51*	*0.068 $\pm$ 0.018*	*0.183 $\pm$ 0.019*
*T4-A**	45.10	1105	1948	0.040	0.176
*T4-B**	44.24	1115	1997	0.082	0.202
*T4-C**	44.04	1051	1978	0.057	0.172
Average $\pm$ STD	*44.46 $\pm$ 0.46*	*1090 $\pm$ 28*	*1974 $\pm$ 20*	*0.060 $\pm$ 0.017*	*0.184 $\pm$ 0.013*

Figure 5.12 demonstrates the repeatability and reliability of both TSHB and DIC data as independent measurements. Figure 5.12a presents the stress equilibrium check for all datasets reported, where the incident, transmitted, and one/two wave analyses are presented on three sub-plots, respectively. This information provides statistical confidence and significance (Appendix A) to the data results. Figure 5.12b plots the DIC strain-time and the TSHB incident bar strain gauge strain-time data for the T2 series tests together on the same plot. It is evident that a very good match is obtained, enhancing the confidence in both TSHB and DIC results. Note that the strain-rates do not perfectly match, the DIC strains lag about 100 /s behind the TSHB calculation. This is likely because on both TSHB and DIC data, it is found as an average of a percentage of the data in the mid range (ends are trimmed) and calculated using equation 2.2.2. The trimming is influencing the calculation. However, as per the strain-rate curves in Figure 5.10, it can be visualized that both predictions are an adequate approximation of the value. Figure 5.12b plots the stress-strain from the TSHB (left y-axis) and the equivalent plastic strain found using DIC virtual strain gauge data (right y-axis). Again, repeatability is demonstrated for both data sources of the TSHB and DIC.

The equivalent plastic strain evolution; as expected, grows exponentially. This indicates that the material is necking very early, however is then able to sustain plastic flow during necking for a prolonged period which reveals that AX500 has high damage tolerance under axisymmetric tension. The fracture stress is then near the initial yield stress of the material. Note also that the equivalent stress is not plotted, only the true stress. The equivalent stress would be a more accurate representation of the stress and would change the plasticity behaviour of the curve after necking, such that the equivalent stress would deviate from the current curve and have a higher fracture stress. It would be required to identify the in-situ necking radius to calculate the equivalent stress, which is possible with image processing and edge detection algorithms. It is recommended to adopt this method for damage modeling as it adequately accounts for the increased damage tolerance of the material.

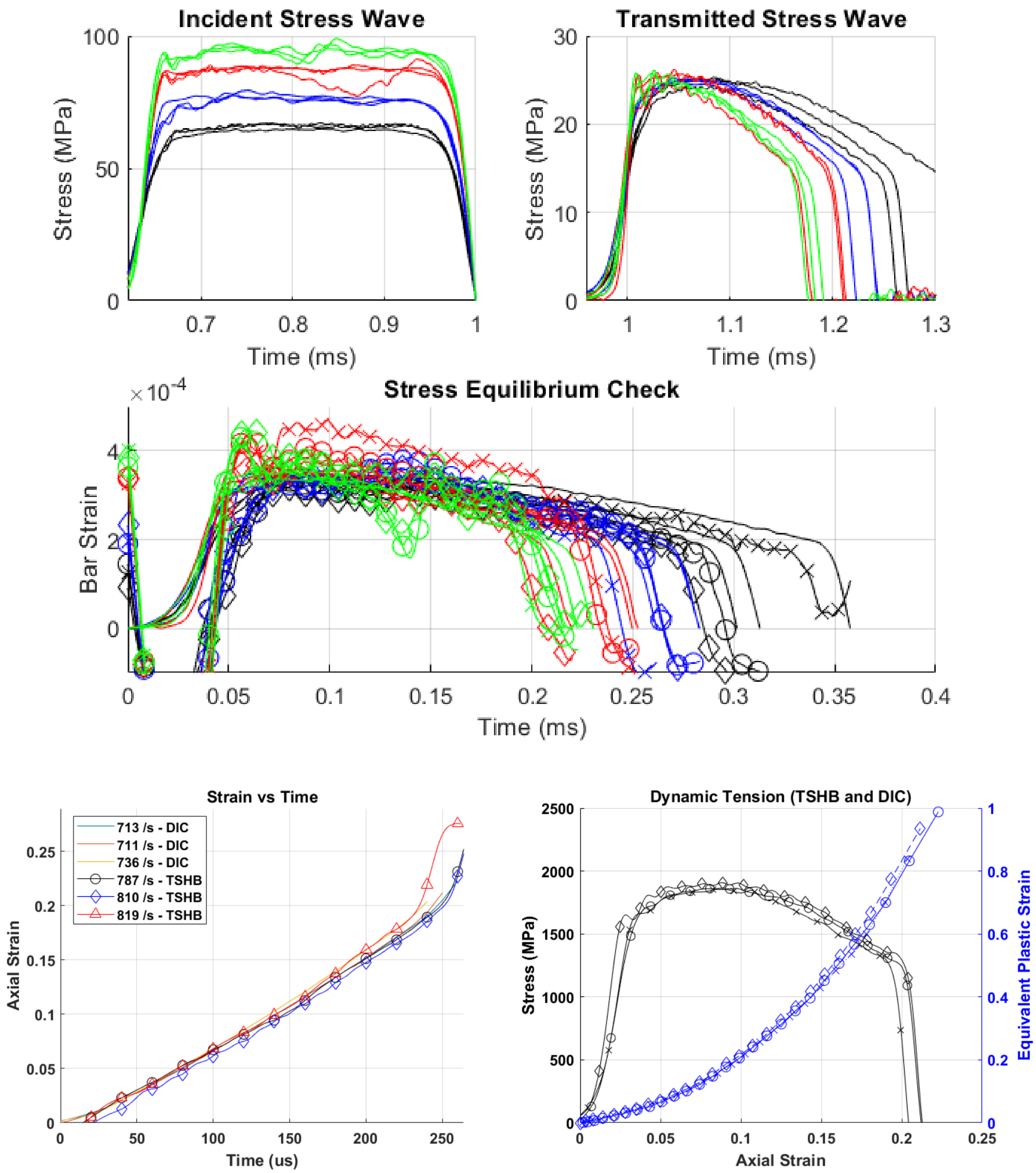

*Figure 5.12a: All repeated tests at four strain-rates (3*4=12) incident and transmitted waves with consistent stress equilibrium. 5.12b: Comparison of strain-time curves for both TSHB incident strain gauge data and DIC virtual extensometer data. 5.12c: Reproducibility of TSHB tests for transmitted strain gauge (left y-axis) and DIC strain gauge data (right y-axis).*

Table 5.4: Dynamic tension DIC strain gauge data for GISSMO

Specimen	Strain-Rate (/s)	Axial Fracture Strain (Ex)	Transverse Fracture Strain (Ey)	Shear Fracture Strain (Exy)	Equivalent Plastic Instability Strain (ε_{eq}^{i})	Equivalent Plastic Fracture Strain (ε_{eq}^{f})
T1-A	560	0.802	-0.233	0.022	0.180	0.826
T1-B	532	0.802	-0.211	0.023	0.174	0.832
T1-C	582	0.840	-0.267	0.014	0.173	0.859
Average ± STD	*558 ± 20*	*0.815 ± 0.018*	*0.237 ± 0.023*	*0.020 ± 0.004*	*0.176 ± 0.003*	*0.839 ± 0.014*
T2-A	713	0.934	-0.189	0.017	0.177	0.988
T2-B	711	0.906	-0.252	0.010	0.187	0.935
T2-C	736	0.815	-0.245	0.033	0.186	0.838
Average ± STD	*720 ± 11*	*0.885 ± 0.051*	*0.229 ± 0.028*	*0.020 ± 0.010*	*0.184 ± 0.004*	*0.921 ± 0.062*
T3-A	877	0.888	-0.201	0.018	0.144	0.932
T3-B	819	0.959	-0.246	0.023	0.058	0.996
T3-C	822	0.915	-0.219	0.006	0.187	0.955
Average ± STD	*839 ± 27*	*0.920 ± 0.029*	*0.222 ± 0.019*	*0.016 ± 0.007*	*0.130 ± 0.053*	*0.961 ± 0.027*
T4-A	1088	0.915	-0.239	0.010	0.131	0.950
T4-B	1010	0.995	-0.245	0.029	0.100	1.037
T4-C	1032	0.990	-0.222	0.027	0.065	1.040
Average ± STD	*1043 ± 33*	*0.967 ± 0.036*	*0.235 ± 0.010*	*0.022 ± 0.008*	*0.099 ± 0.027*	*1.009 ± 0.042*

Table 5.4 presents the DIC virtual strain-gauge data. The strain tensor at fracture is presented (axial, transverse, and shear strains) for all tests as well as the equivalent plastic instability and fracture strains. $\boldsymbol{\varepsilon_{eq}^{i}}$ occurs at the ultimate flow stress, which can be visualized in Figure 5.12b as the T2 series data in the table correlates to the plot. The $\boldsymbol{\varepsilon_{eq}^{f}}$ and the tensor strain data also correlates to the plot at the fracture point and can be effectively visualized. Notably, in quasistatic conditions, axisymmetric round tension specimens have an average $\boldsymbol{\varepsilon_{eq}^{f}} = \mathbf{0.62}$, while at the highest strain-rate (~1043 /s) there is an average $\boldsymbol{\varepsilon_{eq}^{f}} = \mathbf{1.01}$. Furthermore, the strain-rates in between from ~558 /s to ~839 /s have increasing $\boldsymbol{\varepsilon_{eq}^{f}}$ with increasing strain-rate. This suggests further supporting evidence for the increased damage tolerance of dynamic tension with increasing strain rate.

However, due to the high strain-rate and high deformation with respect to subset size, accumulated vector errors on each DIC data point being responsible for the increased $\boldsymbol{\varepsilon_{eq}^{f}}$ cannot be ruled out as a possibility. More supporting evidence is required to indicate that the observed $\boldsymbol{\varepsilon_{eq}^{f}}$ increase is indeed a material property effect with and not an accumulation of DIC error.

5.4 Damage Tolerance in Dynamic Tension

This section presents microscale evidence to explain the macroscopic plasticity behaviour of AX500 under axisymmetric tension. While macroscale evidence is found in the stress-strain and DIC data that there is an increase in work hardening and enhanced plastic flow with increasing strain-rate, this cannot be unequivocally concluded unless a microscale explanation is found to explain the macroscale phenomena. This section provides the evidence for the effect of strain-rate on the microstructure-property relationship of AX500 under axisymmetric tension loading at a constant lode angle parameter (LAP) of 1.

The Scanning Electron Microscope (SEM) was used to conduct fractography on three fractured tension specimens (including a quasistatic specimen) at three different strain-rates of 0.01, 750, and 1000 /s. The specimens were prepared as described in section 3.4.2 and secondary electron micrographs are acquired. Figure 5.13 reveals the central regions of the quasistatic test (0.01 /s) and the T4-B dynamic tension test at the highest strain-rate (~1000 /s). It is easily visually observable that there is a difference between the two images. The dynamic specimen has a much greater density of pronounced voids, and they are also much larger than those in the quasistatic specimen.

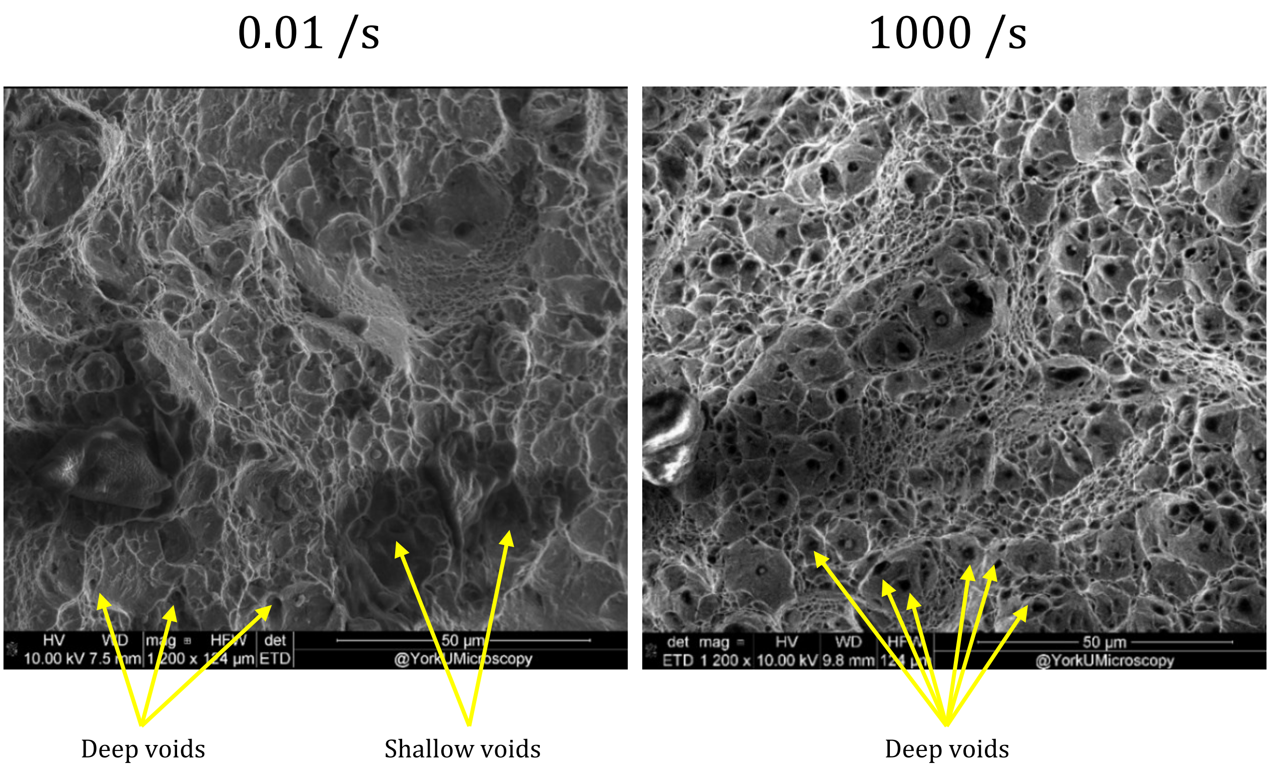

Figure 5.13a: Tensile fracture surface at 0.01 /s. 75b: Tensile fracture surface at 1000 /s with increased void size and density

The increased void density and size in the dynamic specimen is indicative of two possible mechanisms (either or combined):

1. Short-range order microstructural features dominate more at high strain rate, resulting in a higher number of dislocation pileups and consequential void initiation-sites.
2. Increasingly pronounced ductile void growth and coalescence occurs in dynamic tension.

If only the first mechanism were occurring, the material would likely lose ductility without another mechanism in action. Therefore, it can be concluded that the second mechanism is exhibited by AX500 at dynamic strain-rates. Given the density of the voids, it is very likely that the first mechanism is also in action. Figure 5.14 illustrates that the central region sustains a much greater degree of plasticity and damage than the edges. The fracture surface near the edges with equiaxed shear dimples and shallow voids is less evolved like the quasistatic fracture.

Conclusively, it is ascertained that with increasing strain-rate, AX500 exhibits greater work hardening leading to a higher density of void initiation sites. This effect is coupled with greater plastic flow and damage tolerance through enhanced void growth and coalescence. The unknown mechanism for enhanced void growth may be adiabatic heating or a nanoscale toughening effect.

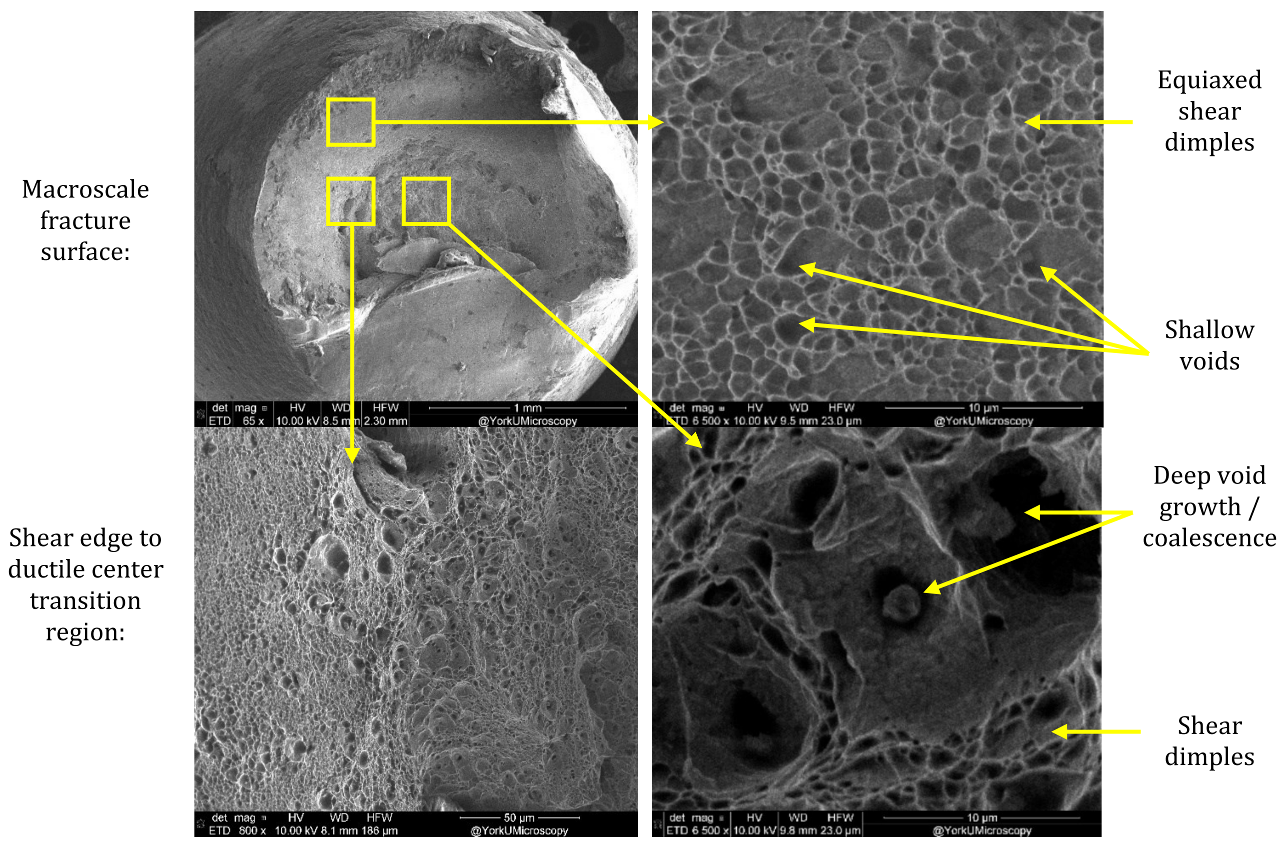

Figure 5.14: Ductile dynamic tensile fracture surface of AX500 at 1000 /s.

5.5 Fracture and Fragmentation in Dynamic Compression

Dynamic compression and compression-shear fracture surfaces are macroscopically observed and mounted onto the SEM for microscopic observations with secondary electron images. Figure 5.15 shows the macroscopic observation, it is notable that the uniaxial specimen (C) has a clearly identifiable hourglass shape of the ASB which is the 2D curvature of the maximum shear plane. It is a well-determined shape from the literature as discussed in section 2.4.3. However, the compression-shear specimen (CS10) shows a much straighter and flatter fracture surface. The CS6 specimen (not shown) is comparable to the CS10 specimen. There is a small intrusion on both sides of the specimen near the impacted surfaces (indicated by blue arrows) where the ASB forms, however the hourglass shape is significantly smaller. This is a very new observation not found in the literature; therefore, it cannot be stated if this is a material dependent phenomenon or solely due to stress-state, or possibly a combination of both. Notably, burning, sparking and fragmentation into multiple fragments occurs in all specimens. Under the SEM, the morphology in the hourglass region of the C and CS10 specimens are investigated further (indicated by the yellow squares in Figure 5.15).

The fracture surfaces are presented in Figure 5.16. On the fracture surfaces, a combination of different brittle and ductile features are observed. Primarily, there is a dominance of patches of severely elongated grains along most of the fracture surfaces indicating prominent mode II fracture. No effect of stress-state could be found on this aspect of the fracture surfaces, their aspect ratios are severely high for all specimens. Interestingly, there are various abrupt transitions in fracture surface morphology within the hourglass regions. For example, in the compression (C) specimen (Figure 5.16a), there is a sudden transition from highly ductile and smeared elongated shear dimple surface to a smooth surface. This is indicative that during the fracture event, based on the crack path there are certain regions which may be sliding against each other post fracture.

Compression (C): **Compression-Shear (CS10):**

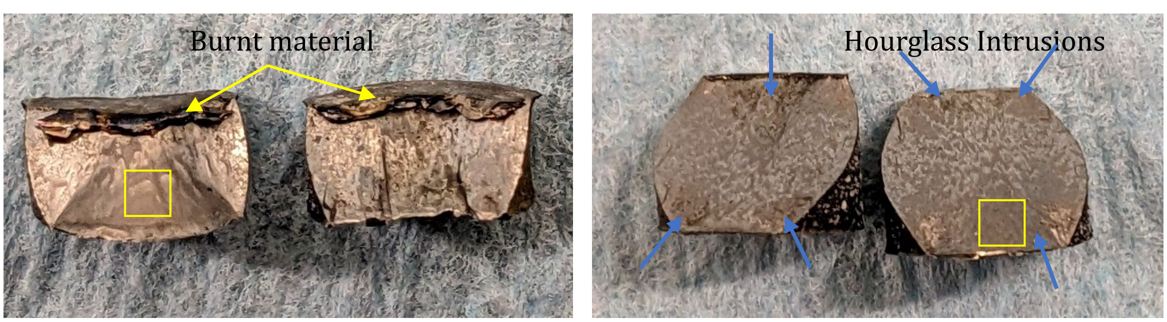

Figure 5.15: Macroscale fractography of the hourglass fracture surfaces of the uniaxial (C) and multiaxial (CS10) specimens

Giovanola has observed this in the adiabatic shear fracture surfaces of torsion specimens [127]. In this study it was observed that when superimposing both sides of the fracture surfaces by alignment of void patch morphology, the knobby morphology did not match and was offset in a step-like fashion, indicating a translation of the fracture plane. This supports the notion that the fracture surfaces may be sliding against each other post failure. This is to be expected for such a high-speed compression event.

Lastly, within the hourglass regions, regions with a high density of microvoid initiation sites are observed (Figure 5.16c). The voids are possible sources for crack initiation. Notably, the voids are small indicating limited deformation after their onset. It is likely that this is a preserved surface from the pre-fracture event as any sliding between surfaces would destroy the voids. A high void density would correlate accordingly with the plasticity curves, due to continuous work hardening until fracture. This indicates; as comparable to axisymmetric tension, that under axisymmetric compression, short range order effects play a larger role than under quasistatic stress-state. This leads to dislocation pileup and accumulation creating favourable conditions for void nucleation.

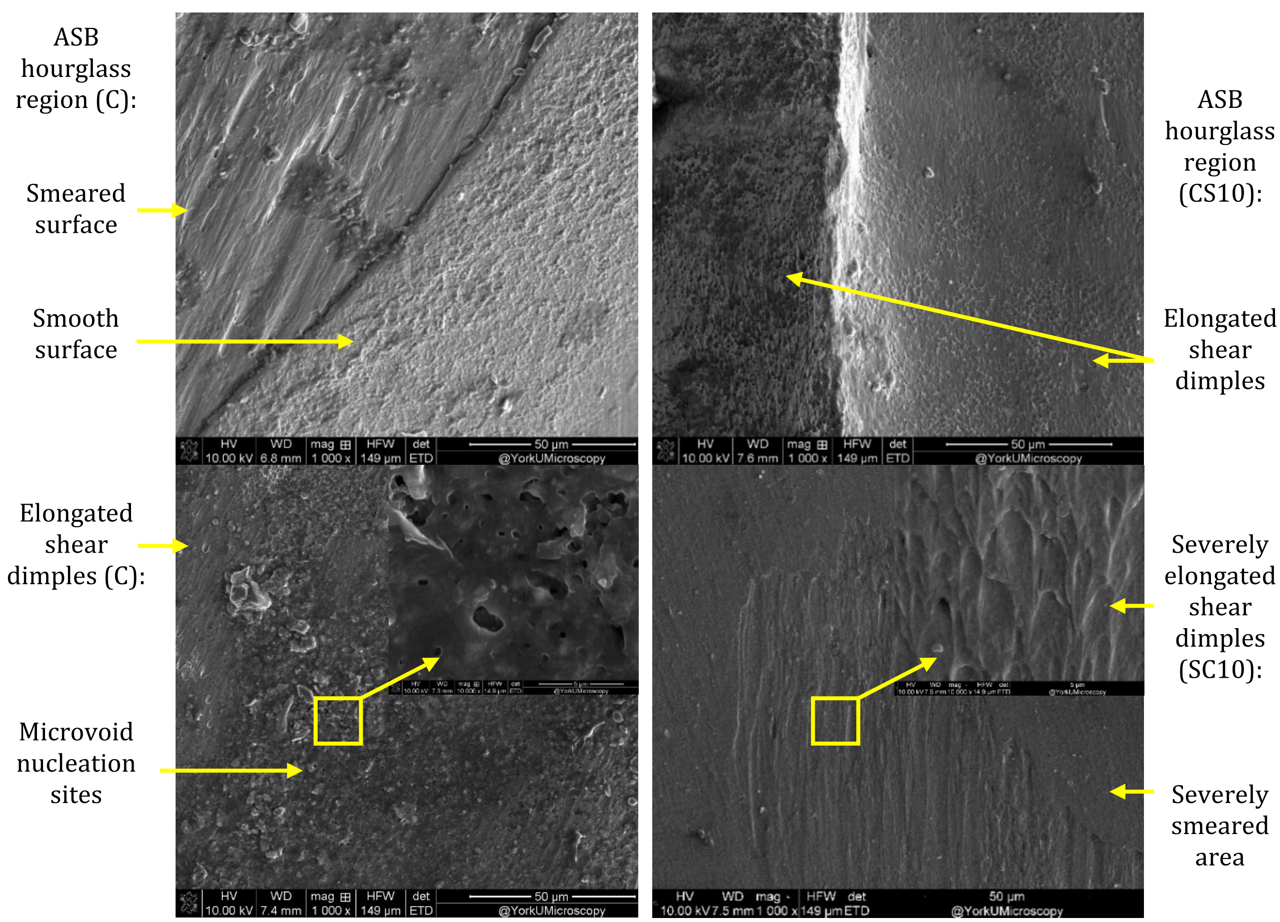

Figure 5.16: SEM micrographs of the fracture surfaces of adiabatic shear bands

5.6 Adiabatic Shear Band Instability

As described in section 3.3.2, 6 compression shear specimens have been impacted and the test interrupted at a pre-determined axial strain. These specimens are the ones used for post-mortem microstructural analysis and characterization. This is achieved using a forged Ti6Al4V stopper ring of a specific high tolerance length. This enables observation of the microstructural evolution at a constant impact momentum/strain-rate with increasing deformation and differentiates the effects of strain and strain-rate. As per chapter 3.4, the specimens' impacted surface is first viewed under the OM and if ASBs are found, characterized by Vickers microhardness testing. Then, they are prepared and viewed under the SEM. Then, selected specimens are prepared for TEM analysis as per 3.4.3, to reveal the underlying atomic scale deformation and failure mechanism of the ASB.

5.6.1 Microstructural Characterization

First and foremost, a practical 6 specimen test matrix is conducted (3 for each λ). The specimens are impacted, measured with calipers, ground and polished, etched, and viewed under the OM. Figure 5.17 reveals an ASB viewed under the OM in an CS10 specimen at 94% of its axial fracture strain. As expected, the ASB follows the curvature of the specimen at an offset location from the edge. Note that in uniaxial compression specimens, the ASB usually articulates on opposite sides of the specimen, thus increasing the total surface area of the ASB havening implications on plastic deformation energy absorbed by the ASB. In the compression-shear specimens, the ASB is only present on one side due to the imposed angle on the specimen. The ASB is clearly visible as the bright white streak following the curvature of the specimen. Also note that in the central left section (second image from the left), there is a secondary ASB with decreased brightness closer to the specimen edge. This secondary ASB indicates AX500 is very susceptible to ASB formation.

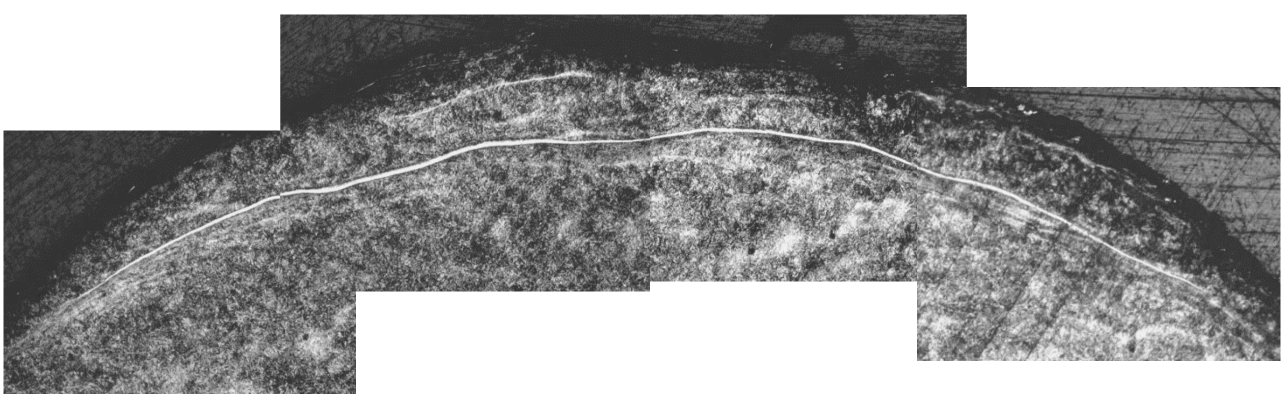

Figure 5.17: Adiabatic Shear Band in compression-shear specimen (light micrograph)

The microstructural evolution of the ASB under multiaxial compression-shear at an impact momentum of 23 kgm/s is revealed in Figure 5.18 to the right. This impact momentum results in a strain-rate of about 2600 /s. Each image is viewed using the 10x objective. Each image has an increasing axial strain, shown as a percentage of the axial fracture strain for that respective specimen in each image. Note that some specimens are CS6 and some are CS10 and it is assumed that based on applied energy, the evolution is assumed to be comparable indpendent of λ. This assumption does not indicate that the underlying deformation mechanism and severity of it is the same for different λ, but rather that with increasing applied energy, the microstructural evolution of the ASB is similar. Based on other tests at lower strain levels, it is observed that the ASB initiates somwehere in between 60% and 80% of the axial fracture strain. Notably, in the OM, the ASBs are sometimes refered to as 'white etching bands' since when chemically etched, the ASBs reveal themselves as white unresolvable streaks under the OM, due to the reflective nature of the refined grains within the ASB. In the first image at the top, a white etched streak is observed with a darkened streak running along the center. When zooming in with a higher objective (Figure 5.19b), it is observed that the darkened region consists of refined laths with decreased aspect ratio surrounded by a shaded region. This may indicate high dislocation activity and initial breakage of lath grains into smaller grains. In the second image, a specimen impacted at the same momentum and interrupted at the same % axial fracture strain, displays a different ASB, slightly more evolved (second image). This ASB materialises as a pure, thin white streak ($\sim 3\ \mu m$), significantly brighter than the white streak in the first

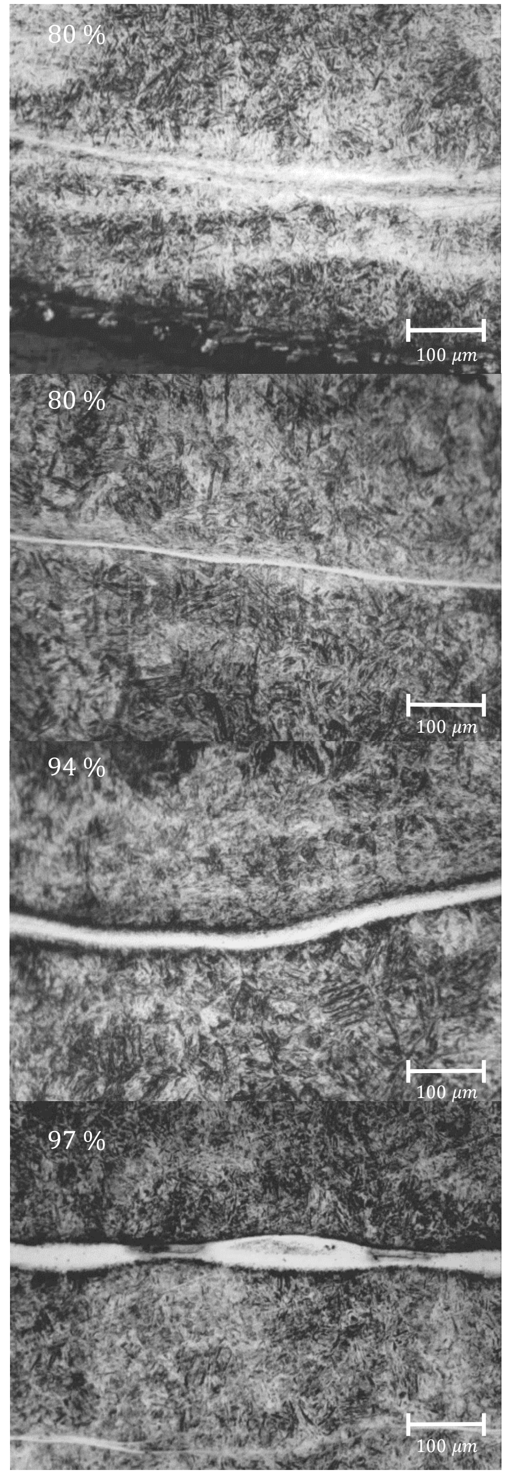

Figure 5.18: Microstructural evolution of adiabatic shear bands in inclined cylindrical compression-shear specimens with increasing strain level indicated by % fracture strain. All specimens were impacted at an impact momentum of 23 kgm/s resulting in an average strain rate of approximately 2600 /s.

image. This indicates that the grains are more refined having an effect in the reflectivity from the surface. It is much thinner than than the white streak in the first image, roughly about the thickness of the darkened streak. In the next image, at 94% of the fracture strain, it is observed that the ASB has grown in thickness ($\sim 10\ \mu m$) and maintains a similar white streak morhpology. Notably, there is a dark region surrounding both sides of the ASB, which is an accumulation of refined martensitic lath structures. In the last image just before fracture on a cracked specimen, the ASB is no longer a homogenous thickness. Rather, it displays thick ($\sim 40\ \mu m$) and thin ($\sim 15\ \mu m$) regions along its path, greater in thickness than the previous specimen. Furthermore, it is still surrounded by darkened refined laths, and cracks materialise at the thin regions and not at the thick regions. It can therefore be ascertained that in the region of greatest energy absorption (the center of the ASB), ASB formation begins with an accumulation of refined martensitic laths with decreased aspect ratio followed by rapid grain refinement. Then, the region of greatest energy absorbtion thickens and expands (essentially thickening the size of the ASB / shear plane), eventually reaching a saturation point such that the ASB (shear plane) locally thickens / expands in certain regions along its path, while materialising cracks in regions which were maintained thin and did not expand as much.

The specimen which deformed up to 94% of its axial fracture strain (named CS10-94) is placed under the SEM to take a closer look. Figure 5.19 presents SEM micrographs of the ASB, which is about 10 μm thick. It is evident in the micrographs that a lath size gradient exists as with refined lath grains in the transition between the matrix and the ASB. Eventually these laths transition into sub-micrometer refined equiaxed nanosized grains in the center. Figure 5.19b reveals with a high magnification (50x) that there are refined martensitic lath grains along the center of the ASB.

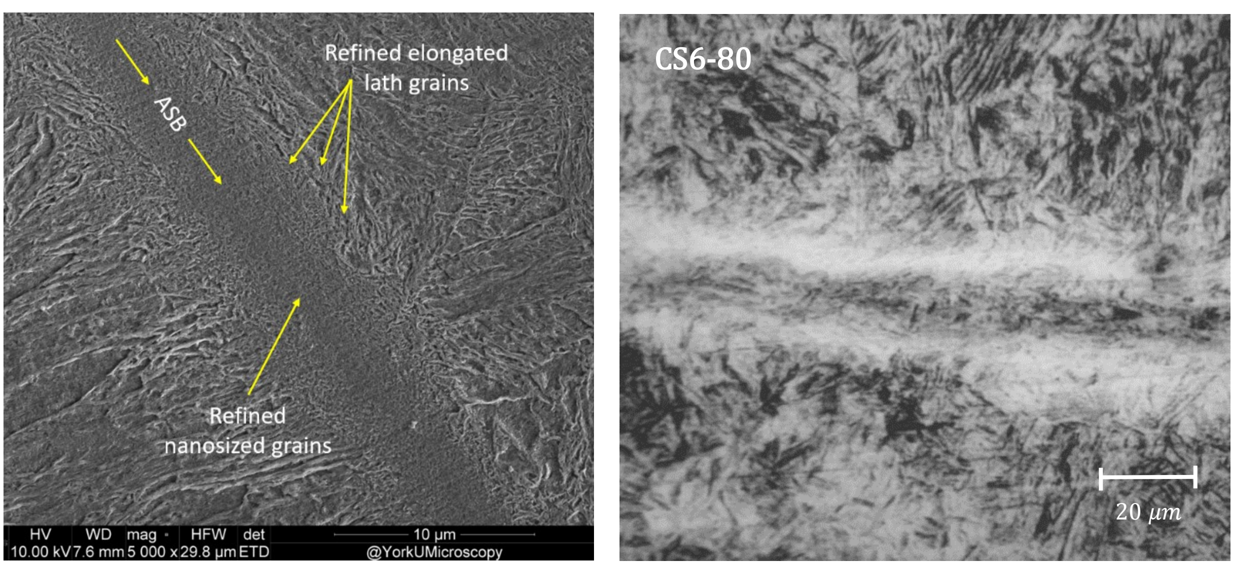

Figure 5.19: Nanosized grain refinement in CS10-94% deformed specimen (SEM micrographs)

The cracked specimen at 97% axial fracture strain (CS6-97) reveals multiple mechanisms materialising in AX500 under dynamic compression-shear. Figure 5.20 reveals microcracking in the the thin regions of the ASB (Figure 5.20a), secondary / tertiary ASBs with microcracking and bifurcation (Figure 5.20b), cracks running parallel along the ASB path (Figure 5.20c), and crack morhpology which is non-parallel to the ASB (Figure 5.20d). This reveals two primary observations:

1. AX500 is highly suceptible to ASB initiation and evolution, as ASBs materialise in regions close but not on the plane of maximum shear due to intense shear stresses.
2. Multiple deformation / energy absorbing mechanisms are present in the material giving rise to multidirectional cracking, ASB bifurcation, and crack bifurcation.

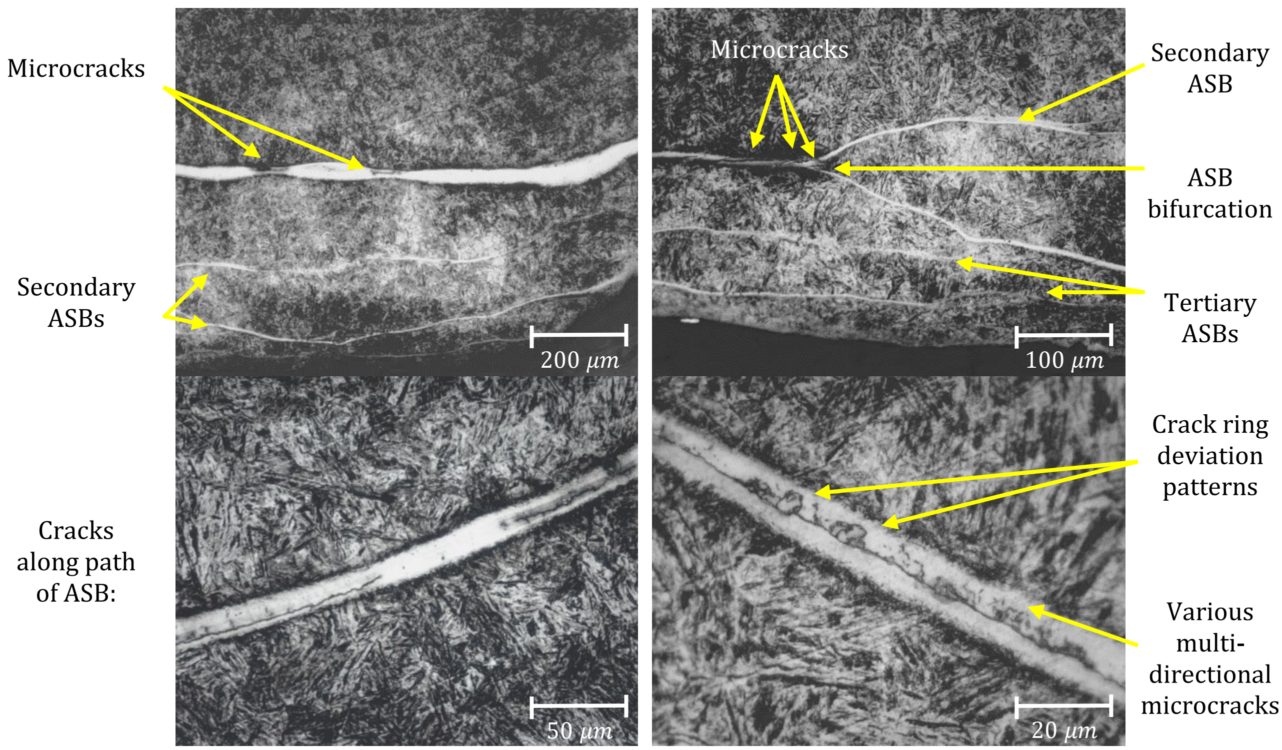

Figure 5.20: Specimen CS6-97 reveals crack initiation sites, secondary ASBs, bifurcation, and multi-directional cracking in the ASBs (light micrographs)

Taking a closer look at CS6-97 under the SEM, increasingly detailed observations can be made. Figure 5.21 reveals in greater resolution the crack morphology and vicinity. Where nescessary, the bounds of the ASB are indicated in orange dashed lines. It can be observed that on one side of the dashed lines; laths are prominent (matrix) and on the other side, it is mianly unresolvable (ASB-nanosized grains). Primarily, as per Figure 5.20c-d and Figure 5.21c, there is a dominating primary crack along most of the ASB path on the impacted surface. However, as per Figure 5.21a-b, there are certain regions where there is double parallel cracking along the ASB path, usually in regions with the highest damage to the point where the crack has opened sufficiently to peak inside the ASB.

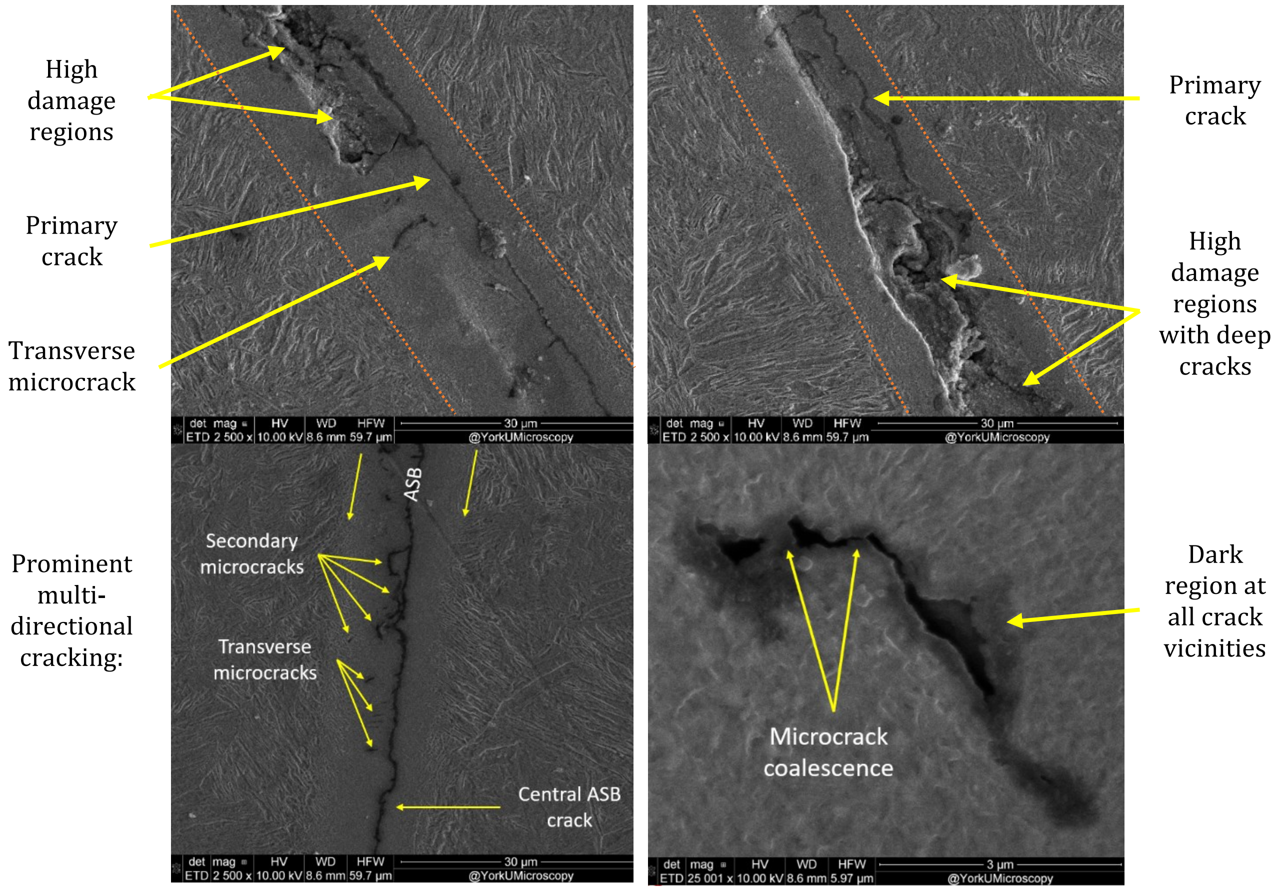

Figure 5.21: Severe damage, fragmentation, deep cracks, microcrack coalescence, and transverse and multi-directional cracking within the ASB in the CS6-97 specimen at fracture initiation

Notably, there are regions along the path of the ASB (Figure 5.21a, b) where the primary crack is not along the path of greatest energy absorption (the center of the ASB). This is also visible in Figure 5.20c. This observation suggests that there is a microstructural mechanism which redirects or deviates the crack from its idealized path, and the crack is able to find a new path along the ASB. Interestingly, as per Figure 5.21a and b, the most severely damaged dection with deep cracks and exposed nanograins is along the central region of the ASB, interconnected with the primary crack. Also of interest, is the onset of small secondary microcracks and transverse microcracks (Figure 5.21c). This indicates that there is a mechanism of energy absorption in AX500 that takes some energy away from primary crack propagation in the microstructural evolution and development of cracks which are not coplanar with the infenetismally thin plane of maximum shear. However, it also indicates that AX500 has various sources of crack initiation and is thus highly suceptible to adiabatic shear localization and crack initiation. Lastly, it is intriguing to note that there is a dark region of concealed nature around all crack vicinities (Figure 5.21d). This may be attributed to dislocation driven crack initiation, however admitabbly there is not enough evidence to conclude this and it remains conjecture.

Lastly, five specimens are tested using the Vickers microindenter. A deformed uniaxial specimen, and two of each of the CS6 and CS10 specimens (CS6-80, CS6-97, CS10-80, CS10-94). The results are summarized in Figure 5.22, illustrating evidence that the ASBs are hardened material. This would agree with the stress-strain curves of the uniaxial compression specimens, where ASBs are observed at strain levels along which work hardening is still increasing.

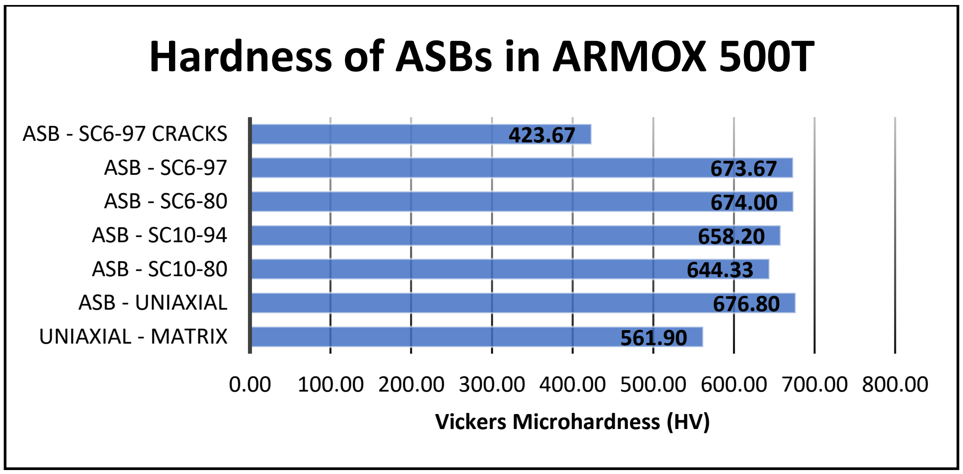

Figure 5.22: Microhardness of ASBs (HV)

5.6.2 Instability Criterion for GISSMO

Figure 5.23 illustrates the onset of initiation of ASBs in the same specimens already characterized in the above section. They are shown differently, to envisage how the ASB initiates as a function of increasing strain level defined in terms of the % axial fracture strain for each stress-state (λ).

To summarize, the % of the axial fracture strain can be correlated to the DIC and hardness data. Note that for all compression shear specimens, the average fracture strain of the three tests was used which has a standard deviation of less than 5 %. Any of the tests may be used to correlate given the reliability in results consistency. Table 5.5 summarizes the correlation of the observation ASB to the DIC and hardness data. Note that time and equivalent plastic strain are linearly interpolated based on the DIC data and actual axial strain of the stop ring experiment. The equivalent plastic strain at the onset of the ASB shall be defined as the instability strain in GISSMO. This provides an innovative microstructurally driven instability strain criteria for GISSMO at high strain rate to empirically characterize the effect of ASBs on material plasticity. In other words, a physics driven phenomenon is captured by a phenomenological calibration procedure to quantify the ASB instability.

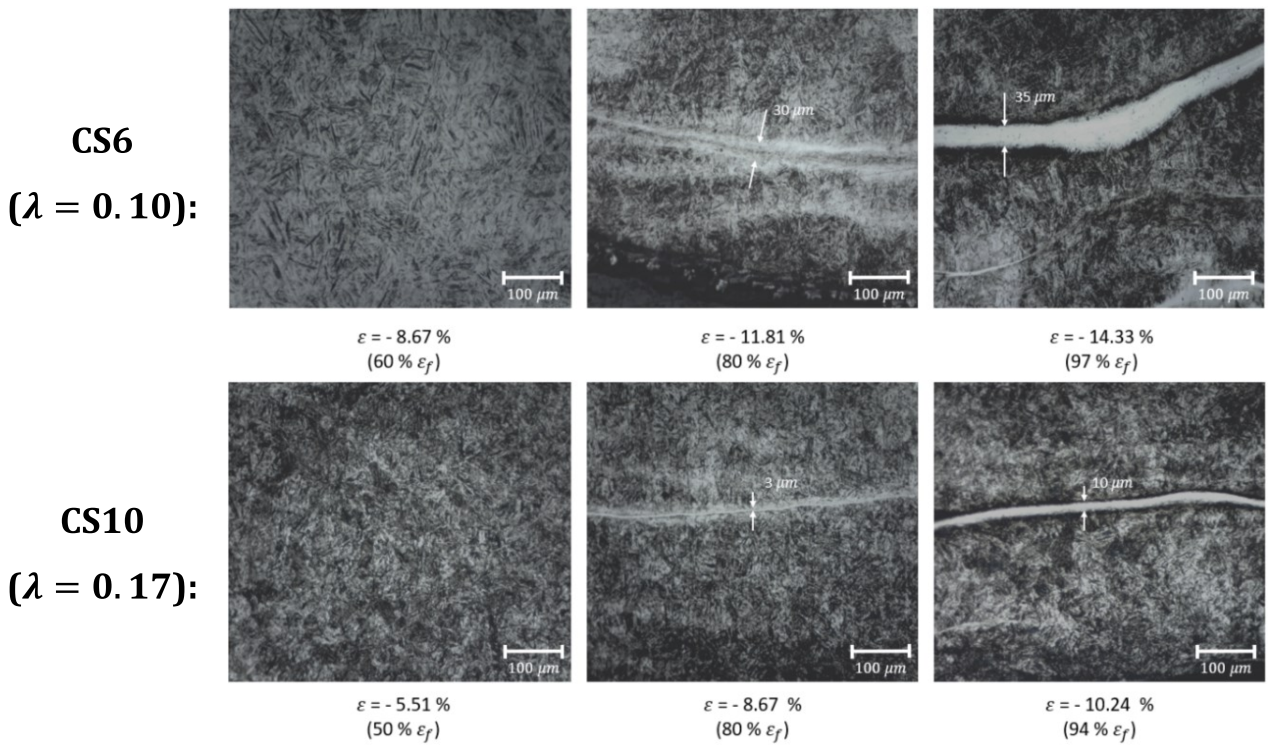

Figure 5.23: ASBs with increasing strain levels in compression-shear specimens.

Table 5.5: Correspondence of strain-path evolution with incremental elongation to ASBs.

Specimen	Axial Elongation (%)	% Fracture Strain	Time (us)	ASB Hardness (HV)	Equivalent Plastic Strain
Axisymmetric Compression - C $(\lambda = 0)$	20.20	66.28	180	-	0.206
	24.70	81.04	210	676	0.245
	26.99	88.56	230	677	0.268
Compression-Shear - CS6 $(\lambda = 0.10)$	8.98	60.35	71	-	0.102
	11.81	79.37	77	674	0.159
	14.33	96.31	89	674	0.198
Compression-Shear - CS10 $(\lambda = 0.17)$	7.56	69.00	50	-	0.085
	8.67	79.13	59	644	0.113
	10.24	93.46	67	658	0.151

5.6.3 Nanoscale Microstructural Evolution

Three compression-shear specimens with increasing % fracture strain at a constant impact momentum were selected for TEM observation. The specimens selected were CS10-80, CS10-94, and CS6-97, which in this section shall be referred to as A80, B94, and C97. They were selected according to their perceived stage of evolution in the OM, such that CS10-80 had an ASB which had just formed, CS10-94 had a very well evolved ASB significantly larger and 'whiter' than SC10-80, and an ASB with a crack along its center just before fracture. A total of 4 TEM specimens were created using FIB milling. One from each of the ASB regions for the three specimens, and one 75 μm away and parallel to the ASB in the specimen with the greatest % fracture strain, SC6-97. The specimen away from the ASB shall be referred to as C97-b. Figure 5.24 reveals the FIB process for the cracked SC6-97 specimen, where voids are observed. The tracked surface microcrack is also retained throughout the process, which illustrates the orientation of the specimen within the ASB and preservation of microstructural features.

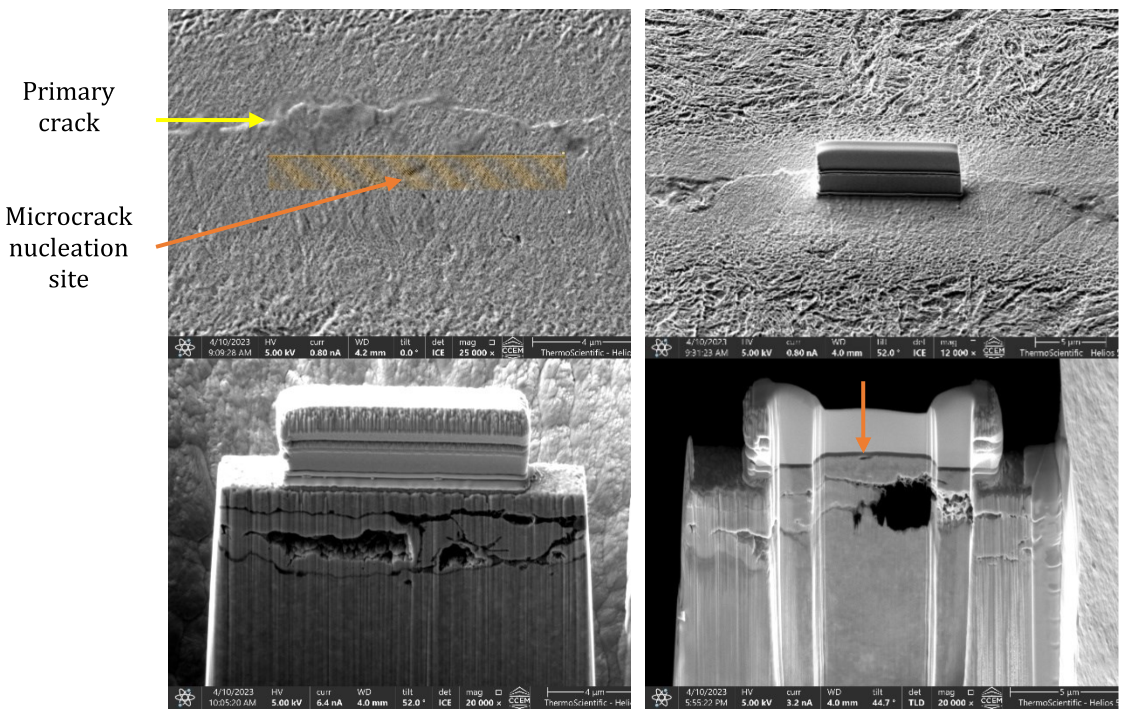

Figure 5.24: The FIB milling process for cracked specimen SC6-97 in crack vicinity

In Figure 5.25, a region within the ASB of specimen B94 is shown alongside a region away from the ASB of specimen C97-b. It is evident that the microstructure in each region has evolved differently after impact. The region away from the ASB reveals evidence of severe cold working deformation, however, microstructural features from section 4.1.2.3 of the as-received pre-impact sample are recognizable and retained. Carbides along the lath boundaries are observed, albeit slightly diffused.

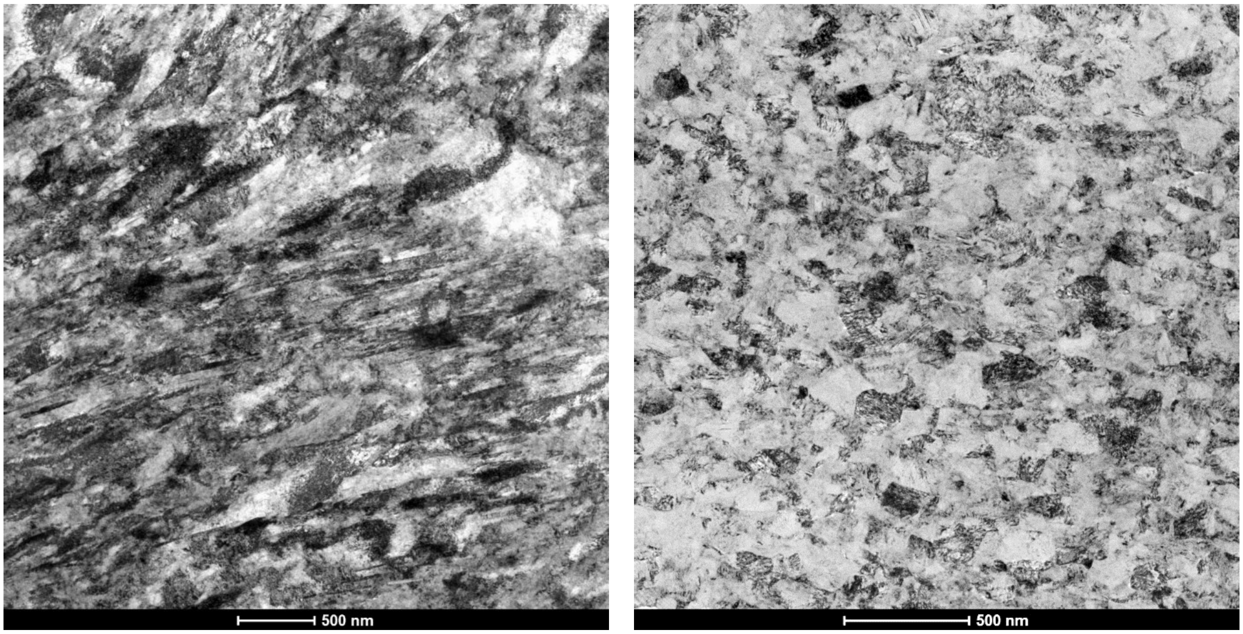

Figure 5.25a: Region away from ASB (C97-b) and 5.25b: Region within ASB (B94).

In addition, lath grains and even a martensite packet boundary can be identified albeit with elongated grains and clear evidence of plastic deformation with increased dislocation density and pileups observable. In the B94 specimen, severe nanosized grain refinement is observed indicating a severe microstructural evolution.

In Figure 5.26, the A80 specimen is shown at 80% fracture strain. As expected from the OM images, there is evidence of grain refinement with nanosized equiaxed grains revealed. In Figure 5.26a, it is well illustrated that the FIB process resulted in obtaining a specimen in which a part of the ASB (3 μm thick) is acquired, and when penetrating the bulk specimen further, a region outside of the ASB is captured as well, a dashed orange line indicates the transition. This occurs due to the ASB following the shear plane (45 degree to the impact direction) and the FIB extracts a specimen in the impact direction. Therefore a few μm below the surface, what is the ASB on the surface is no longer part of the ASB. This is further supported by SADP (indicated by green and blue dots in 5.26a) shown in Figure 5.26f, revealing that regions away from the ASB maintain their BCT lattice structure, while regions in the ASB evolve into nanosized grains with a high density distribution of atomic plane directions. In Figure 5.26b, lath grains are observed in a region away from the ASB. Dislocations are observed with a higher density in comparison to the pre-impact microstructure, and they are observed to transfer between lath grain boundaries in some regions. Figure 5.26c-d reveals dislocation structures in the regions away from the ASB, revealing their high mobility and activation during plastic deformation. Furthermore, in Figure 5.26e, transverse dislocation

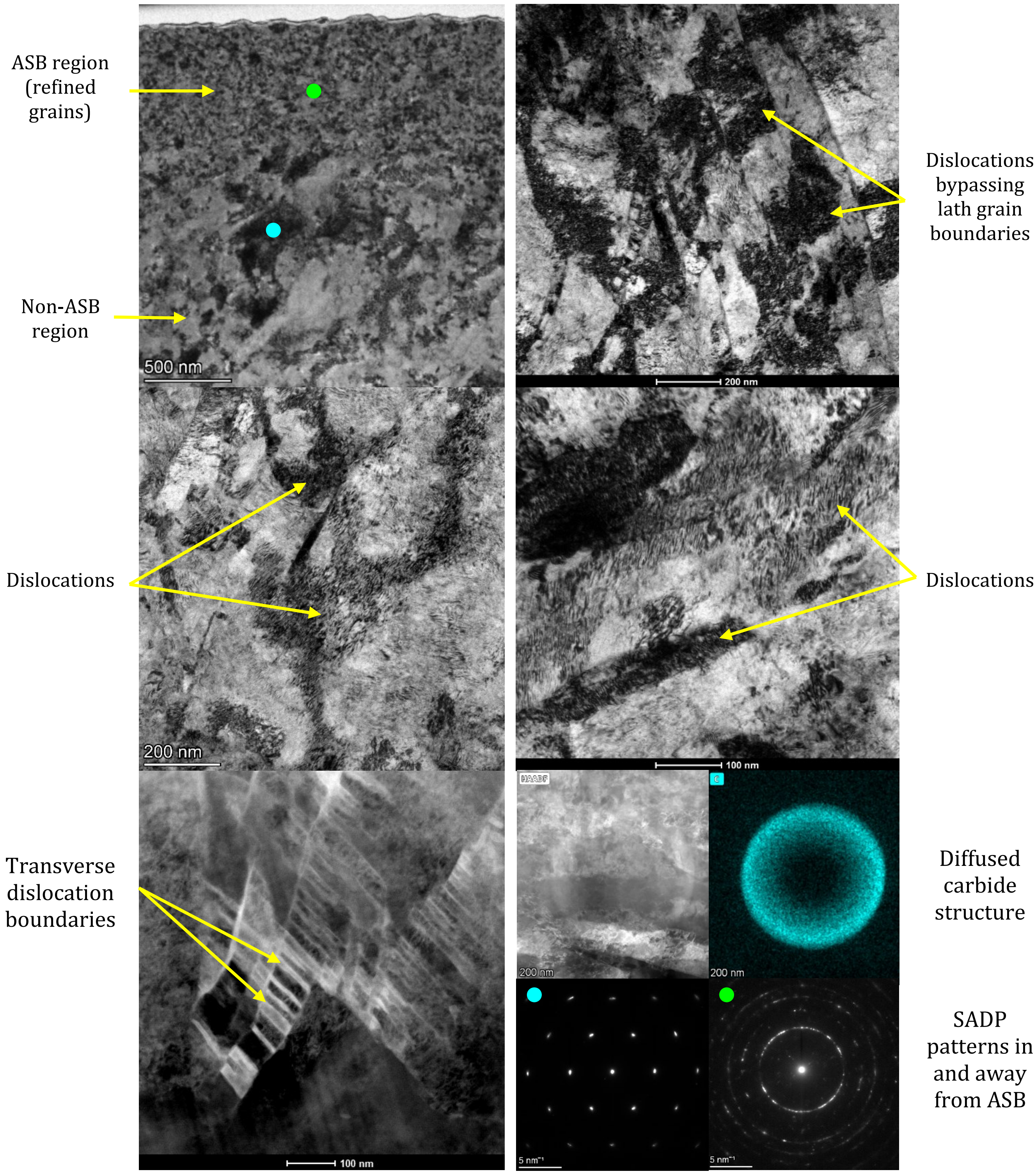

Figure 5.26a: TEM micrographs of the ASB in specimen A80 (CS10-80) at 80% fracture strain.

boundaries along lath grains are observed. This is a critical observation, as it is not seen in higher % fracture strain specimens, and therefore depicts a process which occurs in the early stages of ASB formation. Dislocations are piling up and forming boundaries across lath grains relative to the grain orientation. These boundaries are the sources for the development of new grain boundaries which create the refined equiaxed nanosized grains. Intriguingly, in Figure 5.26f, a spherical carbide is found identified by EELS, which is barely observable in bright field images and unobservable by dark field images. This region is void of iron, and consists of a carbide and silicon ring, with an unknown central composition. Presumably, the carbide is in the process of dissolution. Dislocation rich regions are observed predominantly throughout the structure sue to the onset and severe evolution of plastic deformation.

In Figure 5.27, the B94 and C97 specimens are shown at 94% and 97% fracture strain, respectively. Severe nano-twinning, grain refinement, and high dislocation density throughout the structure is prominent in the microstructure. There is not much difference between the two specimens, except that increasing density of twins were observed in the C97 specimens. The twinning scale is on the near atomic scale such that twins are only about 20 nm in length, and the individual atomic planes can be observed. The activation stress required for twinning is very high, and it is found that under the conditions of severe localized plastic shear deformation in ARMOX 500T, this stress is reached and triggers twinning, an energy absorbing mechanism. Twinning is evidence of a toughening mechanism for plastic deformation in ductile metals. Notably, this only occurs in some grains. This is indicative that under specific conditions, AX500 can absorb some of the impact energy into the creation of twins, which can be leveraged for ASB resistance as it takes away from energy used for crack initiation and growth.

Deformation nanotwins within the ASBs are presented in Figure 5.27a-d. This is indicative that with increased plastic deformation after the onset of the ASB, the ASB can incrementally absorb energy by the continuing creation of nano-twins. This is dependent on the stacking fault energy of AX500, which is favourable to create conditions for the onset of twins during extreme plastic shear stresses. In addition to twinning, Figure 5.27e-f reveals extensive misorientation between grains, and various dislocation free grains. Also revealed are sub-grain formations with comparable orientation within nano-grains, on the scale of < 100 nm. By pure conjecture only, it is conceivable that grain misorientation and dissociation as well as possible rotational dynamic recrystallization is occurring in the ASB, and that multiple concurring plastic deformation mechanisms occur in the ASB.

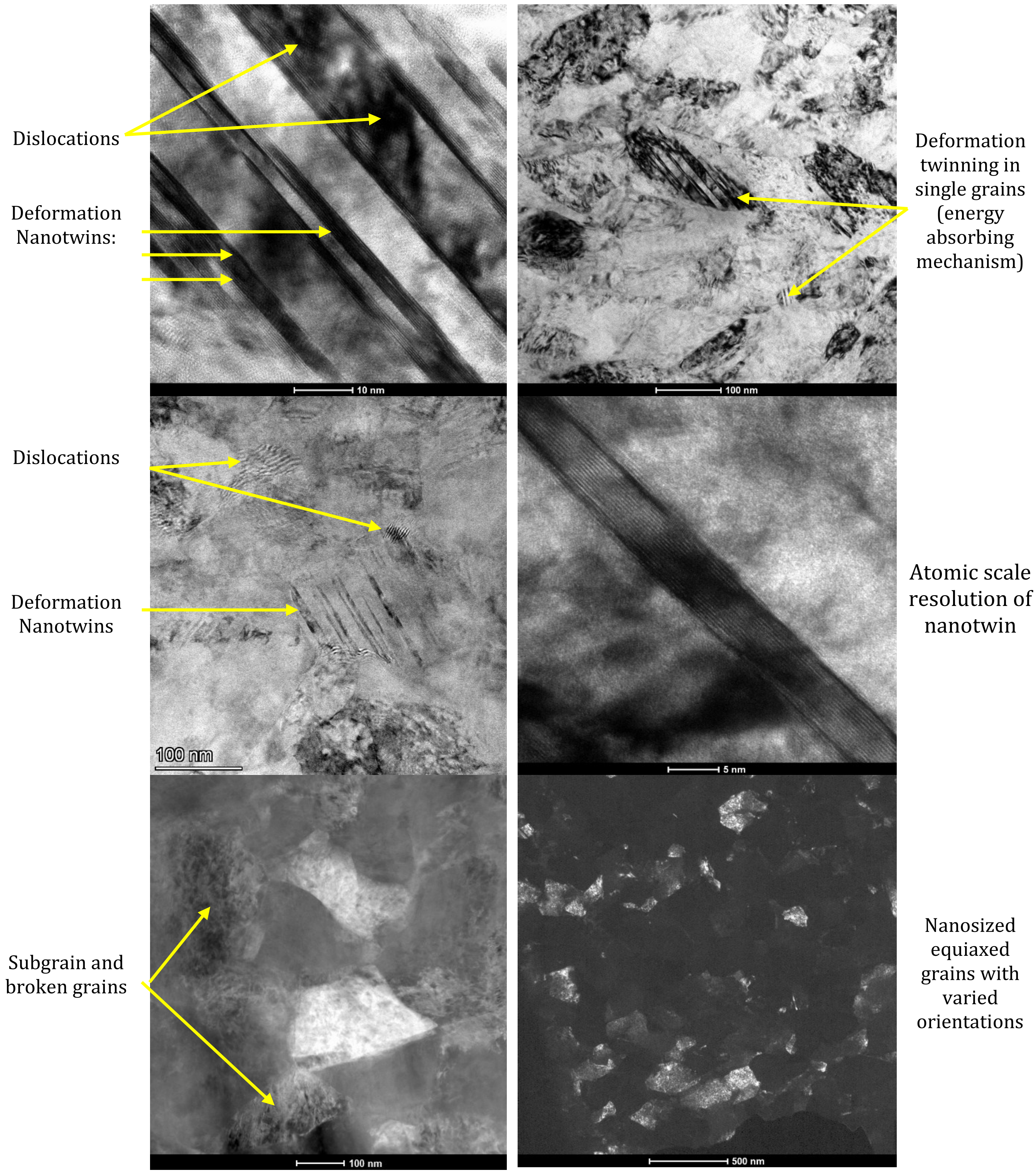

Figure 5.27: TEM micrograph ASB within specimen B94 (CS10-94)and C97 (CS6-97) at 94% and 97% fracture strain.

Without further quantitative image substantiation and processing, not much more can be concluded. However, it can be stated that there are various plastic deformation mechanisms such as nanoscale twinning, generation of transverse dislocation boundaries leading to creation of nanosized equiaxed grains, and nanosized grain structure evolution is occurring in AX500 after the onset of ASBs within the ASB, enabling the material to maintain its load bearing capacity after ASB initiation. However, severe strain localization in this region will occur ultimately leading to cracking and premature failure of the material.

5.7 Summary

In summary, there are significant strain-rate and stress-state effects on the plasticity and fracture behaviour of AX500. These effects have been quantified in terms of the degree of strengthening effect with increasing strain-rate for axisymmetric tension and compression and the equivalent plastic surface strain path evolutions for all stress-states at all strain-rates. These effects have underlying microstructural mechanisms which are responsible for the behaviour of the material, and that behaviour has been captured for dynamic tension, compression, and compression-shear.

Figure 5.28 illustrates the asymmetric plasticity behaviour of AX500 in axisymmetric tension and compression. The asymmetricity influences the plasticity parameters during parameterization of the GISSMO. Furthermore, the confidence in the material responses (continuous work hardening in compression, prolonged necking in tension after initial work hardening) is increased due to the discernment of the microstructural evolution which provides a reasonable explanation for the observed plasticity behaviour. The hardness of the ASBs, toughening mechanisms, and dislocation source activation and evolution within the ASBs explains the continuous work hardening under compression. Meanwhile, the high density of void initiation sites due to increased dislocation pileup is responsible for the initial high level of work hardening in tension, followed by prolonged necking due to large void growth and coalescence resulting in the high plastic flow capacity of AX500.

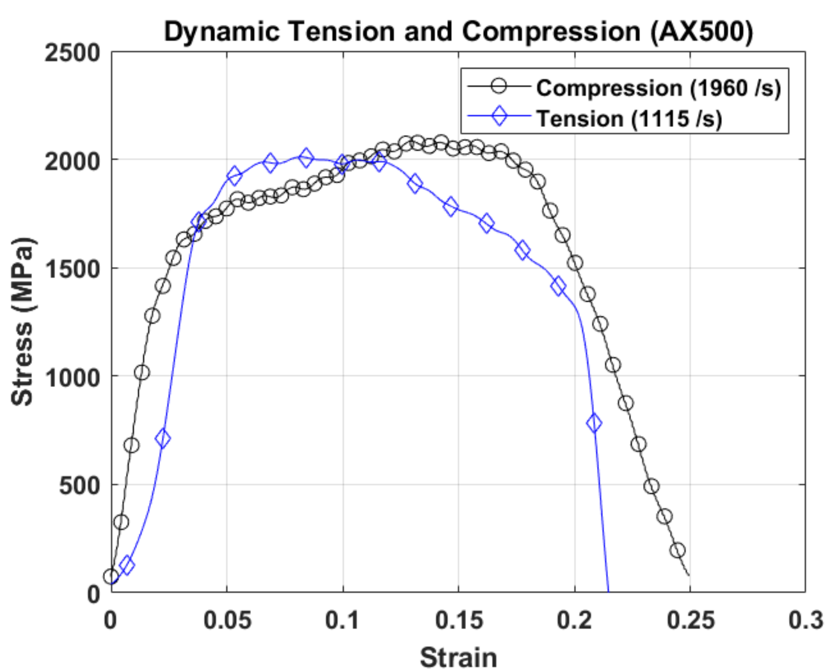

Figure 5.28: Asymmetricity of axisymmetric dynamic tension and compression

Furthermore, the effect of stress-state on ASBs in AX500 had been captured in an unprecedented manner. Using specimens with proven consistent stress-states until fracture, the effect of lode angle; defined by continuum mechanics and stress transformation formulations, on adiabatic shear band initiation and evolution is captured. It is found that with increasing lode angle by increasing the shear stress component, there is a severe loss of ductility due to enhanced strain localization along the plane of maximum shear which creates favourable conditions for the onset of adiabatic shear bands. Thus, increased susceptibility to ASB formation embrittles AX500. Simultaneously, the effect of strain-rate is captured in combination with the lode angle effect between quasistatic and high strain-rate material behaviour. Evidently, at some intermediate strain-rate there is an isothermal to adiabatic transition which leads to severe strain localization and changes the local microstructural deformation mechanism to nano-twinning and other mechanisms not materialised in quasistatic slip. This severely embrittles AX500 and decreases its global plasticity capacity due to severely enhanced localized strains on the shear plane resulting in ASB initiation. Both effects are summarized and captured in Figure 5.29.

Lastly, all quasistatic and dynamic values of equivalent plastic instability and plastic strain for GISSMO parameterization capturing strain-rate and stress-state effect have been quantified using DIC. Table 5.6 reports the average results for all tests for the final GISSMO parameterization values.

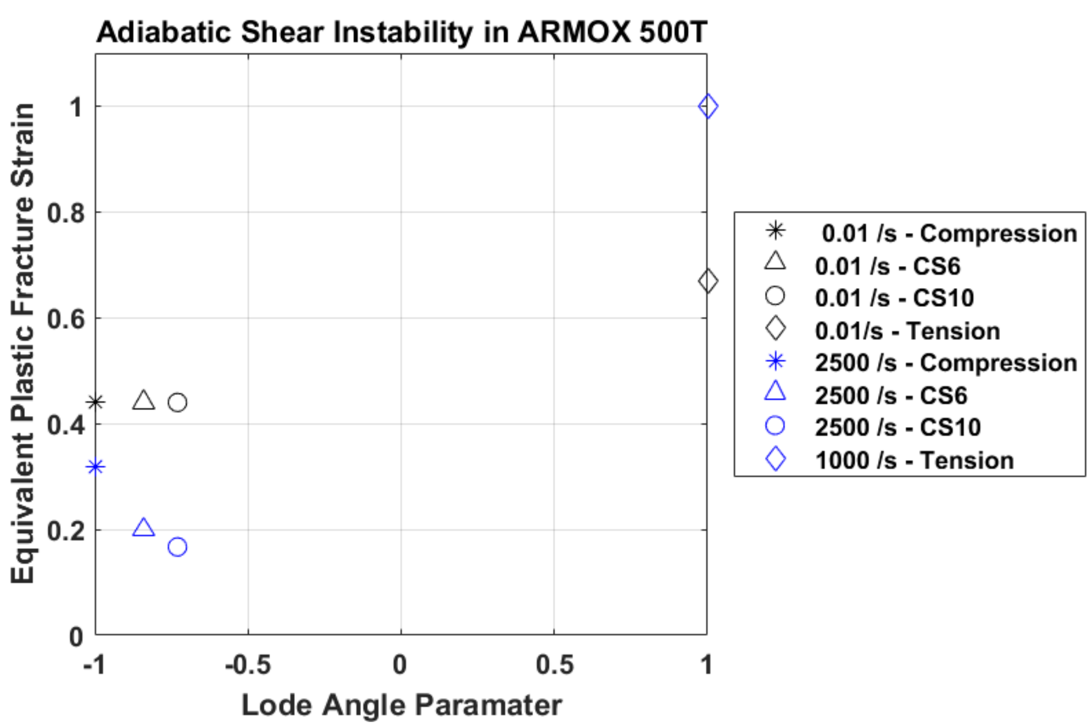

Figure 5.29: Effect of lode angle and strain-rate on equivalent plastic strain, revealing the ASB embrittlement phenomenon.

Table 5.6: Equivalent plastic instability and fracture strains for GISSMO for all tests

Stress State	Specimen	Strain-Rate (/s)	Initial Triaxiality (η)	Initial Lode Angle Parameter (ζ)	Equivalent Plastic Instability Strain (ε_{eq}^{i})	Equivalent Plastic Fracture Strain (ε_{eq}^{f})
Uniaxial Tension	Hole Tensile	0.01	1/3	1	**0.067**	**0.342**
	Flat Tensile (R6)	0.01	0.43	0.67	**0.068**	**0.304**
	Flat Tensile (R2)	0.01	0.52	0.31	**0.052**	**0.188**
Tensile Plane Strain	Grooved flat plate	0.01	0.58	0	**0.041**	**0.067**
	Grooved flat plate (R8)	0.01	0.65	0	**0.034**	**0.044**
	Grooved flat plate (R4)	0.01	0.71	0	**0.023**	**0.023**
	Grooved flat plate (R2)	0.01	0.84	0	**0.009**	**0.010**
Axisymmetric Tension	Round Tensile	0.01	1/3	1	**0.068**	**0.672**
		700	1/3	1	**0.176**	**0.839**
		800	1/3	1	**0.184**	**0.921**
		950	1/3	1	**0.130**	**0.961**
		1100	1/3	1	**0.099**	**1.009**
	Round Tensile (R12)	0.01	0.45	1	**0.070**	**0.336**
	Round Tensile (R6)	0.01	0.56	1	**0.072**	**0.255**
	Round Tensile (R3)	0.01	0.74	1	**0.093**	**0.215**
Axisymmetric Compression	Compression L/D = 1.1	0.01	- 1/3	-1	**0.153**	**0.386**
		2200	- 1/3	-1	**0.245**	**0.319**
		2500	- 1/3	-1	**0.245**	**0.319**
		2700	- 1/3	-1	**0.245**	**0.319**
		3000	- 1/3	-1	**0.245**	**0.319**
	Shear Compression 6	0.01	- 2/7	-0.84	**0.201**	**0.381**
		2500	- 2/7	-0.84	**0.144**	**0.213**
	Shear Compression 10	0.01	- 1/4	-0.73	**0.339**	**0.396**
		2500	- 1/4	-0.73	**0.113**	**0.155**
Pure Shear	Shear (Angle=0)	0.01	0	0	**0.928**	**1.067**
Shear-Tension	Shear (Angle=10)	0.01	[0, 1/3]	[0, 1]	**0.469**	**0.717**
	Shear (Angle=30)	0.01	[0, 1/3]	[0, 1]	**0.181**	**0.305**

6.0 Conclusions and Future Work

Conclusions

Conclusively, throughout this thesis, all experimental and material property data produced shall be used for parametrization of an empirical GISSMO, to be implemented into terminal ballistics simulations for simulation driven design of medium caliber armour systems. Test matrices were designed carefully to isolate the effects of triaxiality, lode angle, and strain-rate. In addition, quantitative metallographic characterization of the microstructural evolution and failure mechanisms enable a quantitative reference for future possible multiscale modeling. The following facts about AX500 are experimentally quantified with unprecedented evidence:

1. The plastic strain ratio (R-value) under plane stress flat tension and as-received Vickers microhardness testing quantifies rolling texture.
2. On the macroscale, the differentiated effects of triaxiality, lode angle, and strain-rate on material properties are quantified by the equivalent plastic instability and fracture strains.
    a. Effect of lode angle on stress and ductility, quantifying a severe loss of ductility of one order of magnitude from round tension (LAP of 1) to plane strain to (LAP of 0).
    b. Effect of triaxiality on plane stress, shear, round tension, and plane strain stress-states, quantifying a progressive ductility loss under all stress-states with increasing triaxiality. This provides constitutive material property data for subsequent development of a fracture surface for GISSMO parameterization.
    c. Effect of strain-rate on round tension (LAP=1). There is greater damage tolerance due to enhanced work hardening and plastic flow with increasing strain-rate.
    d. Effect of strain-rate on the plastic deformation capacity in negative lode angles. High plasticity in quasistatic loading, severe embrittlement at high strain-rate.
    e. Effect of lode angle on stress and ductility in negative lode angles at quasistatic and dynamic strain-rates. Increased lode angle embrittles AX500.
3. On a multiscale perspective, underlying microstructural deformation and failure mechanisms are discerned to provide supporting evidence and confidence in the results of macroscale behaviour.
    a. Under axisymmetric tension (LAP=1), increasing strain rate enhances short-range order effects in the microstructure, increasing the density of void initiation sites due to increased dislocation pileup. This results in increased initial work hardening and greater ultimate flow stress with increasing strain-rate. In addition, enhanced void

growth occurs resulting in enhanced plastic flow with increasing strain-rate ultimately enhancing the damage tolerance of AX500 in dynamic tension.

b. High plastic deformation capacity under slip deformation mechanism in negative lode angles of compression-shear and compression stress-states in quasistatic loading. With increasing strain-rate, due to an isothermal to adiabatic transition of localized deformation along the shear plane, adiabatic shear bands severely affect the plasticity capacity of AX500. Enhanced strain localization occurs with increasing strain-rate, leading to severe localized dislocation source activation and density, severe grain refinement, and high localized hardness regions creating dislocation driven crack initiation sites, crack propagation, and subsequent fracture of the material. The fracture is highly ductile due to the high local shear strains, however ultimately embrittles the global plastic deformation capacity of the material due to the ASB instability.

c. Effect of stress-state on ASB initiation. Increased LAP from -1 towards 0 quantified by an increasing shear/compression load ratio (λ), results in enhanced strain localization along the plane of maximum shear due to the greater shear stress component. This creates favourable conditions for dislocation source activation and ASB initiation leading to premature crack initiation and consequential embrittlement of the material.

d. Ultimately, at high strain-rate, AX500 has high damage tolerance under mode I tensile fracture. With decreasing lode angle, mode II fracture begins to dominate which heavily embrittles AX500 especially for all negative lode angles up to 0.

Recommended Future Work

TSHB:

- Support the incident bar with wear-resistant plastic liner ~ may minimize wave dispersion due to the poisson ratio and mitigate vibrations with increased support.
- Implement a more adequate momentum trap and flange with impedance matched design. Rather than using a flange mounted linear ball bearing, a sleeve bearing such as Oilite copper bearings may reduce noise, less energy loss, and provide an overall cleaner loading.
- Larger bore size and stroke for pneumatic cylinder would enable greater momentum at lower pressures, ultimately increasing the strain-rate range of the machine.
- Addition of some Loctite grease on the specimen-bar thread interface. This will increase contact area between the threads promoting wave propagation and reduce load rise time.

Testing (all points are believed by the author to enable more accurate modeling):

- Conduct 5 repeated tests to increase statistical significance.
- Add torsion and biaxial punch at high strain rates to have a 4 stress-state HSR calibration for strengthening data.
- Perform quasistatic torsion testing and compare to pure shear specimen and use as a reference for high strain-rate torsion.
- Add intermediate strain-rates with high-speed load frames and drop towers. Ignoring this regime may not capture certain phenomena such as ductility increases or losses. The isothermal to adiabatic transition critical strain-rate can also be captured.
- Add Taylor tests for even higher strain rates (10^4-10^5 /s) expected in localized zones for KEP impacts which occur at 500-2000 m/s.
- Investigate the compression-shear specimen behavior at relatively low (~1000 /s) and high (up to 10,000 /s) strain rates to identify possible strain-rate effects on ASB initiation.
- Perform high speed thermal camera tests on dynamic tension and torsion specimens. To quantify the degree of plastic work to heat to identify the TQ coefficient (tension and torsion) and measure the in-situ ASB temperature on torsion specimens.
- Depending on the target application, reduce quasistatic testing to axisymmetric tension/compression, torsion, plane strain and notched plane strain, notched round tension & biaxial (no plane stress testing).
- Perform flat top hat specimen testing with 3 different angles. Ranging from compression-shear to pure plane strain shear, to tension shear. All specimens are along the LAP=0 curve. It would be interesting to note if in quasistatic loading, there is some correlation with the shear and shear-tension specimen on model calibration. If so, it would be prudent to attempt the high strain rate characterization effect on ASBs.

Materials:

- Characterize the effect of heat treatment on the high stain rate behavior of AX500. Higher tempering temperature or over tempering may effectively increase the ASB resistance of AX500 due to larger carbide morphology and increased toughness. However, it may adversely affect the high damage tolerance under dynamic tension.
- Characterize different promising armour materials such as other martensitic steels, nitrogen steels, multi-phase and metastable steels, bainitic steels, and high entropy alloys.

References

[1] Strong Secure Engaged : Canada's Defence Policy.

[2] Vuong and Jennifer, "Security and disruptive technologies Security Materials Technologies Roadmap Synthesis Report prepared by the Security Materials Technologies Industry Steering Committee, National Research Council of Canada Security Materials Technologies Program, and Defence Research and Development Canada."

[3] 'Number of disclosed main battle tanks committed to Ukraine as of May 2023, by type and donor country'. Published by Statista Research Department, Aug 8, 2023. https://www.statista.com/statistics/1364974/ukraine-military-aid-tanks/

[4] S. Cimpoeru et al., The Science of Armour Materials. Woodhead Publishing, 2016.

[5] H. Couque, "The use of the direct impact Hopkinson pressure bar technique to describe thermally activated and viscous regimes of metallic materials," Philosophical Transactions of the Royal Society A: Mathematical, Physical and Engineering Sciences, vol. 372, no. 2023, Aug. 2014, doi: 10.1098/rsta.2013.0218.

[6] B. M. Mcdonald, "Characterising Material Effects in Blast Protection," 2019.

[7] C. J. Hu, P. Y. Lee, and J. S. Chen, "Ballistic performance and microstructure of modified rolled homogeneous armor steel," Journal of the Chinese Institute of Engineers, Transactions of the Chinese Institute of Engineers, Series A/Chung-kuo Kung Ch'eng Hsuch K'an, vol. 25, no. 1, pp. 99–107, 2002, doi: 10.1080/02533839.2002.9670684.

[8] A. A. Tiamiyu and C. A. Schuh, "Particle flattening during cold spray: Mechanistic regimes revealed by single particle impact tests," Surf Coat Technol, vol. 403, Dec. 2020, doi: 10.1016/j.surfcoat.2020.126386.

[9] Y. song Guo, P. wan Chen, A. Arab, Q. Zhou, and Y. Mahmood, "High strain rate deformation of explosion-welded Ti6Al4V/pure titanium," Defence Technology, vol. 16, no. 3, pp. 678–688, Jun. 2020, doi: 10.1016/j.dt.2019.10.002.

[10] J.-F. Croteau, E. Cantergiani, N. Jacques, A. E. M. Malki, G. Mazars, and G. Avrillaud, "Mechanical characterization of OFE-Cu at low and high strain rates for SRF cavity fabrication by electro-hydraulic forming."

[11] H. R. Z. Rajani and S. A. A. A. Mousavi, "On critical criteria for shifting towards plastic strain localization during explosive cladding of Inconel 625 on low-carbon steel," Combust Explos Shock Waves, vol. 49, no. 2, pp. 244–253, 2013, doi: 10.1134/S0010508213020172.

[12] K. Roll, A. Haufe, F. Neukamm, M. Feucht, A. Haufe, and K. Roll, "On closing the Constitutive Gap between Forming and Crash Simulation Enhanced Formability Assessment of AHSS Sheets View project On closing the Constitutive Gap between Forming and Crash Simulation," 2008. [Online]. Available: https://www.researchgate.net/publication/312039751

[13] F. Kerstens, A. Cervone, and P. Gradl, "End to end process evaluation for additively manufactured liquid rocket engine thrust chambers," Acta Astronaut, vol. 182, pp. 454–465, May 2021, doi: 10.1016/j.actaastro.2021.02.034.

[14] P. R. Gradl, T. Teasley, C. Protz, M. Garcia, C. Kantzos, and D. Ellis, "Advancing GRCop-based Bimetallic Additive Manufacturing to Optimize Component Design and Applications for Liquid Rocket Engines," in AIAA Propulsion and Energy Forum, 2021, 2021. doi: 10.2514/6.2021-3231.

[15] E. G. Smith and V. D. Linse, "DEVELOPMENT OF EXPLOSIVE-WELDING TECHNIQUES FOR FABRICATION OF REGENERATIVELY COOLED THRUST CHAMBERS FOR LARGE-ROCKET-ENGINE REQUIREMENTS."

[16] E. Cantergiani et al., "Niobium superconducting rf cavity fabrication by electrohydraulic forming," Physical Review Accelerators and Beams, vol. 19, no. 11, 2016, doi: 10.1103/PhysRevAccelBeams.19.114703.

[17] L. L. Amador et al., "Electrodeposition of copper applied to the manufacture of seamless superconducting rf cavities," Physical Review Accelerators and Beams, vol. 24, no. 8, Aug. 2021, doi: 10.1103/PhysRevAccelBeams.24.082002.

[18] F. Neukamm, M. Feucht, D. Ag, and S. A. Haufe, "Forming and Crash Induced Damage Evolution and Failure Prediction Part 2: A comparison of damage models," 2007.

[19] L. ten Kortenaar, "Failure Characterization of Hot Formed Boron Steels with Tailored Mechanical Properties," 2016.

[20] R. Östlund, Microstructure based modelling of ductile fracture in quench-hardenable boron steel. 2015.

[21] A. Naji, "Parametric Analysis of a Turbofan Engine with Intercooling and Heat Recuperation," 2017, doi: 10.13140/RG.2.2.30792.21769.

[22] B. Blakey-Milner et al., "Metal additive manufacturing in aerospace: A review," Mater Des, vol. 209, Nov. 2021, doi: 10.1016/j.matdes.2021.110008.

[23] S. Hennig, I. Armin Huß, H. Honermeier, M. Jagic, and M. Schönborn, "Simulation of containment-tests at a generic model of a large-scale turbocharger with LS-DYNA."

[24] J. Liu, Y. Li, X. Gao, and X. Yu, "A numerical model for bird strike on sidewall structure of an aircraft nose," Chinese Journal of Aeronautics, vol. 27, no. 3, pp. 542–549, 2014, doi: 10.1016/j.cja.2014.04.019.

[25] T. Smith, "Producing Next Generation Superalloys Through Advanced Characterization and Manufacturing Techniques." [Online]. Available: www.nasa.gov

[26] D. O. Svensson, "High Entropy Alloys: Breakthrough Materials for Aero Engine Applications? Diploma work in the Master programme Applied Physics."

[27] S. Gorsse, J. P. Couzinié, and D. B. Miracle, "From high-entropy alloys to complex concentrated alloys," Comptes Rendus Physique, vol. 19, no. 8. Elsevier Masson SAS, pp. 721–736, Dec. 01, 2018. doi: 10.1016/j.crhy.2018.09.004.

[28] M. Dada, P. Popoola, S. Adeosun, and N. Mathe, "High Entropy Alloys for Aerospace Applications." [Online]. Available: www.intechopen.com

[29] "High Entropy Alloys: Development and Applications," Nov. 2015. doi: 10.15242/iie.e1115005.

[30] C. C. Juan et al., “Enhanced mechanical properties of HfMoTaTiZr and HfMoNbTaTiZr refractory high-entropy alloys,” Intermetallics (Barking), vol. 62, pp. 76–83, Jul. 2015, doi: 10.1016/j.intermet.2015.03.013.

[31] J. Macfarlane, I. Waugh, E. Moore, A. Greig, and W. Dick-Cleland, “Additive manufacture of rocket engine combustion chambers using the ABD®-900AM nickel superalloy ADDITIVE MANUFACTURE OF ROCKET ENGINE COMBUSTION CHAMBERS USING THE ABD R-900AM NICKEL SUPERALLOY.” [Online]. Available: https://www.researchgate.net/publication/350278621

[32] C. Katsarelis et al., “Additive Manufacturing of NASA HR-1 Material for Liquid Rocket Engine Component Applications.”

[33] S. Pourbabak, M. L. Montero-Sistiaga, D. Schryvers, J. van Humbeeck, and K. Vanmeensel, “Microscopic investigation of as built and hot isostatic pressed Hastelloy X processed by Selective Laser Melting,” Mater Charact, vol. 153, pp. 366–371, Jul. 2019, doi: 10.1016/j.matchar.2019.05.024.

[34] W. P. Schonberg, “Studies of hypervelocity impact phenomena as applied to the protection of spacecraft operating in the MMOD environment,” in Procedia Engineering, 2017, vol. 204, pp. 4–42. doi: 10.1016/j.proeng.2017.09.723.

[35] G. T. Gray, “Material response to shock/dynamic loading: Windows into kinetic and stress-state effects on defect generation and damage evolution,” in AIP Conference Proceedings, 2012, vol. 1426, pp. 19–26. doi: 10.1063/1.3686214.

[36] K. Wen, X. wei Chen, and Y. gang Lu, “Research and development on hypervelocity impact protection using Whipple shield: An overview,” Defence Technology, vol. 17, no. 6. China Ordnance Industry Corporation, pp. 1864–1886, Dec. 01, 2021. doi: 10.1016/j.dt.2020.11.005.

[37] P. Labbé, A. Ghanmi, and M. Abdelazez, “Defence Research and Development Canada Scientific Report Current and future hypersonic threats, scenarios and defence technologies for the security of Canada,” 2022.

[38] “Orbital Debris Management & Risk Mitigation.” [Online]. Available: www.nasa.gov

[39] “Penetration of targets by long rod-AD0595793”.

[40] L. W. Meyer, E. Staskewitsch, and A. Burblies, “Adiabatic shear failure under biaxial dynamic compression/shear loading,” 1994.

[41] S. Zhu, Y. Guo, H. Chen, Y. Li, and D. Fang, “Formation of adiabatic shear band within Ti–6Al–4V: Effects of stress state,” Mechanics of Materials, vol. 137, Oct. 2019, doi: 10.1016/j.mechmat.2019.103102.

[42] S. Boakye-Yiadom, “MICROSTRUCTURAL EVOLUTION OF ADIABATIC SHEAR BANDS IN STEEL BY IMPACT,” 2014.

[43] F. et al. Wang, “‘Localized plasticity in silicon carbide ceramics induced by laser shock processing.’ ,” Materialia 6 (2019): 100265..

[44] S. J. Cimpoeru, “The Mechanical Metallurgy of Armour Steels.”

[45] I. Barényi, O. Híreš, and P. Lipták, “Changes in Mechanical Properties of Armoured UHSLA Steel ARMOX 500 After Over Tempering *.”

[46] S. Boakye Yiadom, A. Khaliq Khan, and N. Bassim, “Effect of microstructure on the nucleation and initiation of adiabatic shear bands (ASBs) during impact,” Materials Science and Engineering A, vol. 615, pp. 373–394, Oct. 2014, doi: 10.1016/j.msea.2014.07.095.

[47] M. C. Jo et al., “Role of retained austenite on adiabatic shear band formation during high strain rate loading in high-strength bainitic steels,” Materials Science and Engineering: A, vol. 778, p. 139118, Mar. 2020, doi: 10.1016/J.MSEA.2020.139118.

[48] W. Burian and J. Janiszewski, “Static, dynamic and ballistic properties of bainite-austenite steel for armours.” [Online]. Available: https://www.researchgate.net/publication/269398082

[49] “bainite at a low temperature in a steel designed for a specif-ic structural application. 12) 2. Experimental Techniques,” 2003.

[50] T. Lolla, G. Cola, B. Narayanan, B. Alexandrov, and S. S. Babu, “Development of rapid heating and cooling (flash processing) process to produce advanced high strength steel microstructures,” Materials Science and Technology, vol. 27, no. 5, pp. 863–875, May 2011, doi: 10.1179/174328409X433813.

[51] H. K. D. H. Bhadeshia, “Preface: Adventures in the physical metallurgy of steels,” Materials Science and Technology (United Kingdom), vol. 30, no. 9. Maney Publishing, pp. 995–997, 2014. doi: 10.1179/0267083614Z.0000000724.

[52] M. C. Jo et al., “Enhancement of ballistic performance enabled by transformation-induced plasticity in high-strength bainitic steel,” J Mater Sci Technol, vol. 84, pp. 219–229, Sep. 2021, doi: 10.1016/J.JMST.2020.12.059.

[53] M. Nilsson, “Weapons and Protection SE-147 25 Tumba Constitutive Model for Armox 500T and Armox 600T at Low and Medium Strain Rates,” 2003.

[54] A. Popławski, P. Kędzierski, and A. Morka, “Identification of Armox 500T steel failure properties in the modeling of perforation problems,” Mater Des, vol. 190, May 2020, doi: 10.1016/j.matdes.2020.108536.

[55] M. A. Iqbal, K. Senthil, P. Sharma, and N. K. Gupta, “An investigation of the constitutive behavior of Armox 500T steel and armor piercing incendiary projectile material,” Int J Impact Eng, vol. 96, pp. 146–164, Oct. 2016, doi: 10.1016/j.ijimpeng.2016.05.017.

[56] M. Saleh, M. M. Kariem, V. Luzin, K. Toppler, H. Li, and D. Ruan, “High strain rate deformation of ARMOX 500T and effects on texture development using neutron diffraction techniques and SHPB testing,” Materials Science and Engineering A, vol. 709, pp. 30–39, Jan. 2018, doi: 10.1016/j.msea.2017.09.022.

[57] A. Saxena, A. Kumaraswamy, N. Kotkunde, and K. Suresh, “Constitutive Modeling of High-Temperature Flow Stress of Armor Steel in Ballistic Applications: A Comparative Study,” J Mater Eng Perform, vol. 28, no. 10, pp. 6505–6513, Oct. 2019, doi: 10.1007/s11665-019-04337-z.

[58] M. C. Jo et al., “Understanding of adiabatic shear band evolution during high-strain-rate deformation in high-strength armor steel,” J Alloys Compd, vol. 845, Dec. 2020, doi: 10.1016/j.jallcom.2020.155540.

[59] Pan, B., Qian, K., Xie, H., & Asundi, A. (2009). Two-dimensional digital image correlation for in-plane displacement and strain measurement: A review. Measurement Science and Technology, 20(6). https://doi.org/10.1088/0957-0233/20/6/062001.

[60] Bigger, R., Blaysat, B., Boo, C., Grewer, M., Hu, J., Jones, A., Klein, M., Lava, P., Pankow, M., Raghavan, K., Reu, P., Schmidt, T., Siebert, T., Simonsen, M., Trim, A., Turner, D., Vieira, A., & Weikert, T. (2018). A Good Practices Guide for Digital Image Correlation (E. Jones & M. Iadicola, Eds.). https://doi.org/10.32720/idics/gpg.ed1/print.format

[61] Pérez Caro, L., Schill, M., Haller, K., Odenberger, E. L., & Oldenburg, M. (2020). Damage and fracture during sheet-metal forming of alloy 718. International Journal of Material Forming, 13(1), 15–28. https://doi.org/10.1007/s12289-018-01461-4.

[62] Xiao, Y., & Hu, Y. (2019). An extended iterative identification method for the GISSMO model. Metals, 9(5). https://doi.org/10.3390/met9050568.

[63] Johnsen, J., Holmen, J. K., Gruben, G., Morin, D., & Langseth, M. (n.d.). 6 th International LS-DYNA ® Users Conference Calibration and Application of GISSMO and *MAT_258 for Simulations Using Large Shell Elements.

[64] M. Dunand and D. Mohr, “Predicting the rate-dependent loading paths to fracture in advanced high strength steels using an extended mechanical threshold model,” Int J Impact Eng, vol. 108, pp. 272–285, Oct. 2017, doi: 10.1016/j.ijimpeng.2017.02.020.

[65] G. Owolabi, D. Odoh, A. Odeshi, and H. Whitworth, “FULL FIELD MEASUREMENTS OF THE DYNAMIC RESPONSE OF AA6061-T6 ALUMINUM ALLOY UNDER HIGH STRAIN RATE COMPRESSION AND TORSION LOADS,” 2012. [Online]. Available: http://asmedigitalcollection.asme.org/IMECE/proceedings-pdf/IMECE2012/45240/189/4261958/189_1.pdf

[66] G. Owolabi, D. Odoh, A. Peterson, A. Odeshi, and H. Whitworth, “Measurement of the Deformation of Aluminum Alloys under High Strain Rates Using High Speed Digital Cameras,” World Journal of Mechanics, vol. 03, no. 02, pp. 112–121, 2013, doi: 10.4236/wjm.2013.32009.

[67] G. M. Owolabi, D. T. Bolling, A. G. Odeshi, H. A. Whitworth, N. Yilmaz, and A. Zeytinci, “The Effects of Specimen Geometry on the Plastic Deformation of AA 2219-T8 Aluminum Alloy Under Dynamic Impact Loading,” J Mater Eng Perform, vol. 26, no. 12, pp. 5837–5846, Dec. 2017, doi: 10.1007/s11665-017-3061-4.

[68] F. Pierron, H. Zhu, and C. Siviour, “Beyond hopkinson’s bar,” Philosophical Transactions of the Royal Society A: Mathematical, Physical and Engineering Sciences, vol. 372, no. 2023, Aug. 2014, doi: 10.1098/rsta.2013.0195.

[69] V. Vilamosa, A. H. Clausen, E. Fagerholt, O. S. Hopperstad, and T. Børvik, “Local measurement of stress-strain behaviour of ductile materials at elevated temperatures in a split-hopkinson tension bar system,” Strain, vol. 50, no. 3, pp. 223–235, 2014, doi: 10.1111/str.12084.

[70] Michael Vollmer, Klaus-Peter Möllmann, Infrared Thermal Imaging: Fundamentals, Research and Applications. Wiley-VCH. 2018.

[71] Bruce Hapke, Theory of reflectance and emittance spectroscopy. 2nd edition. Cambridge University Press, 2012.

[72] Schlosser Rebeiz, P. (n.d.). HAL Id: tel-00384405 https://tel.archives-ouvertes.fr/tel-00384405v2 Influence of thermal and mechanical aspects on deformation behaviour of NiTi alloys. https://tel.archives-ouvertes.fr/tel-00384405v2

[73] Krstulović-Opara, L., Surjak, M., Vesenjak, M., Tonković, Z., Kodvanj, J., & Domazet, Ž. (2015). Comparison of infrared and 3D digital image correlation techniques applied for mechanical testing of materials. Infrared Physics and Technology, 73, 166–174. https://doi.org/10.1016/j.infrared.2015.09.014

[74] Alan T. Zehnder, Pradeep R. Guduru, Ares J. Rosakis, et al. Million Frames per second infrared imaging system. Review of Scientific Instruments 71, 3762 (2000); https://doi.org/10.1063/1.1310350

[75] Marchand, A., & Duffy, J. (1988). AN EXPERIMENTAL STUDY OF THE FORMATION PROCESS OF ADIABATIC SHEAR BANDS IN A STRUCTURAL STEEL. In J. Me&. Ploys. So/i& (Vol. 36, Issue 3).

[76] Guo, Y., Ruan, Q., Zhu, S., Wei, Q., Chen, H., Lu, J., Hu, B., Wu, X., Li, Y., & Fang, D. (2019). Temperature Rise Associated with Adiabatic Shear Band: Causality Clarified. Physical Review Letters, 122(1). https://doi.org/10.1103/PhysRevLett.122.015503

[77] Rittel, D., & Wang, Z. G. (2008). Thermo-mechanical aspects of adiabatic shear failure of AM50 and Ti6Al4V alloys. Mechanics of Materials, 40(8), 629–635. https://doi.org/10.1016/j.mechmat.2008.03.002

[78] Goviazin, G. G., Shirizly, A., & Rittel, D. (2023). A Comparative Study of the Performance of IR Detectors vs. High-Speed Cameras Under Dynamic Loading Conditions. Experimental Mechanics, 63(1), 115–124. https://doi.org/10.1007/s11340-022-00907-w

[79] Soares, G. C., Patnamsetty, M., Peura, P., & Hokka, M. (2019). Effects of Adiabatic Heating and Strain Rate on the Dynamic Response of a CoCrFeMnNi High-Entropy Alloy. Journal of Dynamic Behavior of Materials, 5(3), 320–330. https://doi.org/10.1007/s40870-019-00215-w

[80] P. W. Bridgman. Studies in large plastic flow and fracture. McGraw-Hill, New York, 1952.

[81] Clausing, D. P. (1970). Effect of plastic strain state on ductility and toughness. International Journal of Fracture Mechanics, 6(1), 71-85. doi:10.1007/BF00183662

[82] McClintock, F.A. Plasticity aspects of fracture, volume III of Fracture An Advanced Treatise, chapter 2, pp. 47–307. Academic Press, New York and London, 1971.

[83] Hancock, J. W., & Mackenzie, A. C. (1976). On the mechanisms of ductile failure in high-strength steels subjected to multi-axial stress-states. Journal of the Mechanics and Physics of Solids, 24(2-3), 147-160. doi:10.1016/0022-5096(76)90024-7

[84] Wilkins ML, Streit RD, Reaugh JE. Cumulative-strain-damage model of ductile fracture: simulation and prediction of engineering fracture tests. Technical Report UCRL-53058, Lawrence Livermore National Laboratory; October 1980.

[85] Halford, G.R., Morrow, J. On low-cycle fatigue in torsion, volume 62 of American Society for Testing and Materials proceedings, pp. 695–707. American Society for Testing and Materials, 1962.

[86] Johnson, G. R. (1985). FRACTURE CHARACTERISTICS OF THREE METALS SUBJECTED TO VARIOUS STRAINS, STRAIN RATES, TEMPERATURES AND PRESSURES. In EngineeringFracture Mechanics (Vol. 21, Issue I).

[87] Bao, Y., & Wierzbicki, T. (2004). On fracture locus in the equivalent strain and stress triaxiality space. International Journal of Mechanical Sciences, 46(1), 81–98. https://doi.org/10.1016/j.ijmecsci.2004.02.006

[88] Tomasz Wierzbicki, Yingbin Bao, Young-Woong Lee, Yuanli Bai. ''Calibration and evaluation of seven fracture models'', Impact and Crashworthiness Laboratory, Massachusetts Institute of Technology, Cambridge, MA 02139, 2005.

[89] T. Wierzbicki and L. Xue. On the effect of the third invariant of the stress deviator on ductile fracture. Technical report, Impact and Crashworthiness Laboratory, Massachusetts Institute of Technology, Cambridge, MA, 2005.

[90] Liang Xue, ''Damage accumulation and fracture initiation in uncracked ductile solids subject to triaxial loading'', International Journal of Solids and Structures, Volume 44, Issue 16, 2007, Pages 5163-5181, ISSN 0020-7683, https://doi.org/10.1016/j.ijsolstr.2006.12.026.

[91] Y. Bai and T. Wierzbicki. A new model of metal plasticity and fracture with pressure and lode dependence. Int. J. Plasticity., 24(6):1071 – 1096, 2008.

[92] Y. Bai. Effect of loading history in necking and fracture. PhD thesis, Massachusetts Institute of Technology, 2008.

[93] Y. Bai, X. Teng, and T. Wierzbicki. On the application of stress triaxiality formula for plane strain fracture testing. J. Eng. Mater. Technol., 131(2):021002, 2009.

[94] M Basaran. Stress state dependent damage modeling with a focus on the lode angle influence. PhD Thesis, RWTH Aachen University, 2011.

[95] Dunand, M.. "Hybrid experimental-numerical determination of the loading path to fracture in TRIP780 sheets subjected to multi-axial loading." MSc Thesis. (2010).

[96] Mohr, Dirk, and Fabien Ebnoether. "Plasticity and Fracture of Martensitic Boron Steel Under Plane Stress Conditions." International Journal of Solids and Structures 46, no. 20 (October 2009): 3535–3547. © 2009 Elsevier Ltd.

[97] Neukamm F, Feucht M, Haufe A, Roll K. On closing the constitutive gap between forming and crash simulation. Proceedings of the 10th international LS-DYNA users conference. Detroit; 2008.

[98] Chen and Song, "Split Hopkinson Bar." [Online]. Available: www.springer.com/series/1161

[99] R. Gerlach, C. Kettenbeil, and N. Petrinic, "A new split Hopkinson tensile bar design," Int J Impact Eng, vol. 50, pp. 63–67, Dec. 2012, doi: 10.1016/j.ijimpeng.2012.08.004.

[100] Christian C. Roth, Dirk Mohr, Effect of strain rate on ductile fracture initiation in advanced high strength steel sheets: Experiments and modeling, International Journal of Plasticity, Volume 56, 2014, Pages 19-44, ISSN 0749-6419, https://doi.org/10.1016/j.ijplas.2014.01.003.

[101] D. Anderson, S. Winkler, A. Bardelcik, M.J. Worswick, Influence of stress triaxiality and strain rate on the failure behavior of a dual-phase DP780 steel, Materials & Design, Volume 60, 2014, Pages 198-207, ISSN 0261-3069, https://doi.org/10.1016/j.matdes.2014.03.073.

[102] Meyers, M. A. (1994). Dynamic failure : mechanical and microstructural aspects. Journal de Physique IV Proceedings, 4(C8), 4. https://doi.org/10.1051/jp4:1994893ï

[103] Woei-Shyan Lee, Chi-Feng Lin, Plastic deformation and fracture behaviour of Ti–6Al–4V alloy loaded with high strain rate under various temperatures, Materials Science and Engineering: A, Volume 241, Issues 1–2, 1998, Pages 48-59, ISSN 0921-5093, https://doi.org/10.1016/S0921-5093(97)00471-1.

[104] Bassim, N., & Boakye-Yiadom, S. (2015). Mechanism of grain refinement and its effect on Adiabatic Shear Bands in 4340 steel and pure copper during impact. EPJ Web of Conferences, 94. https://doi.org/10.1051/epjconf/20159402001

[105] Boakye-Yiadom, S., Khan, A. K., & Bassim, N. (2014). Deformation Mapping and the Role of Carbides on the Microstructure and Properties of Evolved Adiabatic Shear Bands. Metallurgical and Materials Transactions A: Physical Metallurgy and Materials Science, 45(12), 5379–5396. https://doi.org/10.1007/s11661-014-2495-7

[106] A.G. Odeshi, M.N. Bassim, S. Al-Ameeri, Effect of heat treatment on adiabatic shear bands in a high-strength low alloy steel, Materials Science and Engineering: A, Volume 419, Issues 1–2, 2006, Pages 69-75, ISSN 0921-5093, https://doi.org/10.1016/j.msea.2005.11.059.

[107] Tiamiyu, A. A. (2015). DEFORMATION AND DAMAGE MECHANISMS IN SELECTED 2000 SERIES ALUMINUM ALLOYS UNDER BOTH QUASI-STATIC AND DYNAMIC IMPACT LOADING CONDITIONS.

[108] Meyer LW, Manwaring S. Critical adiabatic shear strength of low alloyed steel under compressive loading. In: Murr LE, Staudhammer KP, Meyers MA, editors. Metallurgical applications of shock-wave and high-strain-rate phenomena. New York: Marcel Dekker Inc.; 1986. p. 657–74

[109] Couque, H. (n.d.). A hydrodynamic hat specimen to investigate pressure and strain rate dependence on adiabatic shear band formation.

[110] PURSCHE, F., & L. W. MEYER. "Correlation Between Dynamic Material Behavior and Adiabatic Shear Phenomenon for Quenched and Tempered Steels." *Engineering Transactions* [Online], 59.2 (2011): 67–84. Web. 17 Feb. 2022.

[111] Rittel, D., Lee, S. and Ravichandran, G. A Compression-shear Specimen for Large Strain Testing. Experimental Mechanics, 2002, 42(1), 58-64.

[112] Whittington, W. R., Oppedal, A. L., Turnage, S., Hammi, Y., Rhee, H., Allison, P. G., Crane, C. K., & Horstemeyer, M. F. (2014). Capturing the effect of temperature, strain rate, and stress state on the plasticity and fracture of rolled homogeneous armor (RHA) steel. Materials Science and Engineering A, 594, 82–88. https://doi.org/10.1016/j.msea.2013.11.018

[113] Walters, C. L. (2009). Development of a Punching Technique for Ductile Fracture Testing Over a Wide Range of Stress States and Strain Rates.

[114] Wang, B., Xiao, X., Astakhov, V. P., & Liu, Z. (2019). The effects of stress triaxiality and strain rate on the fracture strain of Ti6Al4V. Engineering Fracture Mechanics, 219. https://doi.org/10.1016/j.engfracmech.2019.106627

[115] Herzig, N., Abdel-Malek, S., Meyer, L. W., & Cimpoeru, S. J. (2017). Modeling of Ductile Failure in High Strength Steel. Procedia Engineering, 197, 285–293. https://doi.org/10.1016/j.proeng.2017.08.106

[116] Polyzois, I., & Toussaint, G. (2020). Defence Research and Development Canada Scientific Report Fracture Characterization of AlgoTuf 400F Steel for Simulating Blast Damage.

[117] NJ Edwards. Mechanistic prediction of adiabatic shear bands in 2024-T351 Aluminium. PhD Thesis, Swinburne University of Technology, 2021.

[118] Kumar N, Ying Q, Nie X, Mishra RS, Tang Z, Liaw PK, Brennan RE, Doherty KJ, Cho KC (2015) High strain-rate compressive deformation behavior of the Al0.1CrFeCoNi high entropy alloy. Mater Des 86:598–602

[119] Moon J, Hong SI, Bae JW, Jang MJ, Yim D, Kim HS (2017) On the strain rate-dependent deformation mechanism of CoCrFeMnNi high-entropy alloy at liquid nitrogen temperature. Mater Res Lett 5:472–477

[120] Cao, C. M., Tong, W., Bukhari, S. H., Xu, J., Hao, Y. X., Gu, P., Hao, H., & Peng, L. M. (2019). Dynamic tensile deformation and microstructural evolution of AlxCrMnFeCoNi high-entropy alloys. Materials Science and Engineering A, 759, 648–654. https://doi.org/10.1016/j.msea.2019.05.095

[121] Wang, C. T., He, Y., Guo, Z., Huang, X., Chen, Y., Zhang, H., & He, Y. (2021). Strain Rate Effects on the Mechanical Properties of an AlCoCrFeNi High-Entropy Alloy. Metals and Materials International, 27(7), 2310–2318. https://doi.org/10.1007/s12540-020-00920-5

[122] Zener, C., & Hollomon, J. H. (1944). Effect of strain rate upon plastic flow of steel. Journal of Applied Physics, 15(1), 22–32. https://doi.org/10.1063/1.1707363

[123] Zhu, S., Guo, Y., Ruan, Q., Chen, H., Li, Y., & Fang, D. (2020). Formation of adiabatic shear band within Ti-6Al-4V: An in-situ study with high-speed photography and temperature measurement. International Journal of Mechanical Sciences, 171. https://doi.org/10.1016/j.ijmecsci.2019.105401

[124] Nie, Y., Claus, B., Gao, J., Zhai, X., Kedir, N., Chu, J., Sun, T., Fezzaa, K., & Chen, W. W. (n.d.). In situ Observation of Adiabatic Shear Band Formation in Aluminum Alloys.

[125] Weaver, J. S., Livescu, V., & Mara, N. A. (2020). A comparison of adiabatic shear bands in wrought and additively manufactured 316L stainless steel using nanoindentation and electron backscatter diffraction. Journal of Materials Science, 55(4), 1738–1752. https://doi.org/10.1007/s10853-019-03994-8

[126] Barthelat, F., Wu, Z., Prorok, B. C., & Espinosa, H. D. (2003). Dynamic Torsion Testing of Nanocrystalline Coatings Using High-Speed Photography and Digital Image Correlation.

[127] Giovanola, J. H. (1988). ADIABATIC SHEAR BANDING UNDER PURE SHEAR LOADING PART II: FRACTOGRAPHIC AND METALLOGRAPHIC OBSERVATIONS. In Mechanics of Materials (Vol. 7).

[128] Landau, P., Osovski, S., Venkert, A., Gärtnerová, V., & Rittel, D. (2016). The genesis of adiabatic shear bands. Scientific Reports, 6. https://doi.org/10.1038/srep37226

[129] Witman, MA Meyers, Pak. Observation of Adiabatic Shear Band in AISI 4340 Steel Meyers by High-Voltage Transmission Electron Microscopy. (98). Metallurgical Transactions A.

[130] Boakye-Yiadom, S., Bassim, M. N., & Al-Ameeri, S. (2012). On the persistence of adiabatic shear bands. EPJ Web of Conferences, 26. https://doi.org/10.1051/epjconf/20122602002

[131] M. T. Perez-Prado, J. A. Hines And K. S. Vecchio, Microstructural Evolution In Adiabatic Shear Bands In Ta And Ta-W Alloys, Acta Materialia 49 (2001) 2905-2917

[132] J. A. Hines And K. S. Vecchio, Dynamic Recrystallization In Adiabatic Shear Bands In Shock-Loaded Copper, Proceeding Of The 1995 International Conference On Metallurgical And Materials Applications Of Shock-Wave And High-Strain-Rate Phenomena, EXPLOMET, Elsevier (1995) 421-428

[133] Krauss, G. (n.d.). The 2000 Edward DeMille Campbell Memorial Lecture ASM International Deformation and Fracture in Martensitic Carbon Steels Tempered at Low Temperatures.

[134] Wilsdorf, H. G. F. (1975). VOID INITIATION, GROWTH, AND COALESCENCE IN DUCTILE FRACTURE OF METALS. In Journal of Electronic Materials (Vol. 4, Issue 5).

[135] Shahzamanian, M., Lloyd, D., Partovi, A., & Wu, P. (2021). Study of Influence of Width to Thickness Ratio in Sheet Metals on Bendability under Ambient and Superimposed Hydrostatic Pressure. Applied Mechanics, 2(3), 542–558. https://doi.org/10.3390/applmech2030030

[136] Selini, N., Elmeguenni, M., & Benguediab, M. (2013). Effect of the Triaxiality in Plane Stress Conditions Triaxiality Effect in a PVC material. In Technology & Applied Science Research (Vol. 3, Issue 1). www.etasr.com

[137] Abedini, A., Butcher, C. & Worswick, M.J. Fracture Characterization of Rolled Sheet Alloys in Shear Loading: Studies of Specimen Geometry, Anisotropy, and Rate Sensitivity. Exp Mech 57, 75–88 (2017). https://doi.org/10.1007/s11340-016-0211-9

[138] R. Hibbeler, Mechanics of Materials, 11th ed. Pearson, 2022.

[139] Barkey, M. E., & Lee, Y. L. (2012). Strain-Based Multiaxial Fatigue Analysis. In Metal Fatigue Analysis Handbook (pp. 299–331). Elsevier Inc. https://doi.org/10.1016/B978-0-12-385204-5.00008-2

[140] Vecchio, K. S., & Jiang, F. (2007). Improved pulse shaping to achieve constant strain rate and stress equilibrium in split-Hopkinson pressure bar testing. Metallurgical and Materials Transactions A: Physical Metallurgy and Materials Science, 38 A(11), 2655–2665. https://doi.org/10.1007/s11661-007-9204-8

[141] Data sheet 195 Armox 500T 2017-04-19, SSAB.

[142] Dwight D. Showalter, William A. Gooch, Matthew S. Burkins, and R. Stockman Koch. 'Ballistic Testing of SSAB Ultra-High Hardness Steel for Armour Applications'. ARL-TR-4632, 2008.

Appendix A: Statistical Significance of All Data

For computational modeling, statistically robust data is necessary. To check whether each different tested condition produces values which are 'statistically significant', a students T-Test is conducted. This is done by finding the p-value for two different sets of tests, which must be less then 0.05 to break the null hypothesis. The null hypothesis indicates that the two different sets of data are not statistically significant, and there is no real statistical correlation between the two. The null hypothesis is true when random data is compared, or the same phenomenon is compared.

To apply this to the material property data in perspective, for varied input conditions (e.g., strain-rate), the null hypothesis should be broken to ensure that a different test condition is being conducted. If there is a strain-rate dependent effect such as strengthening in dynamic tension, the hull hypothesis should again be broken. Conversely, if there is no strain-rate dependent effect such as tensile elongation, the null hypothesis should be met.

The p-value is calculated for all tests and the table to which it correlates to is hyperlinked. It is also indicated which two test conditions are being compared. Sometimes a wider range of compared test conditions is necessary to create statistically significant data. Green cells indicate the null hypothesis is broken (p-value < 5%) and red cells indicate it is met (p-value > 5%).

Table 4.1: UNIAXIAL FLAT TENSION PLASTIC STRAIN RATIO:

Test Condition / Datasets Compared	Reported Value	Yield Strength (MPa)	Ultimate Strength (MPa)	Elongation (%)	R-value
90	Average	1284	1865	12.37	0.8711
90/45	p-value	0.308	0.001	0.003	0.437
45	Average	1263	1899	10.90	0.8651
45/0	p-value	0.012	0.023	0.006	0.479
0	Average	1191	1794	11.39	0.8681
90/0	p-value	0.087	0.044	0.015	0.439

Comments: The null hypothesis is broken for stress but met for the R-value. This provides statistically meaningful confidence that there is texture dependent difference in ultimate stress, but the plastic strain ratio is consistent and unaffected by the rolling direction.

Table 4.2: AXISYMMETRIC TENSION:					
Specimen	**Dataset**	**Ultimate Strength (MPa)**	**Axial Elongation (%)**	**Equivalent Plastic Instability Strain**	**Equivalent Plastic Fracture Strain**
Round Tension (U)	Average	1793	12.06	0.068	0.672
U/R12	p-value	0.028	0.002	0.302	0.001
R12	Average	2113	7.23	0.070	0.336
R12/R6	p-value	0.182	0.019	0.311	0.047
R6	Average	2280	5.16	0.072	0.255
R6/R3	p-value	0.043	0.020	0.008	0.070
R3	Average	2541	3.69	0.093	0.215
U/R3	p-value	0.000	0.000	0.000	0.000
Comments: While some intermittent tests slightly affect the data, very low p-values when comparing the two extremities of uniaxial (U) and greatest triaxiality (R3) indicates that statistically significant data is attained. Triaxiality dependent strength increase, and ductility loss can therefore be concluded. It would be prudent to conduct 5 repeated tests in future work as it would increase the statistical significance.					

Table 4.3: HOLE AND NOTCHED TENSION:					
Test Condition / Datasets Compared	**Reported Value**	**Ultimate Strength (MPa)**	**Axial Elongation (%)**	**Equivalent Plastic Instability Strain**	**Equivalent Plastic Fracture Strain**
Uniaxial - U	Average	1865	12.37	0.14	0.3445
U/R6	p-value	0.051	0.000	0.035	0.110
R6	Average	2126	5	0.07	0.3038
R6/R2	p-value	0.014	0.074	0.091	0.045
R2	Average	2607	4.80	0.05	0.1884
U/R2	p-value	0.021	0.001	0.009	0.004

Table 4.4: TENSILE PLANE STRAIN:					
Specimen	**Dataset**	**Ultimate Strength (MPa)**	**Axial Elongation (%)**	**Equivalent Plastic Instability Strain**	**Equivalent Plastic Fracture Strain**
Plane Strain (U)	Average	1952	5.13	0.041	0.067
U/R8	p-value	0.051	0.108	0.083	0.030
R8	Average	2155	3.30	0.034	0.044
R8/R4	p-value	0.256	0.052	0.148	0.021
R4	Average	2197	1.86	0.023	0.023
R4/R2	p-value	0.130	0.167	0.137	0.130
R2	Average	2305	0.73	0.009	0.010
U/R2	p-value	0.003	0.070	0.120	0.017

Comments: Low strains results in the lack of precision in the data. Notably, the stress and equivalent plastic strain have low p-values for two extremes.

Table 4.5: PURE SHEAR AND SHEAR-TENSION:					
Test Condition / Datasets Compared	**Reported Value**	**Maximum Principal Strain**	**Minimum Principal Strain**	**Equivalent Plastic Instability Strain**	**Equivalent Plastic Fracture Strain**
Pure Shear	Average	0.476	-0.506	0.885	0.979
S/ST10	p-value	0.085	0.111	0.015	0.050
Shear Tension 10	Average	0.376	-0.400	0.469	0.717
ST10/ST30	p-value	0.018	0.017	0.008	0.002
Shear Tension 30	Average	0.223	-0.207	0.181	0.305
S/ST30	p-value	0.021	0.015	0.002	0.011

Table 5.1: LODE ANGLE DEPENDENT ELONGATION EMBRITTLMENT				
Test Condition / Datasets Compared	**Reported Value**	**Impact Momentum (Kgm/s)**	**Strain Rate (/s)**	**Axial Fracture Elongation**
C	Average	23.21	2448	-0.286
C/CS6	p-value	0.081	0.447	0.022
CS6	Average	22.95	2643	-0.149
CS6/CS10	p-value	0.192	0.490	0.023
C10	Average	23.21	2644	-0.109
C/CS10	p-value	0.073	0.427	0.012

Comments: At a constant impact momentum, a change in stress-state (increase LAP / shear stress) results in embrittlement.

Table 5.2: LODE ANGLE DEPENDENT SURFACE STRAIN EMBRITTLEMENT							
Test Condition / Datasets Compared	**Reported Value**	**Strain-Rate**	**Axial Fracture Elongation**	**Axial Fracture Strain (Ex)**	**Transverse Fracture Strain (Ey)**	**Equivalent Plastic Instability Strain**	**Equivalent Plastic Fracture Strain**
C	Average	2686	-0.286	0.231	-0.278	0.232	0.305
C/CS6	p-value	0.388	0.03	0.008	0.009	0.010	0.001
CS6	Average	2643	-0.149	0.133	-0.2	0.138	0.213
CS6/CS10	p-value	0.490	0.018	0.183	0.027	0.030	0.022
CS10	Average	2644	-0.109	0.107	-0.146	0.113	0.155
C/CS10	p-value	0.378	0.012	0.025	0.004	0.003	0.002
Comments: Statistically significant DIC data reveals that for a constant strain-rate, severe embrittlement due to stress-state occurs.							

Table 5.3: STRAIN RATE DEPENDENT STRENGTHENING						
Test Condition / Datasets Compared	**Reported Value**	**Impact Momentum (kgm/s)**	**Strain Rate (/s)**	**Ultimate Flow Stress (MPa)**	**Axial Instability Strain**	**Axial Fracture Strain**
C1	Average	15.92	1679	1954	-0.090	-0.153
C1/C2	p-value	0.004	0.003	0.210	0.053	0.013
C2	Average	17.39	1815	2001	-0.111	-0.199
C2/C3	p-value	0.002	0.004	0.080	0.023	0.068
C3	Average	18.63	1946	2097	-0.137	-0.239
C3/C4	p-value	0.001	0.004	0.017	0.032	0.020
C4	Average	19.67	2076	2138	-0.163	-0.276
C1/C3	p-value	0.000	0.002	0.005	0.008	0.006
C2/C4	p-value	0.002	0.001	0.031	0.027	0.019
C1/C4	p-value	0.000	0.000	0.003	0.007	0.002
T1	Average	30.18	679	1854	0.091	0.213
T1/T2	p-value	0.006	0.007	0.316	0.357	0.133
T2	Average	35.58	805	1875	0.087	0.197
T2/T3	p-value	0.000	0.026	0.271	0.121	0.203
T3	Average	40.84	939	1913	0.068	0.183
T3/T4	p-value	0.014	0.001	0.163	0.369	0.495
T4	Average	44.46	1090	1974	0.060	0.184
T1/T3	p-value	0.002	0.002	0.028	0.164	0.058
T2/T4	p-value	0.002	0.004	0.008	0.074	0.113
T1/T4	p-value	0.000	0.000	0.034	0.100	0.116
Comments: Clearly, for different input conditions of strain-rate, there is a strengthening effect when comparing at least every second input condition. Some input conditions may be too close, and therefore perhaps only three						

different strain-rates (instead of 4) is acceptable. The central two can be combined to increase statistical significance. There is also no rate-dependent elongation difference (axial strain) in tension.

Table 5.4: STRAIN-RATE DEPENDENT DYNAMIC TENSION

Test Condition / Datasets Compared	Reported Value	Strain-Rate	Axial Fracture Strain (Ex)	Transverse Fracture Strain (Ey)	Shear Fracture Strain (Exy)	Equivalent Plastic Instability Strain	Equivalent Plastic Fracture Strain
T1	Average	558	0.815	-0.237	0.020	0.176	0.839
T1/T2	p-value	0.001	0.141	0.388	0.499	0.143	0.134
T2	Average	720	0.885	-0.229	0.020	0.184	0.921
T2/T3	p-value	0.018	0.248	0.298	0.375	0.149	0.254
T3	Average	839	0.920	-0.222	0.016	0.130	0.961
T3/T4	p-value	0.001	0.045	0.198	0.259	0.292	0.068
T4	Average	1043	0.967	-0.235	0.022	0.099	1.009
T1/T3	p-value	0.003	0.027	0.309	0.087	0.173	0.014
T2/T4	p-value	0.003	0.141	0.393	0.403	0.030	0.166
T1/T4	p-value	0.001	0.011	0.480	0.391	0.022	0.010

Comments: Perhaps three different strain-rates or a wider range of input pressure / impact momentum would improve the statistical significance. Regardless, the input condition strain-rates are statistically significant and when comparing the extremes and eliminating outliers, both strain-rate dependent instability and fracture strain effects are observed.

Appendix B: TSHB Safety and Operation

Safety Factor

1. Doing bolted joint analysis (https://mechanicalc.com/reference/bolted-joint-analysis), the safety factors for the load transfer components in the Hopkinson bar are acquired.
    a. The bolt stiffness is acquired based on the joint geometry.
    b. Based on preload stress of 66% of the yield stress, the seating torque and initial stresses on the bolt and threaded part are acquired
    c. The torque for all Hex bolts in shear for the gas gun mounts is 17.4 Nm. Other fasteners are not as important and can be set by a socket wrench.
    d. Based on the yield strength of the bolt and mount material or the bar material, and the applied force induced stresses on the bolt, the safety factors are acquired.
2. The Von Mises stress at the Al7075-T6 bar-specimen interface is reported (more extreme than the flange-bar interface). Note that if an alloy weaker than Al7075-T6 is used, the internal thread shear (6.43) safety factor would decrease. However, as described below, given the extremity of the calculation, this will never be an issue.
3. The gas gun mounts have 8 bolts on both sides of the gas gun (primarily in shear). Therefore there are 16 total bolts taking the load.
4. Assuming 16 bolts take the load, and that the impact velocity of 35 m/s is used at the design limit pressure of 200 psi, and the load impulse is transferred as per the stress wave pulse length, a force of about 190 kN is acquired. In reality, the force is transferred over a significantly longer period of time, and there are frictional and dissipative loses resulting in a much lower force. Conclusively, the reported values are worse case scenarios that will never be materialised and the system is acceptable. A more realistic approach for the force can be acquired from the gas gun bore and applied pressure which provides values more than an order of magnitude lower.

Safety Factor	Steel Bolt (Grade 5)	Al7075-T6
Von Mises Stress	2.66	1.15
Ext Thread Shear - Bolt	6.43	6.38
Int Thread Shear - Mount	6.43	7.66

Tensile Split Hopkinson Bar

York University

Safety Operations Procedure (SOP)

Diego Mateos

Reference Images:

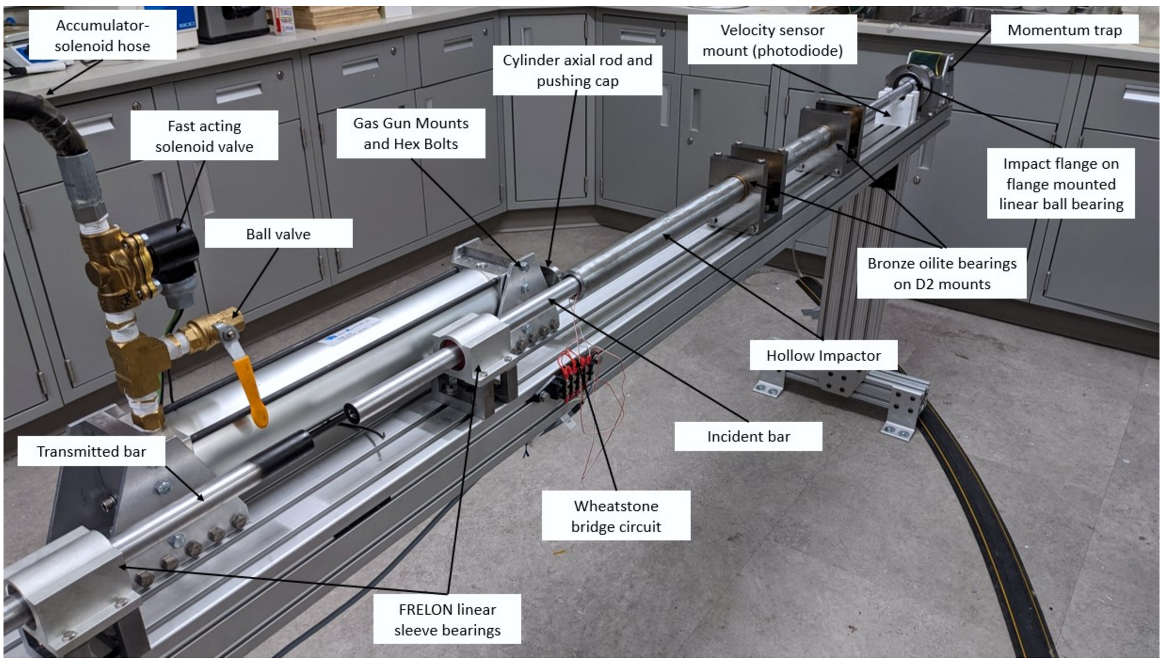

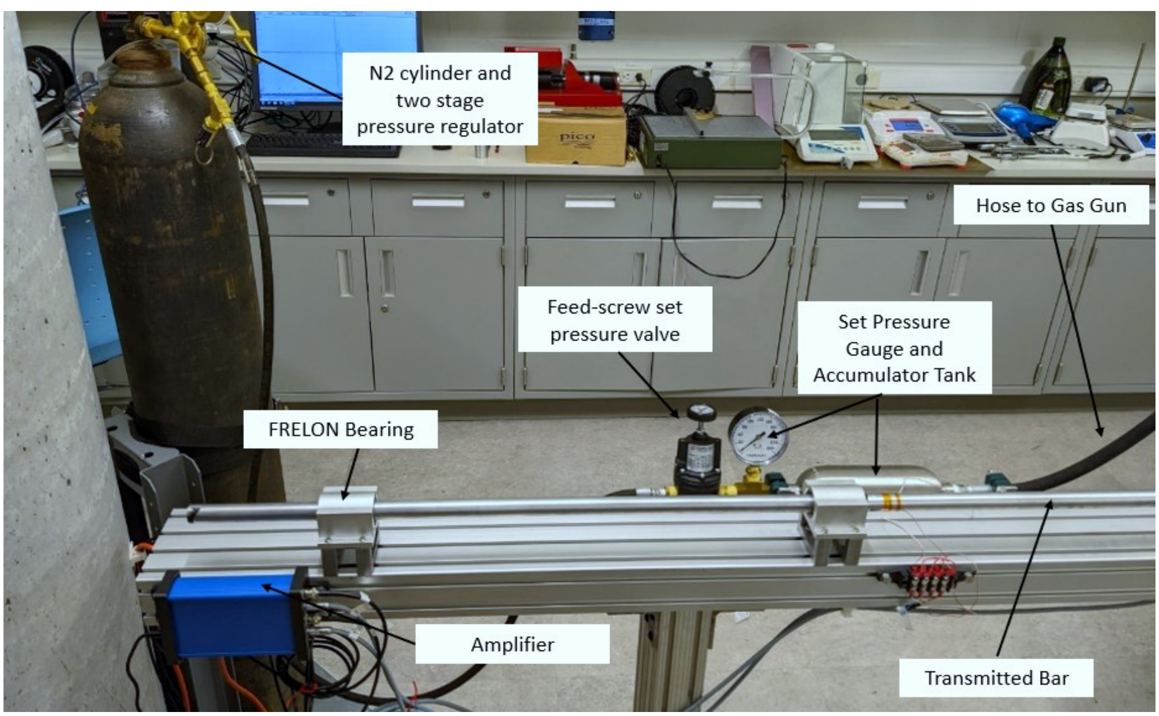

Machine Parameters:

Bar/Impactor/Flange Material	Al 7075-T651
E - Elastic Modulus (GPa)	71.70
p - Density (kg/m³)	2810
v - Poisson ratio	0.33
K - Bulk Modulus (MPa)	70.30
Yield Strength (MPa)	500
Max impact velocity (m/s)	71.15
C - Elastic wave speed (m/s)	5002
Pulse length (us)	360
L - Length of Bars (mm)	1829
r – Radius of bars (mm)	12.70
Bars aspect ratio	72
Location of strain gauges	L/2
Length of Impactor (mm)	900
Impactor cross section (mm)	44.45 OD x 6.35 WT
Impact Flange OD (mm)	50.8
Gas gun bore (mm)	76.2
Gas gun stroke length (mm)	406

Testing Procedure

1. Never exceed 200 psi. Always check all bolt heads with socket / torque wrench.
2. Ensure all preload checks are done on all critical hex screws using a wrench/ socket wrench in frequency as defined in this SOP.
    a. On gas gun mounts; four on each side and two mounts (4x2x2) = 16 hex bolts
    b. On momentum trap end block at the end of the incident bar – 8 hex bolts
    c. On Aluminum extrusions (**at high pressures, the whole extrusion assembly oscillates which may slowly unfasten the bolts over time**)
        i. Primarily the Allen bolts on the steel L brackets between the long extrusion and the legs; 8 on each face of the bracket and two legs (8x2x2) = 32 Allen bolts.
    d. All bolts must be preloaded to > 50 % of their yield strength
        i. Achieved with a socket wrench / Allen Key – at least one full turn beyond finger tight.
        ii. No single screw of all above may be loose before testing.
    e. This must be done anytime the system has not been used for greater than 3 months or after every 50 low pressure (<100 psi) tests or 10 high pressure (> 150 psi) tests.
3. Before turning on pressure, ensure there are two steps to arm and fire the system which opens the normally closed solenoid valve. (Ensure switches are off)
4. Ensure ball valve is open, adding another redundancy.
5. Ensure set pressure gauge is at 0 and feed-screw valve is completely unscrewed
6. Ensure incident bar is appropriately threaded to the impact flange and impact flange is appropriately mounted to the flange mounted linear bearing (FMLB).
7. Fully open the nitrogen gas cylinder valve and then close by ¼ turn as per pressurized gas training procedure

8. Set the pressure at desired value
    a. If necessary, increase the allowable pressure through the first hose on the two stage pressure regulator
9. Place specimen between the bars
    a. May be done before, can be done with set pressure on. Make sure step 1-5 are completed first.
    b. Must thread specimen by rotating specimen onto the incident bar first.
    c. Then, must rotate transmitted bar onto the specimen, ensure to maintain the incident bar always fixed (no rotation) since wires are short to avoid tangling.
    d. When threading the transmitted bar onto the specimen, take care not to break the strain gauge wires. This can be done by tangling the wires on the opposite threading direction, such as to untangle and re-tangle in the other direction when threading in the specimen. Do not break the wires. DAQ will not work.
    e. Use 5 or 6mm wrench to torque specimen on both ends
    f. Careful not to load the specimen in torsional or compressive loading throughout step 9
10. Double check all sources of DAQ are on (trigger on DAQ, cameras if used).
    a. See TSHB data acquisition document for details
11. Ensure pneumatic cylinder (gas gun) rod is fully inside the cylinder (ball valve must be open to push rod back into the cylinder).
12. Ensure no one is near the impact flange area
13. Close ball valve
14. Perform test
    a. Turn on power to circuit which provides signal to the primary valve
    b. Switch on the fire switch, and after test is done, immediately turn off the fire switch
    c. Turn off the power switch
    d. Release the trapped pressure by opening the ball valve, test is now finished.
15. Take off specimen
    a. Abide by step 9b in reverse.
16. May return to step 8 if more tests required
17. Return pneumatic cylinder rod to position inside the cylinder
18. Close the set pressure feed screw valve
19. Close the nitrogen gas cylinder
20. Open the set pressure feed-screw valve to release remaining hose pressure
21. Close the feed-screw valve again
22. Close the ball valve (prevents dust entering cylinder).
23. Triple check that all pressure gauges read zero.
24. Check step 23 again.

Appendix C: Specimen Engineering Drawings

FLAT TENSION:

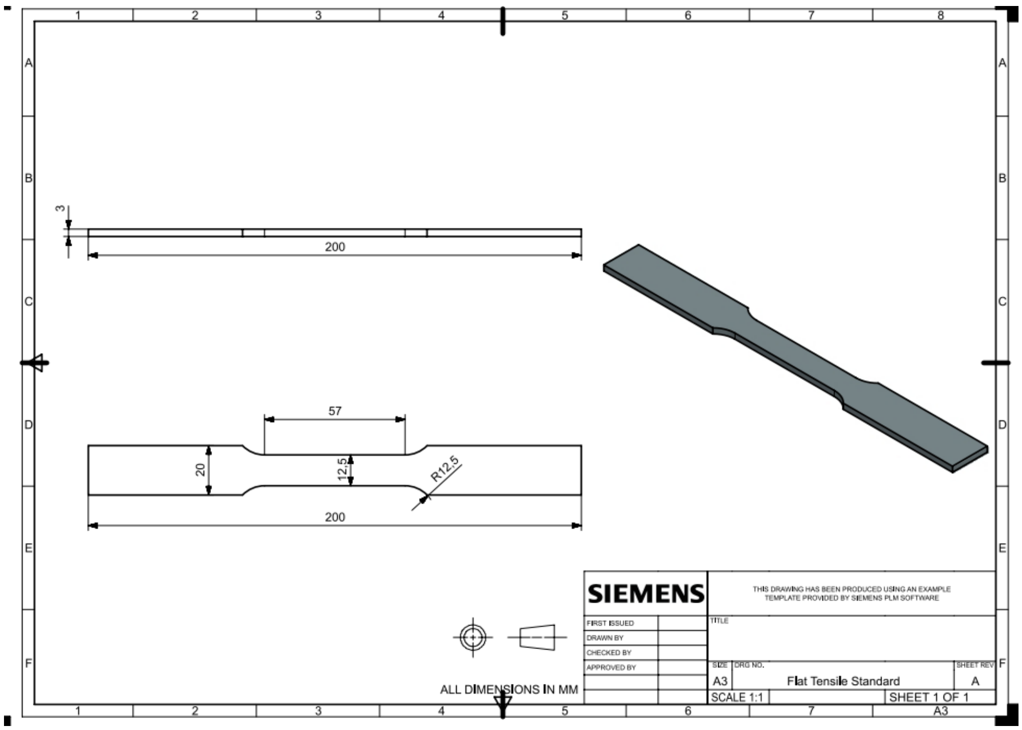

HOLE TENSION:

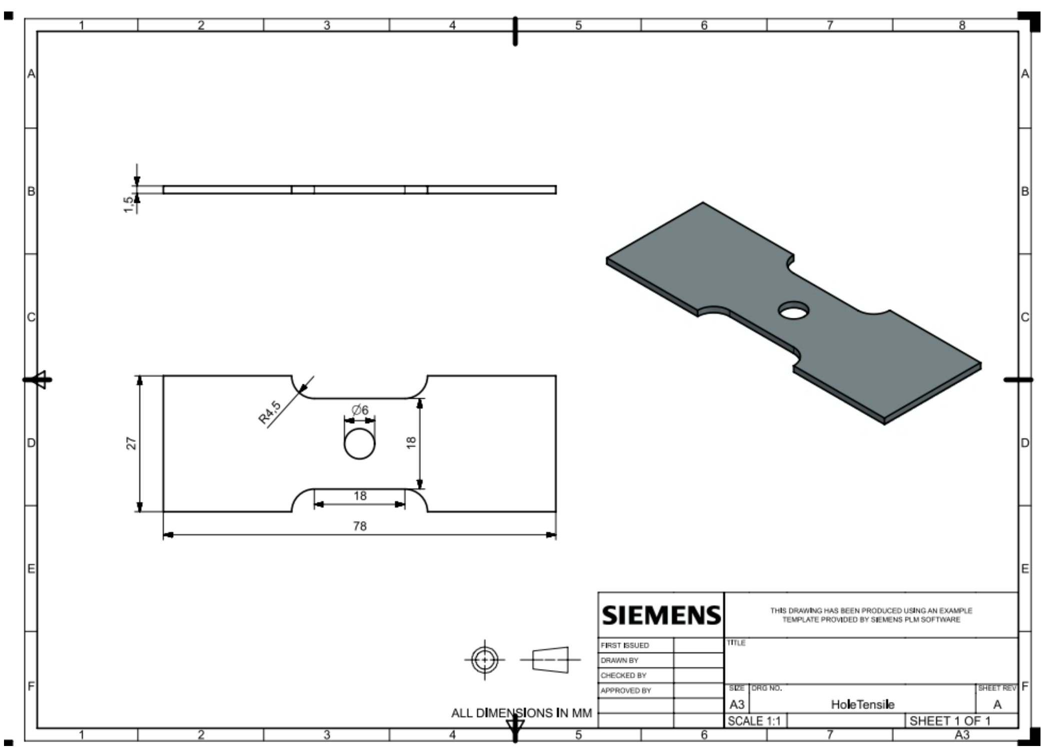

NOTCHED FLAT TENSION (R = 6, 2 MM):

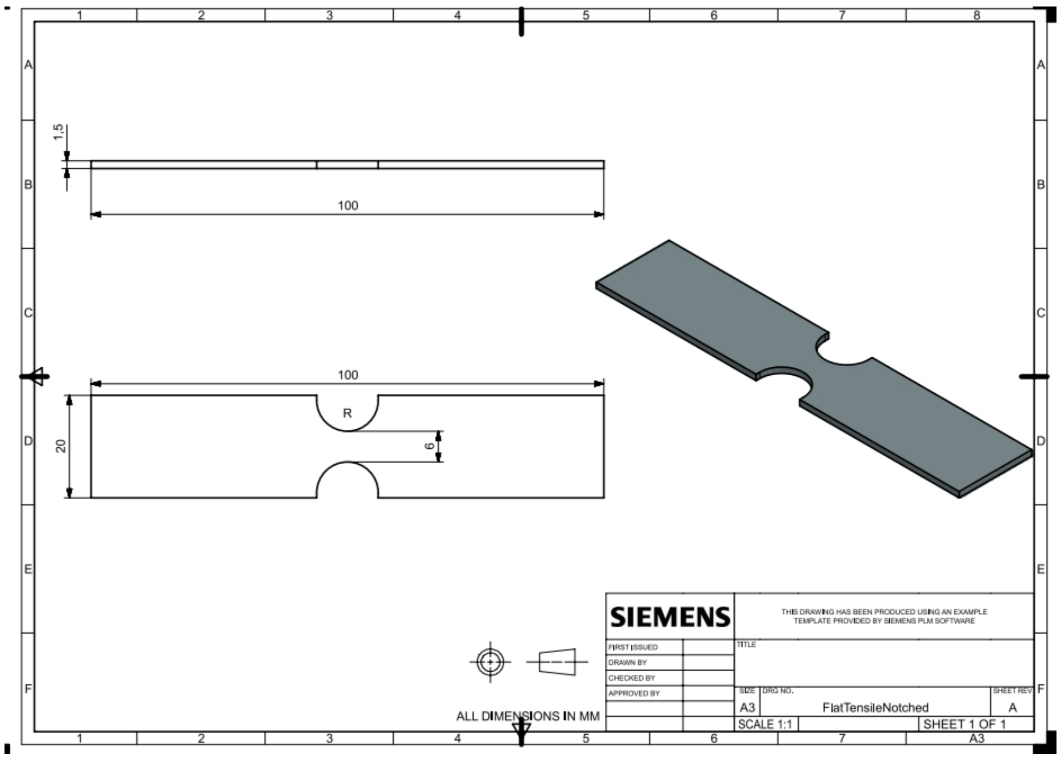

TENSILE PLANE STRAIN:

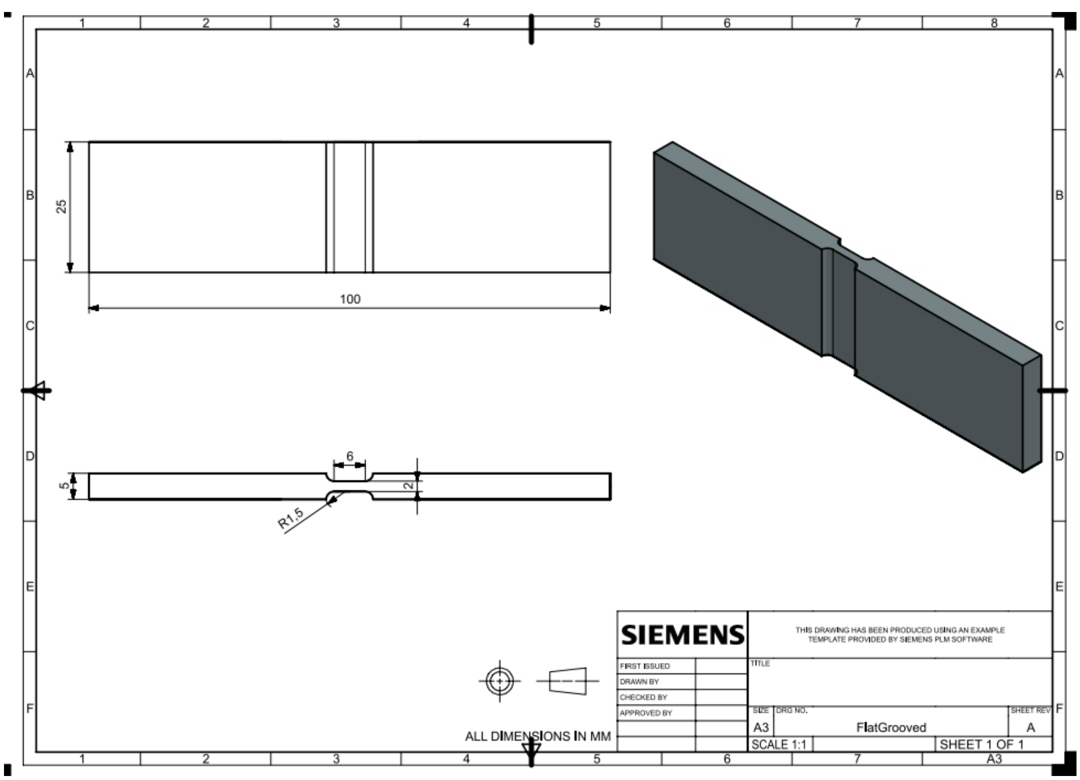

NOTCHED TENSILE PLANE STRAIN (R = 8, 4, 2 MM):

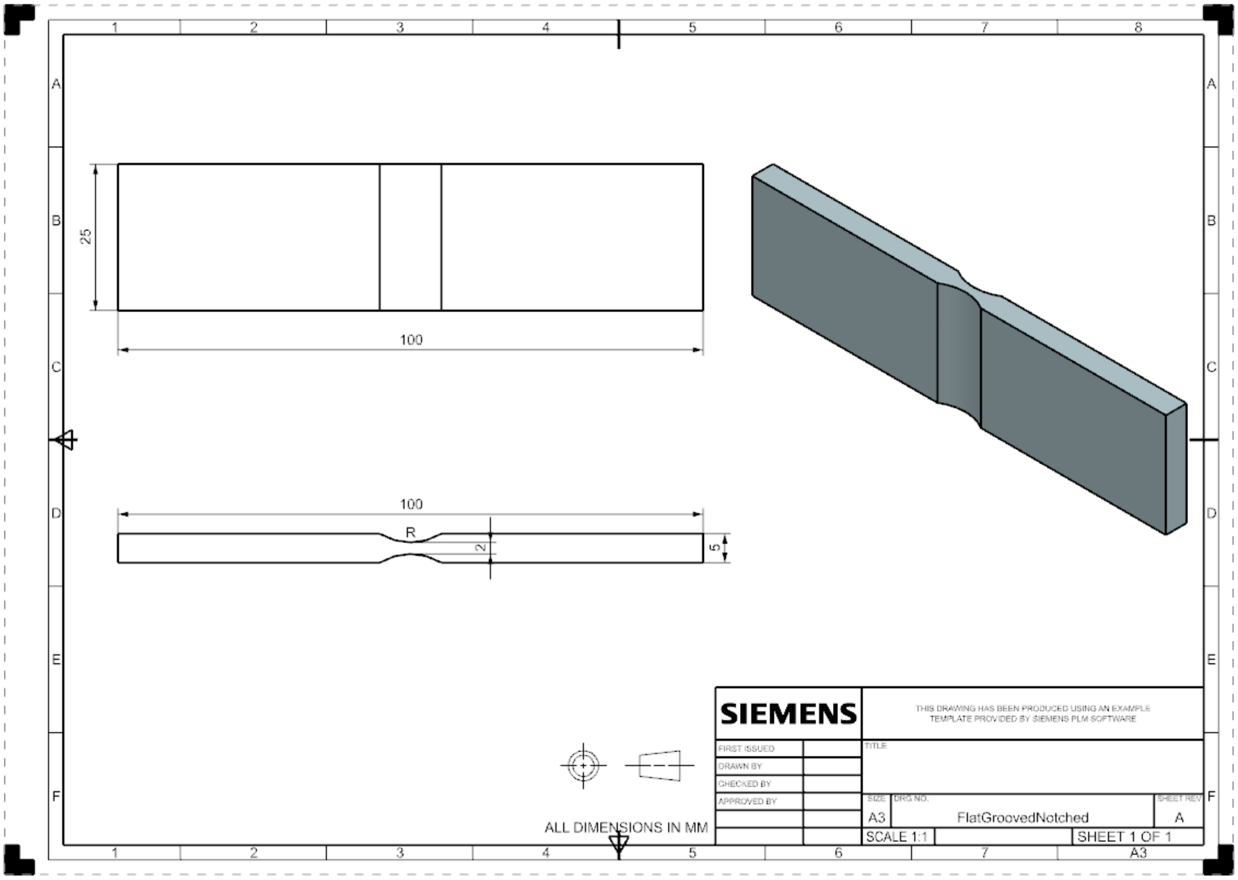

ROUND TENSION:

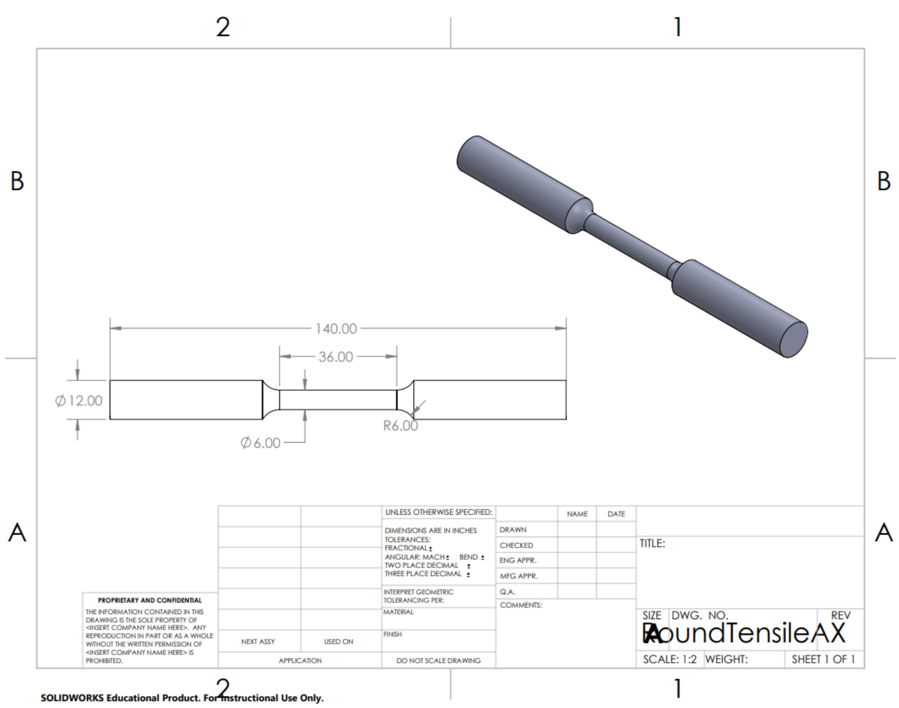

NOTCHED ROUND TENSION (R = 12, 6, 3 MM):

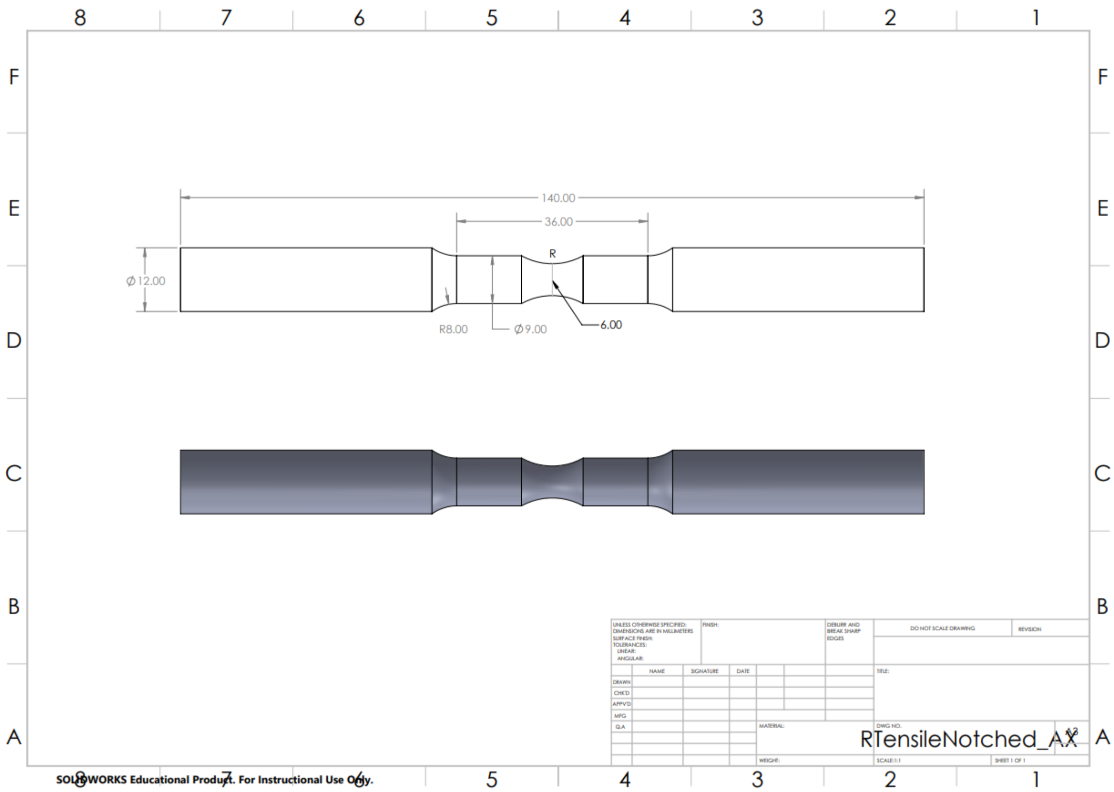

PURE SHEAR:

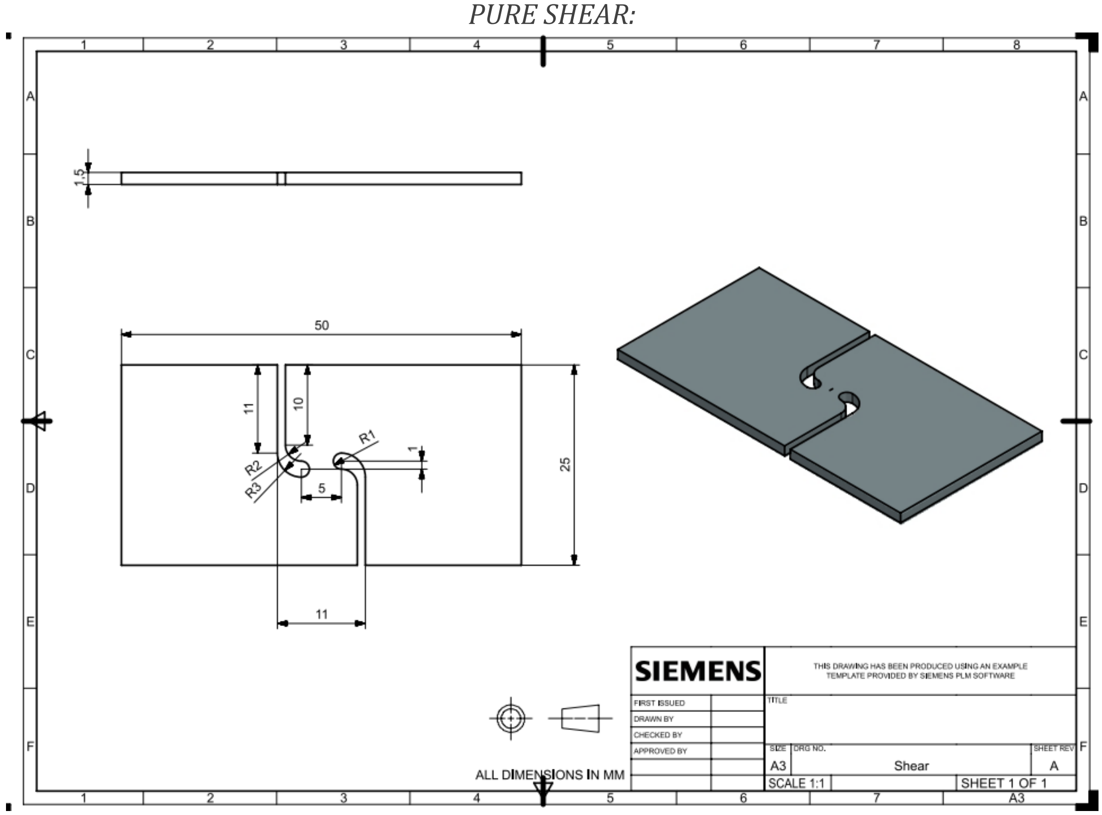

SHEAR-TENSION (10, 30):

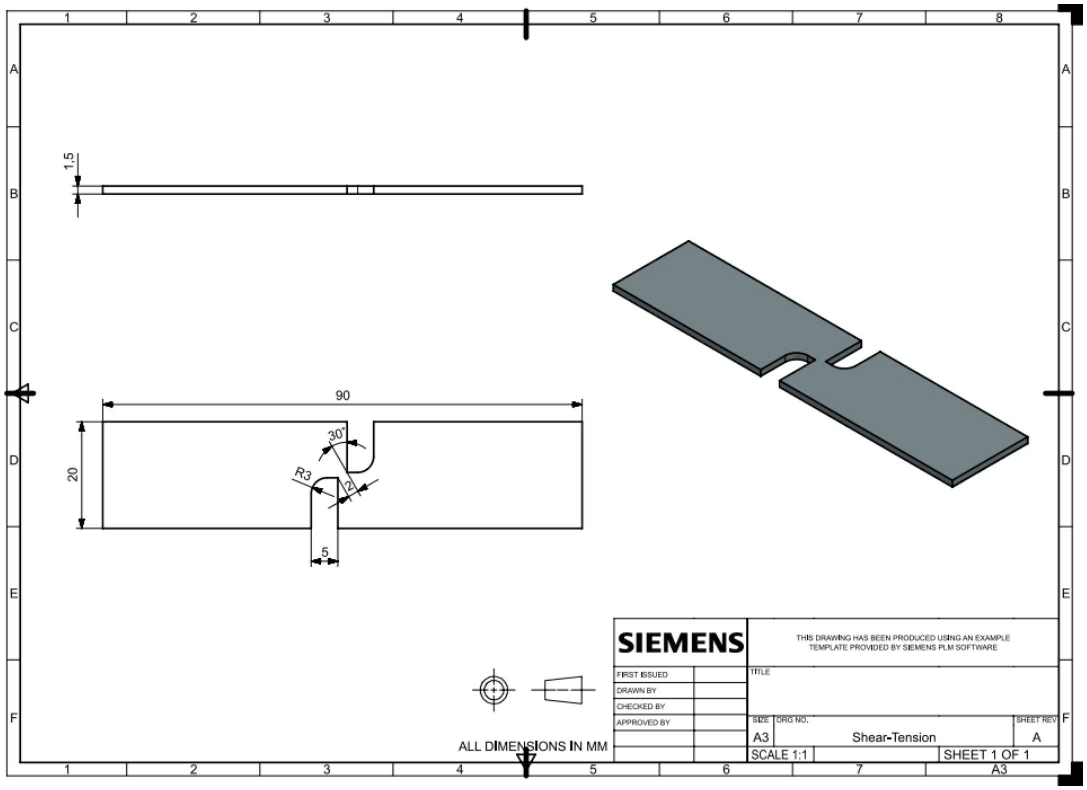

DYNAMIC AXISYMMETRIC COMPRESSION CYLINDER:

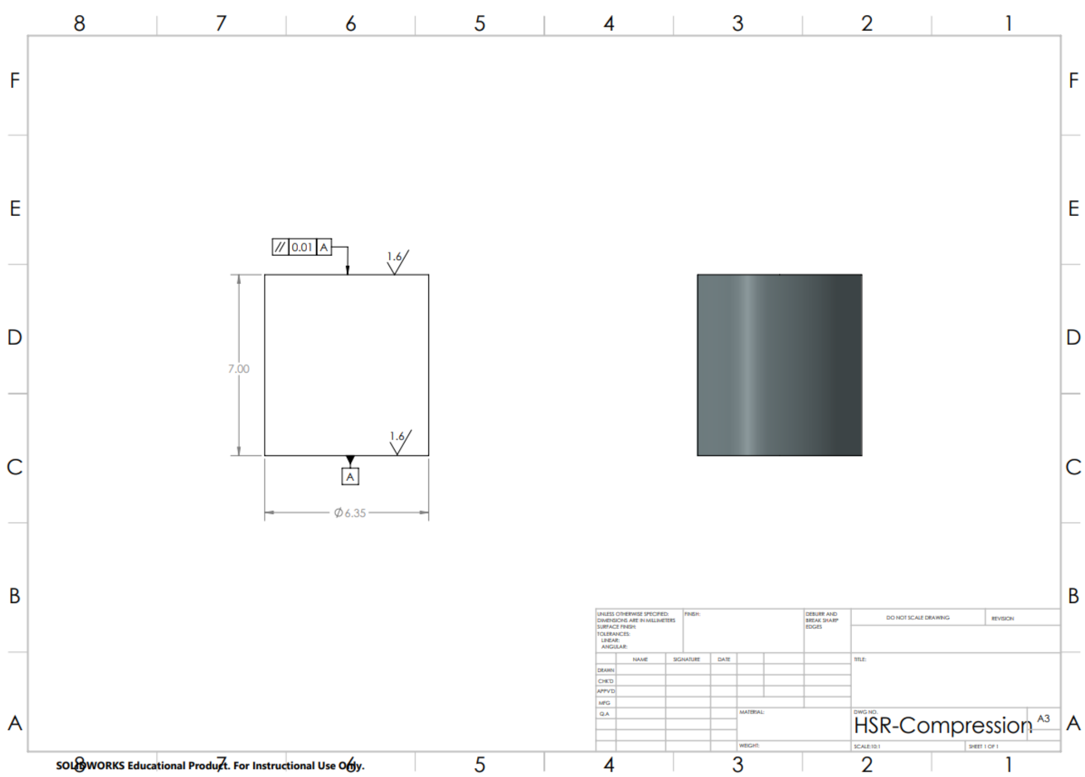

DYNAMIC AXISYMMETRIC COMPRESSION-SHEAR (CS10):

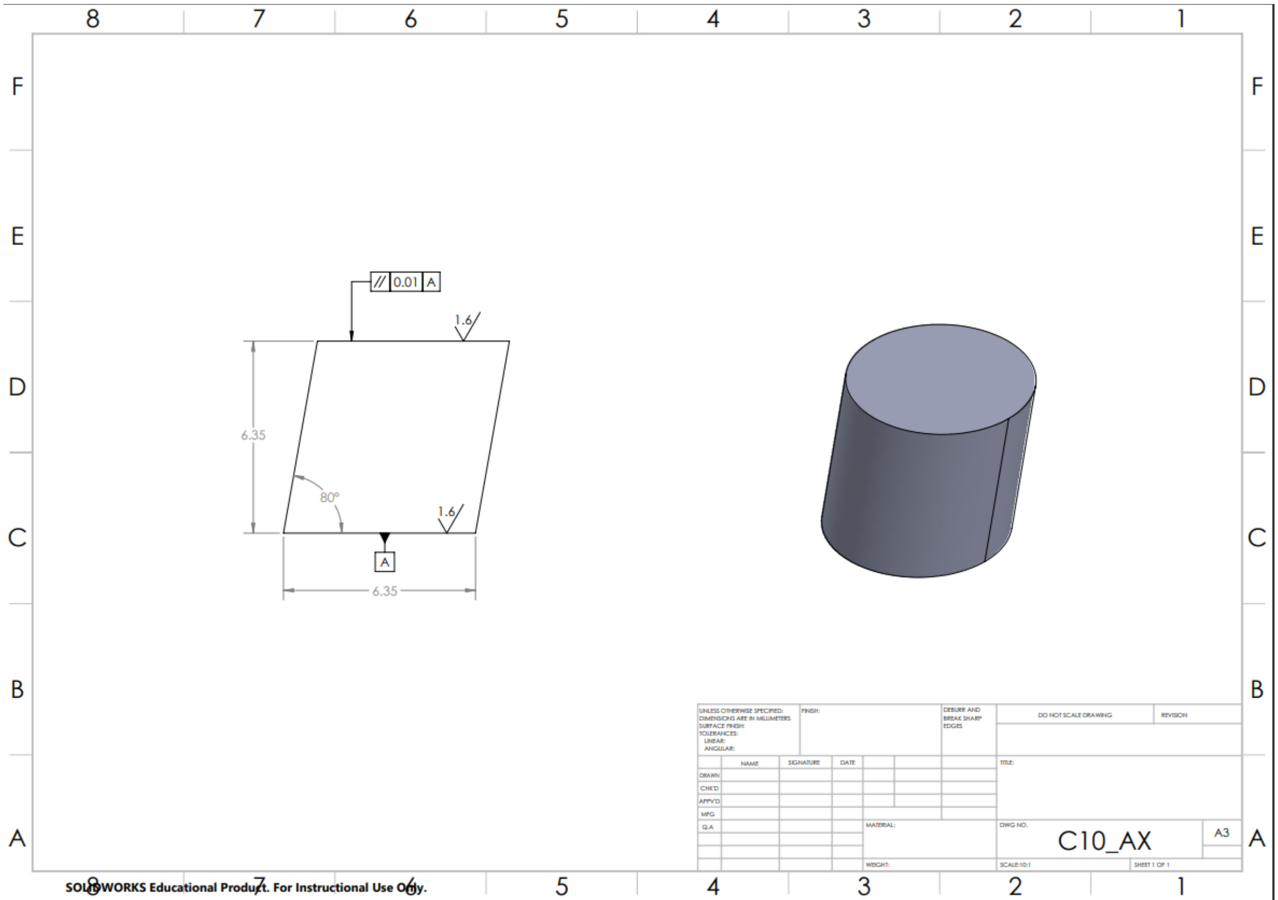

DYNAMIC AXISYMMETRIC TENSION: